Morphogenesis of curved structural envelopes under fabrication constraints

Xavier Tellier

UNIVERSITÉ PARIS-EST

École doctorale Science, Ingénierie et Environnement

Manuscrit préparé pour l'obtention du grade de docteur de l'Université Paris-Est

Spécialité: Structures et Matériaux

Morphogenesis of curved structural envelopes under fabrication constraints

Xavier Tellier

Soutenue le 26 mai 2020

Devant le jury composé de :

Rapporteurs	Helmut Pottmann	TU Viennes / KAUST
	Christopher Williams	Bath / Chalmers Universities
Présidente du jury	Florence Bertails-Descoubes	INRIA
Directeurs de thèse	Olivier Baverel	École des Ponts ParisTech
	Laurent Hauswirth	UGE, LAMA laboratory
Co-encadrant	Cyril Douthe	UGE, Navier laboratory

Abstract

Curved structural envelopes combine mechanical efficiency, architectural potential and a wide design space to fulfill functional and environment goals. The main barrier to their use is that curvature complicates manufacturing, assembly and design, such that cost and construction time are usually significantly higher than for parallelepipedic structures. Significant progress has been made recently in the field of architectural geometry to tackle this issue, but many challenges remain. In particular, the following problem is recurrent in a designer's perspective: Given a constructive system, what are the possible curved shapes, and how to create them in an intuitive fashion?

This thesis presents a panorama of morphogenesis (namely, shape creation) methods for architectural envelopes. It then introduces four new methods to generate the geometry of curved surfaces for which the manufacturing can be simplified in multiple ways. Most common structural typologies are considered: gridshells, plated shells, membranes and funicular vaults. A particular attention is devoted to how the shape is controlled, such that the methods can be used intuitively by architects and engineers. Two of the proposed methods also allow to design novel structural systems, while the two others combine fabrication properties with inherent mechanical efficiency. The feasibility of these new structural morphologies is demonstrated by the construction of two research pavilions.

A video presentation giving an overview of this doctoral work can be found online at the following URL address: https://doi.org/10.5281/zenodo.3956351

Résumé

Les structures à double courbure allient performance mécanique et expressivité architecturale. Elles offrent également de vastes possibilités formelles permettant dans un projet d'atteindre à la fois des critères fonctionnels et environnementaux. Le principal obstacle à leur utilisation est la complexité qu'elles engendrent, tant du point de vue de la fabrication et de la mise en place que de la conception. D'importants progrès ont été accomplis récemment sur cet aspect par le récent domaine de la géométrie architecturale. Cependant, il reste de nombreux défis. En particulier, du point de vue d'un concepteur, le problème suivant revient régulièrement : quelles formes sont réalisables avec un système constructif donné ? Comment atteindre ces formes de façon intuitive ?

Cette thèse commence par présenter un panorama des méthodes de morphogenèse, c'est-à-dire de création de forme, sous contrainte de fabrication. Puis, quatre nouvelles méthodes de génération de forme sont introduites. Elles permettent chacune d'obtenir des propriétés constructives simplifiant les procédés de fabrication. Les principales typologies de structures courbes sont considérées : gridshells, membranes tendues, voutes maçonnées, et coques discrètes. Une attention particulière est accordée à la façon dont les formes sont contrôlées, afin de garantir une génération intuitive.

Parmi ces méthodes, deux permettent de concevoir de nouveaux systèmes structurels, et deux autres permettent de combiner propriétés mécaniques et efficacité mécanique. Leur potentiel est démontré par la construction de deux pavillons.

Une présentation résumant ces travaux a été enregistrée en vidéo, et est accessible au lien suivant : https://doi.org/10.5281/zenodo.3956351

Acknowledgement

I would like to start this manuscript by expressing my gratitude to all the people who made this PhD possible, who helped me at some point of the journey, or who just contributed in making this experience so enjoyable and enriching.

I would like to first thank the members of the jury for taking the time to assess my work, provide their valuable feedbacks, and initiate fascinating discussions.

I would then like to thank my supervisors and advisors: Laurent Hauswirth for his enthusiasm and patience in bringing me into his world of mathematics, Olivier Baverel for his guidance and enthusiasm, which initiated fruitful and exciting work, and Cyril Douthe for his nourished help on all the kinds of difficulties I encountered. I much appreciated working with the three of you.

I would also like to thank the researchers who helped me overcoming scientific obstacles. In particular, Laurent Monasse for his precious help on numerical methods, Sebastien Brisard for his valuable feedbacks on shell mechanics, Johannes Wallner and Pierre Alliez for their help on discrete differential geometry models and Mathieu Lerouge for his great work on coding algorithms to construct Caravel meshes. I am also grateful to the anonymous reviewers of the research articles, some comments were highly instructive and improved the quality of the present manuscript. I also warmly thank all the people involved in the IASS and Coriolis pavilions (figures 4.2 and 4.1), in particular Alexandre, Sonia, Thibault and Guillaume for their bright design work.

En Français maintenant, je remercie tous ceux qui m'ont donné des opportunité d'enseignement, à l'Ecole des Ponts et aux ENSA de Paris Malaquais et Belleville, tant cela a été une expérience enrichissante pendant ces trois ans. Un grand merci à Raphaël Fabbri pour m'avoir accueilli dans son équipe d'enseignement de géométrie et partagé son expertise sur le sujet.

J'aimerais remercier toute l'équipe du laboratoire Navier de rendre cet endroit à la fois chaleureux et stimulant. Je remercie tout d'abord Marie-Françoise pour nous simplifier autant la vie, et l'équipe technique, en particulier Adrien et Christophe du fablab, et Hocine et Gilles pour leur précieuse aide. Je remercie aussi la joyeuse équipe des doctorants MSA, Philippe, Katya (auteur de la remarquable mise en contexte de la figure 5.1), Charlotte, Vianney, Leo, Tristan, tous les Julien, tous les Nicolas, tous les Paul, tous les Romains, tous les Pierre, Robin, Marie, Lionel, Laura, Deborah, Leila, Koliann, Le Hung, Sébastien et tous les autres (certains sont d'ailleurs visibles sur la figure 3.8). Je remercie Nicolas pour tous ses retours sur mon travail, et aussi pour nos discussions géométriques palpitantes.

Je remercie aussi tous mes amis. Merci de m'avoir écouté patiemment parler de géométrie pendant ces années, et de m'avoir aidé à me changer joyeusement les idées. J'ai une pensée particulière pour Alberto, Hellwig, Stéphane, Charlotte, Alexia, Marie, Bianca, Vincent, William, Matthieu, Cyril, Zaza, Floriane, Gaëlle, Cécile et Meggie, vous avez été un soutien essentiel ! Je remercie bien sûr mes parents, ma famille pour leur soutien dans cette grande aventure.

Compte-tenu des évènements de 2020, la soutenance de thèse a dû être reportée et finalement soutenue à distance, sans autre membre du jury présent et sans public. L'expérience aurait été bien triste si je n'avais pas été si bien entouré. Tout d'abord de Luc-Emmanuel, que je remercie chaleureusement pour avoir mis en place un studio professionnel dans mon salon pour la retransmission, et aussi pour m'avoir aidé à décompresser, par exemple en utilisant le fond vert installé pour l'occasion pour présenter la météo avec un professionnalisme déconcertant. Et entouré, enfin, de Carolina, qui a comme à son habitude rempli cette journée de joie.

Outline

Chapter 1 Problem statement

1.1 Double curvature structures

Double curvature surfaces offer a very rich design potential, and can be used to design unique building envelopes. They have been a major trend in architecture in the past decades. The expressivity of many recent landmark buildings, such as the Gherkin tower in London relies on curvature. The rise of double curvature in contemporary architecture started in particular with the deconstructivist movement. An iconic example is the Guggenheim museum in Bilbao (Figure 1.1). This museum was a key stone of a massive investment project to re-dynamize the city after an industrial crisis. The curved façade of the museum, design by architect Frank Gehry, has redefined the image of the city, now modern and anchored in the XXIth century. The success of this program, in term of attraction of tourists and investments, has been such that is now known as the Bilbao effect (Plaza 2007). This success has incited many cities to invest in iconic buildings, which most often have double curvature envelopes, such as the centre Pompidou in Metz of the Louvre Abu Dhabi (Rothenthal *et al.* 2018).

Figure 1.1: Iconic curved structures. Left: Guggenheim museum in Bilbao (©Mike Reeve) Right: Pompidou Metz (©Guido Radig)

Beyond their aesthetic potential, double curvature structures can also offer high mechanical performances. It is what gives a light egg shell its remarkable strength. Engineers are well aware that an arch is more efficient than a straight beam. Similarly, a curved vault can resist a much higher vertical load compared to a flat slab with the same amount of material. The CNIT near Paris (Figure 1.2) illustrates well this potential: its concrete shell spans 218 m for a thickness of only 8 cm. This efficiency is magnified in funicular structures: these can withstand a given load with pure axial forces. The absence of bending moment makes stresses in the section more uniform, thus avoiding waste of material. Curvature can be used structurally for buildings of all sizes, from the impressive span of the CNIT to the much cozier vaults of the Oyster bar in New York (Figure 1.2). Double curvature, compared to single curvature, is interesting

when stability is critical in design. Local and global buckling resistance is significantly increased by Gaussian curvature, which quantifies the double curvature (a cylindrical vault has zero Gaussian curvature). The buckling strength of the CNIT is for example greatly increased by its corrugations, which increase the double curvature and give structural height to the shell.

Figure 1.2: Left: The concrete shell of the CNIT (©Alexandre Prevot).
Right: Guastavino vault of the Grand Central Oyster bar in Manhattan (©Flicker4Jazz)

Curvature and complex geometries also allows to fulfill other building functions, and to optimize an envelope for other criteria, such as control of sun shading (Wang *et al.* 2013), sun energy collection (Kotelnikova-Weiler 2012) or the Life Cycle Analysis.

1.2 Complexity

Complexity is the main barrier for the construction of curved shapes. It tends to make these project much more expensive than parallelepipedic buildings.

Complexity comes first from fabrication. Construction materials come out of the factory as straight beams or planar sheets. To assemble them in a curved configuration, factory transformations are needed, and often have a significant cost. An example is curved glass. Theoretically, any shape is possible in glass. However, in practice, curved glass panels are up to thirty times more expansive to produce than planar ones, and fabricators can only obtain certain primitives.
This complexity is increased by two factors. First, curved geometries often require a tighter tolerance, hence a higher precision is needed in the manufacturing. Secondly, in most curved structures, all elements are different. This often results in the need for costly tailored solutions. An example is the nodes of the great roof of the British Museum. Because of the complexity of their shapes and the fact that they are all different, they had to be plasma-cut out of 20 cm thick steel plate (Sischka *et al.* 2001).
Geometrical complexity can even make a structure unfabricable. A famous example is the Sidney Opera House. The original shape was not buildable, such that it took engineering office Arup seven years to rationalize the shape, which eventually was transformed into portions of spheres (Schodek *et al.* 2005).

The design process is also greatly complexified. Architectural design needs to take many factors into account, such as function, structure, aesthetic, norms, acoustics, environment... With curved structure, the geometrical complexity and the fabrication constraints are added. The geometry is often optimized to simplify fabrication. As a result, some complexity due to fabrication is transferred to the design phase. Such an optimization takes engineering time, which also has a cost. This can alter mechanics or aesthetic of the patterning, for example resulting in kink or high variations of face shapes and sizes (by *patterning*, we refer to the configuration of elements on the surface; it can be described by a network of lines, which can represent beam layout or panel junctions). Such kinks are for example visible on the façade of the Cité

de la Mode et du Design in Paris (Figure 1.3) – although in this building, kinks were intended by the architects Jakob and MacFarlane.

Complexity also appears in structural validation. For example, in a gridshell, each node has a different geometry and different internal forces, this multiplies the number of required checks – which can be especially tedious for welded connections. Furthermore, curved structures can be very efficient… or the opposite. There has been many examples throughout histories of vaults that collapsed during removal of formwork, like the Cuernavaca Chapel (designed by Felix Candela). More recently, two gridshells designed by the office SBP collapsed because the connections were not as rigid as expected (Schober 2015). The MIT Kresge auditorium suffered from higher than expected deflections during decentering, resulting in costly reinforcement work. Terminal 2E it the Charles de Gaulle Airport, a thin concrete barrel vault, tragically collapsed in 2004. The collapse mode, by punching shear, typically does not happen in planar slabs because these are much thicker. Also, one difficult aspect of optimized curved vaults is that they can be highly sensitive to imperfections, this tightens even more the precision requirement on fabrication and placement.

Special detailing is also required for non-structural aspects. In particular, waterproofing is more complex to realize. For example, the unusual geometry of the Stata center on the MIT campus resulted in unexpected leaking and drainage issues (Pogrebin and Zezima 2007).

Organization and planning also need special attention. When all elements are different, no spare part can be ordered. Additional work is required to identifying each elements and planning their fabrication and delivery to site in the right order (Rabagliati *et al.* 2014). Although manageable, this can increases cost and is a potential source of errors and delays. (Rabagliati *et al.* 2014) also point out the importance of finding proper suppliers. Facing an unusual geometry, suppliers might propose very different solutions depending on their knowledge and equipment, which might result in very different cost and production times.

Figure 1.3: Sudden changes in beam orientations and aspect ratios may hurt some sensitive eyes (©Guilhem Vellut)

1.3 Recent advances

Many problems related to construction of curved envelopes have been solved in the past decades, mostly with the help of new computational methods and digital fabrication tools.

Description of geometry

To construct a curve surface, a first task is to describe precisely its geometry. Before the advent of CAD software, options were limited, and tended to restrict surfaces to simple primitives that are well described analytically, like spheres, cylinders, tori, or hyperbolic paraboloids (“hypars”). Nowadays, designers have access to powerful generation technics. Methods like NURBS and subdivision surfaces allow to design

complex surface intuitively by controlling handle points – providing however no understanding of the constructive or mechanical properties.

Parametric design tools also significantly simplified the production of fabrication drawings. As each element is different, drawings used to be manually edited one by one – a process that is now more and more automatized on complex geometries.

Validation of mechanical behavior

An important challenge of curved envelopes before the 70's was the validation of mechanical strength. Again, options were limited. Hanging models allowed to check and find the shape of complex funicular structures. They were notably used in the work of Gaudi, or by Poleni to check the integrity of the dome of St-Peter in Roma after the apparition of cracks (Poleni 1748). In the XXth century, advances in shell mechanics yielded many analytical models to compute the strength and stiffness of simple primitives like spheres or cylinders. In order to build his concrete hypars, Felix Candela had to develop a custom mechanical model (Candela 1955). Nowadays, highly complex shapes can be checked with finite elements.

Manufacturing and materials

As discussed earlier, curved envelopes require a higher construction precision. Such a precision can be obtained with modern digital fabrication technics like CNC milling, laser cutting, water-jet cutting, additive fabrication or robotics, even if each element has a complex geometry. These methods however introduce specific geometrical constraints that need to be accounted for in design (Krolikowski and Eley 2014).

There has also been developments in materials. High performance fiber reinforced concrete allows to obtain cladding panels with complex shape and patterns. The timber industry has also made impressive progress. For example, CLT allows to get wide and strong wooden panels. Joinery technics that used to be confined to furniture can now be adapted to create large span plated shells (Robeller 2015).

Numerical and theoretical tools

In the past couple decades, computer graphics have developed a vast array of numerical methods to address geometrical problems specific to architecture (Pottmann *et al.* 2015). These advances have been backed up by the development of discrete differential geometry. This field focuses on discrete equivalents of smooth surfaces and their properties, and often relies on meshes, which are facetted surfaces. Many of the mesh geometrical structures that have been developed in this context have direct applications to architecture. An example is circular meshes, which combine several properties that simplify fabrication and connections of a gridshell – they will be introduced in section 2.2.3.

Combining design and analysis

Ten years ago, numerical tools for design and structural analysis were separate things, as pointed out in (Bagneris 2009). A designer often had to juggle between a CAD and a finite-element software to design a complex structure. Nowadays, parametric tools allow a designer to get rapid structural feedbacks on a given geometry. This makes structurally informed exploration much easier. Examples can be found in (Preisinger and Heimrath 2014; Teschemacher *et al.* 2018).

1.4 Challenges

Despite the impressive progress achieved in the past decades, there is still a large room for improvement to make curved structures more affordable.

1.4.1 Timing of rationalization

In traditional projects, fabrication is usually not an issue, and can be only accounted for in later project phases. For a curved envelope, rationalization – the modification of the geometry to improve constructability – can have a critical impact. As described in Figure 1.4, as the project develops and gets defined, the design freedom decreases, and so does the potential for rationalization. In the literature, rationalization methods are split in three categories depending on the timing at which they are implemented in a project.

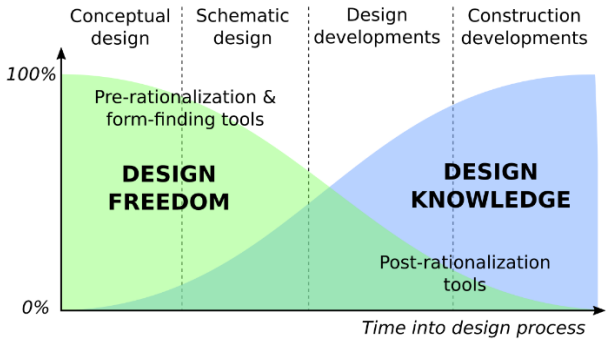

Figure 1.4: Relationship between design freedom and design knowledge in building design projects (image modified from (Paulson 1976; Mueller 2014))

Post-rationalization

Post-rationalization refers to the case where fabrication is accounted for only at a late project phase. At this point, a reference surface is usually defined, and often a patterning. Many rationalization methods have been proposed by the computer graphics community to address that. This approach has the benefit of not focusing on fabrication at previous design stages, but often has a limited impact, unless large deformations are still acceptable. One trap is that designers are often not aware of this limitation, which might result in lengthy back and forths between an optimization specialist and the architect. Also, these methods do not give intuition to the user on what shapes are adequate for the desired constraints, they rather output *one* optimized solution – which does not let room to adjust the shape for other criteria.

Pre-rationalization

At the other end of the spectrum are pre-rationalization methods: They are design tools that automatically incorporate a given set of constraints. The design freedom is then reduced to a constrained space, but they often allow a real time exploration, such that a designer can quickly look for multiples solutions. One example is scale-trans surfaces, which are very popular for gridshells covered by planar glass panels (Schober 2015). One limitation is that the constructive system must be known early enough in the project. A second limitation is that the variety of pre-rationalization methods is limited at the moment: Not many fabrication constraints can be explored, and the accessible design space might not be sufficient for the project constraints. For example, during the design of the gridshell of the Palacio de Comunicaciones by the engineering office SBP, scale-trans surfaces could not fit satisfyingly the imposed boundaries (Schlaich *et al.* 2009).

Co-rationalization
Intermediate approaches, that attempts to overcome the limitations of the previous approaches, are often labelled as co-rationalization. For example, the design of Zaha Hadid's Galaxy Soho was rationalized in two stages, before and after tender (Ceccato 2012). In the same spirit, the design of a wooden ceiling of the Burj Khalifa by Franck Gehry was based on a flexible parametrized framework, that allowed fabrication constraints to be added in later project phases (Meredith and Kotronis 2012). Literature on this approach is mostly project specific.

1.4.2 Need for intuitive fabrication-aware design tools

Being able to generate shapes that combine fabrication and mechanical properties is one thing. Being able to make such shapes fit other project constraints like ground implantation is better. But the best option is to be able to control intuitively the shape, as it is then possible to take into account aspects that cannot be expressed formally. The challenge raised by intuitive shape generation was highlighted in (Mesnil 2017). (Yang and Zhao 2015) makes the same observation about the new possibilities of 3D printing to design objects with special physical function allowed by the control of their complex micro-structure (deformability, mechanical behavior…): intuitive user-friendly methods are crucial for them to be adopted by makers.

1.4.3 Integrated tools

Curved envelopes, even more than in other types of architectural projects, need to combine constraints that can be contradictory. Focusing solely on fabrication can result in shapes not efficient mechanically – For example, the shells of the Sidney Opera, rationalized as sphere portions for constructability, had to be stiffened with concrete 1.2 m deep ribs, which is quite a difference from the uniform 8 cm of the CNIT. On the other hand, focusing on mechanics alone can result in unbuildable structures. This is for example one major limitation of topology optimization, which research recently started to address (Stromberg *et al.* 2011; Mesnil *et al.* 2017).
Two approaches are possible to deal with multiple constraints, like fabrication and structural behavior. The first one is to have shape generation methods that take all parameters into account. The second one is to have a method that takes only a few aspects into account, but that gives a design space wide enough to fulfil other constraints.

1.4.4 Open geometrical problems

Many geometrical problems have not been satisfyingly solved yet from the point of view of a designer. For example, paneling algorithms allow to obtain some degree of repetition in the panels of a curved facade. However, on an arbitrary shape, there is no guarantee that this type of algorithm will succeed with reasonable surface modification, and there is currently no tool at the moment that allows to explore shapes fulfilling this repetitivity constraint, and to design based on it.

1.4.5 Environmental considerations

Curved structures can be very efficient mechanically, and are one way to reduce the amount of material used by the construction industry. Funicular structures are intensively researched for that purpose However, the complexity of these structures often result in other forms of environmental impact.

Typologies like concrete shells require a massive amount of formwork, which is often dumped after construction. (Kuzmenko *et al.* 2019) recently pointed out that resorting to robotics to optimize material use can have significant impact on the overall life cycle analysis. Furthermore, the re-use of elements after deconstruction is much more difficult when all elements are different. Also, new materials that are well suited for complex shape, such as high performance concrete for 3D printing or engineered wood products, have a higher environmental cost because in particular of the additive and glue they require.

1.5 This manuscript

1.5.1 Goals

The goal of this manuscript is to make curved structures more accessible. In particular, make them more affordable by allowing a simplification of manufacturing processes, and less complicated to generate, so that design complexity is not a barrier.

This goal is pursued by proposing morphogenesis methods:

- For families of surfaces with geometrical properties that simplify the fabrication, and allow to obtain mechanical performance, such that cost and environmental impact can be reduced;
- Intuitive to use, such that they can be used by non-experts in geometry;
- That allows to explore a large panels of solutions, such that other constraints than fabrication and mechanics can be accounted for;
- For new structural systems for curved structures, which are based on new rationalization methods.

1.5.2 Organization of dissertation

Chapter 2 draws a panorama on fabrication-aware morphogenesis of surfaces. The following four chapters introduce each a generation method for specific families of surfaces, with particular fabrication and mechanical properties.

Chapter 3 pertains to surfaces with planar curvature lines and their application to gridshells. It draws on XIXth century differential geometry to propose a fast and intuitive generation method for this rich family of surfaces. Chapter 4 introduces a new mesh geometrical structure: Caravel meshes. The properties of these meshes allow to simplify all the connections of a gridshell: connections between beams, and connections between cladding panels and beams. It also allows to build plated shells.

The following two chapters take mechanics into account and propose methods to construct two families of funicular meshes. In chapter 5, a generation method is presented for S-CMC meshes, a discrete model of surfaces with constant mean curvature (CMC). For a gridshell, the resulting geometries combine fabrication and mechanical properties. In chapter 6, we address generation of Linear Weingarten surfaces. This family of surfaces contains minimal, CMC, developable surfaces and pseudo-spheres, but also many other surfaces in-between. The method can be used to design tensile membranes, masonry vaults, and gridshells. These surfaces are addressed both in Euclidian and isotropic geometry, such that structures funicular for two different load cases can be obtained: uniform normal pressure or uniform vertical load.

1.5.3 Methods

This manuscript relies on methods from different scientific fields. Surface theory and discrete differential geometry are used jointly. In particular, most chapters rely on the Gauss map to describe the node axes of curved structures. Part B of chapter 6 is based on isotropic geometry, in which the Gauss map is defined relatively to a paraboloid instead of a sphere. Optimization algorithms are used in chapters 4 to 6. The last chapter also resorts to mechanics of membranes and arcs.

References

Bagneris, M. (2009) *Contributions à La Conception et à La Réalisation de Morphologies Non-Standard : Les Formes Pascaliennes Comme Outil*.

Candela, F. (1955) 'Structural applications of hyperbolic paraboloidical shells', *ACI Journal Proceedings*, 51(1), 397–416.

Ceccato, C. (2012) 'Material Articulation: Computing and Constructing Continuous Differentiation.', *Architectural Design*, 82(2), 96–103.

Kotelnikova-Weiler, N. (2012) *Optimisation Mécanique et Énergétique d'enveloppes En Matériaux Composites Pour Les Bâtiments*.

Krolikowski, D., Eley, D. (2014) 'The Leadenhall Building. Design for fabrication- digital workflow and downstream fabrication system performance', in Gramazio, F., Kohler, M. and Langenberg, S., eds., *Fabricate*.

Kuzmenko, K., Gaudilliere, N., Dirrenberger, J., Baverel, O. (2019) 'Assessing the Environmental Viability of 3D Concrete Printing Technology', in *Design Modeling SYmposium. Impact: Design With All Senses*.

Meredith, N., Kotronis, J. (2012) 'Self-Detailing and Self-Documenting Systems for Wood Fabrication: The Burj Khalifa', in *Advances in Architectural Geometry*, 185–198.

Mesnil, R. (2017) *Structural Explorations of Fabrication-Aware Design Spaces for Non-Standard Architecture*.

Mesnil, R., Baverel, O., Douthe, C., Caron, J.F., Leger, B. (2017) 'Structural morphology and performance of plated structures with planar quadrilateral facets', *Journal of the International Association for Shell and Spatial Structures*, 58(1), 7–22.

Mueller, C.T. (2014) *Computational Exploration of the Structural Design Space*.

Paulson, B.C. (1976) 'Designing to Reduce Construction Costs', *Journal of the Construction Division*, 102(4), 587–592.

Plaza, B. (2007) 'The Bilbao effect (Guggenheim Museum Bilbao)', *Museum news*, 86(5).

Pogrebin, R., Zezima, K. (2007) 'M.I.T. Sues Frank Gehry, Citing Flaws in Center He Designed', *The New York Times, https://www.nytimes.com/2007/11/07/us/07mit.html, accessed 2020 Jan 29*, Nov. 7.

Poleni, G. (1748) *Memorie Istoriche Della Gran Cupola Del Tempio Vaticano*, e-rara.ch.

Pottmann, H., Eigensatz, M., Vaxman, A., Wallner, J. (2015) 'Architectural geometry', *Computers and Graphics (Pergamon)*, 47, 145–164.

Preisinger, C., Heimrath, M. (2014) 'Karamba - A toolkit for parametric structural design', *Structural Engineering International: Journal of the International Association for Bridge and Structural Engineering (IABSE)*, 24(2), 217–221.

Rabagliati, J., Huber, C., Linke, D. (2014) 'Balancing complexity and simplicity', in *Fabricate*, 43–51.

Robeller, C.W.M. (2015) *Integral Mechanical Attachment for Timber Folded Plate Structures*, available: https://infoscience.epfl.ch/record/205759/files/EPFL_TH6564.pdf.

Rothenthal, G., Ziegler, R., Spasis, D. (2018) 'Oasis of Light – Manufacturing the Cladding of the Louvre Abu Dhabi', in *Advances in Architectural Geometry*, 274–285.

Schlaich, M., Burkhardt, U., Irisarri, L., Goñi, J. (2009) 'Palacio de Comunicaciones – a single layer glass grid shell over the courtyard of the future town hall of Madrid', in *Proceedings of the IASS Symposium, Evolution and Trends in Design, Analysis and Construction of Shell and Spatial Structures*, 1338–1348.

Schober, H. (2015) *Transparent Shells: Form, Topology, Structure*, Ernst & Sohn.

Schodek, D., Bechthold, M., Griggs, K., Kao, K.M., Steinberg, M. (2005) *Digital Design and Manufacturing*, John Wiley & Sons.

Sischka, J., Brown, S., Handel, E., Zenkner, G. (2001) 'Die Überdachung des Great Court im British Museum in London', *Stahlbau*, 70(7), 492–502.

Stromberg, L.L., Beghini, A., Baker, W.F., Paulino, G.H. (2011) 'Application of layout and topology optimization using pattern gradation for the conceptual design of buildings', *Structural and Multidisciplinary Optimization*, 43(2), 165–180.

Teschemacher, T., Bauer, A.M., Oberbichler, T., Breitenberger, M., Rossi, R., Wüchner, R., Bletzinger, K.U. (2018) *Realization of CAD-Integrated Shell Simulation Based on Isogeometric B-Rep Analysis* [online], Advanced Modeling and Simulation in Engineering Sciences, Springer International Publishing, available: https://doi.org/10.1186/s40323-018-0109-4.

Wang, J., Jiang, C., Bompas, P., Wallner, J., Pottmann, H. (2013) 'Discrete line congruences for shading and lighting', *Computer Graphics Forum*, 32, 53–62.

Yang, S., Zhao, Y.F. (2015) 'Additive manufacturing-enabled design theory and methodology: a critical review', *International Journal of Advanced Manufacturing Technology*, 80(1–4), 327–342.

Chapter 2
A panorama of generation methods for curved structural envelopes

2.1 Introduction

2.1.1 Scope and aims of the review

This chapter proposes a review of numerical fabrication-aware shape generation methods, geared towards designers. It will strive to highlight the links between a desired manufacturing process, how it results in geometrical constraints, how these constraints affect the design space, and the existing generation methods to explore the possible shapes. Outline of the review is depicted in Figure 2.1. First, in section 2.2, we review common fabrication constraints, and how they can be expressed in geometrical terms. Then, section 2.3 highlights the impact of constraints on design freedom. Finally, section 2.4 gives a panorama of relevant methods for generation of form and pattern. The example of a gridshell with planar glazing illustrates the division of the chapter (bottom of Figure 2.1).

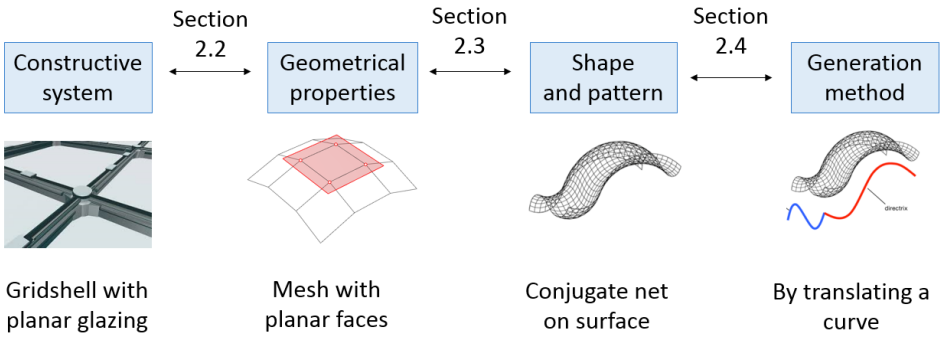

Figure 2.1: Organization of chapter

2.1.2 Existing literature reviews

There exists already many reviews related to shape generation or fabrication-aware design. This section starts by "reviewing the reviews" in order to highlight the originality of this chapter.

Classifying morphogenesis methods
Williams (2000) and Bagneris et al. (2008) decompose morphogenesis methods in three families. A first one encompasses methods focusing mostly on designing mechanically efficient structures – sometimes referred to as mechanically-constrained approach. A second family, often called geometrically-constrained approach, is based on geometrical principles. These methods usually resort to intuitive generation methods, such as a combination of simple primitives, or the motion of a curve through space. This way of generating a surface often result in good fabrication properties. A third family is based purely on form, without consideration of fabrication or mechanics. The form might be based on function or aesthetic. For example, the shape of the Canopee des Halles in Paris mostly derives from the necessity to evacuate smoke in case of fire. A forth family could be added, which is to take greater and greater importance: designing for low environmental impact. We refer more precisely to the case where environmental considerations are driving the shape. This includes a combination of geometrical issues (e.g. related to fabrication, thermal performance, potential re-use…), mechanics and types of materials.

Reviews
Numerical mechanically constrained methods have been studied since the 70's. Reviews of form-finding methods of funicular[1] structures can be found in (Adriaenssens *et al.* 2014). A review of applications of dynamic relaxation, a wide-spread method, is proposed in (Barnes 1999).

Methods based on geometry and fabricability have received a lot of attention recently. Pottmann, Asperl, et al. (2007) offer a wide review of the geometrical concepts relevant to architecture. Fischer (2012) exposes the evolution of the practice of rationalization in a non-technical manner. (Pottmann 2013) and (Pottmann *et al.* 2015) review the contributions to architectural geometry from the computer graphics community. The focus is on computational aspects, and might be out of reach for a designer. Bermano et al. (2017) reviews recent advances in fabrication-aware design methods for small scale objects. Schober (2015) reviews pre-rationalization methods that have been used on numerous gridshell projects of the structural engineering firm SBP. Schodek (2005) reviews practical design and production aspects for complex geometries. Austern (2018) reviews the type and timing of rationalization used in 500 industrial and academic projects – without particular focus on double curvature.

Reviews of generation methods that do not account for constraints can also be a great source of inspiration and exploration. Delarue (1992) proposes a panorama of morphogenesis methods for his architecture students, focusing on methods that can be apprehended intuitively. The website Mathcurve.com, by Robert Ferréol, presents a vast list of surfaces along with their geometrical properties. Krivoshapko and Ivanov (2015) attempt to give an exhaustive list of analytical surfaces. Farin et al. (2002) presents in-depth numerical methods used in CAD.

The present review
The scope of this review is the fabrication-aware numerical generation of building-size double curvature structures. Compared to other reviews on the topic (in particular (Pottmann *et al.* 2015)), this review targets designers, and will try to help in answering the following question. Given a set of constraints due to the site and the current level of definition of the project, what are the available fabrication-aware shape generation methods? What are their input, freedom and properties?

[1] A structure is said to be funicular if it can resist a given load with pure axial stress, without bending stresses.

2.2 Geometrical formalization of fabrication and mechanical constraints

This section looks at the geometrical properties that simplify (or *make possible*) the fabrication of the main constitutive elements of a curved structure. The most common typologies of curved structures are considered: gridshells, discrete and continuous shells, membranes, masonry vaults. By gridshell, we broadly mean a network of beams with shell-like mechanical behavior.

2.2.1 Cladding panels

Panels are used in gridshells as cladding elements, or in discrete shells as structural elements. They are usually cut out of planar sheets, this introduces specific desired properties to limit additional manufacturing steps.

Planar panels

A common constraint on panels is planarity. Although most materials can be given curved shapes, planar panels are usually much cheaper to produce. For example, curved glass panels can be more than 30 times more expensive than flat panels (Eigensatz *et al.* 2010) – this being mostly due to the cost of molds. Although some types of panels can be elastically bent at low cost, most are not flexible enough, like CLT or composite panels. For double-glazing, beyond the fabrication cost, curved panels also face issues with thermal dilatation of the insulating layer, which is restrained by the geometrical stiffness of the panels.

The level of constraint of face planarity depends on the type of facets. For example, with a triangular pattern, faces are always planar. However, in an arbitrary quadrangular or hexagonal pattern, faces are usually not planar. The planarity constrain becomes stronger as the number of edges increases, as shown in Figure 2.2. In particular, for hexagonal meshes, faces cannot be convex on an anticlastic surface[2], as will be detailed in section 4.1.

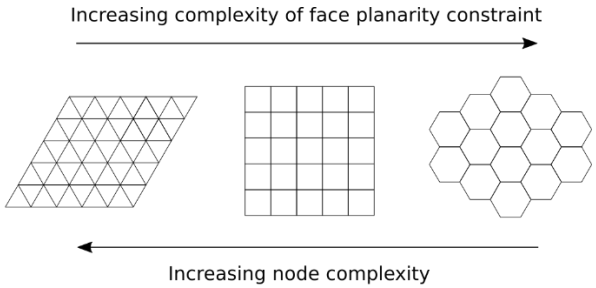

Figure 2.2: Pattern and the balance between node complexity and panel complexity

Single curvature panels

Flexible sheet materials can be cheaply elastically bent into curved shapes. Thin panels then naturally take the shape of developable surfaces[3]. Metallic developable panels have been a trademark of architect Frank Gehry (Shelden 2002). Single curvature panels are also popular for glass facades. Small curvatures can be obtained by cold bending, for example on the new Strasbourg train station envelope (Blassel and Pfadler 2008). A more important curvature requires hot bending, which is done in factory. Depending on the supplier, only cylindrical shapes might be possible (like for the Fondation Vuitton in Paris) or conical

[2] A surface is called anticlastic if at any point, the geometry of the surface in the neighborhood of the point is shaped like a saddle – and not like a dome. Mathematically, this means that the Gaussian curvature is everywhere negative.

[3] Developable surfaces are smooth surfaces that can be deformed into a planar configuration without stretching the material, with only bending deformations. Mathematically, their Gaussian curvature is null at any point.

shapes. Although single curvature panels are mostly used for cladding, (Leduc *et al.* 2018) demonstrated with the Euplectela Folie Pavilion how they can be used to construct highly rationalized lightweight structures.

Shaped as given primitives

More complex panel shapes can be obtained by a combination of pressure and heat. For example, glass panels can be heated to take the form of molds. These molds need a very smooth surface finish. They are therefore usually not available in arbitrary shapes, but in a collection of primitives, for example spherical or paraboloids.

Repetition

Repetition of panels can significantly reduce project costs. Exact face repetition is a very strong constraint, and yields non smooth shapes (Huard 2014). However, small kinks and gaps in the paneling can be accommodated at the joints between panels. Hence, identical panels can fit faces of slightly different sizes. For curved glass, two strategies allow for partial repetition. A first one is to deform identical panels into different shapes. For example, panels of the Fondation Vuitton are cylinders obtained by bending panels with standard rectangular size. A second one is to use the same molds with different trimming (Eigensatz *et al.* 2010).

Size

Cladding panels are cut out of large standard size panels. There is therefore an upper boundary on the size of faces. A notable example are glass panels, which cannot be larger than a factory float line. Fiber-reinforced concrete panels are often used as façade elements. Although theoretically of unlimited size, their width is limited to allow road transportation from factory (Fabbri and Corvez 2013). A high variation of panel sizes is also often undesirable for aesthetic and structural reasons.

Nearly rectangular or square panels

Near-rectangular or near square panels are the most likely to limit waste from nesting on standard rectangular sheets (Pottmann *et al.* 2015). Furthermore, they avoid acute angles. With glass, they can offer better light transmission, and arguably better aesthetic, than skewed quadrangles.

Conical meshes, plated shell with plates of constant thickness

To design a plated shell with planar plates of constant thickness, if one takes the offset of an arbitrary mesh with planar faces, complex junction appear at the panel corners, as shown in Figure 2.3. This complexifies milling and alters the aesthetic. This problem is highly increased if angles between adjacent faces is high, which is for example the case for folded surfaces made of CLT panels (Buri and Weinand 2008). Conical meshes, introduced in (Liu *et al.* 2006), do not have these kinks. They are meshes with planar faces such that there exists at each vertex a right circular cone tangent to each adjacent faces, with the cone apex located on the vertex. They guaranty that the bisecting planes of each edge around a node meet on a common axis.

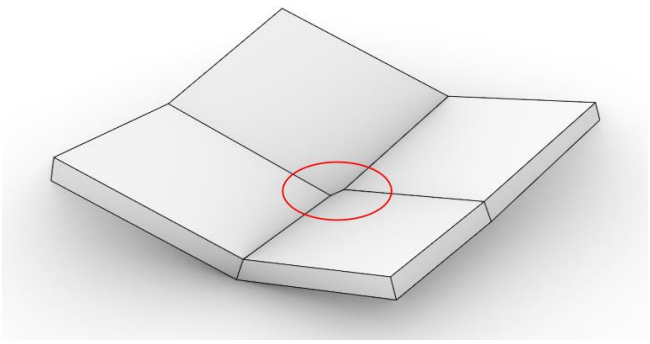

Figure 2.3: Offsetting a non-conical planar mesh results in kinks at panel junctions

No kink angle between panels and beams
In a curved envelope, there is usually a kink angle between cladding panels and support beams. This angle complexifies the connection. It has not been addressed by the literature, and will be discussed in detail in chapter 4.

Minimum slope
For rain water to be evacuated properly, panels must have a sufficient slope everywhere on the surface.

2.2.2 Beams

Some geometrical properties can significantly simplify the fabrication of beams. In a curved structure, beams can be continuous, in which case they are curved, or they can be discrete and span from one node to the other, in which case they may be straight or curved. This yields to different desired properties

Repetition
As for panels, project costs can be decreased if many beams have the same geometry. This requires a constant length on the mesh. For example, the beams of the dome of the Neckarsulm swimming pool (Figure 2.17) are all identical. This property is not as interesting as node repetition, as it it is relatively easy to cut beams at different lengths.

Circular beams
A common method to produce curved steel beams is to roller bend initially straight beams. This method has a much better precision if the beam has a constant radius of curvature and is planar. This point will be addressed in chapter 3.

Cut perpendicularly to a beam face
Machining of beams can simplify their connection with other elements. This process can be simplified by some geometrical properties. For example, cutting a wooden beam with an arbitrary orientation is more complex than cutting in a plane perpendicular to a face of the beam, which can be done with a good precision by hand using inexpensive equipment. This property was used for the fabrication of the timber Caravel pavilion, discussed in chapter 4. It was also used for the fabrication of the aluminum heX-Mesh pavilion (also in chapter 4). Its beams are laser-cut, a process that can only cut perpendicularly to a plate, like 3-axes CNC milling (a process significantly cheaper than the 5-axes CNC required when cuts are not perpendicular).

Dealing with geometrical torsion
If we draw an arbitrary curve on a surface, the normal vector undergoes torsion (or twisting): it rotates around the tangent vector. Because of this torsion, many geometrical issues appear when passing from a skeleton geometry – where beams are modelled as lines – to a 3D structure. These problems increase with the torsion of the curve and the beam height. There are five common approaches to deal with torsion, illustrated in Figure 2.4:

i. Set all the node axes in the same direction. For example, if all the axes are vertical, they can be connected by vertical planes, which can be used to define beams midplanes. This strategy was for example used in the design of the France pavilion at the Milan World Expo 2015, constructed by timber specialist Simonin. However, this solution causes many issues when the surface has a high slope. Firstly, the top surface of the beams is at a high angle with the surface, thus making difficult the connection with cladding panels. Secondly, structural efficiency with respect to wind load is reduced. Finally, there is a high obstruction of light and view.

ii. Twist beams. Torsion can be accommodated using twisted beams. This twist can be imposed by elastic deformations. It can also be obtained by milling timber profiles. However, as wood fibers become discontinuous, mechanical performance may be strongly altered.
iii. Use circular profiles. Thanks to their symmetry, circular profile can accommodate any geometrical torsion at their end. However, if the structure needs to support another structural layer, this one will also encounter issues due to torsion. Yet, this is not the case for the gridshell of the Jay Pritzker Pavilion in Chicago.
iv. Accommodate torsion at nodes. Figure 2.4 shows a node with torsion in the steel gridshell MyZeil (Knippers and Helbig 2009). Another example is the Crossrail at Canary Wharf in London, in which timber beams are connected by steel nodes (Rabagliati *et al.* 2014). In both case, geometric torsion is accommodated through manual welding of a steel connector. The complexity of such a connection is highly increased with deep section beams.
v. Find a torsion-free beam layout, such that the planes of symmetry of beams meet on a common axis. Nodes are then said *torsion-free*. To obtain this, one need to find node axes at each nodes, such that two axes sharing a common beam are coplanar. This structure is called a congruence of lines in discrete differential geometry, and is related to the existence of parallel meshes. Torsion-free layouts can be obtained by aligning beams with principal curvature directions, as will be discussed in section 2.4.2. Conical meshes, introduced in section 2.2.1, and circular meshes (see section 2.2.3), guaranty this property.

Fabrication from flat strips

Curved beams can be made of built-up sections: Flexible strips can be joined together to form a stiff beam. The structure of the Eiffel Tower restaurant, designed by engineering office RFR (Schiftner *et al.* 2012), follows curvature lines of a surface such that its beams can be assembled from developable surfaces. Geodesics and asymptotic lines, detailed in section 2.4.2, allow to place straight strips on a surface.

Planar arches

Planarity of beams simplifies fabrication and improves tolerances significantly. This point will be discussed in chapter 3.

Reuse beams from stock

Beams are the elements most prone to re-use in a curved structure. Designing a structure from a stock of existing beams poses specific geometrical and mechanical constraints. For example, (Mollica and Self 2016) present the design and a construction of the truss of the Wood Chip Barn out of a collection of tree forks – parts of trees that cannot be used for producing common timber products. (Colabella *et al.* 2017) construct a geodesic dome from out-of-order skis, for which the mechanical characteristics had to be measured and accounted for in design.

Curved geometry from straight beams via active bending

Straight beams can be deformed elastically to form curved structures. The geometry is then the result of a mechanical equilibrium, and necessitates form finding. Elastic gridshells (Douthe 2007; Baverel *et al.* 2012) combine this method with the efficiency of shells, and offer the possibility to construct wide span structures without falsework. They can be assembled effortlessly on the ground if the structure follows a Tchebychev net, a geometry introduced in section 2.4.2

Figure 2.4: Common strategies to deal with geometrical torsion:
i/ Set all the beams in vertical planes (Top left - Picture courtesy of Simonin)
ii/ Twist beams (Top right - ©Didier Boy de la Tour)
iii/ Use circular profiles (Middle - picture in public domain)
iv/ Accommodate torsion at nodes (Bottom left - ©Romains Mesnil)
v/ Find a torsion-free beam layout – Example of a torsion free nodes (Bottom right)

2.2.3 Nodes

In a gridshell, nodes – connections between beams – are usually the most complex elements to fabricate (see for example (Knippers and Helbig 2009)), to a point that most of them are patented. Consequently, they are often the costliest elements of this type of structure.

Low valence

The number of beams meeting at a node is called the *valence*. The higher the valence, the more complex the node is to fabricate. Figure 2.4 (left) shows a 7-valent node of the triangular mesh of the gridshell of MyZeil in Frankfort. The geometry is so complex that this type of node often has to be site welded. Nodes with lower valence are obtained using faces with more edges (Figure 2.2). For example, in quad meshes, most nodes are 4-valent. In hex meshes, most nodes are 3-valent. But then bracings might be needed for in-plane shear strength.

One particular strategy to decrease node valence is nexorades (Baverel 2000), often referred to as reciprocal frames. Used in the ancient times to cover spans longer than available beams, they allow to design a space structure in which beams are connected two by two – i.e. each node is 2-valent. A notable application is lamella roofs and Zollinger trusses. These structures, popular in the early XXth century, take advantage of these properties to form large barrel vaults assembled from short beams, cleverly connected three by three with a single bolt (Figure 2.5). More recently, the hybrid shell-nexorade pavilion at the Navier lab demonstrated that nexorades, when combined with digital form finding methods and robotic fabrication, allow to construct efficient double-curvature envelopes (Figure 2.5) (Douthe *et al.* 2018).

Figure 2.5: In a nexorade, beams are connected two by two. Left: Lamella roof at Auburn University's Rural Studio (©James Diewald) Right: Hybrid shell-nexorade, Navier laboratory.

Torsion-free nodes

The benefits of having torsion-free nodes were discussed in section 2.2.2 and Figure 2.4. They can notably be obtained from conical meshes and circular meshes, introduced in the next sub-section.

Circular meshes: torsion-free nodes, planar faces, and node offset

Meshes in which each face is inscribed in a circle are called circular meshes (Figure 2.6). They combine remarkably three properties: Their faces are planar (a circle is always planar), they admit torsion free-nodes (axes are shown in red, beam midplanes are shown in green), and they also have a so-called node offset. This last property allows to design multi-layer structures, in which the distance between nodes is constant. The layers are defined by parallel meshes: meshes for which corresponding edges are parallel, but may have different lengths. This property allows to standardize node details, and will be used in chapter 3. The global existence of a torsion-free structure on a circular mesh is actually subject to topological constraints, which may not be fulfilled if a mesh has holes (Liu and Wang 2008). Remarkably, circular meshes come with other families of PQ meshes called focal meshes, defined by the intersection of the node axes (Pottmann and Wallner 2007).

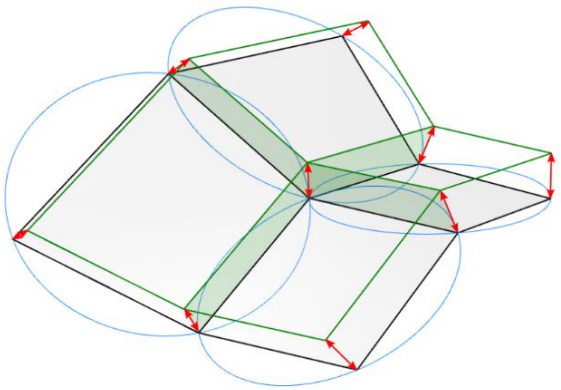

Figure 2.6: A circular mesh with its offset

Node repetition

Generally, in a curved envelope, each element is unique. In particular, each node has a different geometry. Fabrication of unique element can be dealt with by robotic fabrication or CNC milling. However, it requires significant engineering time, and careful planning. In particular, it is not possible for a contractor to order spare nodes, as this would double the number of nodes. Furthermore, specific structural checks need to be performed for each node configuration.

In order to study the repetition of nodes, their geometry needs first to be clearly described. (Stephan *et al.* 2004) propose to assign a reference axis to each node, which defines a reference plane normal to this axis. The geometry of each incoming beam at the node can then be described with three angles, as illustrated in Figure 2.7:

- A vertical angle, between the beam and the reference plane;
- A horizontal angle between beams, which is projected in the reference plane;
- A torsion angle, between the plane of symmetry of the beam and the node axis.

(Schling 2018) identified three main strategies to obtain a repetition of nodes:

- Make all angles identical. This strategy was for example used in (Mesnil *et al.* 2015);
- Use assembly tolerances so that identical nodes can accommodate slightly different angles;
- Design nodes such that they can accommodate variation of one of the three angles, for example with hinges. This solution was for example used by SBP for the gridshell of the Neckarsulm swimming pool (1988), in which only one standard hinged node is used.

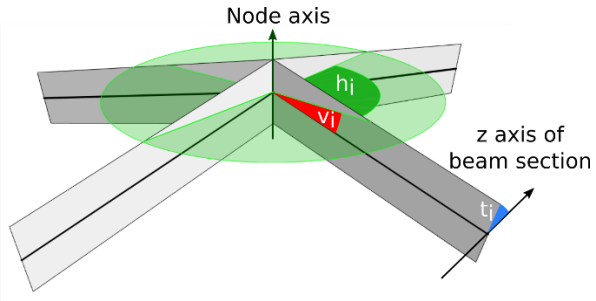

Figure 2.7: Description of the geometry of a node

It is much easier to obtain repetition if curved beams are used. This strategy will be used in chapter 3.

Perfect nodes

A so-called *perfect node* is a torsion-free node for which all the incoming beams at a node have the same vertical angle. (Pottmann, Liu, *et al.* 2007) introduced the notion of *edge offset* meshes: meshes with planar faces in which all nodes are perfect. If an edge offset mesh is built with beams of constant height, the top and bottom flange of the beams will meet exactly at the same height on the nodes, as shown in Figure 2.8 (left). If this is not the case, it is not possible to align flanges at nodes anymore (Figure 2.8 right). This property improves the aesthetic of the nodes, but also allows to build a multi-layer system in which two layers of panels are spaced out by beams of constant section.

Perfect nodes are a strong constraint on the geometry of a mesh, as they constrain all the vertical angles together. This constraint can be easily understood on quadrangular meshes: as the vertical angles are the same for all beams, the only way to accommodate different curvature in two orthogonal directions is to have different edge lengths – shorter beams for higher curvature. In comparison, the constraint of conical meshes can be written as one single constraint on the horizontal angles at each node (Wang *et al.* 2007).

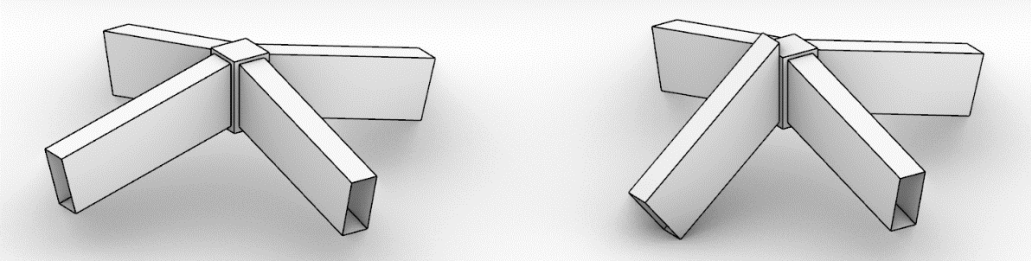

Figure 2.8: Left: A perfect node. Right: Kink due to variation of vertical angles

Regular vertical and horizontal angles

Many industrial gridshell nodes – like the ones described in (Stephan *et al.* 2004) – can accommodate a certain range of horizontal, vertical and torsion angles. The wider the range, the more expensive the node is. Therefore, it is often desired to have a small variation of the angles, in particular for regular meshes like triangular or quadrangular ones. Even for custom welded nodes, like the ones used for the British Museum (Sischka *et al.* 2001), too acute horizontal angles must be avoided, as they can result in bulky nodes – which are both unaesthetic and more complex to weld (Figure 2.9).

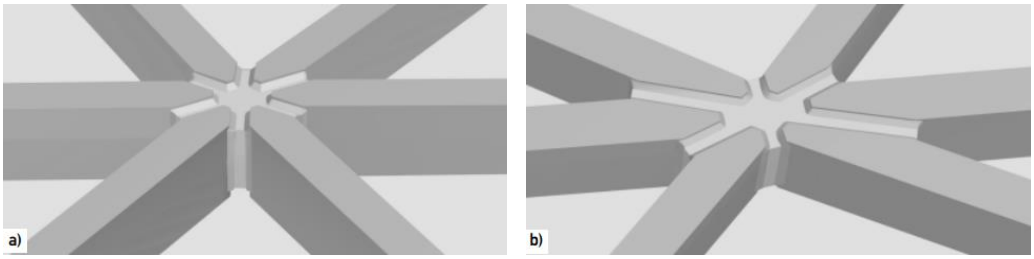

Figure 2.9: For a high-valent node, irregular in-plane angles can cause a high node volume (reproduced with permission from (Sischka *et al.* 2001))

Clamped or hinged

Depending on the pattern and on the presence/absence of bracing, nodes might need to be clamped. A clamped node is significantly more complex to detail, as it needs a high rotational stiffness.

2.2.4 Funicularity

Membranes and masonry vaults resist load through axial stresses, and cannot withstand bending moments. Therefore, their shape needs to be funicular for their main load case: pretension for a membrane, and dead load for a masonry vault. For linear elements of constant sections, funicular shapes for self-weight are catenaries. There is much more formal freedom with 2D elements. Funicularity can be expressed geometrically via force diagrams (see for example (Block 2009; Akbarzadeh *et al.* 2015)).

2.2.5 Mechanical efficiency

Mechanical efficiency of a curved structure is function of many parameters, including especially shape, boundary conditions, joint stiffness, and beam lengths. With good lateral supports at the boundaries, funicular shapes tend to be efficient, but are prone to buckling. The absence of lateral support can be compensated by tension or compression rings. However, in many gridshell projects, loads are mainly resisted by bending. When sections with important structural height are needed, torsion-free nodes and offsets simplify significantly the detailing of nodes. Offsets can notably be used to design structures with two layers of beams, thus increasing sharply the material efficiency. This strategy will be addressed in chapter 3.

For gridshells, the pattern of beams has a significant influence on the mechanical behavior. Triangular patterns have a very high in-plane stiffness, whereas other patterns require bracing or clamped node to have sufficient stiffness. Comparison of performance of various patterns may be found in (Malek 2012; Malek and Williams 2013; Mesnil, Douthe and Baverel 2017; Mesnil, Douthe, Baverel and Léger 2017a).

2.3 Impact of desired properties on form and pattern freedom

Depending on the desired geometrical properties, the design space is more or less restrained. Two aspects are important in this respect: the nature of the properties, and the precision with which they need to be realized.

2.3.1 Nature of constraints

The set of geometrical properties that are desired for the mesh can more or less restrain the design space for forms and patterns. Some geometrical properties do not constrain the shape or pattern at all. For example, triangular meshes can be created on any surface, with any pattern orientation. Some more constraining properties can be obtained on arbitrary surfaces, but the patterning is then constrained more or less strictly. An example is the covering of a surface with planar quadrangles, for which one can prescribe edges in only one direction. Some more constrained properties are possible only on specific surfaces. This is the case of the properties studied in chapter 3. Finally, some properties are so constraining that the only possible surfaces are trivial, like spheres or planes. An example is triangular meshes with torsion-free nodes. As a rule of thumb, the stronger the constraints, the least likely post-rationalization is going to give satisfying results.

2.3.2 Tolerances

Properties often need not be fulfilled exactly. The design freedom might then be significantly expanded.

2.3.2.1 Construction and detail tolerances

Nothing has an absolute precision on a construction site. Most connections allow for some adjustment: Bolted connections have holes oversized by at least 1mm, width of welding grooves can be modified on site by changing the number of passes, screws in timber allow for some tolerance in their positioning, shims can correct misalignment (see for example (Surtees *et al.* 2017), etc... These adjustments can be used to make an "imperfect" geometry work.

Example 1: Tolerance on geometrical torsion at nodes

Most steel gridshell nodes can accommodate a small geometrical torsion (Stephan *et al.* 2004). It is therefore not necessary to have a torsion of exactly zero throughout the mesh. This small amplitude can give interesting freedom in the patterning of a surface.

In order to have a torsion exactly zero, the structure need to be aligned with principal curvature directions, as will be discussed in section 2.4.2. The torsion along a beam not aligned with principal directions can be approximated using differential geometry. If an edge of length L is at an angle θ with a principal direction, the torsion angle can be approximated using the formula for the geodesic torsion of a smooth curve on a surface (do Carmo 1976):

$$\tau_L = \frac{L}{2}\sin(2\theta)(k_1 - k_2) \tag{2.1}$$

Where k_1, k_2 are the principal curvature. If a torsion angle α can be accommodated at the nodes (i.e. an angle $\alpha/2$ for each incoming beam), the beams can deviate from principal directions with an angle of:

$$\theta_{max} = \frac{1}{2}\operatorname{asin}\left(\frac{2\alpha}{L(k_1 - k_2)}\right)$$

We remark that, if $\left|\frac{2\alpha}{L(k_1-k_2)}\right| \geq 1$, i.e. if the length of beams is sufficiently short ($L \leq |2\alpha(k_1 - k_2)|$), then $\theta_{max} > 45°$. The pattern may then have an arbitrary orientation: the torsion can be always accommodated by the node tolerance.

For example, let us consider the surface of the Hippo Haus greenhouse in Berlin Zoo (Figure 2.10). The surface is composed of two paraboloids of revolution connected by an anticlastic transition part. The curvature lines describe an unaesthetic pattern because the junction between sections is not C^2 (there is a discontinuity of surface curvature). However, if a small torsion is allowed at the nodes due to construction tolerances, the patterning might deviate from curvature lines. Figure 2.10 shows the allowed deviation (in degrees) for three different allowable torsion angles at nodes, and for two different bar spacings: one with the actual bar length (approximately 1.2m), and one with a doubled bar length (labelled "coarse mesh" in the figure).

We observe that, even if a very small torsion is allowed at the node, it is sufficient to give the pattern an arbitrary orientation near the top of the domes ($\theta_{max} = 45°$ means that edge orientation can be arbitrary). This is due to the fact that the apexes of the domes are umbilics: they verify $k_1 = k_2$. The difference $k_1 - k_2$ is also very low away from the umbilics, as paraboloids of revolution are near spherical close to their apex. If the mesh is fine, or if a high torsion is allowed, the entire domes can actually be covered with arbitrary pattern and remain within acceptable torsion.

However, in the transition portion, curvature is negative. As a result, the difference $k_1 - k_2$ is much higher (k_1 and k_2 have different signs). As a result the torsion constraint is much more severe on synclastic[4] surfaces, such that construction tolerances do not allow significant freedom.

Figure 2.10 (bottom) shows a similar study on the Galerie Rostoker Hof gridshell. This surface is synclastic, but with a significant difference between curvature directions. We observe that the pattern may deviate significantly from curvature lines if 2° of torsion is allowed, but is much more constrained if only 0.5° are possible. Again, the ratio of the bar lengths to the curvature radius of the surface is critical: If beams are twice longer than in the actual mesh, then the tolerance on torsion has much less effect.

[4] A surface is called synclastic if at any point, the geometry of the surface in the neighborhood of the point is shaped like a dome – and not like a saddle. Mathematically, this means that the Gaussian curvature is everywhere positive.

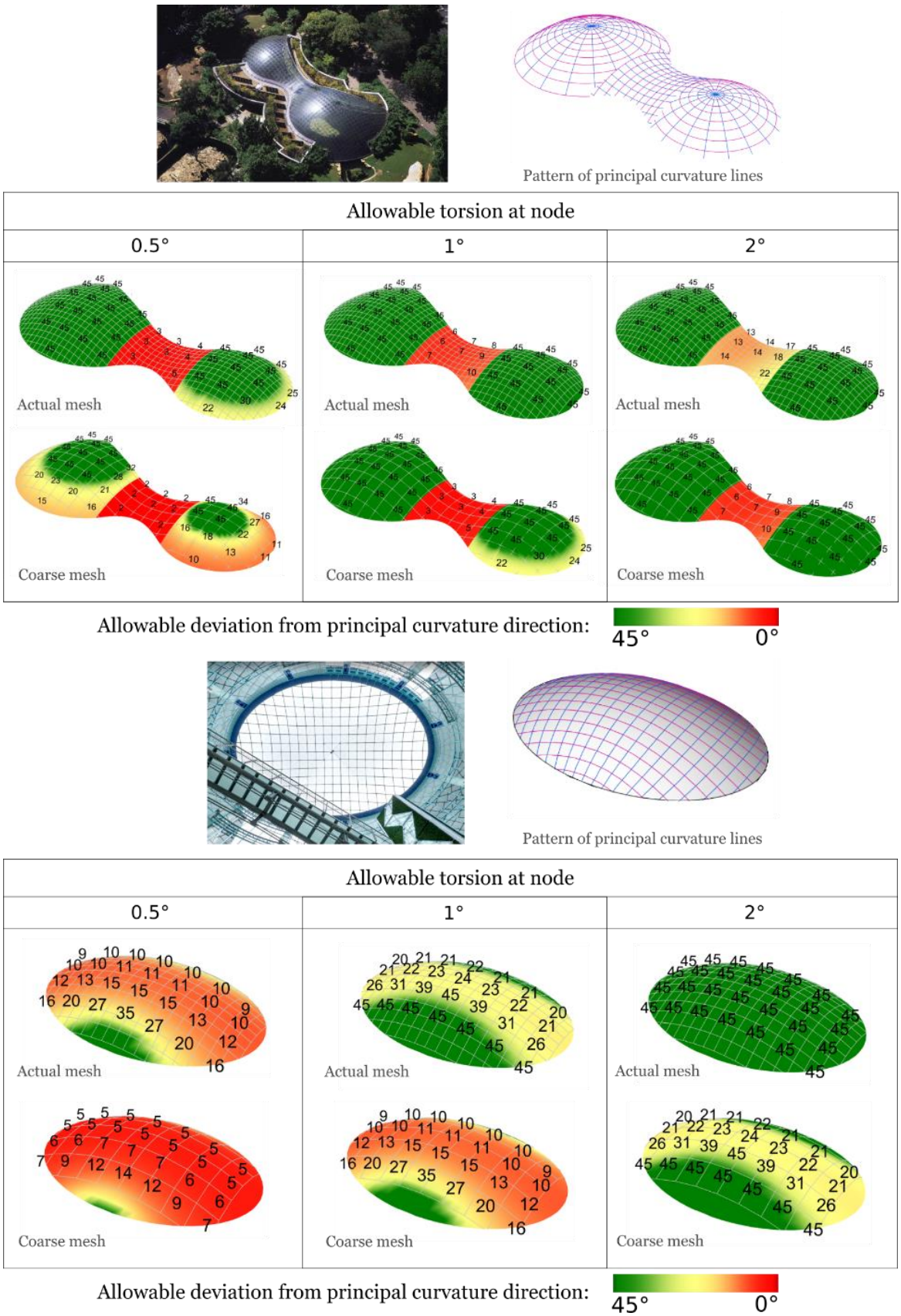

Figure 2.10: Allowable deviation angle of beams from principal curvature directions if a node can accommodate some torsion. When $\theta_{max} = 45°$, beam orientation can be arbitrary. Top: Bottom: HippoHaus. Bottom: Galerie Rostoker Hof.

Example 2: Tolerance on face planarity

Special details can relax significantly geometrical constraints. For example, the Kogod courtyard roof, designed by Foster+Partners (Figure 2.11), is based on a geometry with non-planar quads. Still, the cladding is realized by planar glass panels. This is made possible by the presence of gaps and kinks at panel junctions. This solution requires by specific water tightness details at the joints, which tend to make this type of solution costlier.

Also, the non-planarity of a square pattern, like the Kogod roof, can be seen as a consequence of the torsion of the tangent normal of the Darboux frame along the beams. Its amplitude is therefore proportional to the torsion of the surface normal given by equation (2.1): the discussion on the importance of aligning the mesh with curvature lines for torsion-free nodes also apply to covering with near rectangular planar panels.

Figure 2.11: Kogod courtyard roof (© F+P)

2.3.2.2 Elastic deformations

If some geometrical properties are not fulfilled exactly, elements may still be forced into their desired geometry on-site. One popular example is cold bending of cladding panels: initially flat glass panels may be fitted to some extent on non-planar support structures by applying elastic deformations. This technic was for example used to clad the Amsterdam central bus station (Vakar and Gaal 2004) and the Victoria & Albert Museum (Eekhout and Niderehe 2009). Parametric studies to quantify allowable non-planarity were performed experimentally in (Belis *et al.* 2007) and numerically in (Eversmann *et al.* 2016; Berk and Giles 2017; Fildhuth *et al.* 2018).

2.4 Mesh generation methods

Usually, fabrication considerations come after some shape requirements due to the function and to the configuration of the site. We therefore subdivide the panorama of morphogenesis methods based on these constraints (Figure 2.12):

Case 1: Both surface and pattern are imposed. By *imposed* pattern, we mean that the line orientations, the type of faces (triangles, quadrangles…) and the positions of singularities are imposed. This situation lets little margin for optimization and happens in a context of post-rationalization.

Case 2: A reference surface is determined, but not the patterning. The freedom on the disposition of bars or panels allows to search for many geometrical properties.

Case 3: Only boundaries are imposed and a general idea of the shape. There is then freedom to combine mechanical and fabrication properties.

Case 4: Only some sections are known. This is in a context of pre-rationalization.

Each case will be addressed in a subsection. As mentioned earlier, this subdivision is one way to classify morphogenesis methods from the point of view of a designer: Generation methods from one case can be used for the cases below. For example, if only boundary is imposed (case 3), one can create candidate surfaces and apply methods of case 2. However, algorithms for cases from 4 to 1 tend to have increasing complexity and to be slower. Also, some situations do not fall in the proposed cases. For example, the case when pattern and boundary are imposed is treated in the case 1.

By surface, we broadly refer to a two-dimensional curved object. Numerically, this can be a parametrized surface (for example a NURBS) or a mesh (for which the geometry is faceted, given by the position of vertices, edges and faces). Numerical methods are different depending on whether a mesh or a surface is manipulated. A surface can always be discretized by a triangular mesh, so that a method requiring a mesh as input can be used. However, the opposite is a more complex interpolation problem.

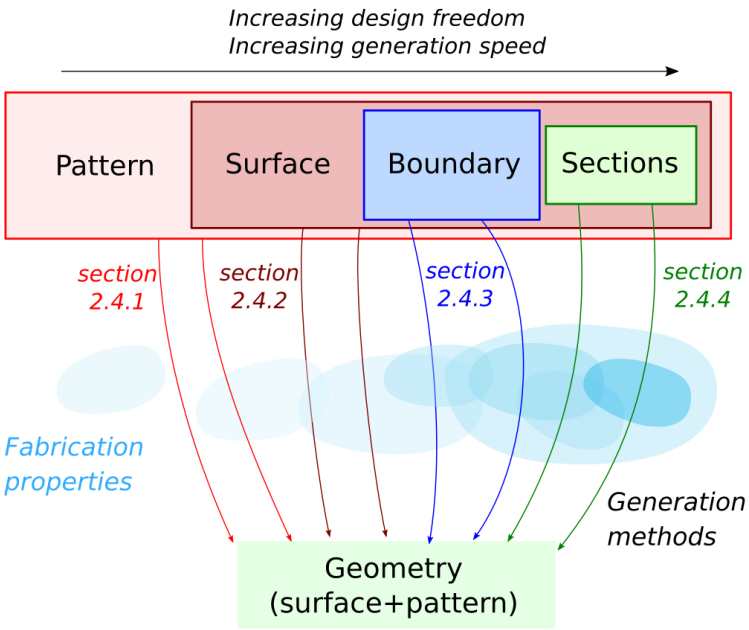

Figure 2.12: Classification of shape generation methods, represented by arrows. More or less fabrication properties (in blue) are picked up in the generation process depending on the method

2.4.1 From surface + pattern

When fabrication is accounted for at a late project phase, a reference surface and a pattern are usually already determined. This lets very limited room to obtain the desired properties. The only rationalization methods are numerical optimization. These method will attempt to deform the geometry to obtain the desired properties, but they will often require significant shape modifications to succeed.

Optimization algorithms

Post-rationalization methods optimize vertex positions to obtain fabrication properties while staying as close as possible to the initial geometry, and while keeping the mesh smooth. This is usually achieved by minimizing an energy like the one given in equation (2.1) that combines linearly three terms, one for each of these constraints.

$$E = E_{constraints} + E_{closeness} + E_{smoothness} \tag{2.1}$$

The smoothness term is required because many optimization goals tend to form zigzags in the pattern. In that framework, a different energy $E_{constraints}$ needs to be found for each required fabrication constraint.

The choice of the formulation of this energy is important for the performance of the algorithm, the example of face planarity will be discussed in the next sub-section. A set of optimization methods can be found for example in the software EvoluteTools and VaryLab.

Some algorithm do not require calculation of energies. They are usually less fast, but are also more versatile, as they can be more simply adapted or scripted by average users. An example is dynamic relaxation. Developed originally for mechanical form-finding, it can also be used for geometric optimization. Geometrical constraints are then expressed as springs, pulling for example vertices to lie on a common circle. This is at the bases of the software Kangaroo 1. (Bouaziz *et al.* 2012) introduced an algorithm based on iterative projections, which fulfills geometrical constraints faster and more robustly than dynamic relaxation. It was released in the free software ShapeOp, and is at the basis of the popular Kangaroo2.

Planarization

There are many ways to optimize a mesh for face planarity. It can for example be imposed by dynamic relaxation (Adriaenssens *et al.* 2012) or by successive projections (Bouaziz *et al.* 2012). The computer graphics community has focused on finding the most effective way to write a planarization constraint in an optimization algorithm. (Liu *et al.* 2006) impose planarity of quadrangles by imposing the sum of the angles to be 360°, which is a highly nonlinear constraint. (Yang *et al.* 2011) expressed planarity as a cubic constraint by imposing the distance between diagonals of a quadrangle to be zero. Finally, (Tang *et al.* 2014) showed that it is possible to render this constraint quadratic by introducing face normals as dummy variables, this increases significantly convergence speed.

Panelization

Panelization algorithms attempt to introduce repetition in the paneling. They all require gaps and kinks at joints, such that repetition can be approximate. Clustering algorithms try to regroup panels in clusters of identical shapes. Algorithms for triangular and quadrangular meshes are proposed respectively in (Singh and Schaefer 2010) and (Fu *et al.* 2010).

When planarization is not successful, panelization aims at limiting the number of molds used to produce curved panels. (Eigensatz *et al.* 2010) propose a method to make planar as many faces as possible, and when impossible, use primitives of increasing complexity and associated cost: cylinders, developable surfaces, cubic surfaces, etc…

From pattern + boundary

When the surface is not imposed, or if large deformations are tolerated, optimization tools can be used to obtain more constraining fabrication properties, or to combine fabrication and mechanical optimization. An example is the design of the courtroof of the Dutch maritime museum (Adriaenssens *et al.* 2012), shown in Figure 2.13. The pattern was imposed, as it had to project vertically to sailing routes of an ancient navigation map, but the surface shape was not predetermined. This freedom was used to optimize both face planarity and structural performance.

Figure 2.13: Gridshell generated from pattern + boundary (©Jean-Luc Deru, Ney & Partners)

2.4.2 From a surface

The following situation often happens in architectural projects: The shape is already determined, but there is a certain flexibility in the patterning, in terms of topology and orientation. There is a wide array of methods to draw patterns on surfaces with particular properties. There are two main approaches:

- If the constraints need to be filled with a high precision, specific families of curve networks need to be used;
- If the fabrication constraints are loose or if other criteria are prevalent, topologies and patterns can be explored, and then optimized using algorithms from the previous sub-section.

Curvature line networks: torsion free structures and planar near-rectangular faces
Principal curvature lines (or curvature lines in short) are the lines following the directions of highest and lowest curvature on a surface. They have many rationalization properties. Firstly, they are the only lines along which there is no geometrical torsion of the surface normal (do Carmo 1976). They can for example be used to obtain torsion free nodes (Figure 2.4). Secondly, their normal vectors describe the straight lines of a developable surface. This allows to construct them with built-up sections composed of thin plates. Furthermore, a network of curvature lines describes a quad mesh in which faces are nearly planar. They can also be used to design planar hexagonal meshes (Wang and Liu 2009) or other types of meshes with periodic patterns and planar faces (the generation of these meshes by optimization will often tend to align them with curvature lines (Jiang *et al.* 2015)). Finally, curvature lines always cross at a right angle. This can be used to obtain near rectangular panels or for node repetition (Bo *et al.* 2011) – for example in the Caravel meshes introduced in chapter 4.

Curvature lines are entirely determined by the geometry of a surface – a designer can only control line spacing. One limitation is that, on an arbitrary surface, they tend to form an erratic network. For example, Figure 2.14 shows the curvature lines on the roof of the Visconti court in Le Louvres, designed by architects Rudy Ricciotti and Mario Bellini. The configuration is badly suited for a gridshell: there is a high variation in the size and aspect ratio of faces, beams have a poor mechanical alignment, and the pattern is subjectively unaesthetic. Consequently, a triangular pattern was chosen for the final structure. Singularities of curvature line networks – called umbilics – are also entirely defined by the geometry. In most surfaces, only two types are observed (Sotomayor 1992), of index +1/2 and -1/2, respectively marked by red and blue dots in Figure 2.14 (the notion of singularity index will be explained more in detail in chapter 4). Other types of singularities appear only with surfaces that have special symmetries.

Many software allow to compute curvature lines of a surface. These can then be discretized by quad meshes by taking the intersection points of the lines, and then optimized to obtain circular or conical meshes (Liu *et al.* 2006; Tang *et al.* 2014). The computation of the whole net of curvature lines can be tedious if done manually: curvature lines usually do not close around umbilics, and may have highly uneven spacing. Automated methods are for example given in (Alliez *et al.* 2003) and (Liu *et al.* 2006).

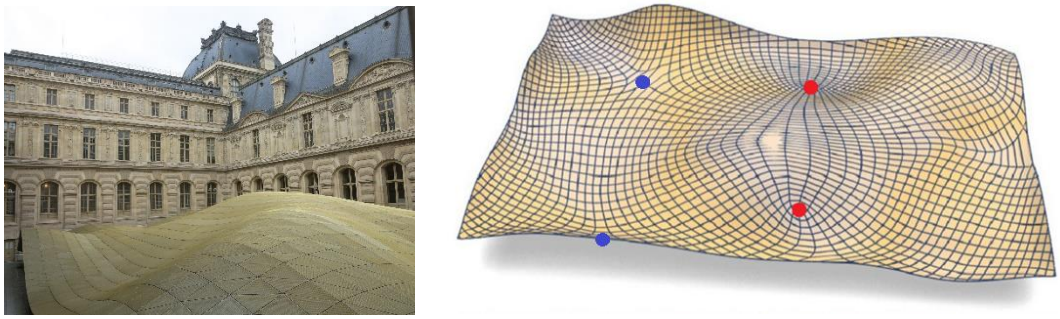

Figure 2.14: Curvature lines of the roof of the Visconti court in Le Louvre (reproduced with permission from (Wallner & Pottmann, 2011))

Conjugate line networks

If planar faces are needed, but torsion or face rectangularity are not strict constraints, the so-called conjugate curve networks are a useful tool[5]. They offer significantly more design freedom than curvature line networks, and can be used notably to obtain meshes with planar quads (Liu *et al.* 2006) or hexagons.

One method to obtain a conjugate line network is to draw a family of (non-intersecting) lines on a surface. At each point of a line, there exists a unique conjugate direction to the line tangent (do Carmo 1976). These conjugate directions can be used to construct by integration a second family of lines – the two families of lines thus forming a quadrangular mesh. However, this methods tend to give highly distorted faces, especially in anticlastic surfaces. Automated methods to obtain fair conjugate networks are given in (Zadravec *et al.* 2010) and (Liu *et al.* 2011). The methods give the user some control over the mesh orientation and position of singularities. Principal curvature nets are a special type of conjugate nets, they are the only ones in which lines cross at 90°.

Geodesic network

Geodesics are the equivalent of straight lines on a surface. For example, the shortest path between two points is along a geodesic – see for example (Pottmann, Asperl, *et al.* 2007) for a more thorough introduction. Geodesics can be used to clad a surface with straight flexible strips. An example is the ceiling of the Terminal 4 of the Madrid airport, which is realized with thin planks of wood (Figure 2.15).

There are two ways to construct a geodesic. The first one is to start from a point, pick a direction, and go "straight" (more precisely, with zero geodesic curvature). The second is to start from two points, and to search for a (locally) shortest path. Generation is more complex when trying to cover an entire surface: how to generate geodesics with a spacing as uniform as possible? How to superpose harmoniously two or three layers of geodesics in different directions? For complex surfaces, it is often necessary to split the surface in patches to obtain a roughly uniform spacing: what is the best splitting pattern? This can be done by creating manually or parametrically each geodesic. (Pottmann *et al.* 2010; Wallner *et al.* 2010) propose multiple optimization formulations to handle this problem algorithmically.

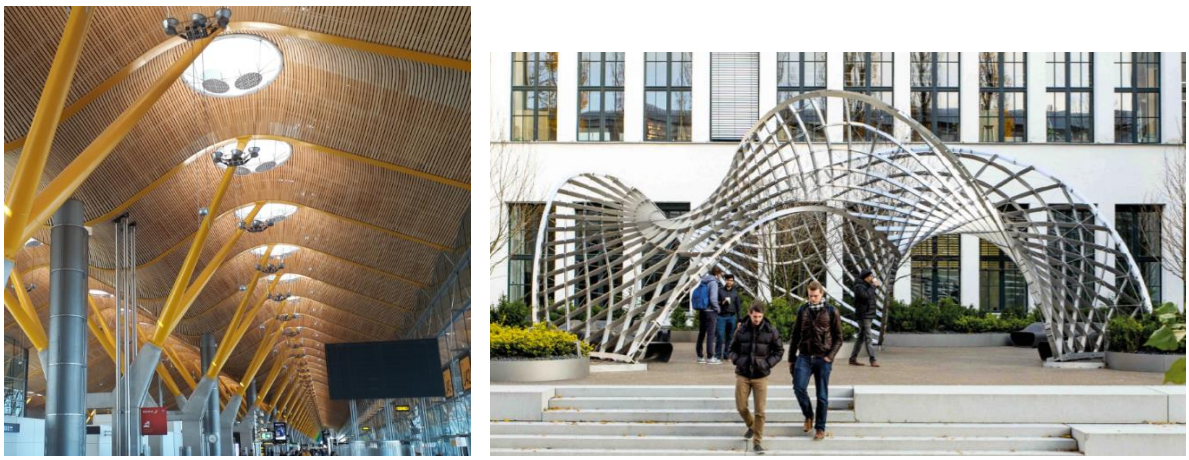

Figure 2.15: Building with straight strips. Left: ceiling of the Madrid Airport, Terminal 4 (picture by the author) Right: Inside-Out pavilion, TU Munich (courtesy of Eike Schling).

Asymptotic net

On an anticlastic surface, there exists lines with zero normal curvature: The asymptotic lines (do Carmo 1976). These can be used to build a curved envelope from straight strips. However, contrary to geodesics, the strips are not laid "flat" on the surface, but stand at 90° on the surface along their edge. Structural and architectural applications were demonstrated in the pavilion Inside-Out at TU Munich by Eike Schling

[5] The iso-lines of a surface parameterization $(u, v) \mapsto x(u, v)$ form a *conjugate net* if at any point $\det(x_u, x_v, x_{uv}) = 0$ (do Carmo 1976).

shown in Figure 2.15 (Schling *et al.* 2017). Like curvature lines, asymptotic lines are entirely determined by the surface geometry: a designer may only control the spacing between curves.

Developable strips

Approximation of a target surface by developable surfaces is a common problem in ship building. The problem is often referred as *lofting*. The same problematic can also appear when cladding a curved architectural envelope by cold-bent panels. There is a great freedom in the possible paneling patterns, such that other parameters can be taken into account. For example, the fondation Vuitton was cladded mostly with bent rectangular glass panels.

Many generation methods have been developed by the computer graphics community. A first family of methods (Chen *et al.* 1999; Stein *et al.* 2018) efficiently covers a shape with developable sheets, but do not give a designer control over the patterning. Methods adapted to architectural needs can be found in (Pottmann *et al.* 2008; Gavriil *et al.* 2019). They consist in drawing a conjugate net on the surface (or a planar quad mesh), converting it into B-Splines, and then optimizing for developability. However, once a refined conjugate net is found, simpler versions of these algorithms can still yield very satisfactory results (Leduc *et al.* 2018).

Figure 2.16: Three applications of conformal maps: circle packings, node repetition in curved beam structures, auxetic structures (reproduced with permission from Schiftner et al. 2009, Bo et al. 2011, Konaković-Luković 2019)

Conformal mapping

Whenever constant in-plane angles are required in a constructive system, conformal maps can be a valuable tool. Intuitively, conformal maps form a covering of a surface by "small squares": quadrangles of varying size, but with shapes that are always close to a square[6]. They can be used for example to cover a surface with triangles that are nearly equilateral, or hexagons that are nearly regular. They are used a lot in computer graphics to apply a texture on a curved surface without distorting the pattern – the pattern only undergoes a local scaling and rotation. Applications to architecture include node repetition (Bo *et al.* 2011), curved auxetic patterns (Konaković-luković *et al.* 2018) and compact circle packings (Schiftner *et al.* 2009) (Figure 2.16).

A designer has some freedom to cover a surface with a conformal map. The number of degrees of freedom depends on the topology of the surface (presence of holes or handles, whether closed or not). If the surface has the topology of a disk, then there are two degrees of freedom. This is very pedagogically detailed in the short movie Conform! by the Discrete Geometry and Dynamics group (Bobenko and Gunn 2018).

Generation can be made via circle packings (Stephenson 1997; Schiftner *et al.* 2009). An algorithms that allows to deal with complex topologies was proposed in (Zeng *et al.* 2009).

The constraint of having "small squares" can be overly restrictive for some applications – one might just need "small rectangles". This happens when constant in-plane angles are required in a structure. To achieve this, a family of algorithms based on the integration of fields of crosses or stars have been proposed in the literature. For example, (Jiang *et al.* 2014) use fields of symmetric 6-branch stars ("6-

[6] More precisely, a surface parameterization $(u, v) \mapsto x(u, v)$ is called *conformal* if at any point $\|x_u\| = \|x_v\|$ and $x_u \perp x_v$ (do Carmo 1976).

RoSy fields") to generate curved honeycomb structures with constant 120° angles between beams. Automated methods to design smooth fields of stars or crosses can be found in (Vaxman *et al.* 2016).

Tchebychev meshes

Tchebychev meshes are quadrangular meshes with constant edge length. Their faces are therefore parallelograms. They are useful to obtain beam repetition and for the design of elastic gridshells (Baverel *et al.* 2012) or woven grids (Garg *et al.* 2014). There is a great freedom in arranging Tchebychev nets on a surface, in the same way as there is many ways to apply a piece of woven fabric on an apple. Limitations are only topological (Hopf 1983): if the total curvature of a surface is above 2π (i.e. $|\iint K\, ds| \geq 2\pi$, this is for example the case of a half-sphere) it is necessary to introduce singularities (non 4-valent vertices) (Masson 2017) or discontinuities – which are analogous to sawing pieces of fabrics together. Illustrations of this patching strategy can be found in (Maia Avelino *et al.* 2019).

The compass method is a simple way to construct a Tchebychev net on a surface (Otto 1974): The designer prescribes the vertices along two secant lines of the mesh, the rest of the mesh is then entirely defined by geometrical rules and can be generated automatically and in real-time (i.e. with a calculation time below 100ms). This method is intuitive for a surface with a low total curvature. However, for more complex surfaces, a complex aspect is the placement of singularities. (Garg *et al.* 2014) and (Sageman-Furnas *et al.* 2019) propose global optimization methods that find singularities which result in a mesh as fair as possible.

Figure 2.17: The same geometrical structure lies behind these four objects: Tchebychev meshes (top left: ©SBP, top right and bottom right: reproduced with permission from Garg et al. 2014 and Lefevre et al. 2017)

Meshes aligned with vector fields

It is sometimes desirable to align the beams of a structure in specific directions. One particular application is for gridshells: The structure can be optimized by aligning beams with the lines of highest membrane stresses, bending moment or shear. This can usually be done by simple integration, potentially followed by smoothing or relaxation. (Schiftner and Balzer 2010) propose, for gridshells, to combine structural efficiency with planar quads by aligning one family of edges of a quad grid with the directions of maximal membrane stress, and to use their conjugate directions to define the second family of edges.

Topology finding

If tolerance on geometrical properties are not too tight (as discussed in section 2.3.2), pattern may deviate significantly from the theoretical ones mentioned above and still yield the desired properties. Patterning tools that do not account for fabrication can then be used as an exploration tool.

(Oval *et al.* 2018, 2019) presents methods to explore different topologies of meshes covering a given surface. A series of candidate topologies can be generated by the designer, and be each evaluated with regards to fabrication and mechanical performances. Another method for topology exploration is given in (Crane *et al.* 2010). Based on the concept of trivial connections, the algorithm allows a user to construct a smooth vector field on a surface, with a control on the position and type of singularities. The resulting vector fields can be integrated to construct a smooth net of curves or a quadrangle covering.

The strength of this approach is the multiplicity of solutions that can be obtained. This can significantly help a designer finding a patterning that fulfill all the project constraints. Examples of topologies for a fixed boundary are shown in Figure 2.18.

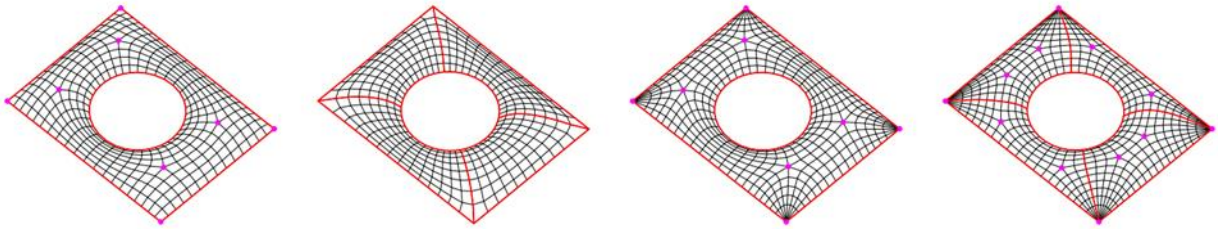

Figure 2.18: If constraints are loose, topologies and patterns can be explored on a given surface (pictures courtesy of Robin Oval)

Constant face size

For some surfaces with complex geometry, the apparently simple task of finding a fair quad patterning, with faces that are roughly square and for which the size does not vary too much, can be actually quite complex, even if no other fabrication property is desired. This is particularly the case for closed surfaces (such as a torus), or surfaces with different levels of details – for example a hand, with its wide flat palm and its thin curvy fingers. The key in this patterning problem is, again, to find a proper topology. Some early methods suggested to use the eigenmodes of the Laplacian (Dong *et al.* 2006). This method is equivalent to sampling in 1D the x-axis with the zeros of the sinus function, a method that indeed gives constant length segments. Other methods propose to generate a mesh from an optimized tensor field on the surface (Kälberer *et al.* 2007). (Bommes *et al.* 2009) present a calculation intensive but effective method that resorts to two levels of MILP optimization. For architectural applications, most of these algorithms let a very limited control of the mesh to a designer, and can be relatively slow to run. This can be a problem for a use in early design stages, in which designers want to explore many different solutions in a creative flow.

Smoothness

For aesthetic and mechanical reasons, it is often desirable to have a smooth mesh, in which beams orientation and panel shape do not vary too abruptly (Figure 1.3). This constraint is often included in the optimization algorithms mentioned above as a smoothness energy. One popular tool to smooth a mesh (without consideration of other geometrical properties) is relaxation, used notably during the design of the great roof of the British Museum (Williams 2001). Visual smoothness of a facetted surface is also highly influenced by the orientation faces. This point is addressed in (Pellis *et al.* 2019).

2.4.3 From boundaries

In some projects, the boundary of a structure is imposed, but not its shape. This happens for example when covering an existing atrium with a gridshell. There is much more design freedom in this configuration, it can be used to obtain more fabrication properties, or to combine manufacturing and mechanical efficiency.

Minimal
Minimal surfaces correspond to the shape of unloaded soap films. The geometry of soap films is ruled by surface tension, which is isotropic and uniform. They thus correspond to the shape of tensile membranes with optimized pre-tension distribution. They can be generated on an imposed boundary, by numerical methods such as dynamic relaxation (Brew and Lewis 2003) or stress density method (Maurin 1998). The geometry of minimal surfaces is extremely rich, both in terms of geometrical properties and of possible shapes. For example, the pavilion showed in Figure 2.15 is generated from the asymptotic lines of a minimal surface. These have the particularity to always cross at 90°, thus allowing to use a standard connection detail. Minimal surfaces can be discretized by curvature lines to build gridshells. Curvature lines tend to form a fair network, unlike the ones showed in Figure 2.14. In particular, minimal surfaces are isothermic, this means that they can be covered by a conformal net of principal curvature lines.

CMC surfaces
When a soap film is pressurized on one side, it forms a bubble, which is a surface with constant mean curvature (CMC). CMC surfaces can also be generated from a boundary curve (Brakke 1992), as will be detailed in chapter 5. They have the remarkable property to be funicular for a uniform pressure load, which they can resist with constant uniform membrane stresses. Like minimal surfaces, they are isothermic and can be covered with a fair curvature line network.

Developable surfaces
Developable surfaces can also be constructed from closed boundary curves. This is equivalent to fitting a sheet of paper on a spatial curve. For a single 3D curve, there are usually at least two developable surfaces interpolating it, which correspond to the convex hull. For complex curves, there can be many more solutions. (Rose *et al.* 2007) presents how these can be obtained algorithmically.

Surfaces of constant slope are a particular type of developable surfaces which is naturally generated from boundary curves. They can be naturally obtained by pouring gently sand on a plate delimited by the target boundary. The Sogn Benedegt Chapel, built in the late 80's in Switzerland, illustrates their use for roof cladding. They can be generated by sweeping a line along the boundary, by computing successive offsets of the boundary at increasing height, or with algorithms based on medial axis calculation.

Form-finding methods
Form-finding encompasses all the methods used to find shapes at equilibrium under a given set of loads. The first numerical one to appear has been the force density method (Schek 1974). It allows a user to prescribe *force densities* in a network of bars with imposed boundaries. Force densities are the ratio of the axial force in a bar over its length. Although this quantity is not relevant for design, it allows to linearize equilibrium equations: Form can then be computed very fast. This speed allows to use efficient optimization algorithms to control the forces in the bar or geometry of the shell (Gründig and Schek 1974).

For surfaces funicular to their self-weight, (Block 2009) introduced the Thrust Network Analysis. A designer can sculpt a surface fitting a boundary by controlling graphically the projection of forces along predefined thrust lines. Equilibrium equations are linearized this time by decoupling the horizontal and the vertical equilibrium.

Finite-elements can also be used as a form-finding tool. Tensile membranes can be designed by tensioning numerically fabric panels. This method allows to model the material behavior, and in particular to take into account the orthotropic structure of membranes. As large deflections happen during the form-finding process, a nonlinear analysis is required. This can be done with algorithms such as the updated reference strategy, introduced in (Bletzinger and Ramm 1999; Bletzinger et al. 2005).

Form-finding of structures in which the final shape is the result of large bending deflections (often referred to as *bending-active* structures) can be done with dynamic relaxation (Otter *et al.* 1966; Adriaenssens *et al.* 1999). This includes in particular the design of elastic gridshells (Douthe 2007; Baverel et al. 2012; Harding et al. 2014; Tayeb 2015). The ShapeOp algorithm described in section 2.4.1 can also be used as a form-finding tool for that purpose (Brandt-Olsen 2016).

Subdivision meshes
Subdivision meshes can be combined with optimization to yield meshes with specific geometrical properties. For example, (Liu *et al.* 2006) propose to alternate subdivision steps with planarity and conical mesh optimization. (Stein *et al.* 2018) combine subdivision with a new formulation of developability of triangular meshes to design objects covered by developable surfaces.

With subdivision meshes, a designer can control a complex mesh at a high level via the initial coarse mesh. The degrees of freedom are intuitive and in small number, which is interesting for time consuming multi-optimization algorithms. This method also allows to generate meshes with complex topologies while keeping control of the boundaries (although this last point often requires scripting).

Geometrical and mechanical optimization
Compared to the cases discussed in section 2.4.1 and 2.4.2, the fact that there is no target reference surface to constrain the geometry gives much more room for optimization methods to succeed. For example, (Pirazzi and Weinand 2006) present a software to design geodesic net by optimizing both surface and net. Contrary to the methods presented in section 2.4.2, the surface is generated at the same time as the geodesic net. This gives a designer more control over the pattern. (Tang et al. 2014) introduce a numerical subdivision method to combine face planarity and funicularity. The user can control the geometry via a coarse mesh, which is iteratively subdivided and optimized. Calculation is made effective and fast by using auxiliary variables – which allow to resort to quadratic optimization.

2.4.4 From sections

There exists many methods that allow to control a shape from section curves. These methods do not give control over the boundary, but are very well adapted for early design stages, as they allow to explore quickly many different shapes. Most of them guaranty fabrication properties exactly.

Scale-trans meshes
Translation meshes are created by translating a polyline along another polyline. The process yields a mesh with planar quadrangles. As the same polylines are repeated, the mesh can be used for the design of a gridshell with identical beams. This method is very intuitive: the designer controls two sections, and the resulting surface can be drawn by hand or algorithmically in real-time. Consequently, it has been used in many gridshell projects (Schober 2015). One example is the new roof of the court of the German History Museum in Berlin, designed by SBP (Figure 2.19).

As the polyline is translated, it is possible to transform it with homotheties of varying amplitude. The resulting meshes are called scale-trans meshes (Glymph *et al.* 2004), and also have planar faces. The scaling gives one additional degree of freedom at each translation, and allows to build more complex shapes than translation surfaces.

Marionette method

Scale-trans meshes do not give access to the entire design space of planar quad meshes. An arbitrary conjugate net of curves (the smooth counterpart of a planar quad-mesh) can actually be entirely reconstructed knowing only two of its curves (that intersect) and the projection of the curves in a plane (Bobenko & Yuris, 2008). (Mesnil, Douthe, Baverel and Leger 2017) propose a discretization of this property as a way to generate planar quad meshes, a method baptized Marionette. It allows to access a richer family of shapes than scale-trans surfaces. Limitations apply to surfaces with holes, which require a specific treatment, and to surfaces with vertical portions.

Figure 2.19: The roof of the German History Museum is a translation surface (©Kai-Uwe Heinrich)

Surfaces of revolution

Surfaces of revolution are generated by the revolution of one curve around an axis. It can be naturally discretized by parallels and meridians. The resulting mesh then has many fabrication properties: planar quadrangles, torsion free nodes, nodes and panels are identical along a parallel, all meridians are identical.

Monge and moulding surfaces

Monge surfaces are a generalization of surfaces of revolution: the axis of rotation is allowed to move as the meridian rotates. These surfaces are best described by two curves (Figure 2.20): a rail (in red), along which a planar section curve (blue) slides and rotates such that its reference plane remains orthogonal to the rail and undergoes no torsion. For use as a gridshell, these surfaces have the same properties as surfaces of revolution – the only exception being node and panel repetition which are lost. However, they offer a great design freedom. In the special case where the rail is planar, one obtains a moulding surface. (Mesnil *et al.* 2015) showed how these can be discretized to recover node repetition.

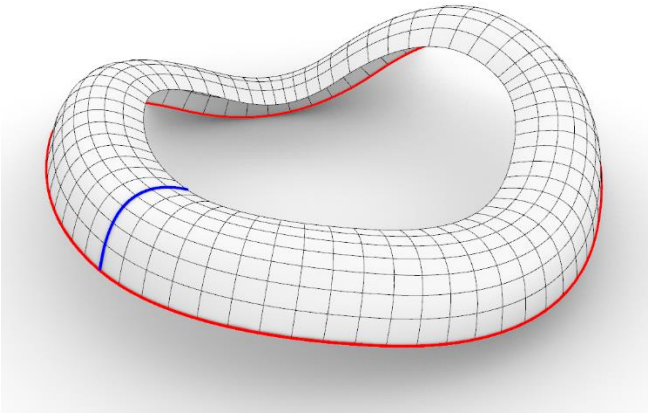

Figure 2.20: A Monge surface

Surfaces with one family of planar curvature lines

Monge surfaces belong to a wider family of surfaces: surfaces with planar curvature lines in one direction. A generation method for these surfaces was given in (Mesnil *et al.* 2018). It takes as input three guide curves: the section, the rail, and a third curve that controls the dilation of the section during it motion along the rail. The method returns circular meshes, which a user can control in real-time via the guide curves.

Ruled surfaces

Surfaces resulting from the motion of a straight line through space are called ruled surfaces. They remarkably allow to create curved shapes out of straight elements. They are an economical solution to build curved concrete shell, as the formwork can be realized from straight planks – a strategy used repeatedly by Felix Candela (Figure 2.21). They have also been used by Elado Dieste as primitives to lay curved brick structures, such as the Atlantida church (Anderson 2005). They can also be obtained cheaply as façade elements by elastically twisting corrugated sheets (Abramczyk 2016). This solution was for example used to cover the tram maintenance station in Le Havre (architect: Marc Mimram), or the façade of the Dell call center in Montpellier (Bba Architectes), shown in Figure 2.21.

Ruled surfaces can be generated from two curves, or as B-spline patches of degree 1 in one direction.

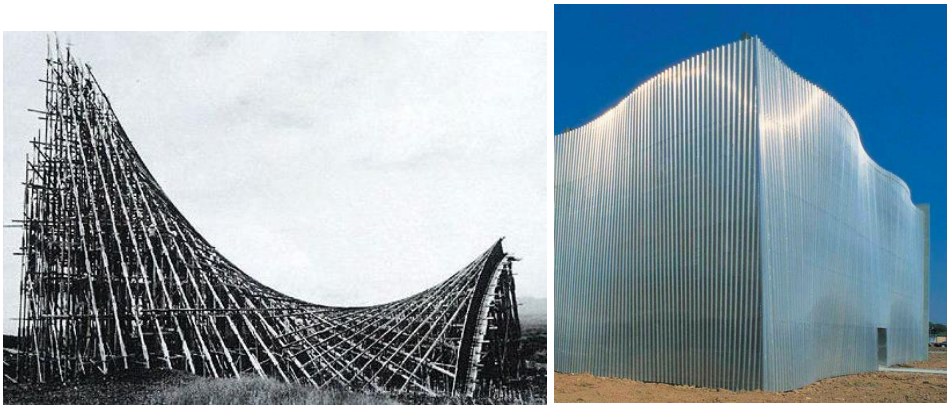

Figure 2.21: Ruled surfaces. Left: Used as formwork for the Chapel Lomas de Cuernavaca. Right: Obtained from corrugated steel sheet (©Kalzip)

Isoradial meshes

Quadrangular circular meshes with constant circle radius are called isoradial meshes. As their diagonals form a Tchebychev net, they can be realized as elastic gridshells. The circular mesh can then be used for cladding with planar panels, thus solving one of the major problems of elastic gridshells. (Douthe *et al.* 2017) present how these meshes can be generated algorithmically from two guide curves.

2.4.5 Other morphogenesis methods

Some popular morphogenesis methods do not fall in the previous four categories, but give interesting properties that simplify manufacturing.

Simple geometric primitives

Simple geometrical primitives like spheres, cylinders, cones and tori offer many rationalization properties. For example, any curve on a sphere has zero geodesic torsion. Although being quire restrictive formally, they can be combined in many different ways. One popular way to discretize the sphere are geodesic domes, obtained by applying subdivision to a platonic solid like the icosahedron and then applying a projection onto a sphere.

From physical models

Physical models play an important role in architectural design. Although this is outside the scope of this review, we mention a few important approaches.

Funicular shapes can be found with hanging models. Famous examples include Gaudi's design of Sagrada Familia and the Mannheim gridshell (Happold and Liddel 1975). (Billington 1985; Isler 1993) use fabric hanging models, that are then rigidified with plaster or ice in order to be inverted. (Bach et al. 1988) performed a large experimental program on soap films, that will be more discussed in chapter 5.

Some physical models allow to take fabrication into account. A notable example is developable surfaces, for which mock-ups can be easily made with paper. This method is dear to the architect Franck Gehry, who used it in particular for the conceptual design of the Bilbao Museum (Figure 1.1) and the Los Angeles Disney concert Hall. Tchebychev nets can also be naturally described by physical nets – for which the distance between nodes is constant. This allowed the Mannheim mockup to include both fabrication and mechanical properties.

From analytical equations

Some particularly interesting shapes can be obtained from analytical equations. These equations depend on parameters, which makes them well adapted to a parametric design environment. The variety of analytical shapes can be observed in (Legendre 2011), while a large overview of families of analytical surfaces is presented in (Krivoshapko and Ivanov 2015). Planar patterns can also be designed analytically, using complex functions. For example, (Nsugbe and Williams 2001) describe the micro-structure of bones with complex analytic functions (a tool that will be used in chapter 6 - section 6.8.3.2).

In architecture, a common family of analytical surfaces are paraboloids, such as parabolic domes or hyperbolic paraboloids. One more advanced example is the great roof of the British museum (Williams 2001): a clever choice of functions allowed to construct a parametric surface which fits the imposed boundaries – a circle inside a rectangle, like the one showed in Figure 5.3.

One special family of analytical surface are algebraic surfaces. These surfaces correspond to the zeros of a polynomial equations in x, y and z. They have many geometrical properties, studied in the field of algebraic geometry. (Narváez-Rodríguez et al. 2015) used properties of quadrics (algebraic surface with equations of degree two) to design a pavilion out of portions of cones with planar intersection lines.

For a designer, a major drawback of analytical surfaces is that it is usually complicated to get intuition on their behavior and to make them fit complex boundary curves.

Transformations

An ellipsoid can be constructed by solving a quadratic equation… or by simply applying unidirectional scalings to a sphere. There exists many ways to deform a geometry, and many of them conserve specific geometrical properties.

Properties like face planarity and torsion-free nodes are for example preserved by affine transformations, but also by parallel transformation, also referred to as Combescure transforms (Figure 2.22). When applied to a mesh, a parallel transformation modifies the lengths of the edges, but do not change the orientation of edges and faces. They are for example used in (Mesnil *et al.* 2015) to deform meshes of revolution while keeping most of their properties (node repetition, face planarity, etc…). (Pottmann, Liu, et al. 2007) use parallel transforms to design multi-layer and torsion-free structures. As the meshes parallel to a given mesh form a linear space, tools of linear algebra like SVD can be used.

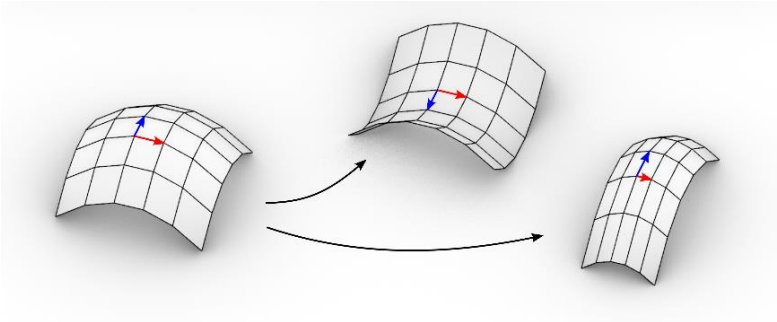

Figure 2.22: Parallel (also called Combescure) transformations modify the edge lengths of a mesh but conserve face planarity and edge orientation

Möbius transformations also conserve face planarity and torsion-free nodes when applied to a circular mesh. Their application to architectural design was studied in (Mesnil, Douthe, Baverel and Léger 2017b). (Vaxman *et al.* 2015) developed a method to conformally deform a mesh by applying different Möbius transform to each face.

Projective transformations are also a rich tool if face planarity is the only constraint. This family contains in particular scalings (homotheties, 1D-scalings), shearing, projections, rigid body motions and tapering. Methods to deform planar quad meshes with projective transformations are proposed in (Vaxman 2012; Poranne *et al.* 2013, 2015).

(Yang et al. 2011) explore a general method to deform a mesh while conserving given geometrical properties. They construct the basis of mesh deformations that do not modify the properties at the 1st or 2nd order. Iteratively small deformations along these modes allow to deform a mesh globally, while keeping it, for example, circular.

Many more deformations have been identified in surface theory, such as Ribeaucour transforms, Christoffel duality, Backlung transformations… Each of these transformations conserves particular surface properties. These transformations have received a great attention from the discrete differential geometry community (Bobenko and Suris 2008): A complete discrete model of a family of surfaces should contain a discrete model of the transformations that conserve the properties of this family.

From combinatorics

For some highly constrained geometrical structures, the shape is mostly determined by the pattern of connection of elements – their *combinatorics*. One example is surfaces made of equilateral triangles, called Lobel frames. If equilateral triangles are connected in a regular pattern, where six triangles meet at each node, cylinders are the only smooth shapes that can be obtained. The only way to obtain more complex shapes is to introduce singularities: nodes at which more or less than six triangles meet. Still, for one configuration of singularities (i.e. one combinatorics), the design space is extremely narrow, as observed in the numerical experimentations of (Huard 2014). Hence, the placement of singularities is nearly the only design handle that one has on the shape. Another examples are the circles packings introduced in (Bobenko *et al.* 2006) to discretize minimal surfaces. Although the geometry of these packing can also be controlled by angles at the boundaries, their shape comes mostly from their connectivity, a property used in (Bücking 2007) to generate a wide range of periodic discrete minimal surfaces.

From sketches

A recent trend in computer graphics research is the creation of 3D models from 2D hand sketches. The idea is to incorporate the power of digital tools into the most ubiquitous design method. Out of a sketch, only a projection of the desired geometry is known. Hence, the main difficulty is to understand what 3D geometry the designer has in mind when he draws a set of lines. An example of 3D reconstruction is given

in (Nishida *et al.* 2016), which introduces a method to hand draw 3D buildings. The algorithm fits a building to a sketch out of a grammar of parametric building geometries. (Nealen *et al.* 2007) propose a method to deform a surface by sketching on it inside a 3D CAD environment. As these methods resort to geometrical surface primitives, the ones described in sections 2.4.3 and 2.4.4 can be used to reconstruct surfaces with fabrication properties. For example, (Jung *et al.* 2015) use developable surfaces as primitives to generate fabric cutting patterns out of sketches of the cloth worn on somebody.

2.5 Challenges and opportunities

Discussion of panorama

Generation methods from surface and pattern offer limited freedom to obtain construction properties. There already exists efficient algorithms for most problems, there is limited progress left to accomplish with this approach.

Generation from a target surface offer more room to simplify fabrication. Numerical methods for this type of rationalization have also been widely explored. However, there is room left for improving how intuitive the methods are to use. Furthermore, geometry can be used to develop new cost-efficient structural systems.

Generation from sections or boundaries offers a great potential for conceptual design stages. However, there are a limited number of methods available. Furthermore, a recurrent problem is to find a correct topology to work with.

Specific research goals

This thesis introduces generation methods for four families of surfaces with particular rationalization potential. Their properties are summarized in table 2.1. Properties that can be obtained in special cases are in *italic*. The proposed methods fall into three of the generation cases identified in section 2.4: Their input are section curves, boundary curves, or reference surfaces. These types of input are justified by the fact that these surfaces are difficultly attainable from arbitrary target surface and pattern: because of their many geometrical properties, their geometry is relatively constrained. To counterbalance this level of constraint on the shape, a particular focus is devoted to developing methods that allow to explore intuitively a portion as large as possible of the design space.

New rationalization strategies to construct curved shapes are explored in chapter 3 and 4, they are based on new geometrical structures. Although this thesis has a strong focus on gridshells, methods are proposed for other popular typologies of curved structures such as membranes, plated shells and vaults.

	Surfaces with planar curvature lines ***chapter 3***	**Caravel meshes** ***chapter 4***	**S-CMC meshes** ***chapter 5***	**Linear-Weingarten surfaces** ***chapter 6***
Properties for a gridshell	- Planar panels - Torsion-free nodes - Planar / circular beams - *Node repetition*	- No kink angle between panels and beams - Torsion free nodes - *Node repetition* - *Perfect nodes* - *Low valence*	- Planar panels - Torsion-free nodes - Perfect nodes - Alignment of beams with principal stresses	- Planar panels - Torsion-free nodes - Alignment of beams with principal stresses
Other structural applications	- 3D trusses	- Gridshells with various patterns - Plated shells		**- Membranes** **- Funicular shell** (masonry, concrete…)
Design input	2 section curves + 1 parameter	Surface	Boundaries + 1 parameter	Boundaries + **2** parameters
Generation method	1. Construct a Gauss map 2. Apply transformation	1. Discretize surface by curvature lines or conjugate net. 2. Optimize vertex position and orientation of node axes	1. Construct Gauss map from circle packing 2. Apply transformation	Search for critical points of a functionnal
Mesh alignment	Curvature lines	Conjugate nets / Curvature lines	Curvature lines	*Membranes:* None *Gridshells:* Relative curvature lines

Table 2.1 Summary of properties and generation methods for the surfaces addressed in this manuscript

References

Abramczyk, J. (2016) 'Integrated building forms covered with effectively transformed folded sheets', *Journal of the International Association for Shell and Spatial Structures*, 57(2), 121–132.

Adriaenssens, S., Asce, M., Ney, L., Bodarwe, E., Williams, C.J.K. (2012) 'Finding the Form of an Irregular Meshed Steel and Glass Shell Based on Construction Constraints', *Journal of Architectural Engineering*, 18(September), 206–213.

Adriaenssens, S., Barnes, M.R., Williams, C. (1999) 'A new analytic and numerical basis for the form-finding and analysis of spline and gridshell structures', in *Computing Developments in Civil and Structural Engineering*, 83–91.

Adriaenssens, S., Block, P., Veenendaal, C., Williams, C.J.K. (2014) *Shell Structures for Architecture. Form Finding and Optimization*, Routledge.

Akbarzadeh, M., Van Mele, T., Block, P. (2015) 'On the equilibrium of funicular polyhedral frames and convex polyhedral force diagrams', *CAD Computer Aided Design*, 63, 118–128, available: http://dx.doi.org/10.1016/j.cad.2015.01.006.

Alliez, P., Cohen-steiner, D., Devillers, O., Bruno, L., Desbrun, M. (2003) 'Anisotropic Polygonal Remeshing', *Transactions on Graphics*, 22(3), 485–493.

Anderson, S. (2005) *Eladio Dieste: Innovation in Structural Art*, Princeton Architectural Press.

Austern, G., Capeluto, I.G., Grobman, Y.J. (2018) 'Rationalization methods in computer aided fabrication : A critical review', *Automation in Construction*, 90, 281–293, available: https://doi.org/10.1016/j.autcon.2017.12.027.

Bagneris, M., Motro, R., Maurin, B., Pauli, N. (2008) 'Structural morphology issues in conceptual design of double curved systems', *International Journal of Space Structures*, 23(2), 79–87.

Barnes, M.R. (1999) 'Form finding and analysis of tension structures by dynamic relaxation.', *International Journal of Space Structures*, 14(2), 89–104.

Baverel, O. (2000) *Nexorades: A Family of Interwoven Space Structures*.

Baverel, O., Caron, J.F., Tayeb, F., Peloux, L. Du (2012) 'Gridshells in composite materials: Construction of a 300 m2 forum for the solidays' festival in Paris', *Structural Engineering International: Journal of the International Association for Bridge and Structural Engineering (IABSE)*, 22(3), 408–414.

Belis, J., Inghelbrecht, B., Callewaert, D. (2007) 'Cold bending of laminated glass panels', *Heron*, 52(1), 123–146.

Berk, A., Giles, H. (2017) 'Quadrilateral panelization of freeform surface structures', *Automation in Construction*, 76, 36–44, available: http://dx.doi.org/10.1016/j.autcon.2017.01.007.

Bermano, A.H., Funkhouser, T., Rusinkiewicz, S. (2017) 'State of the Art in Methods and Representations for Fabrication-Aware Design', *Computer Graphics Forum*, 36(2).

Blassel, J., Pfadler, A. (2008) 'La gare de Strasbourg', *Construction métallique*, 45(1), 15–36.

Bletzinger, K., Ramm, E. (1999) 'A General Finite Element Approach to the Form Finding of Tensile Structures by the Updated Reference Strategy', *International Journal of Space Structures*, 14(2), 131–145.

Bletzinger, K.U., Wüchner, R., Daoud, F., Camprubí, N. (2005) 'Computational methods for form finding and optimization of shells and membranes', *Computer Methods in Applied Mechanics and Engineering*, 194(30-33 SPEC. ISS.), 3438–3452.

Block, P. (2009) *Thrust Network Analysis. Exploring Three-Dimensional Equilibrium*.

Bo, P., Pottmann, H., Kilian, M., Wang, W., Wallner, J. (2011) 'Circular arc structures', *ACM Trans. Graph.*, 30(4), 101:1–101:12, available: http://doi.acm.org/10.1145/2010324.1964996.

Bobenko, A.I., Gunn, C. (2018) *Conform!* [online], Springer, available: http://conformmovie.de/.

Bobenko, A.I., Hoffmann, T., Springborn, B.A. (2006) 'Minimal surfaces from circle patterns : Geometry from combinatorics', *Annals of Mathematics*, 164, 231–264.

Bobenko, A.I., Suris, Y.B. (2008) 'Discrete differential geometry. Integrable Structure.', *Graduate Studies in Mathematics*, 98.

Bommes, D., Zimmer, H., Kobbelt, L. (2009) 'Mixed-Integer Quadrangulations', *ACM Transactions On Graphics*, 28(3).

Bouaziz, S., Deuss, M., Schwartzburg, Y., Weise, T., Pauly, M. (2012) 'Shape-Up : Shaping Discrete Geometry with Projections', *Eurographics Symposium on Geometry Processing*, 31.

Brakke, K.A. (1992) 'The surface evolver', *Experimental Mathematics*, 1(2), 141–165.

Brandt-Olsen, C. (2016) *Calibrated Modelling of Form-Active Structures*.

Brew, J.S., Lewis, W.J. (2003) 'Computational form-finding of tension membrane structures - Non-finite element approaches: Part 2. Triangular mesh discretization and control of mesh distortion in modelling minimal surface membranes', *International Journal for Numerical Methods in Engineering*, 56(5), 669–684.

Bücking, U. (2007) 'Approximation of conformal mappings by circle patterns and discrete minimal surfaces', *PhD diss., Technischen Universität Berlin*.

Buri, H., Weinand, Y. (2008) 'ORIGAMI – Folded Plate Structures', in *10th World Conference on Timber Engineering*.

do Carmo, M.P. (1976) *Differential Geometry of Curves and Surfaces*, Prentice-Hall, Inc.

Chen, H., Lee, I., Leopoldseder, S., Pottmann, H., Randrup, T., Wallner, J. (1999) 'On Surface Approximation using Developable Surfaces', *Graphical Models and Image Processing*, 61(2), 110–124.

Colabella, S., D'Amico, B., Hoxha, E., Fivet, C. (2017) 'Structural Design with Reclaimed Materials : an Elastic Gridshell out of Skis', in *IASS Annual Symposium*.

Crane, K., Desbrun, M., Schröder, P. (2010) 'Trivial connections on discrete surfaces', *Computer Graphics Forum*, 29(5), 1525–1533.

Delarue, J.-M. (1992) *Morphogenèse*, U.P.A., 'Ecole d'Architecture Paris Villemenin.

Dong, S., Bremer, P.T., Garland, M., Pascucci, V., Hart, J.C. (2006) 'Spectral surface quadrangulation', *ACM SIGGRAPH*, 1057–1066.

Douthe, C. (2007) *Etude de Structures Élancées Précontraintes En Matériaux Composites , Application à La Conception Des Gridshells*.

Douthe, C., Mesnil, R., Baverel, O., Gobin, T., Tellier, X., Ducoulombier, N., Montagne, N. (2018) 'Design and construction of a shell-nexorade hybrid timber structure', *Proceedings of the IASS Symposium 2018: Creativity in Structural Design, Boston, USA*, (July), 1–8.

Douthe, C., Mesnil, R., Orts, H., Baverel, O. (2017) 'Isoradial meshes : covering elastic gridshells with planar facets', *Automation in Construction*, 83, 222–236.

Eekhout, M., Niderehe, S. (2009) 'The cold bent glass roof of the Victoria & Albert Museum, London', in *GLASS PERFORMANCE DAYS*, 408–412.

Eigensatz, M., Kilian, M., Schiftner, A., Mitra, N., Pottmann, H., Pauly, M. (2010) 'Paneling Architectural Freeform Surfaces', *ACM Trans. Graph.*, 29(4)(45).

Eversmann, P., Schling, E., Ihde, A., Louter, C. (2016) 'Low-Cost Double Curvature : Geometrical and Structural Potentials of Rectangular , Cold-Bent Glass Construction', in *Proceedings of the IASS Annual Symposium*.

Fabbri, R., Corvez, D. (2013) 'Rationalisation of complex uhpfrc facade shapes', in *RILEM-Fib-AFGC Int. Symposium on Ultra-High Performance Fibre-Reinforced Concrete, UHPFRC 2013*, 27–36.

Farin, G., Hoschek, J., Kim, M.S. (2002) *Handbook of Computer Aided Geometric Design*, Elsevier Science B.V.

Fildhuth, T., Schieber, R., Oppe, M. (2018) 'Design and Construction with Curved Glass', in *Engineered Transparency 2018. Glass in Architecture and Structural Engineering,* 369–381.

Fischer, T. (2012) 'Geometry Rationalization for Non-Standard Architecture', *Architecture Science.*, 5(5), 25–47.

Fu, C.W., Lai, C.F., He, Y., Cohen-Or, D. (2010) 'K-set tilable surfaces', *ACM SIGGRAPH 2010 Papers, SIGGRAPH 2010*.

Garg, A., Pauly, M., Wardetzky, M. (2014) 'Wire Mesh Design', *Transactions on Graphics*, 33(4).

Gavriil, K., Schiftner, A., Pottmann, H. (2019) 'Optimizing B-spline surfaces for developability and paneling architectural freeform surfaces', *CAD Computer Aided Design*, 111, 29–43, available: https://doi.org/10.1016/j.cad.2019.01.006.

Glymph, J., Shelden, D., Ceccato, C., Mussel, J., Schober, H. (2004) 'A Parametric Strategy for Freeform Glass Structures Using Quadrilateral Planar Facets', *Automation in Construction*, 13(2), 187–202.

Gründig, L., Schek, H.J. (1974) 'Analytical form finding and analysis of prestressed cable networks.', in *International Conference on Tension Roof Structures, London*.

Harding, J., Pearson, W., Lewis, H., Melville, S. (2014) 'The Ongreening Pavilion', in *Advances in*

Architectural Geometry, 295–308.

Hopf, H. (1983) *Differential Geometry in the Large, Lecture Notes in Math*.

Huard (2014) 'Planar Panelization With Extreme Repetition'.

Jiang, C., Tang, C., Vaxman, A., Wonka, P., Pottmann, H. (2015) 'Polyhedral Patterns', *ACM Transactions on Graphics (TOG)*, 34(6).

Jiang, C., Wang, J., Wallner, J., Pottmann, H. (2014) 'Freeform honeycomb structures', in *Computer Graphics Forum*, 185–194.

Jung, A., Hahmann, S., Rohmer, D., Begault, A., Boissieux, L., Cani, M., Jung, A., Hahmann, S., Rohmer, D., Begault, A., Boissieux, L., Jung, A., Hahmann, S. (2015) 'Sketching Folds : Developable Surfaces from Non-Planar Silhouettes', *ACM Transactions on Graphics*, 34(5), 155.

Kälberer, F., Nieser, M., Polthier, K. (2007) 'QuadCover - Surface parameterization using branched coverings', *Computer Graphics Forum*, 26(3), 375–384.

Knippers, J., Helbig, T. (2009) 'Recent developments in the Design of Glazed Grid Shells', *International Journal of Space Structures*, 24(2), 111–126.

Konaković-luković, M., Konaković, P., Pauly, M. (2018) 'Computational Design of Deployable Auxetic Shells', in *Advances in Architectural Geometry*, 94–111.

Krivoshapko, S.N., Ivanov, V.N. (2015) *Encyclopedia of Analytical Surfaces*, Springer International Publishing.

Leduc, N., Caron, J.F., Douthe, C., Vaudeville, B., Aubry, S. (2018) 'An Innovative Fabrication Process from Rolled Helicoidal Steel Strips', in *40th IABSE Symposium, Tomorrow's Megastructures*, S14,15-S14,32.

Liu, Y., Pottmann, H., Wallner, J., Yang, Y.-L., Wang, W. (2006) 'Geometric modeling with conical meshes and developable surfaces', *ACM Transactions on Graphics*, 25(3), 681.

Liu, Y., Wang, W. (2008) 'On Vertex Offsets of Polyhedral Surfaces', in *Proceedings of Advances in Architectural Geometry*, 61–64.

Liu, Y., Xu, W., Wang, J., Zhu, L., Guo, B., Chen, F., Wang, G. (2011) 'General planar quadrilateral mesh design using conjugate direction field', *ACM Transactions on Graphics*, 30(6), 1.

Maia Avelino, R., Baverel, O., Lebée, A. (2019) 'Design strategies for gridshells with singularities', *Journal of the International Association for Shell and Spatial Structures*, 60(3), 189–200.

Malek, S., Williams, C. (2013) 'Structural Implications of using Cairo Tiling and Hexagons in Gridshells', *Proceedings of the International Association for Shell and Spatial Structures (IASS) Symposium*, (September 2013), 3–6.

Malek, S.R. (2012) *The Effect of Geometry and Topology on the Mechanics of Grid Shells*.

Masson, Y. (2017) 'Existence et construction de réseaux de Chebyshev avec singularités et application aux gridshells', available: https://cermics.enpc.fr/~massony/thesis.pdf.

Maurin, B. (1998) *Morphogenese Des Membranes Textiles Architecturales*.

Mesnil, R., Douthe, C., Baverel, O. (2017) 'Non-standard patterns for gridshells : fabrication and structural optimization', *Journal of the International Association for Shell and Spatial Structures*, 58(4), 277–286.

Mesnil, R., Douthe, C., Baverel, O., Leger, B. (2017) 'Marionette Meshes : Modelling free-form architecture with planar facets', *International Journal of Space Structures*, 32(3–4), 184–198.

Mesnil, R., Douthe, C., Baverel, O., Léger, B. (2017a) 'Linear buckling of quadrangular and kagome gridshells: A comparative assessment', *Engineering Structures*, 132, 337–348.

Mesnil, R., Douthe, C., Baverel, O., Léger, B. (2017b) 'Generalised cyclidic nets for shape modelling in architecture', *International Journal of Architectural Computing*, 15(2), 148–168.

Mesnil, R., Douthe, C., Baverel, O., Léger, B. (2018) 'Morphogenesis of surfaces with planar lines of curvature and application to architectural design', *Automation in Construction*, 95, 129–141.

Mesnil, R., Douthe, C., Baverel, O., Léger, B., Caron, J.F. (2015) 'Isogonal moulding surfaces: A family of shapes for high node congruence in free-form structures', *Automation in Construction*, 59, 38–47.

Mollica, Z., Self, M. (2016) 'Tree Fork Truss Geometric Strategies for Exploiting Inherent Material Form', in *Advances in Architectural Geometry*, 138–153.

Nealen, A., Sorkine, O., Alexa, M., Cohen-Or, D. (2007) 'A sketch-based interface for detail-preserving mesh editing', *ACM SIGGRAPH 2007 Papers - International Conference on Computer Graphics and Interactive Techniques*, 1–6.

Nishida, G., Garcia-Dorado, I., Aliaga, D.G., Benes, B., Bousseau, A. (2016) 'Interactive sketching of urban procedural models', *ACM Transactions on Graphics*, 35(4).

Otter, J., Cassel, A., Hobbs, R. (1966) 'Dynamic relaxation', in *Proceedings of the Institution of Civil Engineers*, 633–656.

Otto, F. (1974) *IL10 Gitterschalen*, Institut für leichte Flächentragwerke (IL).

Oval, R., Rippmann, M., Mesnil, R., Van Mele, T., Baverel, O., Block, P. (2018) 'Topology Finding of Structural Patterns', in *Advances in Architectural Geometry*, 342–363, available: www.architecturalgeometry.org/aag18.

Oval, R., Rippmann, M., Mesnil, R., Van Mele, T., Baverel, O., Block, P. (2019) 'Feature-based topology finding of patterns for shell structures', *Automation in Construction*, 103(March), 185–201, available: https://doi.org/10.1016/j.autcon.2019.02.008.

Pellis, D., Kilian, M., Dellinger, F., Wallner, J., Pottmann, H. (2019) 'Visual smoothness of polyhedral surfaces', *ACM Transactions on Graphics*, 38(4).

Pirazzi, C., Weinand, Y. (2006) 'Geodesic lines on free-form surfaces - Optimized grids for timber rib shells', *9th World Conference on Timber Engineering 2006, WCTE 2006*, 1, 72–78.

Poranne, R., Chen, R., Gotsman, C. (2015) 'On Linear Spaces of Polyhedral Meshes', *IEEE transactions on visualization and computer graphics*, 21(5), 652–662.

Poranne, R., Ovreiu, E., Gotsman, C. (2013) 'Interactive Planarization and Optimization of 3D Meshes', 32(1), 152–163.

Pottmann, H. (2013) 'Architectural Geometry and Fabrication-Aware Design', *Nexus Network Journal*, 15(2), 195–208.

Pottmann, H., Asperl, A., Hofer, M., Kilian, A. (2007) *Architectural Geometry*, Bentley Institute Press.

Pottmann, H., Eigensatz, M., Vaxman, A., Wallner, J. (2015) 'Architectural geometry', *Computers and Graphics (Pergamon)*, 47, 145–164.

Pottmann, H., Huang, Q., Deng, B., Schiftner, A., Kilian, M., Guibas, L., Wallner, J. (2010) 'Geodesic patterns', *ACM Transactions on Graphics*, 29(4), 1, available: http://portal.acm.org/citation.cfm?doid=1833351.1778780.

Pottmann, H., Liu, Y., Wallner, J., Bobenko, A.I., Wang, W. (2007) 'Geometry of multi-layer freeform structures for architecture', *ACM Transactions on Graphics*, 26(3), 65.

Pottmann, H., Schiftner, A., Bo, P., Schmiedhofer, H., Wang, W., Baldassini, N., Wallner, J. (2008) 'Freeform surfaces from single curved panels', *ACM Transactions on Graphics*, 27(3), 1.

Pottmann, H., Wallner, J. (2007) 'The focal geometry of circular and conical meshes', *Advances in Computational Mathematics*, 29(3), 249–268.

Rabagliati, J., Huber, C., Linke, D. (2014) 'Balancing complexity and simplicity', in *Fabricate*, 43–51.

Rose, K., Sheffer, A., Wither, J., Cani, M., Thibert, B. (2007) 'Developable Surfaces from Arbitrary Sketched Boundaries', *Eurographics Symposium on Geometry Processing*, 163–172.

Sageman-Furnas, A.O., Chern, A., Ben-Chen, M., Vaxman, A. (2019) 'Chebyshev Nets from Commuting

PolyVector Fields', *ACM Transactions on Graphics*, 38(4), 1–14, available: http://dl.acm.org/citation.cfm?doid=3306346.3322962.

Schek, H.J. (1974) 'The force density method for form finding and computation of general networks', *Computer Methods in Applied Mechanics and Engineering*, 3(1), 115–134.

Schiftner, A., Balzer, J. (2010) 'Statics-Sensitive Layout of Planar Quadrilateral Meshes', in *Advances in Architectural Geometry*, 221–236.

Schiftner, A., Höbinger, M., Wallner, J., Pottmann, H. (2009) 'Packing circles and spheres on surfaces', *ACM Transactions on Graphics*, 28(5), 1, available: http://portal.acm.org/citation.cfm?doid=1618452.1618485.

Schiftner, A., Leduc, N., Bompas, P., Baldassini, N., Eigensatz, M. (2012) 'Architectural Geometry from Research to Practice: The Eiffel Tower Pavilions', in *Advances in Architectural Geometry*, 213–228.

Schling, E. (2018) *Repetitive Structures*, *PhD Manuscript, TUM, Fakultät für Architektur*.

Schling, E., Hitrec, D., Barthel, R. (2017) 'Designing Grid Structures Using Asymptotic Curve Networks', *Humanizing Digital Reality, Design Modelling SYmposium, Paris*.

Schober, H. (2015) *Transparent Shells: Form, Topology, Structure*, Ernst & Sohn.

Schodek, D., Bechthold, M., Griggs, K., Kao, K.M., Steinberg, M. (2005) *Digital Design and Manufacturing*, John Wiley & Sons.

Shelden, D.R. (2002) *Digital Surface Representation and the Constructibility of Gehry's Architecture by*.

Singh, M., Schaefer, S. (2010) 'Triangle surfaces with discrete equivalence classes', *ACM SIGGRAPH 2010 Papers*, July.

Sischka, J., Brown, S., Handel, E., Zenkner, G. (2001) 'Die Überdachung des Great Court im British Museum in London', *Stahlbau*, 70(7), 492–502.

Sotomayor, J. (1992) 'Lines of curvature and umbilic points on surfaces', *Séminaire de théorie spectrale et géométrie*, 10(January 1992), 9–12, available: http://tsg.cedram.org/item?id=TSG_1991-1992__10__9_0.

Stein, O., Grinspun, E., Crane, K. (2018) 'Developability of triangle meshes', *ACM Transactions on Graphics*, 37(4), 1–14.

Stephan, S., Knebel, K., Sanchez-Alvarez, J. (2004) 'Reticulated Structures On Free-Form Surfaces', *Stahlbau*, 73(April), 562–572.

Stephenson, K. (1997) 'The approximation of conformal structures via circle packing', in *Computational Methods and Function Theory*, 551–582.

Surtees, T., Petschke, T., Viola, J. (2017) 'Engineering the Oculus – World Trade Center PATH Transportation Hub', in *39th IABSE Symposium – Engineering the Future September*.

Tang, C., Sun, X., Gomes, A., Wallner, J., Pottmann, H. (2014) 'Form-finding with Polyhedral Meshes Made Simple', *Transactions on Graphics*, 33(4).

Tayeb, F. (2015) 'Simulation numérique du comportement mécanique non linéaire de gridshells composés de poutres élancées en matériaux composites et de sections quelconques', available: https://pastel.archives-ouvertes.fr/tel-01260287.

Vakar, L., Gaal, M. (2004) 'Cold Bendable, Laminated Glass – New Possibilities in Design', *Structural Engineering International*, 14(2).

Vaxman, A. (2012) 'Modeling Polyhedral Meshes with Affine Maps', in *Eurographics Symposium on Geometry Processing*.

Vaxman, A., Campen, M., Diamanti, O., Panozzo, D., Bommes, D., Hildebrandt, K., Ben-Chen, M. (2016) 'Directional field synthesis, design, and processing', *Computer Graphics Forum*, 35(2), 545–572.

Vaxman, A., Müller, C., Ofir, W. (2015) 'Conformal Mesh Deformations with Möbius Transformations', *ACM Transaction on Graphics*, 34(4).

Wallner, J., Schiftner, A., Kilian, M., Fl, S., Mathias, H., Deng, B., Huang, Q., Pottmann, H. (2010) 'Tiling Freeform Shapes With Straight Panels : Algorithmic Methods .'

Wang, W., Liu, Y. (2009) 'A Note on Planar Hexagonal Meshes', in *Nonlinear Computational Geometry*, 221–233.

Wang, W., Wallner, J., Liu, Y. (2007) 'An angle criterion for conical mesh vertices', *Journal for Geometry and Graphics*, 11(2), 199–208, available: http://www.ams.org/mathscinet-getitem?mr=MR2420633%5Cnpapers2://publication/uuid/46BDD67F-8A04-4C78-B2B6-1218E4E8A8A5.

Williams, C.J.K. (2000) 'The definition of curved geometry for widespan enclosures', in M. Barnes and M. Dickson, ed., *Widespan Roof Structures*, Thomas Telford, London, 41–59.

Williams, C.J.K. (2001) 'The analytic and numerical definition of the geometry of the British Museum Great Court Roof', *Mathematics & design*, 200, 434–440.

Yang, Y.-L., Yang, Y.-J., Pottmann, H., Mitra, N. (2011) 'Shape Space Exploration of Constrained Meshes', *ACM Transactions on Graphics (TOG)*, 30(6).

Zadravec, M., Schiftner, A., Wallner, J. (2010) 'Designing Quad-Dominant Meshes with Planar Faces', in *Computer Graphics Forum*, Oxford, UK: Blackwell Publishing Ltd., 1671–1679.

Zeng, W., Yin, X., Zhang, M., Luo, F., Gu, X. (2009) 'Generalized Koebe's method for conformal mapping multiply connected domains', in *Proceedings of the SIAM/ACM Joint Conference on Geometric and Physical Modeling*, 89–100.

Chapter 3 Surfaces with planar curvature lines

The first family of surfaces which shall be investigated in this thesis are those with planar curvature lines, which are of particular interest for gridshells, and more particularly the ones with continuous beams. For this type of structures, beam planarity improves significantly fabrication precision and reduces costs. Beam planarity can be easily obtained by itself from a reference surface, but combining it with torsion-free nodes, planar faces and offset is an open problem. We tackle it by studying how circular meshes with planar lines can be generated.

This problem turns out to be too constrained for optimization from an arbitrary surface, it requires a dedicated method. The proposed one relies on the differential geometry of surfaces with planar curvature lines, developed in the XIXth century. Based on this work, a geometrical structure for the discrete Gauss map naturally appears. From two target planar guide curves, such a Gauss map can be constructed, and deformed by a parallel transformation to fit the guide curves. This generation methods allows an intuitive control in real-time of circular meshes with planar lines. Geometry of curved continuous beams can be recovered using the theory of cyclidic nets. In the last part of this chapter, structural applications of these surfaces are explored.

3.1 Introduction

3.1.1 Curved beam fabrication

Planarity of a curved beam simplifies significantly its fabrication. For a timber structure, glulam is a very popular solution to fabricate curved beams. Thin strips of wood are elastically bent and glued together in a curved configuration, such that the beam keeps its shape once the glue has set. For a non-planar beam, there is a curvature in two directions (up/down and left/right). Hence, strips need to be subdivided into thin rods. An example is shown in Figure 3.1 (left), the red lines indicate how a beam of the centre Pompidou in Metz was subdivided. The forming process is therefore much more complex than for a planar beam.

For a steel structure, the most common method to produce curved beams is to roller bend initially straight beams. This process is precise for a planar beam with constant curvature radius. It is however less precise for a continuously varying radius. If the beam is also not planar, it becomes nearly impossible to obtain the required precision for a curved facade structure.

Figure 3.1: Left: A nonplanar gluelam beam (Courtesy of Design-To-Production (Zürich)) Right: Cold-bending of a steel profile (©Mallela Gbrs)

In both steel and wood, non-planarity of beams make the fabrication process more complex, time consuming, and costly. The Schubert Marine Band Shell in Minnesota (USA), showed in Figure 3.2 (Schober 2015), does have planar beams with constant radius. Yet, it has an interesting double-curvature. Its geometry is based on a portion of torus: It allows to combine planar beams with all the properties of a circular meshes – offset, planar faces and torsion free nodes.

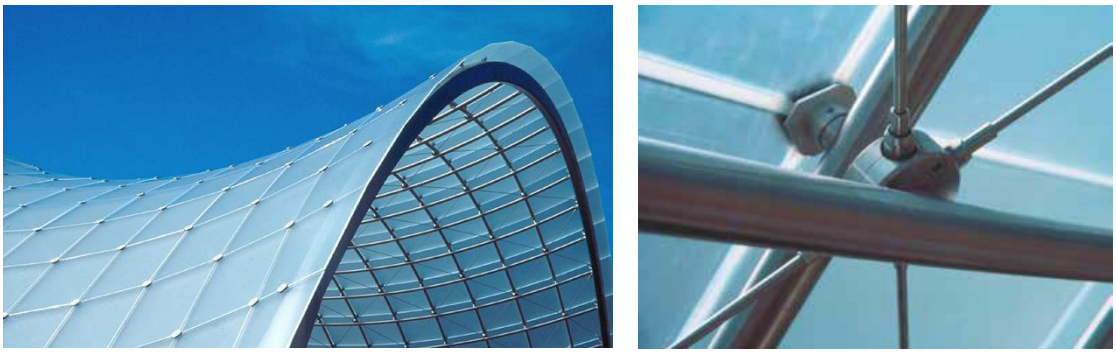

Figure 3.2: Schubert Marine Club Band Shell. Left: Overview. Right: connection detail (©Brian Gulick) (pictures courtesy of James Carpenter Design Associates)

3.1.2 Planar quad mesh with planar lines

Translation meshes can be used to obtain a geometry with planar quadrangles and planar lines: one just need to take as input a planar section and a planar rail. However, they do not solve entirely the geometrical problem of covering a net of planar beams with planar panels. Indeed, beams centerlines and panels are necessarily spaced out in a real structure (Figure 3.2, right). If a translation mesh is used for the geometry of panels, its offset will not have planar lines. Similarly, if a translation mesh is used to obtain a grid of planar beams, its offset will not have planar faces, which will cause paneling issues.

3.1.3 Circular meshes with planar lines

These observation leads naturally to the following geometrical object: circular meshes with planar lines, showed in Figure 3.3. More precisely, we mean that the edge polylines of any quad strip are planar. We will describe these meshes as having planar curvature lines, even though this term is usually reserved for

surfaces. Circular meshes are discrete equivalent of surfaces parametrized by curvature lines (Bobenko 2008). These meshes are therefore discrete equivalents of surfaces with planar curvature lines. This family of surfaces contains in particular the torus, the reference surface of the Schubert Club Band Shell. This work is related to the one presented in (Mesnil *et al.* 2018) that looked at circular meshes for which curvature lines are planar in only one direction.

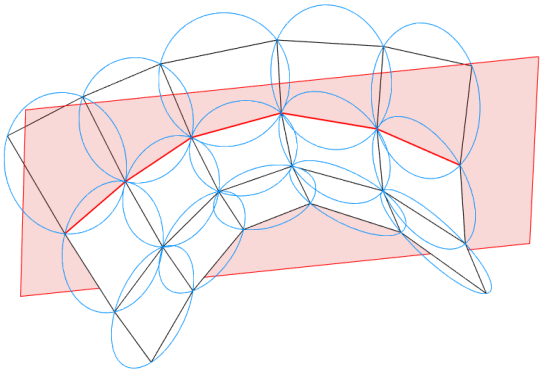

Figure 3.3: A circular mesh with planar lines

3.1.4 Overview of the chapter

The goal of this chapter is to propose a method to generate intuitively surfaces with planar curvature lines, and in particular to answer the following question: When combining planar beams, planar panels, torsion-free nodes and node-offset, what are the possible shapes beyond the torus?

Given these strong geometric constraints, the generation of these meshes is badly suited for post-rationalization: One cannot expect to obtain these properties by deforming an arbitrary mesh with small deformations. A bottom-up generation method is therefore developed. It is presented in section 3.3, it allows to control surfaces by two section curves. It relies on the geometry of surfaces with planar curvature lines, introduced beforehand in section 3.2. Section 3.4 shows how the proposed tool can be used to design curved envelopes. Section 3.5 discusses the strengths and limitations of the method. Finally, section 3.6 presents technological applications of the method.

3.2 Discretization of surfaces with planar curvature lines

In this section we present relevant properties of surfaces with planar curvature lines and then propose a circular discretization.

3.2.1 Smooth surfaces with planar curvature lines

3.2.1.1 Early work

Surfaces with planar curvature lines were studied for the first time by Monge at the beginning of the 19th century. In (Monge 1805), which is a pioneering work for the use of differentials for the study of surfaces, Monge studied the particular case of surfaces for which family of curvature lines lie on parallel planes: the so-called molding surfaces. Later on, Bonnet (Bonnet 1853) derived the general differential equations ruling the geometry of these surfaces. Other notable contributions to the understanding of these surfaces were made by Adam (Adam 1893), who studied the isothermic surfaces with planar curvature lines, and

by Darboux and Bianchi (Darboux 1896; Bianchi 1894). Darboux (Darboux 1896) discovered that surfaces with planar curvature lines are the envelope of the radical planes of two families of spheres whose centers lie on focal conics (i.e. conics lying in orthogonal planes such that the apex of one is the focal point of the other) and whose radii are arbitrary functions (the radical plane of two intersecting spheres is the plane containing the intersection circle, see (Coxeter and Greitzer 1967) for the case of non-intersecting spheres). Figure 3.4 shows a surface constructed using this property with spheres of constant radii centered on two parabolas, thus yielding an Enneper surface (Berger and Gostiaux 1992).

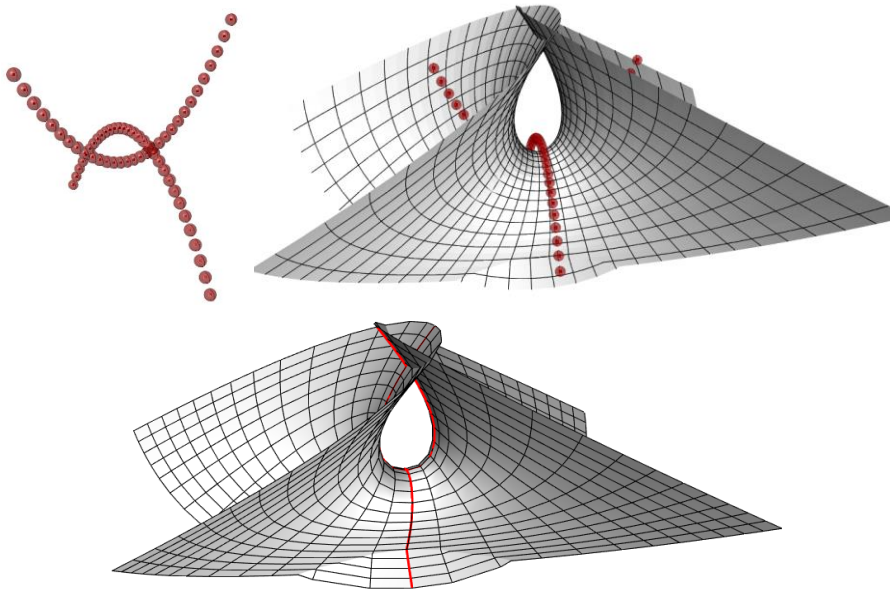

Figure 3.4: A surface with planar curvature lines. Top: generated from the envelope of radical planes of two families of spheres centered on focal parabolas. Bottom: the same surface generated by the method presented in this chapter

3.2.1.2 Gauss map geometry

On any point of a smooth surface, the unit normal vector can be described by a point on the unit sphere, S^2. The spherical surface described by all the normals is called the *Gauss map*. We shall now have a close look at the very particular structure of the Gauss map of surfaces with planar curvature lines.

The theorem of Joachimsthal states that if the intersection curve of two surfaces is a curvature line for both surfaces, then the angle between the two surfaces along the curve is constant, which means that the angle between the normal vectors of the two surfaces is constant along the curve. Since any planar curve is a curvature line of its plane, the angle between the normal of the surface and the plane of the curvature line is constant. The Gauss map of this curve is therefore constrained to a cone: it is an arc of circle. Curvature lines always intersect at a right angle, and so do their Gauss maps. As a result, the Gauss map of a surface with planar curvature lines is a system of orthogonal arcs of circle on the unit sphere. (Eisenhart 1909) showed that a system of orthogonal circles on the sphere has necessarily the following geometric properties:

- Circles can be decomposed in two families. For each family, all the planes of the circles intersect on a common axis (thus forming a so-called *pencil* of planes).
- The axes of the two families are *polar reciprocal*. This property is shown in Figure 3.5 and can be explained as follows. Let us assume that the position of one axis L_1 is known and is such that it intersects the sphere (centered at O) at two points A and B. In the plane (OAB), the lines tangent to the sphere at A and B intersect at a point M_2. The polar reciprocal line to L_1 is the line passing through M_2 orthogonally to the plane (OAB).

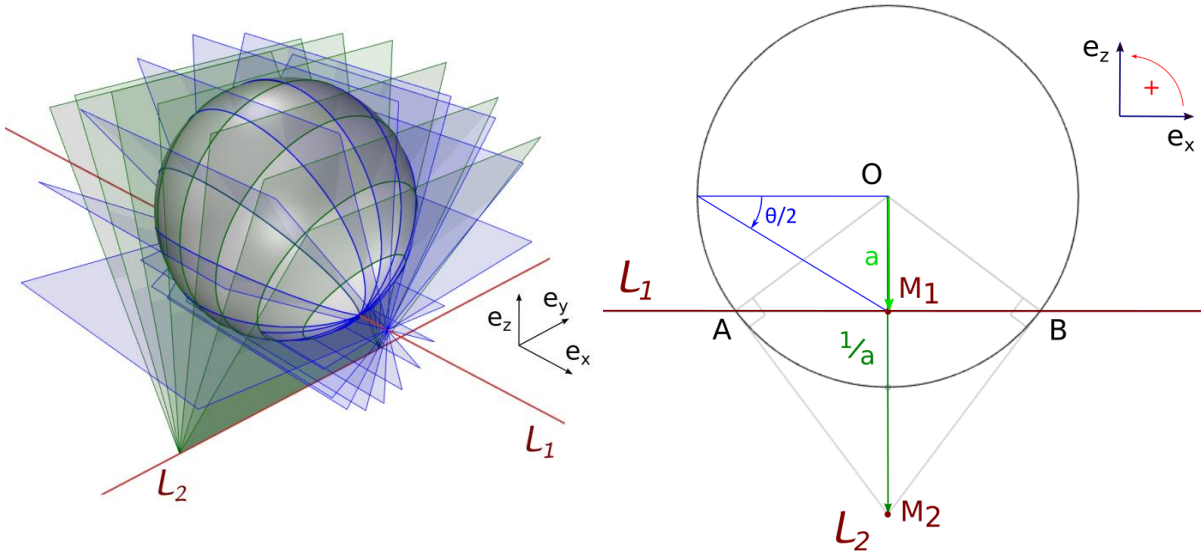

Figure 3.5: Geometry of orthogonal circles on a sphere and associated polar reciprocal axes

Considering a unit sphere centered at O = (0,0,0), the equation of these axes may be written as:

$$L_1 = \{ M_1 + \lambda\, e_x \ , \lambda \in R \}$$

$$L_2 = \{ M_2 + \mu\, e_y \ , \mu \in R \}$$

Where: $M_1 = (0,0,a)$, $M_2 = \left(0,0,\frac{1}{a}\right)$, $a \in R$

The position of the two axes determines the structure of the Gauss map, and there is only one degree of freedom (the constant a) for positioning these axes relatively to each other. Figure 3.6 shows how the structure of the Gauss map varies for values of a ranging from 0 to 1. It can be observed that only two orthogonal circles (in thick lines) do not vary, these circles are great circles of the sphere. The parameter a has the following symmetries (Figure 3.5):

- If a is replaced by $1/a$, the heights of the two axes are exchanged, which is equivalent to applying a rotation of 90° around e_z.
- Replacing a by $-a$ is equivalent to applying a symmetry about plane (O, e_x, e_z).
- The cases a → + ∞ and a → - ∞ yield the same axes positions: L_2 is the axis (O,e_x), and L_1 is at infinity.

In order to manipulate a variable that highlights these symmetries, we introduce a reparametrization of the variable a by the variable θ defined as follows:

$$a = \tan(\frac{\theta}{2})$$

The symmetries of the problems are then reflected as follows:

- Exchanging the heights of the two axis is done by taking the complementary angle $\pi - \theta$;
- Mirroring the axis positions about (O, e_x, e_z) is done by negating the angle;
- The identical cases a → + ∞ and a → - ∞ correspond to $\theta = +\pi$ and $\theta = -\pi$, which are equal angles (modulo 2π). θ does not take infinite values, and is therefore easier to handle in a programming environment.

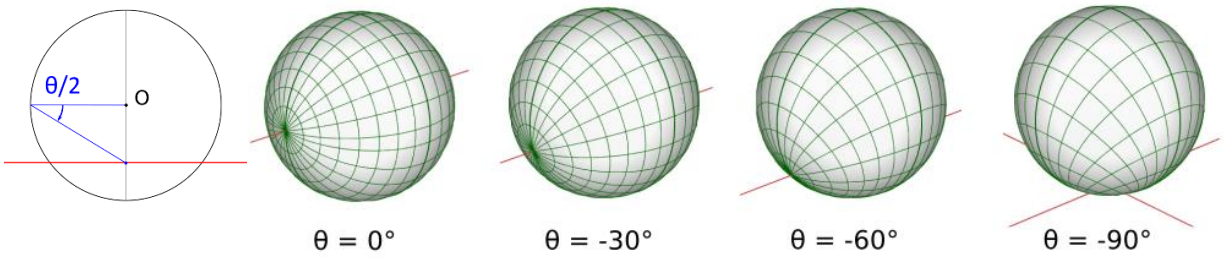

Figure 3.6: Structure of the Gauss map of a surface with planar curvature lines parametrized by curvature lines, for different distances between polar reciprocal axes

3.2.1.3 Developable surfaces

The Gauss map of developable surfaces with planar curvature lines is degenerated into a single curve. Therefore the structure shown in Figure 3.6 is of little help to understand their structure. However, their geometry is well known. First, we can observe that the rulings of a developable surface form its first family of curvature lines, these are obviously planar. For the 2nd family of curvature lines, we have to look separately at the three types of smooth developable surfaces: Cylinders, cones, and envelopes of the tangent lines to a 3D curve. The second family of curvature lines is always planar for cylinders and for right cones with a circular base. The more complex 3rd type was studied by Bonnet (Bonnet 1853). He proved that surfaces generated by the tangent to a general helix (i.e. a curve which tangent has a constant angle with a given axis) are the only developable surfaces of this type with planar curvature lines. Example are shown in Figure 3.7 and Figure 3.8.

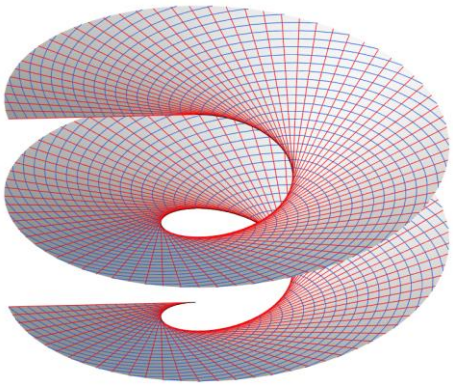

Figure 3.7: Tangents to a general helix form a developable surface with planar curvature lines (shown in blue and red).

Figure 3.8: These brave PhD students from the Navier laboratory try to get to the top of the mountain with the shortest path. Due to the limited friction of their skis on this April snow, they naturally follow a curve of constant slope, which is a general helix. Hence, theirs skis describe a developable surface with planar curvature lines.

3.2.2 Circular quad mesh with planar lines

Meshes for which each face is inscribed in a circle are called *circular meshes*, as introduced in chapter 2. Quad circular meshes are interesting for architectural gridshell design, as they have planar faces, torsion-free nodes and vertex offset. The offset allows to easily give a depth to the mesh for materialization and structural purposes. Circular meshes can be seen as a discretization of surfaces parametrized by curvature lines (Pottmann and Wallner 2006). In this section, we will introduce a discretization of surfaces with planar curvature lines by circular meshes with planar lines.

3.2.2.1 Gauss map discretization

Our discretization is based on a discretization of the Gauss map. It turns out that the orthogonal circles discussed in section 3.2.1.2 and shown in Figure 3.6 naturally yield a circular mesh with vertices on the unit sphere. We can summarize this result as follows:

Proposition 3.1
The intersection points of two orthogonal families of circles on a sphere define the vertices of a circular mesh with planar lines.

Proof:
We start by the case where the two reciprocal axes are tangent to the sphere (the case $\theta = \pm 90$). We use the stereographic projection of the sphere centered at the point of tangency with the two axes. This transformation projects the sphere on a plane, as shown on Figure 3.9 (left). The circles all pass through the center of the projection, and are therefore mapped to straight lines on the plane. The stereographic projection conserves intersection angles: Since the circles intersect at 90°, their projections also intersect at a right angle. As a result, the projection of two pairs of circles are straight lines that intersect at 90°, thus forming a rectangle, which is a circular quad. Since the projection and its inverse map circles to circles, we conclude that the four intersection points on the sphere are cocyclic.

In the case where the axes are not tangent to the sphere (Figure 3.9, right), we consider the stereographic projection from an intersection point of a reciprocal axis with the sphere. This projection transforms the circles passing through the pole into straight lines (which are concurrent with the reciprocal axis). The circles from the other family are mapped to circles, which are orthogonal to the straight lines since the projection is conformal. As a result, the projection of four intersection points are the intersection of two concentric circles and two of their rays, and are therefore cocyclic.

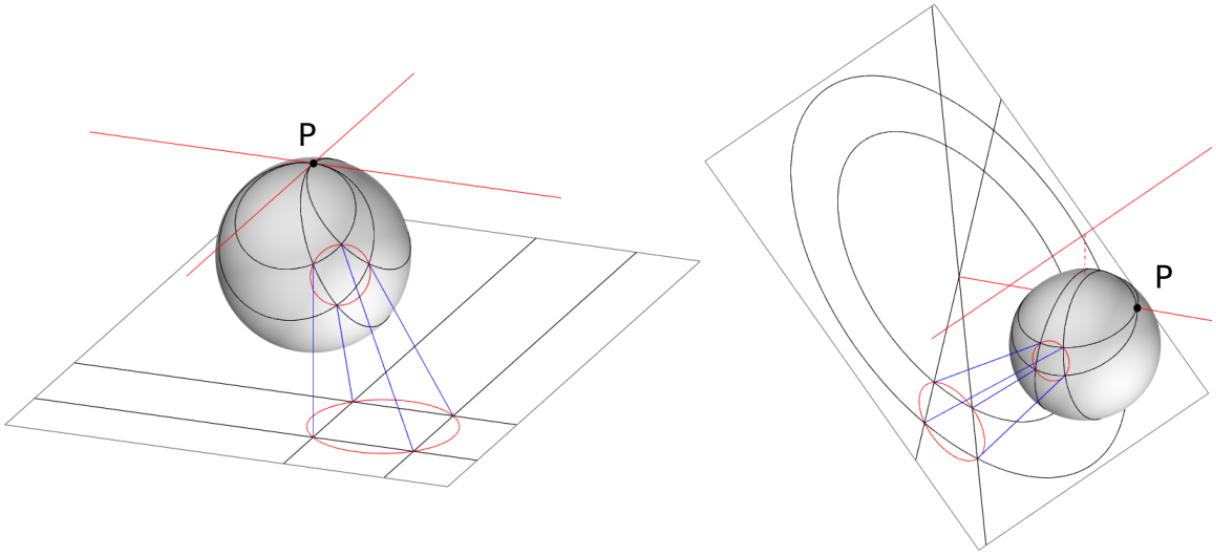

Figure 3.9 - Stereographic projection of orthogonal circles from a pole P. Left: case where Θ = ±90°. Right: general case

3.2.2.2 Property of the discrete Gauss map

Two orthogonal families of circles on the sphere have the following property (Eisenhart 1909): a cone tangent to the sphere along a circle of one family has its apex on the reciprocal axis of that family. An example is visible in Figure 3.10 (cone shown in orange). This property can be interpreted as a property of the Gauss map of a smooth surface with planar curvature lines: along the Gauss map of the maximum (resp. minimum) curvature line, the tangent vectors in the minimum (resp. maximum) curvature direction belong to a cone. Our discrete Gauss map model happens to have a discrete equivalent of this property:

Proposition 3.2
If a strip of quads is inscribed in a sphere and if its longitudinal edges are coplanar, then its transversal edges belong to an oblique circular cone with apex on the reciprocal axis.

Such a cone is visible in blue in Figure 3.10 (in blue). This rather abstract property will be used in section 3.4.6 to prove an important property of the proposed discrete model.

***Proof*:**
Let us consider a strip of quads with vertices on orthogonal circles on the sphere, as shown in Figure 3.10. Vertices of the strip belong to two circles C_1 and C_2. We pick two vertices Q_1 and Q_2 of the mesh. The tangents to circles C_1 and C_2 at Q_1 and Q_2 belong to a same cone (in orange) with apex on the reciprocal axis L_2. They are therefore coplanar. As a result, Q_1Q_2 is a ruling of the developable surface connecting C_1 and C_2. The developable surfaces connecting two cospherical circles are quadratic cones (Glaeser *et al.* 2016). Consequently, the transversal edge Q_1Q_2 is a ruling of one of these quadratic cones (in blue). Since all the rulings passing through vertices of the strip also intersect the reciprocal axis L_1, the apex of this cone is necessarily on L_1.

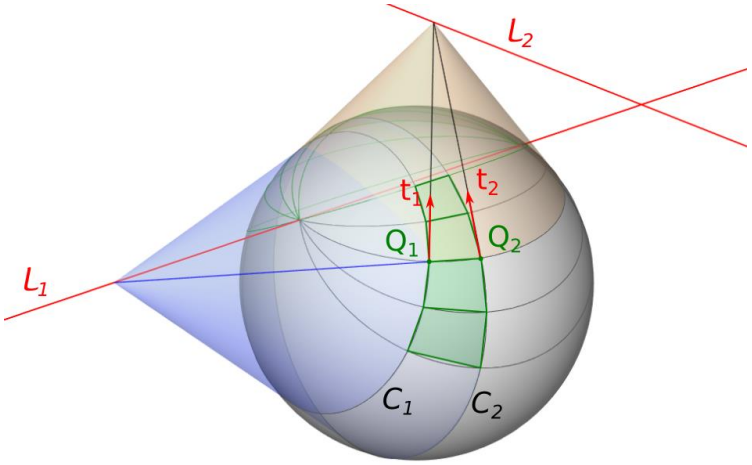

Figure 3.10: Edges of a strip of quad on the discrete Gauss map belong to a cone with apex on a reciprocal axis.

3.2.2.3 Surface discretization

The previous sections shows a natural discretization of the Gauss map of any surface with planar curvature lines. Smooth surfaces are related to their Gauss map by a Combescure transform: at any given point of the surface, the tangent vectors in principal curvature directions are parallel to the corresponding tangent vectors on the Gauss map. Combescure transforms can be discretized using the notion of mesh parallelism. Two meshes are said to be parallel if their corresponding edges are parallel. They are then said to be related by a discrete Combescure transform (Pottmann *et al.* 2007). A discrete Combescure transform conserves the planarity of a face and the vertex angles, it therefore conserves the circularity of meshes.

Using these notions, a surface with planar curvature lines can be discretized as follows:

- Compute its Gauss map parametrized according to principal curvature directions, and discretize it into a circular mesh;
- Discretize the Combescure transform that maps the smooth Gauss map to the surface, and apply it to the discrete Gauss mesh.

In Section 3.3, we will address how this fact can be used for generation purposes.

3.2.3 Conical quad mesh

Conical meshes is a family of quad meshes introduced in (Liu *et al.* 2006) with planar faces and torsion-free nodes. Whereas circular meshes have node-offsets, conical meshes have face-offsets: we can build a parallel mesh such that corresponding faces are at a constant distance. (Pottmann and Wallner 2006) showed the existence a duality between circular and conical meshes: from any circular mesh with rectangular combinatorics, one can construct a two-parameter family of conical meshes. The method consists in building at each node a plane normal to the node axis. These planes form the faces of the dual conical mesh, and the intersection lines of these planes form its edges. It turns that this construction conserves the planarity of lines, thus allowing to generate conical meshes with planar lines:

Proposition 3.3
The conical dual of a circular mesh with planar curvature lines also has planar lines.

Proof:
We will show this property by building the conical dual of a circular Gauss mesh with planar lines (following the construction of (Pottmann and Wallner 2006)), and by showing that it also has planar lines.

General conical meshes with planar lines can then be obtained by applying Combescure transforms to this conical Gauss image.

Let us consider two families of orthogonal circles on the sphere. The cones that are tangent to the unit sphere along the circles of one family have their apex on the axis of the other family. On Figure 3.11, we show the apexes B_1 and B_2 of the cones tangent to the circles C_1 and C_2 (the cone tangent to C_2 is shown in blue). The blue lines are the tangents to the unit sphere along C_3 and C_4 at the intersection points of the circles. We then build the conical dual (shown in green) to the circular quad formed by the four circles. The faces of this dual mesh are the tangent planes to the sphere at the circle intersection points. These planes also correspond to tangent planes to the cones (tangency occurs along the blue lines). As such, their intersection line passes through the cones apex. Therefore, the edges e_1 and e_2 of the conical dual are aligned with the points B_1 and B_2. e_1 and e_2 are each in a plane that contains axis (B_1B_2). Since these two edges have a point in common, these two planes are identical. If we were to build the next edge e_3, it would also belong to that same plane. We conclude that the conical dual has planar lines. We finally note that each quad of this conical dual is tangent to the unit sphere, and can therefore be interpreted as a conical Gauss image in the sense of (Pottmann and Wallner 2006).

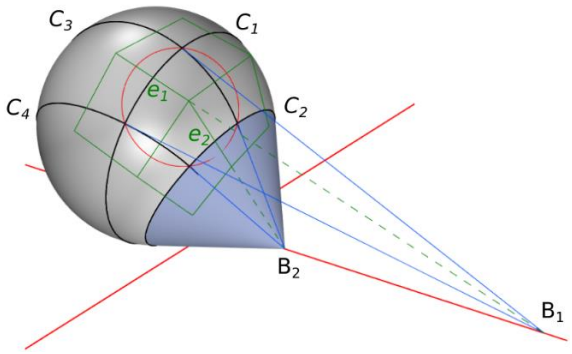

Figure 3.11: The conical dual mesh of a circular mesh on the sphere with planar curvature lines also has planar curvature lines

3.3 Generation method

We propose here a method to construct a circular mesh with planar curvature lines from two input guide curves. Generating a surface from two curves is a method appreciated by designers, as discussed in chapter 2. It provides an intuitive control on the shape. Sweep surfaces and translation surfaces are for example two widely used methods to generate surfaces or meshes on CAD programs. In our method, the guide curves will correspond to curvature lines of the surface. As such, they need to be planar and to intersect at 90°.

3.3.1 Control with characteristic guide curves

In this section, we will explain the generation method in the special case where:

- The planes of the two guide curves are orthogonal, and
- The initial tangent vector of one curve is orthogonal to the plane containing the other curve.

These properties can be easily achieved as follows: Draw one curve in the plane Oxz with initial tangent (O, e_x), and a second curve in plane Oyz with initial tangent (O,e_y). With these properties, the guide curves will correspond to curvature lines of the surface for which the normal vector is coplanar with the curvature line. Such lines are said to be characteristic of the surface, as they stand out visually (see for example

Figure 3.4 and Figure 3.27), and are the most intuitive to control. We note that the orthogonality conditions on the initial tangent vectors can be easily achieved working with B-spline guide curves, for which the initial tangent is aligned with the first two control points.

Our method can be decomposed into the following steps (see Figure 3.12):

1. The guide curves are sampled in points. At each point, the Frenet normal vector is calculated.
2. These normal vectors correspond to points of the Gauss map on S^2, they lie in two orthogonal great circles.
3. The user chooses a parameter θ, that structures the Gauss map as shown on Figure 3.6. This parameter is used to construct the axes of the pencils of planes, as explained in section 3.2.1.2. The direction of the axes is given by the initial tangent vectors of the curves.
   For each point of the Gauss map, a plane passing through this point and containing one axis is constructed. The intersections of these planes with the sphere give two families of orthogonal circles.
4. The intersection points of the circles form a circular mesh, as proven in section 3.2.2.
5. A Combescure transform (as defined in section 3.2.2.3) is applied to this circular mesh to generate a mesh that fits the generatrices. Such a transformation conserves the planarity and circularity of the faces, and the planarity of the lines.

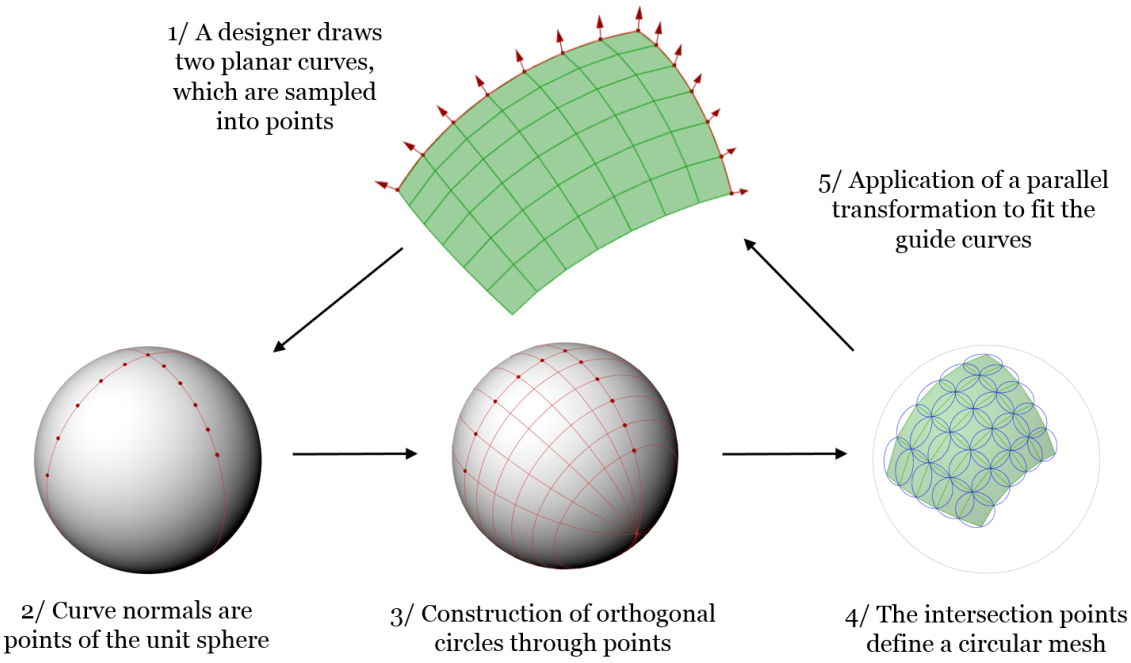

Figure 3.12: Overview of the proposed method. Gauss map shown on the bottom row.

Node axes

The calculation of node axes from an arbitrary circular mesh can be a tedious step. (Liu and Wang 2008) suggest for example to use SVD, and show the non-existence of the node axes for some types of circular meshes. In our method, the Gauss map is calculated, so the node axes are already determined.

3.3.2 Control with arbitrary guide curves

We will now show how the method can be adapted to the general case where the planes of the guide curves are not necessarily orthogonal.

Let us consider Figure 3.13 where two planar guide curves G_1 and G_2 intersect at 90°. The initial tangents of G_1 and G_2 at the intersection point P determines the tangent plane of the surface we are going to build.

We name N_P the normal vector to this plane. Since the guide curves will be curvature lines, the normals to the surface must rotate along the curve like a Darboux frame, also referred to as rotation-minimizing frames in CAD environments. We generate these normals at each point of the guide curves by propagating N_P without torsion along the guide curves. These normals describe two arcs of circles C_1 and C_2 on the unit sphere, as shown on the right of Figure 3.13.

The next step is to build the axis L_1, the first of the two polar reciprocal axes of the Gauss map (as explained in section 3.2.1.2). This axis passes through the apex A_1 of the cone tangent to S^2 along C_1. It also belongs to the plane of C_2. There is one degree of freedom left to choose the orientation of this axis. We parametrize this degree of freedom by constructing its orientation vector e_1 as follows:

$$e_1 = u + \lambda v$$

Where:

- λ is a real variable, the degree of freedom;
- u is the unit vector of the line (A_1Q_2), Q_2 being the center of circle C_2;
- v is a vector normal to u in the plane of circle C2.

For a choice of λ, the value of parameter a of section 3.2.1.2 is given by:

$$a^2 = OK_1^2 = OA_1^2 - A_1K_1^2 = OA_1^2 - \left(\frac{e_1 . \overrightarrow{A_1O}}{\|e_1\|}\right)^2$$

Where K_1 is the orthogonal projection of the center O of the sphere on axis L_1.

This equation can be expressed as a polynomial of degree two in λ. So, one can choose a parameter θ (we recall that $a=tan(\theta/2)$) and find the corresponding value of λ by solving this equation. A sign convention was developed to choose the root amongst the two depending on the sign of θ; this aspect is secondary and will not be detailed here for sake of conciseness. Note that some values of θ are impossible to reach for any choice of λ: since the axis L_1 passes through A_1 and belongs to the plane of C_2, the distance between the sphere center to axis L_1 (that is, the parameter a) is bounded by an upper and lower value.

Once axis L_1 is determined, its polar reciprocal axis L_2 can be constructed as explained in section 2.1.2. We can then proceed in the same way as in section 3.1 to build the Gauss map and the mesh.

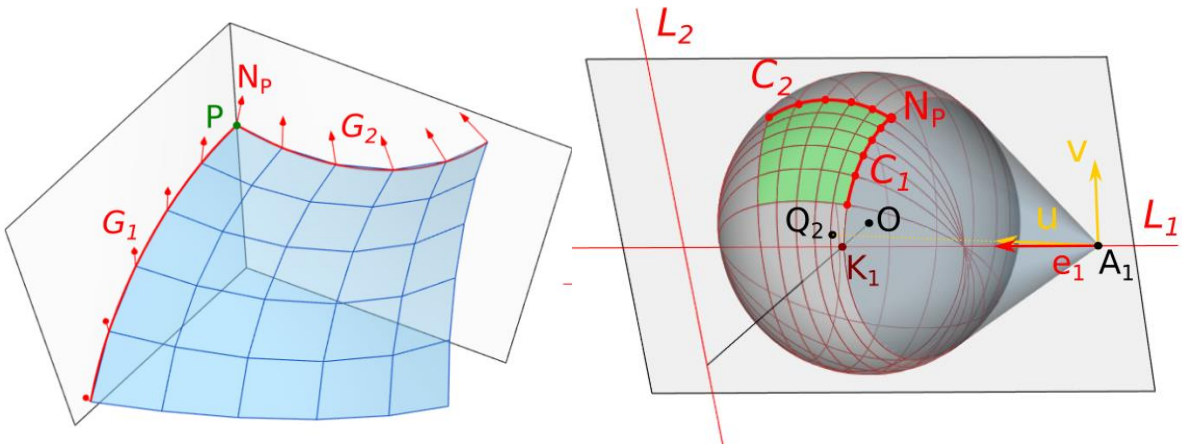

Figure 3.13: Generation method with two arbitrary orthogonal planar curves

3.3.3 Developable surfaces

As discussed in section 3.2.1.3, developable surfaces may also have planar curvature lines. Since they correspond to a case where the Gauss map degenerates to a curve, the method we just presented cannot be used. However, we are going to show in this section that it is actually quite straight forward to generate a discrete circular equivalent of these surfaces for the non-trivial 3rd type of developable surfaces.

As shown in Figure 3.14, a discrete general helix can be defined as a polyline for which each segment has a constant angle α with a reference plane. By extending these segments, we obtain the rulings of a discrete developable surface (two adjacent rulings are coplanar since they intersect), which constitute the first family of curvature lines. The second family is obtained by intersecting these rulings with planes parallel to the reference plane. The mesh built by these curvature lines is circular. Indeed, let us consider a quad ABCD, where (AB) and (CD) intersect at a point O on the generatrix. Since (AB) and (CD) have the same slope, OA = OD and OB = OC. Therefore ABCD is an isoscele trapezoid and is inscribed in a circle.

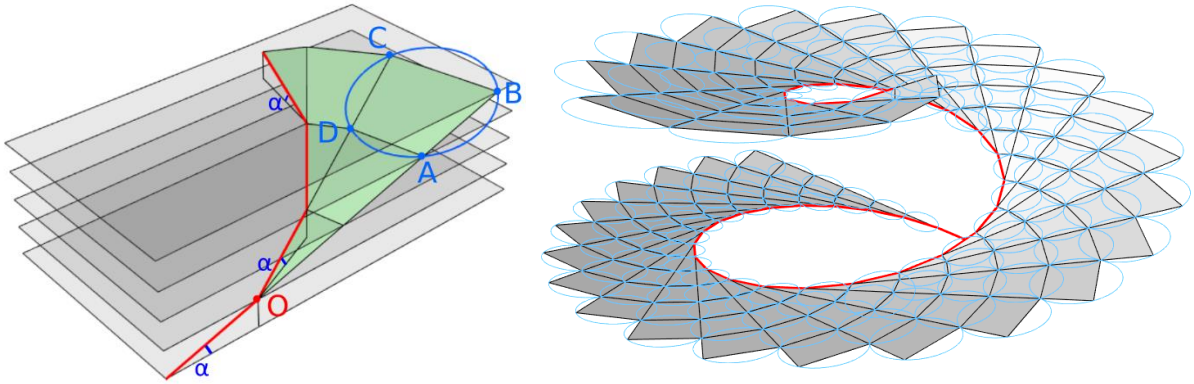

Figure 3.14: Developable circular meshes with planar curvature lines.

3.4 Application to morphogenesis of double-curvature facades

3.4.1 Classic analytical surfaces

Our method can be used to generate some classical surfaces of differential geometry.

Surfaces of revolution
Meshes of revolution correspond to the particular case where $\theta = 0°$ or $\pm 180°$ and one generatrix is a circle. The Gauss map is then a network of parallels and meridians on the sphere. An example is the torus shown on Figure 3.16.

Moulding surfaces
Moulding surfaces are surfaces that can be generated by sliding a planar generatrix along a planar rail curve, such that the plane of the generatrix is always perpendicular to the rail. An example is the surface of the SAGE music center, designed by Foster+Partners, shown in Figure 3.15 (Cook *et al.* 2006). Their potential for fabrication-aware design was investigated in (Mesnil *et al.* 2015). They can be obtained from our method by setting the parameter θ to $0°$ or $\pm 180°$, with any type of guide curves. If $\theta = 0°$, one curve is the generatrix, the other is the rail. If $\theta = 180°$, the roles of the two curves are exchanged. For both

cases, the Gauss map has the same structure as for a surface or revolution. Two moulding surfaces are shown on Figure 3.20.

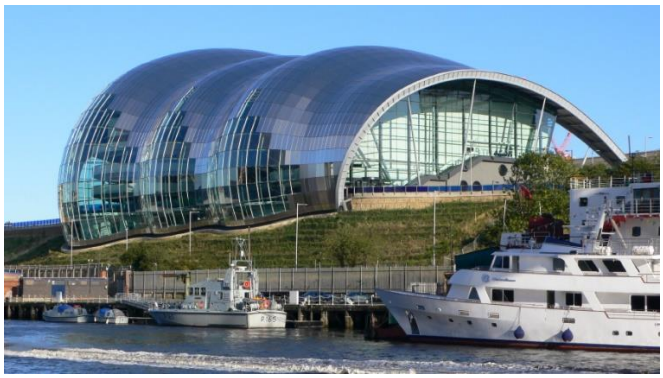

Figure 3.15: The SAGE Music Centre in Gateshade is a moulding surface, a particular class of surfaces with planar curvature lines (© Jim F. Bleak)

Dupin cyclides

Dupin cyclides is a family of surfaces that can be obtained by applying an inversion to a torus. A key property of these surfaces is that their curvature lines are circles, and are therefore planar. They are often used in CAD design, as they can be parametrized by NURBS and they allow a C^1-continuous (i.e. without crease) transition between cylinders, cones, tori, spheres and planes (Pratt 1990; Zube and Krasauskas 2015).

Dupin cyclides can be generated with our method using two orthogonal circles as guide curves. Figure 3.16 shows three different cyclides generated from the two same circles but with different values of the parameter θ. The curvature lines are all inscribed in circles, similarly to the smooth Dupin cyclides. This fact is a consequence of a more general property of our meshes which will be more detailed in section 3.4.6.

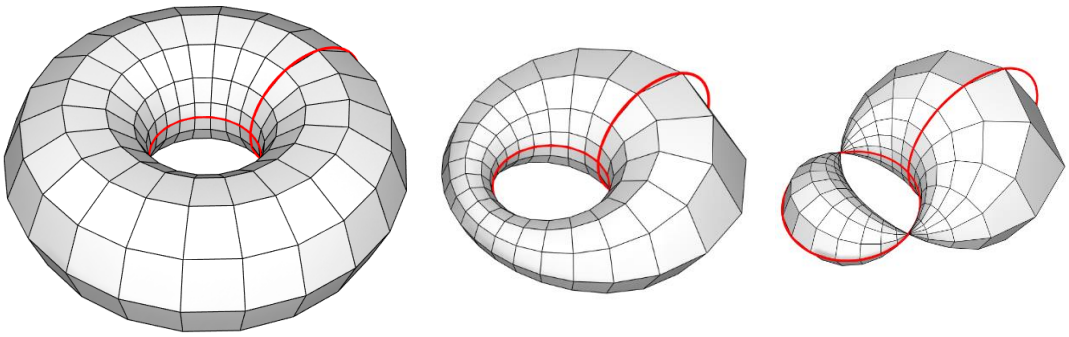

Figure 3.16 - Generation of discrete Dupin cyclides from two circles. Left: Θ=0° (torus). Middle: Θ=30°. Right: Θ=65°.

3.4.2 Free-form surfaces

A large variety of surfaces can be generated by playing with the geometry of the guide curves and the parameter Θ. Two examples are shown in Figure 3.17. In the left image, the guide curves are highlighted in red, and the circles circumscribed to the faces in blue. Some more abstract surfaces are shown in Figure 3.18. Figure 3.4 shows how the proposed method can be used to construct the same surface as one built as an envelope of radical planes of spheres with centers on conics, as explained in section 3.2.1.1. Figure 3.19 shows one surface with self-intersection, generated from a logarithmic spiral and an arc of circle. Its smooth appearance is due to the fineness of the mesh (200 x 70 faces).

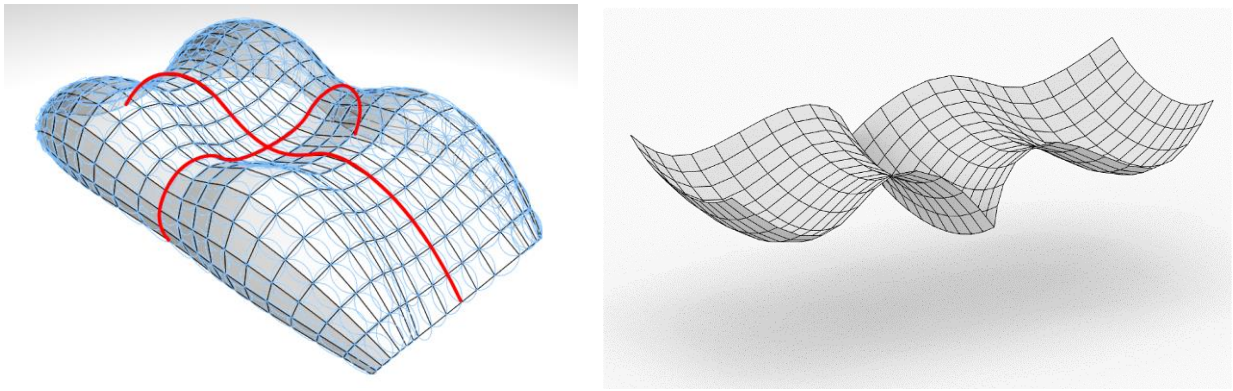

Figure 3.17: Double curvature circular meshes with planar curvature lines

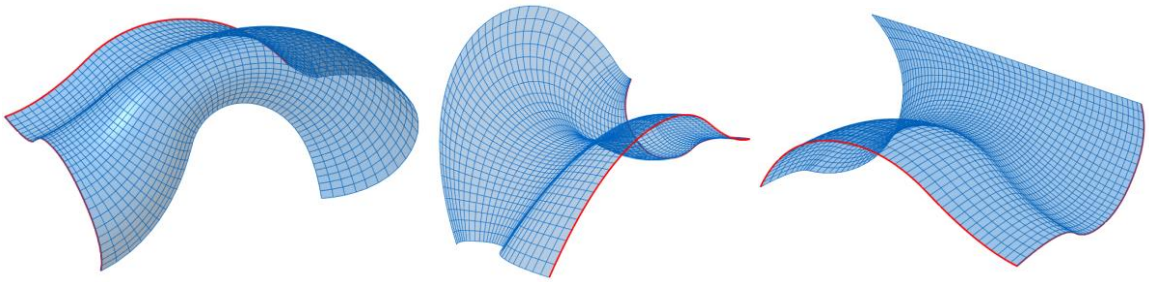

Figure 3.18: Some more circular meshes with planar curvature lines

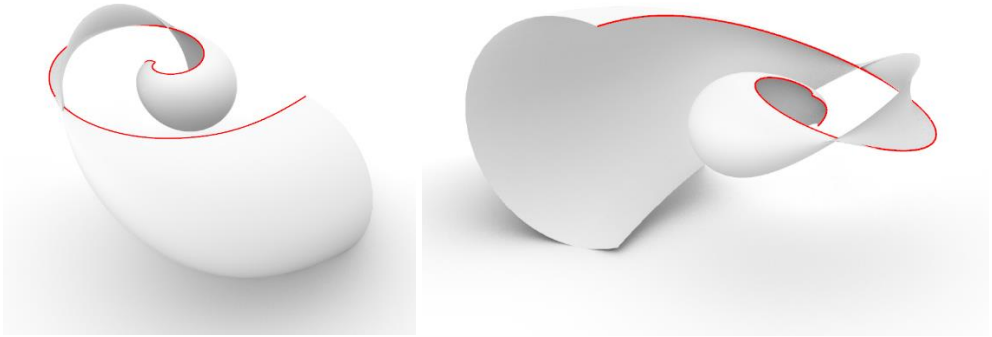

Figure 3.19: A surface with self-intersection

3.4.3 Effect of parameter θ

Figure 3.20 illustrates the family of shapes that can be obtained by the two same curves by varying the parameter θ from -180 to 180°. As discussed in section 3.4.1, the cases θ=-180° and 0° correspond to moulding surfaces. Our method gives access to a full range of surfaces that can be interpreted as the result of a morphing between these two moulding surfaces. There is a discontinuity in the aspect of the surface between θ=45° and 150°. When increasing θ beyond 45°, a portion of the mesh bulges out, the mesh self-intersects, so the mesh is less interesting for architectural purposes. However, when θ is further increased, fair meshes are obtained again, with a very different geometry. At θ=180° the exact same mesh as with θ=-180° is obtained. The range of angles for which the mesh is fair and does not auto-intersect is specific to the chosen guide curves. Figure 3.20 also shows the effect of varying parameter θ with fixed guide curves, but from side views. The rotation of the planes can be clearly observed.

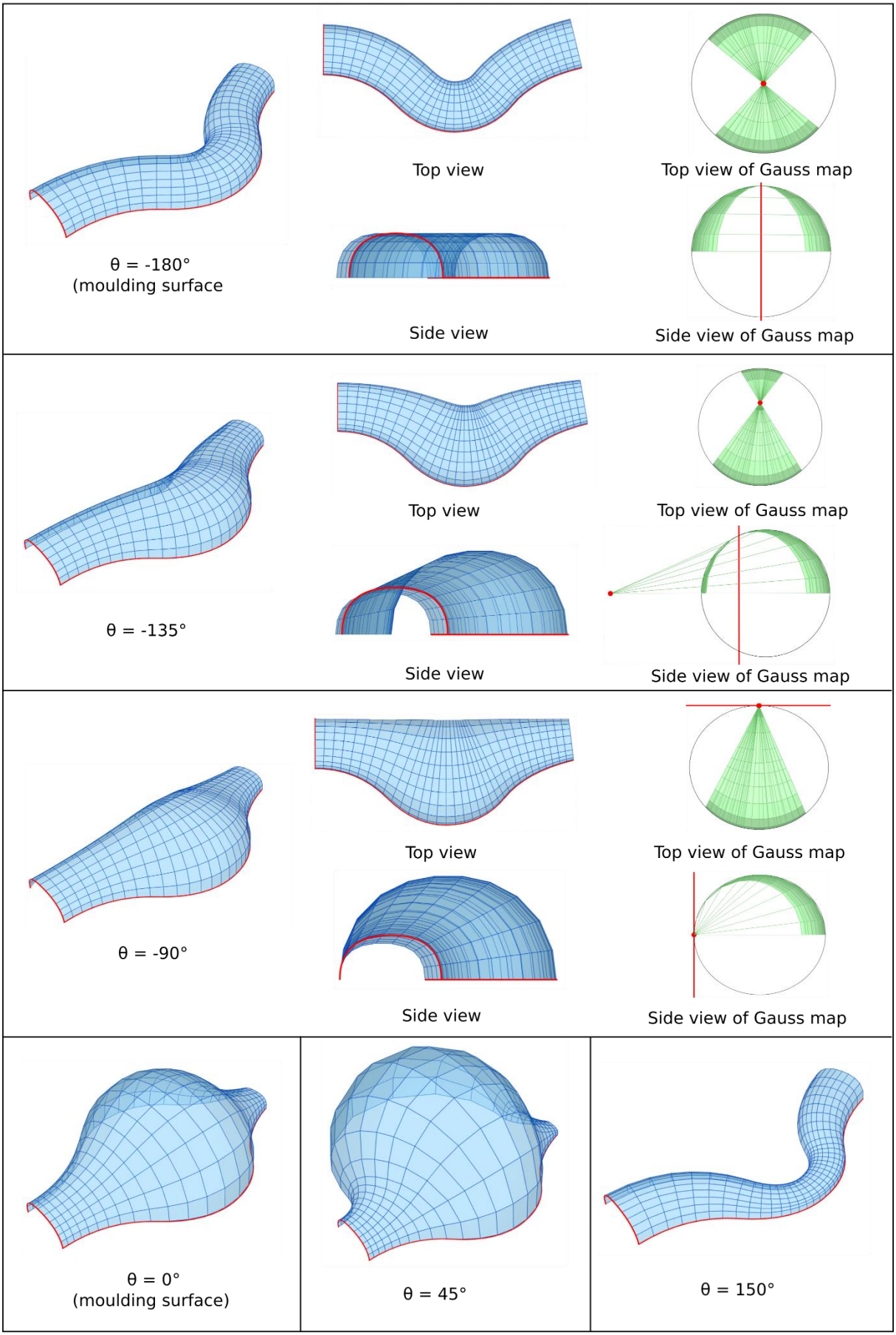

Figure 3.20: Family of meshes that can be generated from two curves with different values of Θ

3.4.4 Smooth surfaces with planar curvature lines

Our method can be used to generate a mesh as fine as needed: the discretization steps of the generatrices can be arbitrarily small. However, in some applications, it is desirable to work with a smooth surface or smooth edges. Smooth surfaces can be obtained from our circular meshes by generating a patch of Dupin cyclide on each quad, thus forming a so-called cyclidic net (McLean 1985). Cyclidic nets are C^1-continuous surfaces (the surface and its tangent planes are continuous), and their curvature lines are composed of circular arcs. (Bobenko and Huhnen-Venedey 2012) showed that these nets can be generated on any circular mesh with the topology of a disk. These nets are used in (Bo *et al.* 2011) to generate the geometry of gridshells where beams are arcs of circles and nodes are identical. There are three degrees of freedom to generate such a net. They correspond to the orientation of one reference frame that defines the orientation of the curvature line tangents at one vertex.

The successive arcs of circle that compose a curvature line of a cyclidic net usually lie in different planes – the curvature lines are therefore not planar across the net. However, when the underlying circular mesh has planar lines, it is possible to construct a cyclidic net with planar curvature lines.

Let us first see how such a net can be constructed. A circular mesh with planar lines is showed on Figure 3.21 (only the resulting cyclidic net is shown for clarity, the vertices of this mesh are the vertices of the net). At a vertex A, we compute the normal N_A and the corresponding orthogonal circles C_{AB} and C_{AD} on the Gauss map. We then take the tangent vectors to these circles, t_1 and t_2. These two vectors define the reference frame that generates a cyclidic net with planar curvature lines.

We shall now prove that this resulting cyclidic net actually has planar curvature lines. Since t_1 is coplanar with C_{AB}, the arc AB of the net is coplanar with the plane of A, B and C. Therefore, the bi-arcs[7] ABC and DEF of the net are planar. Their Gauss maps are contained in circles C_{AB} and C_{DE}, we name L_1 the intersection line of the planes of these two circles (this is one of the two polar reciprocal axes). We then pick a point P on arc AD, and build the arcs PQ and QR. Since the patch ABED has planar curvature lines, the plane of the Gauss map of arc PQ contains L_1. The same result holds for the Gauss map of arc QR, so the planes of these two Gauss maps are identical: the Gauss map of bi-arc PQR is planar. At any point of the bi-arc PQR, the tangent vector is tangent to the one of the Gauss map. Therefore, the bi-arc PQR is also planar. We conclude that the whole cyclidic net has planar curvature lines.

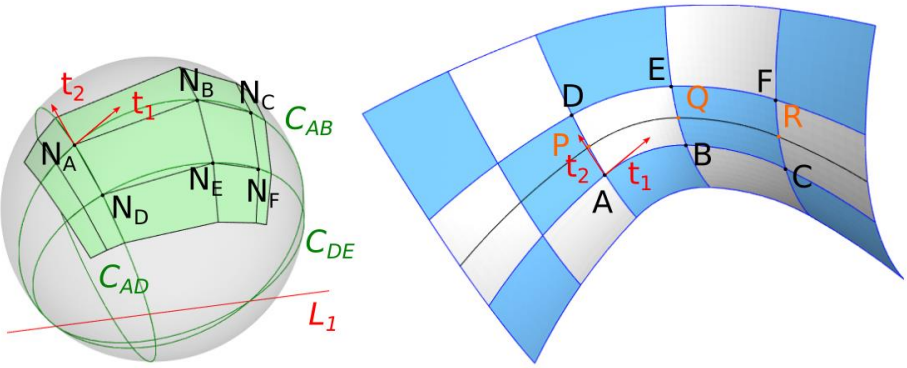

Figure 3.21 - Smooth surface with planar curvature lines and its Gauss map.

[7] A bi-arc is a curve composed of two arcs of circle, with continuity of the orientation of the tangent vector.

3.4.5 Aligning a mesh with boundary planes

Our method can be used to generate meshes where the edge lines are contained in a target plane. One typical application is to align a mesh with a vertical planar facade. For example, Figure 3.22 shows a mesh whose boundaries are contained in four vertical planes. The only requirement to obtain this alignment is that the tangent vectors at the ends of the guiding curves are horizontal.

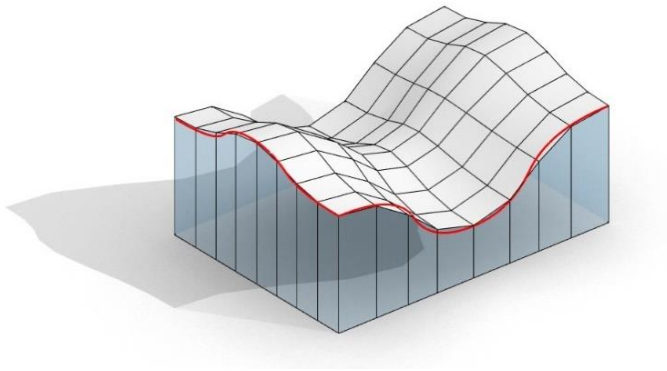

Figure 3.22 - Mesh aligned with four vertical planes

In a more general way, a mesh can be aligned with four planes if two intersection lines have orthogonal directions. This property is shown on Figure 3.23, where the two orthogonal intersection lines are shown in yellow. The following method can then be used to align the mesh with four boundary planes:

i) Pick a value for parameter θ such that the planes P'_i intersect S^2 in a pleasing way (reminder: axis 1 is the axis of the pencil of planes P_1 and P_2, same thing for axis 2 with P_3 and P_4) ;
ii) The green arc on the Gauss map gives the normals of the generatrices ;
iii) To construct the generatrix, we can apply a parallel transformation to the green arc. We can also just draw any curve such that the normals at the tips correspond to the tips of the green arc.

The mesh shown on Figure 3.24 is based on a patch that is fitted on two planes that intersect at 36°. This allows successive reflections to generate a final mesh with a symmetry of order five. The mesh is aligned with the floor and the pentagonal building inside.

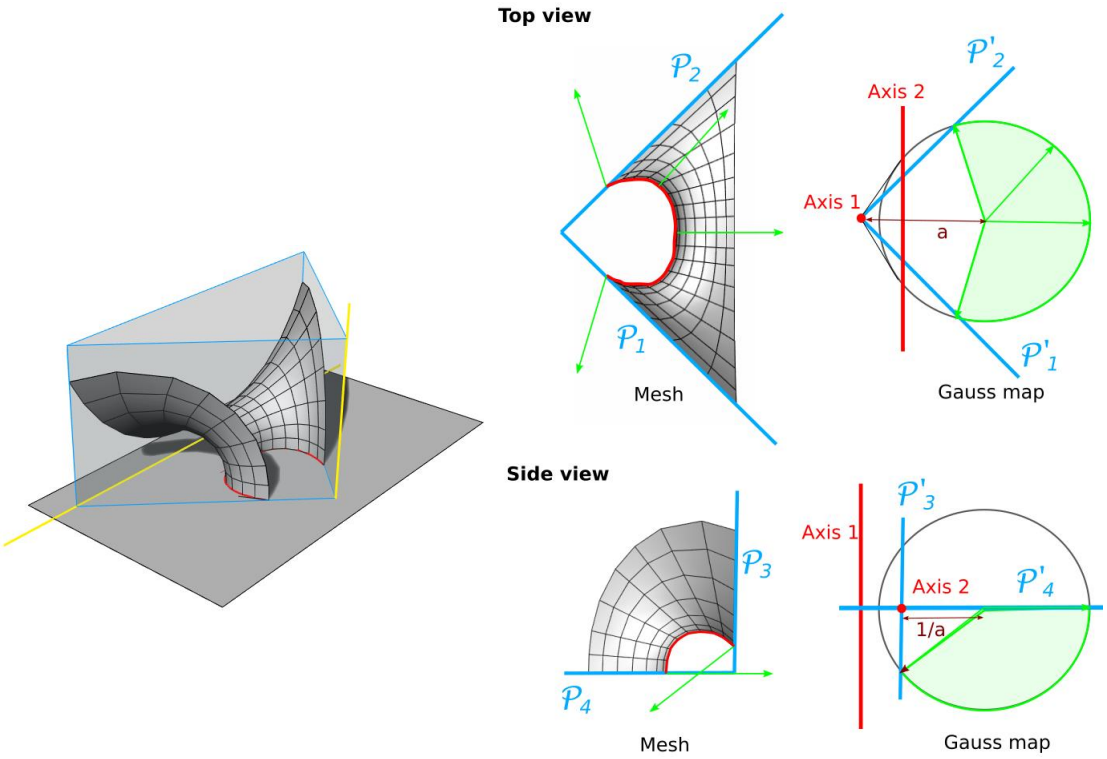

Figure 3.23 - Fitting four boundary planes

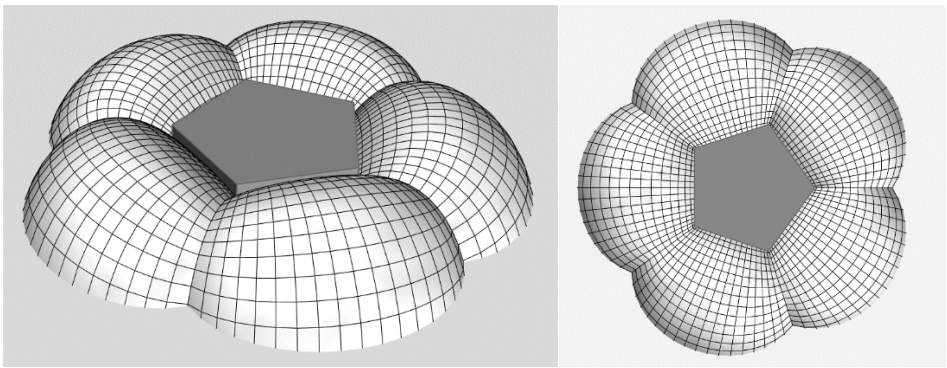

Figure 3.24: Symmetric mesh built from a patch generated by fitting four boundary planes

3.4.6 Piecewise circular curvature lines

(Darboux 1896) showed that if a curvature line of a surface with planar curvature lines is an arc of circle, then all the curvature lines of the same family are also circular. It turns out that our model enjoys a discrete version of this property. There are many interesting applications for fabrication purposes, as it is much simpler technologically to bend a beam if the radius of curvature is constant. This property is used for the shading structure shown in Figure 3.31, which is built entirely from planar bi-arcs. This property can be formalized as follows:

Proposition 3.4
If a polyline of a circular mesh with planar curvature lines is inscribed in an arc of circle (or an n-arc), then all the subsequent curvature lines are also inscribed in arcs of circle (or in n-arcs).

Note: In that proposition, we assume that the change of curvature radius of the n-arcs occurs at nodes, and not in an edge.

Proof:

Referring to Figure 3.25, let us consider two adjacent polylines H_1 and H_2 of a circular mesh with planar lines. Let us assume that the vertices of H_1 are inscribed in a circle. The Gauss map H_1' of H_1 is then homothetic to H_1. We call H_2' the Gauss map of H_2. As proven in section 2.2, the vertices of H_1' and H_2' lie on a common cone.

Since H_1 is homothetic to H_1', and since all the edges between H_1 and H_2 are parallel to the ones between H_1' and H_2', the edges between H_1 and H_2 are also located on a cone. This cone is homothetic to the one of the Gauss map. Since the plane of H_1 (resp. H_2) is parallel to the plane of H_1' (resp H_2'), and since the vertices of H_1 are inscribed in a circle, the vertices of H_2 are also included in a circle.

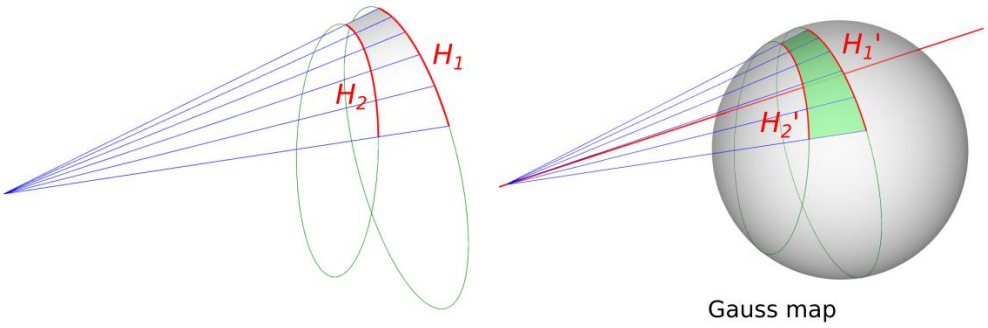

Figure 3.25: If a guide curve H_1 is an arc of circle, the subsequent curvature lines (e.g. H_2) will also be inscribed in an arc of circle

3.4.7 Piecewise planar curvature lines

One important application of the proposed meshes is for the fabrication of gridshells. For such structures, beams never span the whole length of the building: several beam segments are spliced together. If we allow a change of the orientation of the plane of a beam at each splice, the variety of possible surfaces becomes significantly richer. One way to generate surfaces with piecewise planar curvature lines is to use cyclidic nets. As discussed in section 3.4.4, these nets can be built on any circular mesh with topology of a disk, and their curvature lines are piecewise circular. However, the resulting surfaces are often highly wavy. (Mesnil, Douthe, Baverel and Léger 2017) suggest to minimize the Willmore energy of the surface by optimizing the orientation of the reference frame. However, convergence towards a desired surface aspect is not guaranteed when the net is built on an arbitrary circular mesh.

Our method can be used to design meshes in which curvature lines are piecewise planar. One way to obtain this is to generate a first patch with a given value of θ, and to use one of its boundary as a guide curve to generate a second patch with a different value of θ. This method is applied in the mesh shown in Figure 3.26. A first patch is generated from the two blue guide curves. The second patch it then generated using the two red guide curves, where one is the boundary of the previous patch. The C^1 continuity of the beams is guaranteed by the C^1 continuity of the bottom guide curves. The rest of the mesh is obtained by symmetry. Note that, in order to apply the symmetry, the second patch must end in the plane of symmetry. This fact constrains the value of θ for the second patch. In the resulting surface, the radial curvature lines are planar, while each longitudinal curvature line lies in four different planes.

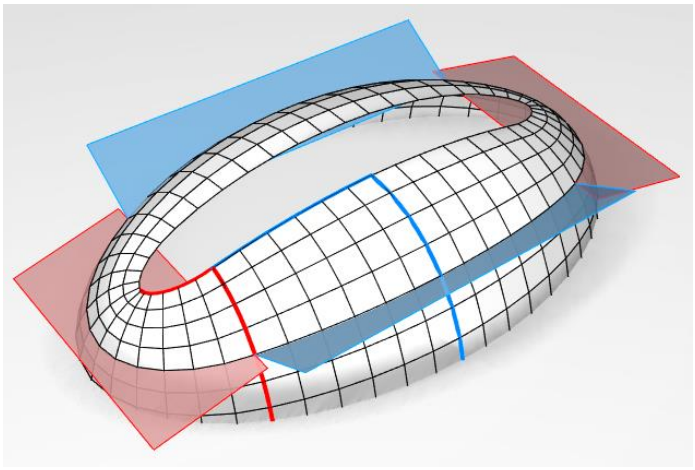

Figure 3.26: Mesh with piecewise planar curvature lines: Each longitudinal line lies in four different planes

Figure 3.27 shows a case study in which we approximated the geometry of the Hippo Haus of the zoo of Berlin, designed by the firm Schlaich Bergermann und Partners, by a circular mesh with piecewise planar lines. The original geometry was derived from two translation surfaces, joined by a transition area. We reconstructed the actual guide curves (G_1, G_2, G_3) used on the project, their geometry being given in (Schlaich and Schober 1998). We then used our method to generate a circular mesh. Similarly to the actual design, we implemented a transition area between the two domes. As a result, there is a twist in the plane of the beams happening at the junctions between the domes and this transition area. The surface has three degrees of freedom, one parameter θ for each patch: θ_1, θ_2 and θ_3. We generated the mesh using G_1 and G_2 as guide curves. For arbitrary values of the parameters θ, the end boundary does not match G_3. In order to match, we choose a value for parameter θ_1, and then optimize the parameters θ_2 and θ_3 in order to minimize the distance between G_3 and the end boundary. G_2 and G_3 are similar to each other, as they are both parabolas, so a nearly perfect fit can be obtained. The optimization is performed with the BOBYQA algorithm (Powell 2007). In order to improve the aesthetic of the mesh, different values of θ are also used for the portions of domes outside guide curves G_2 and G_3 (θ_0 and θ_4).

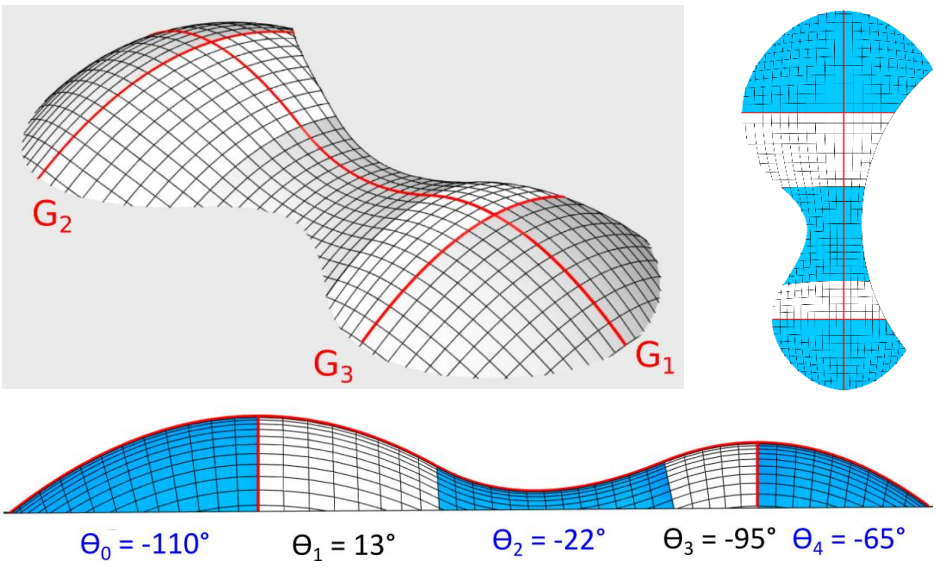

Figure 3.27: A circular mesh with piecewise planar lines with a geometry close to the one of the HippoHaus in Berlin

3.4.8 Minimizing variation of panel size

The discretization of the guide curves allows to control the size of the mesh faces. Although this discretization can be easily controlled manually, it can also be obtained by an optimization process aiming at minimizing the variations of the size of panels. The low computation time (later discussed in section 3.5.1) of our method allows to perform this post-processing quickly. Figure 3.28 compares two meshes obtained from the same two B-spline guide curves, but discretized differently. In the first one, the guide curves are discretized with constant curve parameter increment. Because of the high variation of curvature, some faces are very elongated. In the second one, the discretization is chosen such that variance of the panel areas is minimized, using the BOBYQA algorithm. We observe that the face sizes are much more uniform.

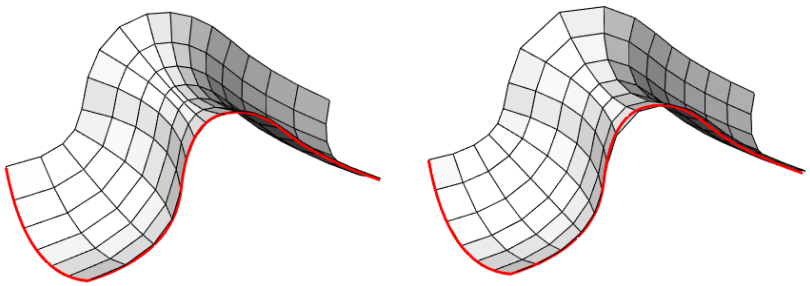

Figure 3.28: Effect of guide curve discretization. Left: Constant increment of B-Spine parameter. Right: Minimizing variation of panel area

3.5 Discussion

3.5.1 Algorithmic performance

The method was implemented in the CAD software Rhinoceros™ via the plugin Grasshopper™, which offers a programming interface. In this section, we shall discuss the performance of the algorithm.

The first main step of the algorithm is to compute the Gauss map. The planes passing through the points of the Gauss map are first computed. Then, the intersection lines of these planes are constructed. Finally, the intersection of the sphere with these lines is calculated. The second main step is the computation of the Combescure transform. This is done by propagation starting from the two guide curves. Each vertex is built by calculating the intersection points between two lines. All these steps can be analytically computed and are thus highly efficient. The computing time increases linearly with the number of faces.

The performance was evaluated on a case study with 100 x 100 faces: computing time is below 75ms on a desktop with 3.5GHz processor and 16GB RAM. This low computation time allows for a real-time design exploration.

3.5.2 Alternative generation method

Another method to obtain circular meshes with planar lines would be to optimize vertex positions to fulfill these geometrical properties. This approach would have two major drawbacks compared to the proposed methods:

- The initial mesh is most likely far from a surface with planar curvature lines. The process would therefore result in high deformations. This would make the process not intuitive as a design tool, and ineffective as a post-rationalization tool.
- The method would require numerous iterations. Hence, calculation would be much slower and yield a mesh where properties are not fulfilled exactly.

3.5.3 Limitations

The following limitations apply to the shapes that can be obtained with our method. First of all, surfaces with planar curvature lines cannot have umbilics, so there cannot be singularities in the mesh. Secondly, self-intersection of the mesh can occur for some combinations of guiding curves. As shown on Figure 3.29, once a guiding curve (e.g. the red one) and the parameter θ are defined, the planes in one direction are entirely defined (as shown on the right-hand figure). These planes, when not parallel, necessarily intersect. The second curve (e.g. the blue one) then needs to lie within some boundaries in order to prevent the mesh to reach these plane intersections. On Figure 3.29, the blue curve is chosen close to that boundaries: a pinching of the mesh can be observed.

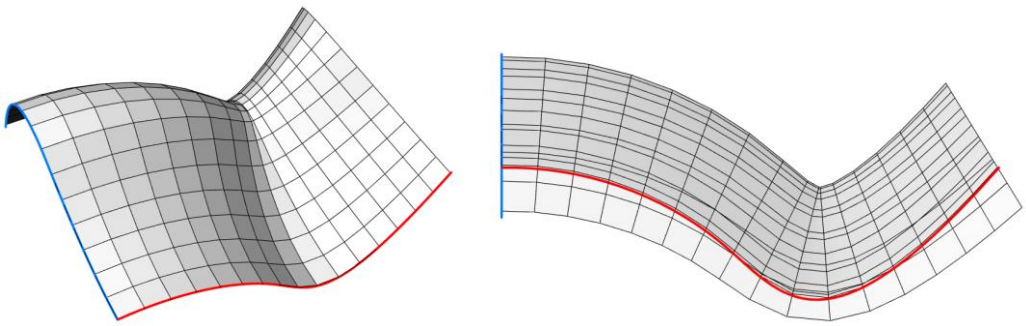

Figure 3.29: Mesh pinching. Pushing up the blue guide curve would cause self-intersection

3.5.4 C^∞ surfaces with planar curvature lines

For some applications, it might be desirable to have a C^∞ surface. One could wonder if surfaces with planar curvature lines can be described by B-splines or NURBS surfaces, as these are ubiquitous in computational design. (Darboux 1896) showed that if one curvature line of a surface with planar curvature lines is polynomial, then all the subsequent curvature lines are also polynomial with the same degree. Hearing this, one might wonder if these surfaces can be modelled by B-splines, with iso-lines being curvature lines, thus forming a new family of principal patches. The answer is unfortunately negative, as shown in the following counter-example in Figure 3.30. A surface with parabolic curvature lines is constructed. It is then approximated by a Bezier patch of degree two (for which all iso-lines are parabolas), such that boundary curves match the surface boundary exactly. We observe that the iso-lines are not aligned with the curvature lines. Nonetheless, the possibility to model surfaces with planar curvature lines by NURBS is an open question. Such a model was for example proposed for Dupin cyclides in (Zube and Krasauskas 2015).

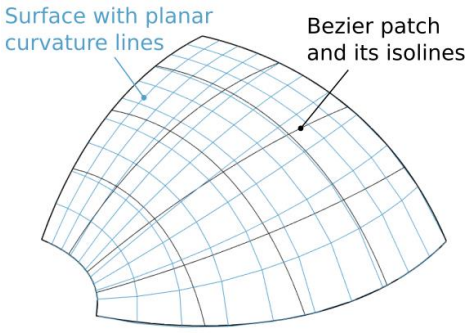

Figure 3.30: Difference of parametrization between a surface with parabolic curvature lines and a 2nd order Bezier patch approximating it

3.6 Structural applications

Gridshells

The benefits of using circular meshes for architectural envelopes was discussed in the introduction: they offer a reference geometry that can be built with a network of beams with torsion-free nodes of constant height, which can be covered with flat panels. Our method has the additional property of having planar curvature lines. In this section, we highlight one significant application of this property to metal-glass gridshells built with curved structural pipes covered with flat quadrangular glass panels. Such structures have the benefit of appearing curved from an indoor perspective, as the beams are then more noticeable than the panels, without having to resort to costly curved glass. In such structures, pipes are produced straight, and are then bent in factory, most often by a roller bender (Figure 3.1). The bending process is much more precise if the target curve is planar and piecewise circular, which is precisely the property of the curvature lines of cyclidic nets built on circular meshes with planar lines.

Figure 3.31 shows an application of our method to the design of a shading structure. This structure is generated from a mesh with three offsets. The top offset is used to lay a quad mesh with planar faces, which defines the geometry of glass panels. The other three layers are used to lay beams: one layer in the ortho-radial direction, and two layers in the radial direction in order to provide a high bending stiffness. All the radial beams are bi-arcs, all the ortho-radial beams are circular. This fact simplifies significantly the beam forming process, and offers the possibility to build the beams by splicing two circular arcs. Due to the vertex offset, all nodes have the same height. Furthermore, beams always cross at a right angle. Thanks to these properties, a single connector detail can be used for all connections. Interestingly, the combination of vertex-offset and piecewise circular beams yields an edge offset: the top and bottom beams are at a constant distance to each other. They are also parallel: a plane that is perpendicular to the bottom chord will be also perpendicular to the top chord. These properties can be used to design standard shear connectors between the top and bottom layers.

Such a structure can for example be fabricated with similar details as the Schubert Club Band Shell, shown in Figure 3.2. We note that this structure has all the fabrication properties described above, since its shape is constrained to a portion of torus, a particular surface with planar curvature lines. Our method allows to obtain a much wider design space.

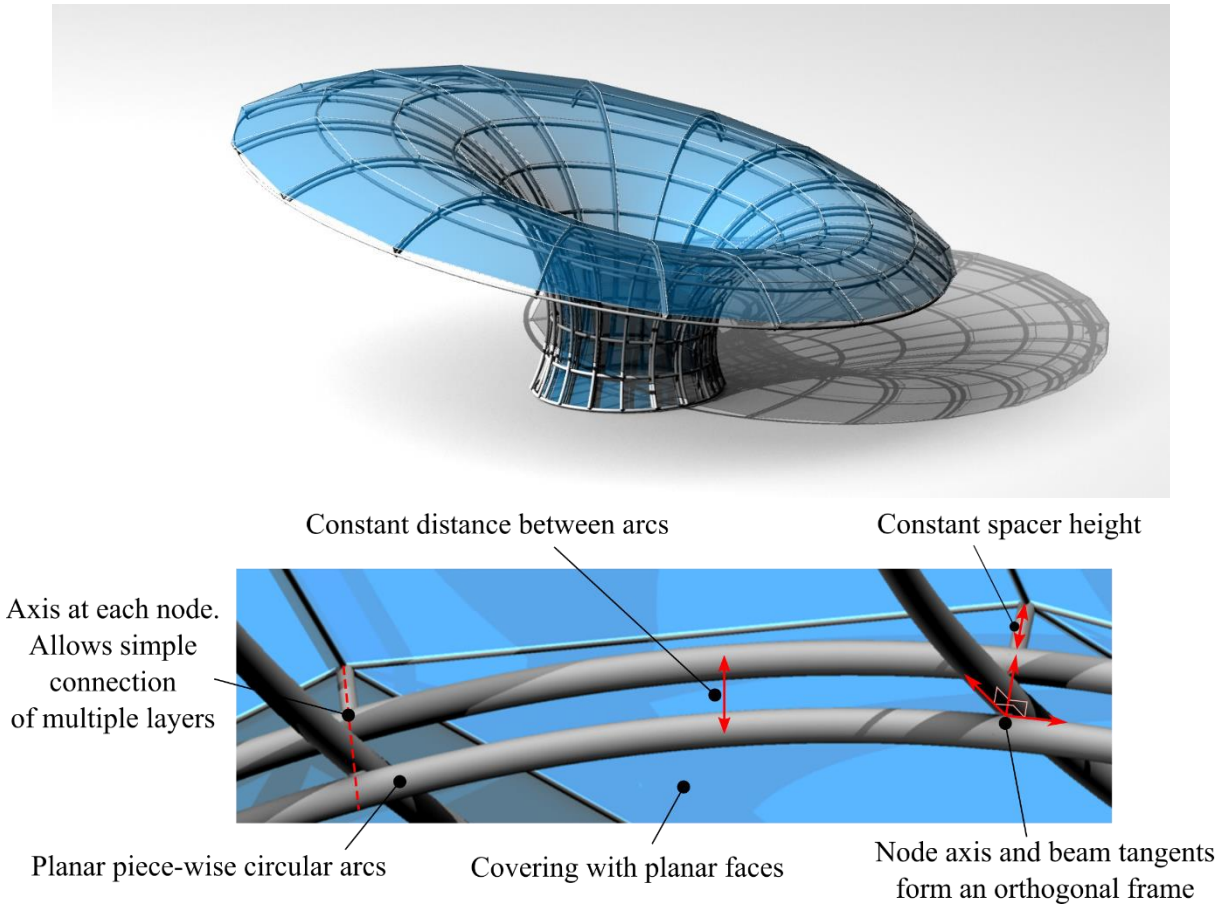

Figure 3.31: Shading structure built from flat bi-arcs, covered with flat panels, and with torsion-free nodes. Top: overall view. Bottom: Summary of geometrical properties (bulky sections used on purpose to highlight properties)

Planar lines are also interesting for timber structures. Curved wooden beam are often fabricated in glued laminated timber (glulam), a process in which thin, flexible strips of wood are glued together. If a beam is not planar, each strip of wood has a geodesic curvature, and therefore needs to be split longitudinally into "sticks": this complexifies significantly milling and gluing. Such a process had to be used for example for the fabrication of the Centre Pompidou in Metz (France) in 2010. The geometries generated with our method have planar lines, therefore they can be fabricated out of regular glulam (in which the strips need not be split into sticks).

Multi-layer structures

Another way to use these properties is suggested in Figure 3.32, where a primary structure is made of trusses with circular members and constant diagonal length. Trusses are assembled via nodes that are all identical. A secondary structure (in blue) supports planar glass panels. This type of structure would have applications for temporary structures such as concert venues.

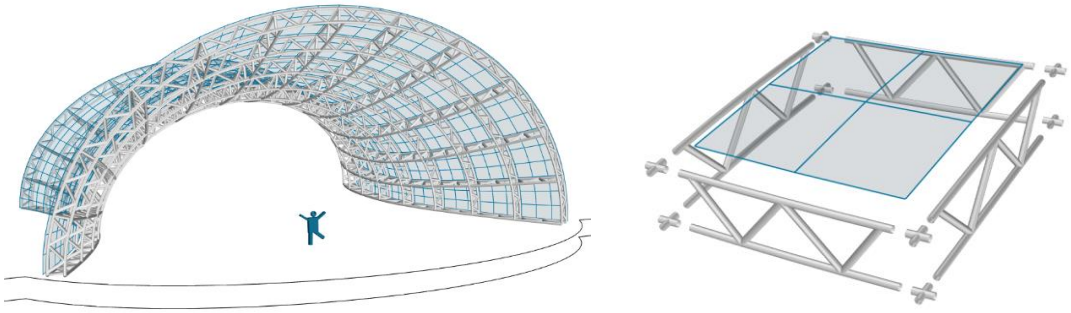

Figure 3.32: Temporary show venue with a demountable structure. Nodes are standard, truss members are circular, covering can be made with planar faces.

3.7 Summary of contributions

In this chapter, we presented a method to generate circular meshes, conical meshes and C1 surfaces with planar curvature lines. The method allows to align a mesh with boundary planes and to build a network of piecewise circular beams that can be covered with flat quads. These properties are all guaranteed exactly by geometrical proofs. The proposed method enables an intuitive, robust and real-time exploration of the full design space. We also introduced a method to design a surface in which curvature lines are piecewise planar in order to get access to a wider range of surfaces. Resulting meshes are of particular interest for the fabrication of gridshells. For these structures, the proposed geometry rationalizes the fabrication of beams and panels, and allows a standardization of the nodes and connectors.

References

Adam, P. 1893. “Sur Les Surfaces Isothermiques À Lignes de Courbures Planes Dans Un Système Ou Dans Les Deux Systèmes. (On Isothermic Surfaces with Planar Curvature Lines in one or two Directions)” Annales Scientifiques de l’E.N.S. Série 3. Tome 10: 319–58. doi.org/10.24033/asens.394. http://www.numdam.org/item/ASENS_1893_3_10__319_0/

Austern, Guy, Isaac Guedi Capeluto, and Yasha Jacob Grobman. 2018. “Rationalization Methods in Computer Aided Fabrication: A Critical Review.” Automation in Construction 90. Elsevier: 281–93. doi:10.1016/j.autcon.2017.12.027.

Berger, Marcel, and Bernard Gostiaux. 1992. Géométrie Différentielle, Variétés, Courbes et Surfaces. (Differential Geometry, Manifolds, Curves and surfaces) Presses universitaires de France. ISBN 978-2-13-044708-5

Bianchi, Luigi. 1894. Lezioni Di Geometria Differenziale (Lesson of Differential Geometry). Edited by Enrico Spoerri. https://gallica.bnf.fr/ark:/12148/bpt6k99684h.image

Bo, Pengbo, Helmut Pottmann, Martin Kilian, Wenping Wang, and Johannes Wallner. 2011. “Circular Arc Structures.” ACM Trans. Graph. 30 (4): 101:1–101:12. doi:10.1145/2010324.1964996.

Bobenko, Alexander I. 2008. Surfaces from Circles. Edited by A.I. Bobenko, P. Schröder, J.M. Sullivan, G.M. Ziegler. Discrete Differential Geometry. Series: Oberwolfach Seminars, Vol. 38. doi:10.1007/978-3-7643-8621-4_1.

Bobenko, Alexander I., and Emanuel Huhnen-Venedey. 2012. “Curvature Line Parametrized Surfaces and Orthogonal Coordinate Systems: Discretization with Dupin Cyclides.” Geometriae Dedicata 159 (1): 207–37. doi:10.1007/s10711-011-9653-5.

Bonnet, Ossian. 1853. “Mémoire Sur Les Surfaces Dont Les Lignes de Courbure Sont Planes ou Sphériques.(Memoir on Surfaces for which Curvature Lines are Planar or Spherical)” Journal de l’Ecole Impériale Polytechnique XX: 118–81. https://gallica.bnf.fr/ark:/12148/bpt6k62971065.texteImage

Coxeter, H. S., and S. L. Greitzer. 1967. Geometry Revisited. Mathematical Association of America. ISBN: 0-88385-600-X

Darboux, Gaston. 1896. “Leçons Sur La Théorie Générale Des Surfaces.(Lesson on the General Theory of Surfaces.)” In , Partie IV-Chapter IX. https://gallica.bnf.fr/ark:/12148/bpt6k77831k

Deng, Bailin, Sofien Bouaziz, Mario Deuss, Alexandre Kaspar, Yuliy Schwartzburg, and Mark Pauly. 2015. “Interactive Design Exploration for Constrained Meshes.” CAD Computer Aided Design 61: 13–23. doi:10.1016/j.cad.2014.01.004.

Douthe, Cyril, Romain Mesnil, Hugo Orts, and Olivier Baverel. 2017. “Isoradial Meshes : Covering Elastic Gridshells with Planar Facets.” Automation in Construction 83: 222–36. doi:10.1016/j.autcon.2017.08.015.

Eisenhart, Luther Pfahler. 1909. A Treatise on the Differential Geometry of Curves and Surfaces. Ginn and Company Proprietors, Boston USA. https://geographiclib.sourceforge.io/geodesic-papers/eisenhart09.pdf

Glaeser, Georg, Hellmuth Stachel, and Boris Odehnal. 2016. The Universe of Conics. Springer Spektrum. ISBN: 9783-662-454497

Glymph, James, Dennis Shelden, Cristiano Ceccato, Judith Mussel, and Hans Schober. 2004. “A Parametric Strategy for Freeform Glass Structures Using Quadrilateral Planar Facets.” Automation in Construction 13 (2): 187–202. doi:10.1016/j.autcon.2003.09.008.

Jiang, Caigui, Chengcheng Tang, Marko Tomicic, Johannes Wallner, and Helmut Pottmann. 2014. “Interactive Modeling of Architectural Freeform Structures – Combining Geometry with Fabrication and Statics.” Block, P., Wang, W., Knippers, J., Editors. - Advances in Architectural Geometry, 94–108. https://doi.org/10.1007/978-3-319-11418-7 7.

Liu, Yang, Helmut Pottmann, Johannes Wallner, Yong-Liang Yang, and Wenping Wang. 2006. “Geometric Modeling with Conical Meshes and Developable Surfaces.” ACM Transactions on Graphics 25 (3): 681. doi:10.1145/1141911.1141941.

Liu, Yang, and Wenping Wang. 2008. “On Vertex Offsets of Polyhedral Surfaces.” In Proceedings of Advances in Architectural Geometry, 61–64. doi:10.1007/978-3-319-11418-7.

McLean, David. 1985. “A Method of Generating Surfaces as a Composite of Cyclide Patches.” The Computer Journal 28 (4): 433–38. doi:10.1093/comjnl/28.4.433.

Mesnil, Romain, Cyril Douthe, Olivier Baverel, and Bruno Leger. 2017. “Marionette Meshes : Modelling Free-Form Architecture with Planar Facets.” International Journal of Space Structures 32 (3–4): 184–98. doi:10.1177/0266351117738379.

Mesnil, Romain, Cyril Douthe, Olivier Baverel, and Bruno Léger. 2017. “Generalised Cyclidic Nets for Shape Modelling in Architecture.” International Journal of Architectural Computing 15 (2): 148–68. doi:10.1177/1478077117714917.

Mesnil, Romain, Cyril Douthe, Olivier Baverel, and Bruno Léger. 2018. “Morphogenesis of Surfaces with Planar Lines of Curvature and Application to Architectural Design.” Automation in Construction 95: 129–41. doi:10.1016/j.autcon.2018.08.007.

Mesnil, Romain, Cyril Douthe, Olivier Baverel, Bruno Léger, and Jean François Caron. 2015. “Isogonal Moulding Surfaces: A Family of Shapes for High Node Congruence in Free-Form Structures.” Automation in Construction 59: 38–47. doi:10.1016/j.autcon.2015.07.009.

Monge, Gaspard. 1805. Application de L'Analyse À La Géométrie (Application of analysis to geometry). Bernard, Paris. https://gallica.bnf.fr/ark:/12148/bpt6k6565456c.texteImage

Pottmann, Helmut. 2013. "Architectural Geometry and Fabrication-Aware Design." Nexus Network Journal 15 (2): 195–208. doi:10.1007/s00004-013-0149-5.

Pottmann, Helmut, Yang Liu, Johannes Wallner, Alexander I. Bobenko, and Wenping Wang. 2007. "Geometry of Multi-Layer Freeform Structures for Architecture." ACM Transactions on Graphics 26 (3): 65. doi:10.1145/1276377.1276458.

Pottmann, Helmut, and Johannes Wallner. 2006. "The Focal Geometry of Circular and Conical Meshes." Advances in Computational Mathematics, no. 29(August): 249–68. doi:10.1007/s10444-007-9045-4.

Powell, Michael. 2007. "A View of Algorithms for Optimization without Derivatives." Mathematics Today - Bulletin of the Institute of Mathematics and Its Applications 43 (5): 170–74. doi:10.1108/13639519910299580.

Pratt, Michael. J. 1990. "Cyclides in Computer Aided Geometric Design I." Computer Aided Geometric Design 7: 221–42. doi:10.1016/0167-8396(90)90033-N.

Schlaich, Jörg, and Hans Schober. 1998. "Glaskuppel Für Die Flusspferde Im Zoo Berlin (Glass dome for the hippopotami in Berlin Zoo)." Stahlbau 67: 307–12. doi:10.1002/stab.199800990

Schober, Hans. 2015. Transparent Shells: Form, Topology, Structure. Ernst & Sohn. ISBN 978-3433031216

Yang, Yong-Liang, Yi-Jun Yang, Helmut Pottmann, and Nilroy Mitra. 2011. "Shape Space Exploration of Constrained Meshes." ACM Transactions on Graphics (TOG) 30 (6). doi:10.1145/2070781.2024158.

Zadravec, Mirko, Alexander Schiftner, and Johannes Wallner. 2010. "Designing Quad-Dominant Meshes with Planar Faces." In Computer Graphics Forum, 29:1671–79. Oxford, UK: Blackwell Publishing Ltd. doi:10.1111/j.1467-8659.2010.01776.x.

Zube, Severinas, and Rimvydas Krasauskas. 2015. "Representation of Dupin Cyclides Using Quaternions." Graphical Models 82: 110–22. doi:10.1016/j.gmod.2015.06.008.

Chapter 4 Caravel meshes

This chapter introduces Caravel meshes, a new family of meshes that offers many geometrical properties susceptible to rationalize the fabrication of curved structural envelopes, in particular gridshells. The most complicated aspect in the fabrication of gridshells is the connection between the structural elements – beams and panels. In Caravel meshes, all the connections are rationalized. Firstly, the connection between beams and cladding panels can be made without kink angle, provided that panels are folded along diagonals. Secondly, beams can be connected to each other by nodes without geometrical torsion. Thirdly, a method is presented to make these nodes repetitive, and to obtain edge offset.

A great variety of mesh combinatorics is possible. Quadrangular and hexagonal topologies are studied more in-depth. Their asymptotic behavior is analysed, and used to estimate feasible shapes and to find proper initialization for generation by optimization methods. Beyond gridshells, Caravel meshes can be applied to design innovative structural systems such as rationalized plated shell structures.

The structural potential of Caravel meshes is demonstrated by the realization of two pavilions: a 60 m² timber pavilion, built on the campus of Ecole des Ponts near Paris (Figure 4.1), and an aluminum pavilion, presented at the IASS symposium 2019 in Barcelona (Figure 4.2).

Figure 4.1: A timber gridshell with a geometry based on a hexagonal Caravel mesh. Only two types of nodes are used throughout the structure: planar nodes, and 120° nodes (picture ©Stefano Borghi)

Figure 4.2: The Caravel heX-Mesh pavilion at the IASS 2019. The geometrical properties of Caravel meshes are used to simplify and standardize all the connections.

4.1 Introduction

In a curved envelope, there is usually a kink angle between cladding panels and support beams, as shown in Figure 4.3. This kink makes the panel-beam connection complex, and has not been addressed by the architectural geometry literature. The few existing curved structures in which this angle is null have double curvature panels lying on curved beams. An example is the Lentille St-Lazare in Paris, designed by Arte Charpentier and RFR (Baldassini 2005). However, the cost of the molds necessary to fabricate double-curvature panels is often prohibitive. The kink angle can be particularly problematic if the ratio of the panel width over the surface curvature radius is high (Figure 4.3, right), i.e. if the surface is coarsely discretized. In a glazed structure, a low kink angle can be accommodated by the elasticity of the EPDM joints, which are necessary for the water tightness. If the kink angle is too high, costly profiles need to be used. In an opaque façade, the kink angle is often accommodated by spacing panels out with small gaps. In both cases, the kink angle prevents the panels from acting as a structural elements, unless a complex machining of the beams is performed, like in the Hybrid Shell-Nexorade Pavilion of Figure 2.5 (Douthe *et al.* 2018).

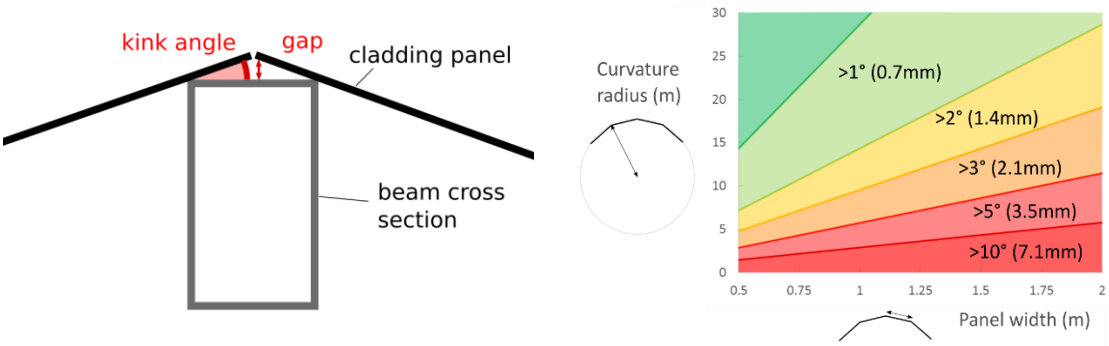

Figure 4.3: Kink angle between a cladding panel and a beam and corresponding gap. Right: value of the angle and gap as a function of panel width and curvature radius of surface. The gap is given for a 80mm wide beam.

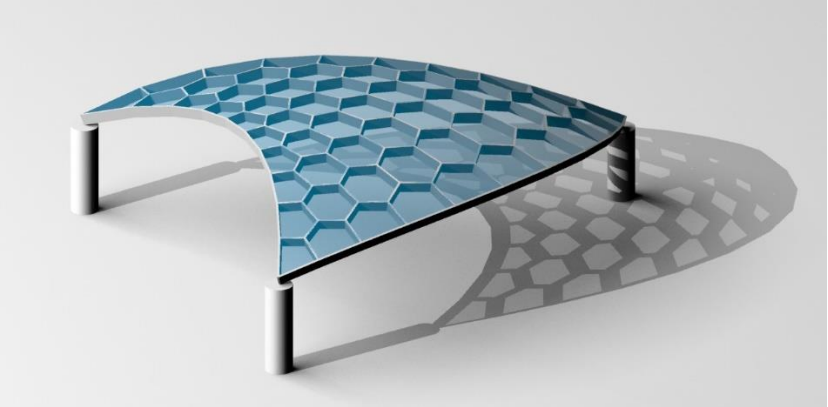

Figure 4.4: A shading structure based on a hexagonal Caravel mesh with only two types of nodes (planar and "120°") and edge offset. The fact that nodes are torsion-free with edge offset allows to easily give structural height to this gridshell, thus making it resistant in bending.

This chapter introduces *Caravel meshes*, a new mesh structure that allows paneling without kink angle between panels and beams, and that also has torsion-free nodes. Many mesh combinatorics are possible, and will be referred to as *Caravel graphs*. The geometrical structure of quadrangular Caravel meshes is presented in Figure 4.5. Node repetition, discussed in section 2.2.3 (in chapter 2), can be also included by decomposing the nodes in two families:

- Planar nodes, with null vertical and torsion angles;
- 3D nodes, with constant in-plane angles and no torsion.

Finally, edge offset (also discussed in section 2.2.3) can be obtained on the top of the previous three properties for a special type of hexagonal Caravel meshes, as illustrated in Figure 4.4.

The fabrication properties of Caravel meshes are obtained by allowing faces to be not planar, contrary to many rationalization approaches in the literature of architectural geometry. The non-planarity can be addressed practically by covering the structure with folded panels, which are common in metal facades.

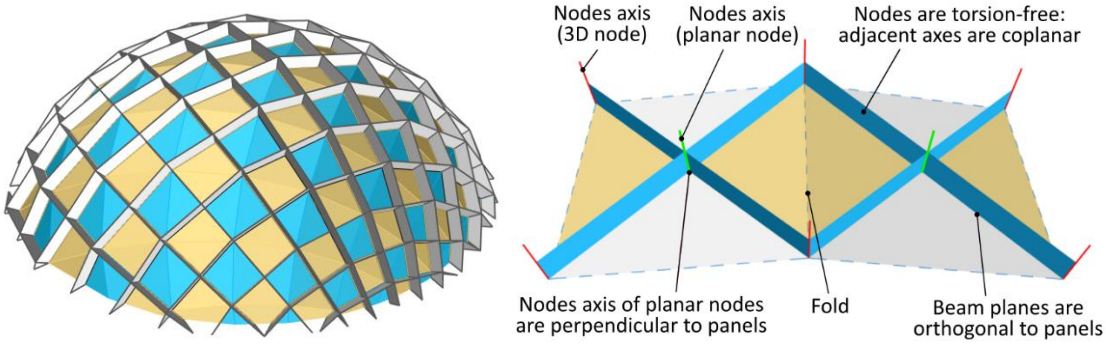

Figure 4.5: A quadrangular Caravel meshes and its local properties.

Overview of chapter

In section 4.2, we analyze the different technical solutions to cover a gridshell without kink angles between cladding panels and beams. In section 4.3, we study one particular solution, which consist in folding cladding panels diagonally. By combining this solution with a torsion-free support structure, we define the concept of Caravel meshes. In section 4.4, we study quadrangular Caravel meshes. These are the simplest and most mechanically efficient Caravel mesh topologies. However, an asymptotic analysis reveals that they are quite constrained formally. For that reason, we turn to hexagonal Caravel meshes in section 4.5. The same asymptotic analysis shows that they can approximate arbitrary smooth surfaces. Furthermore, a subfamily of hexagonal Caravel meshes allows to obtain a high degree of node standardization by decomposing nodes in two families: planar nodes and 120° nodes. Finally, in section

4.6, we present other applications of Caravel meshes. The potential of having repetitive torsion-free nodes has been illustrated by the construction of two full-scale pavilions: one in timber (Figure 4.1), and one in aluminum (Figure 4.2).

Figure 4.6 gives a visual overview of the chapter. It maps the fabrication properties which are addressed (in black), the types of mesh for which they are obtained (in green), and the corresponding generation methods (in red). The arborescence of Caravel meshes is highlighted in light green: from the broad concept of Caravel meshes, we add geometrical properties as we go down the tree. In blue, we highlight the technical solutions detailed in section 4.2 to obtain no-kink angle between beams and panel.

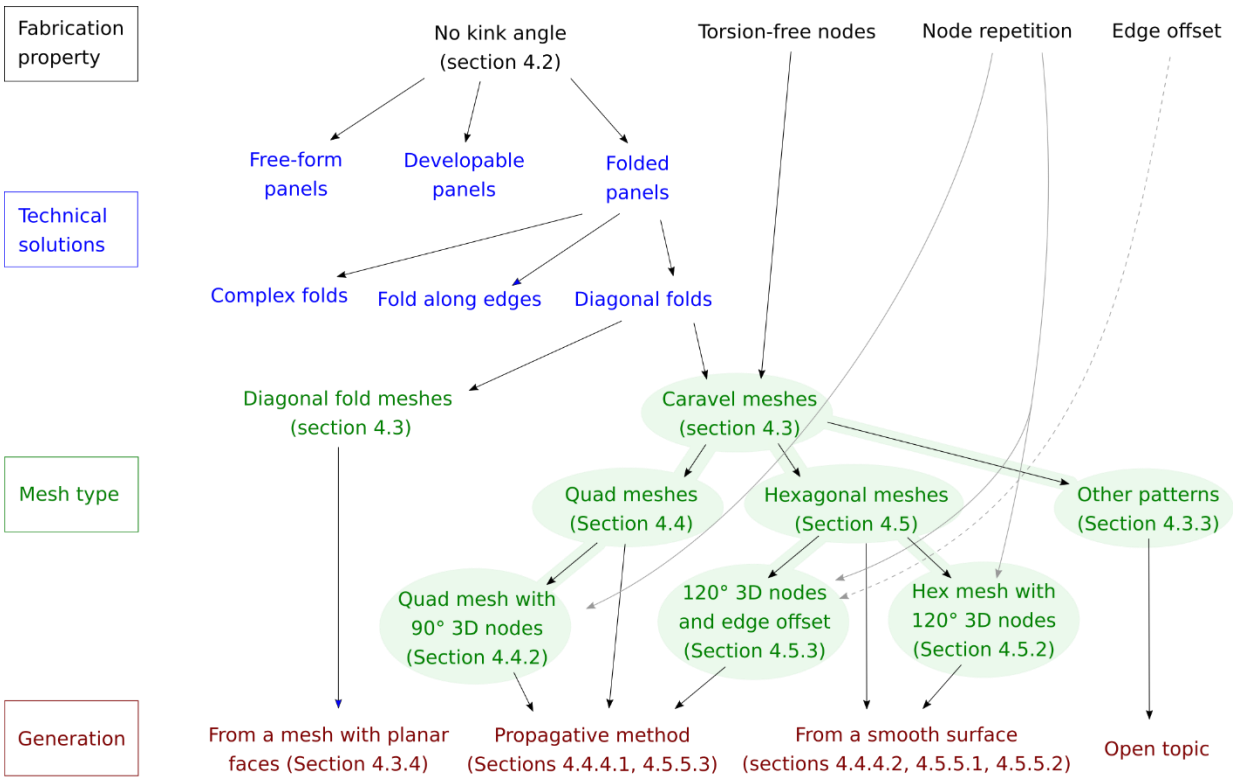

Figure 4.6: Overview of the chapter

4.2 Technical solutions for paneling without kink angle

In this section, we explore the geometrical and technological strategies to obtain a gridshell without kink angle between panels and beams. Since the dihedral angle between adjacent panels is null, the curvature of the envelope needs to be located in the panels. For this purpose, panels may be bent, folded or molded into double curvature shapes. We will discuss the first two options, as the last one does not rise specific geometric issues.

4.2.1 Cold bending

A first solution is to bend initially flat panels. Thin panels can be deformed easily into nearly developable surfaces by hot or cold bending. Cold bending of glass panels is a popular method to cover a gridshell without planar faces with glass. This method was for example used for the facades of Strasbourg train station (Blassel and Pfadler 2008) and Vuitton Foundation in Paris.

In that case the perfect contact between panels and beams implies that the top surface of each beam is also a developable surface. The geometry of a developable surface can be fully described by one curve and one family of normal vectors, which defines the surface normal at any point of the curve. It can be shown (do Carmo 1976) that there is only one developable surface which is incident to a curve and whose rulings are perpendicular to the normals. Therefore, two panels resting along the same beam belong necessarily to the same developable surface: their rulings are identical. As a result, a structure made of bent panels lying flat on their supporting beams can only describe one single developable surface, as illustrated in Figure 4.7.

Generation of developable surfaces is a well-researched topic. Therefore, this option will not be discussed further here.

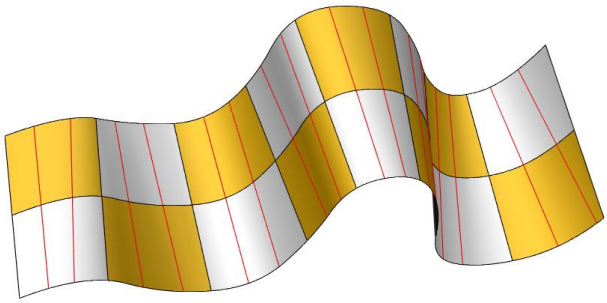

Figure 4.7: Developable panels connected without kink angle form one large developable surface. Rulings showed in red.

Panels can also deform into non-developable surfaces under cold-bending if sufficient retaining forces are applied. This is in particular the case of thick panels: their bending energy has the same order of magnitude as the membrane energy, so their reference surface does not deform in an isometric manner, unlike developable surfaces. The amplitude to which these panels can be deformed is function of the material and panel thickness. (Eversmann *et al.* 2016), (Fildhuth *et al.* 2018) and (Berrubé *et al.* 2019) performed mechanical analysis to study the shape potential of this method.

4.2.2 Folded panels

Folding has been the focus of a lot of research, see for example (Lebée 2015) for a review of folds related to structural application. We will here focus on possible ways to fold one panel to obtain zero kink angle.

(a) A first way to fold the panels is to follow the edge of the supporting beams, as shown in Figure 4.8 (left). This solution can readily be applied to any mesh with planar faces. However, this method requires a lot of folding and cutting. Furthermore, special details are needed at the corner to insure water tightness.

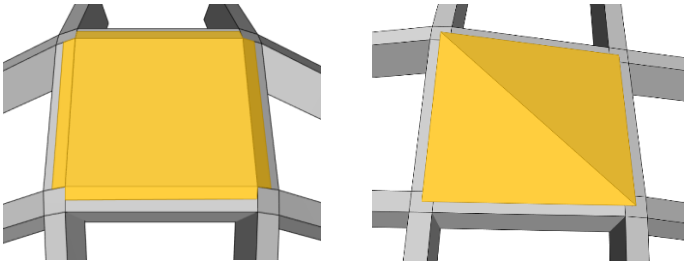

Figure 4.8: Panels folded along the beam edges (left) and along a diagonal (right).

(b) A second way is to follow the diagonals, as shown on Figure 4.8 (right). This type of fold has been often used for doubly curved facades with metallic cladding. Three examples are given in Figure 4.9: the facade of the Bus Terminal of Hamburg Poppenbüttel, the school of architecture EAVT near Paris and the Rhike Park Music Theater and Exhibition hall in Tbilisi. The Kaiser Hawaiian geodesic dome uses a more elaborate type of folding: quads are folded along their diagonals to form series of pyramids.
For materials that cannot be folded, panels may be cut along diagonals. An example is the gridshell of the History Museum of Hamburg (Schober 2015), for which some glass panels had to be cut diagonally in the portions of the surface with the highest curvature.

(c) More complex panel shapes can be obtained by advanced fabrication technics. (Trautz and Herkrath 2009) propose a technique to create complex crease patterns on a metal sheet by incrementally pressing it with a moving dice. Origami folding can also yield complex 3D shapes from a flat panel, in which crease lines converge at a node located inside a panel. Curved folding might be also used. Another method is curved folding, for which applications to facades were for example experimented in (Berrubé *et al.* 2019) and for the ARUM sculpture by Zaha Hadid at the 2012 Venice biennale.

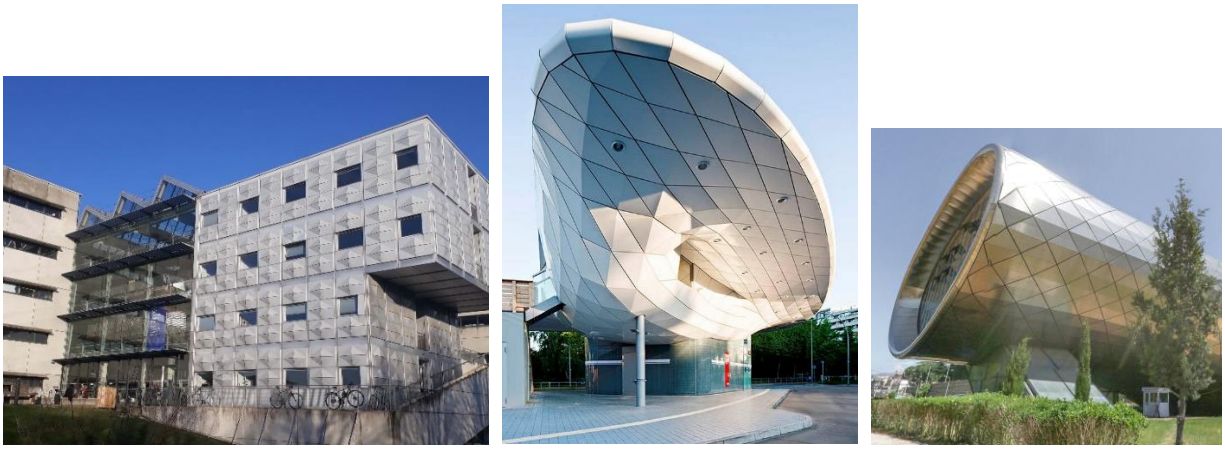

Figure 4.9: Diagonal folds on facades. Left: EAVT in Marne-la-Vallée (Picture: X. Tellier). Middle: Hambürg Poppenbüttel Bus Terminal (© www.archimages.de). Right: Rhike Park Music Theater (© Aslan Juan)

4.2.2.1 Folded panels on nexorades

Nexorades can be covered with folded panels without kink angle, provided that the tips of beams are milled adequately (or that shims are added if Gaussian curvature is negative). A geometry can easily be obtained from a mesh with planar quads, as shown in Figure 4.10.

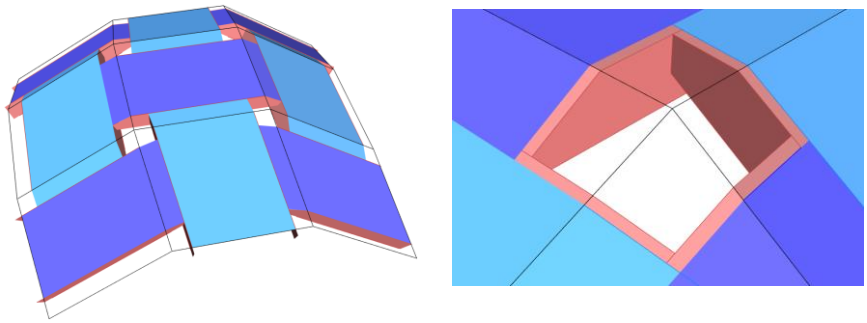

Figure 4.10: One way to cover a quadrangular nexorade with bi-folded panels. Left: global view. Planar-quad mesh shown in black. Right: Close-up on beam cuts. Panels lie flat on beam top surfaces

4.3 Diagonal folds and Caravel meshes

Amongst the technical solutions discussed in the previous section, diagonal folds (Figure 4.8, right) present an interesting compromise between ease of fabrication and formal potential. In this section, we analyze the geometry of this solution, and use it to define Caravel meshes.

4.3.1 Geometric structure

Envelopes covered with folded panels can be geometrically described by two meshes, as shown in Figure 4.11 (in which panels are shown in yellow and grey):

- A *structural mesh*, which represent the top centerline of support beams. This mesh also corresponds to the edges of the panels.
- A *fold mesh* (dashed), which corresponds to all the fold lines. Each node of this mesh has to correspond with one node of the structural mesh. Faces of this mesh are planar.

As seen on Figure 4.11, a node of the structural mesh may or may not be a node of the fold mesh. In the second case, the node is necessarily planar, i.e. all incident planes are coplanar. The fabrication of such nodes is significantly simpler than for a spatial node. Nodes of the structures can therefore be divided into two categories: *planar nodes* and *3D nodes*.

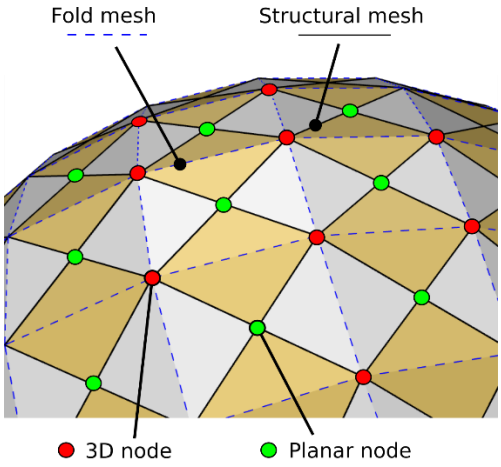

Figure 4.11: Fold mesh and structural mesh

Both meshes play an important role in the aesthetic of an envelope. The structure mesh defines the patterning of the surface, how it is divided into panels. The fold mesh divides the surface into planar faces. Each of these faces has a different angle in space, and will appear to a viewer with a different luminosity.

4.3.2 Topology

The topological relation of fold and structural meshes can be formalized using the theory of graphs. A graph is a set of vertices linked by edges. The topology of a manifold mesh can be described by a simple planar graph, i.e. a graph that can be drawn on a plane without intersection of edges, and such that no more than one edge link two vertices. The faces correspond to the domains enclosed by edges. We propose to name a graph that is compatible with the fold mesh/structural mesh structure a *Caravel graph*, defined as follows:

Definition: A Caravel graph is a simple planar graph that fulfills the following properties:

i. Vertices are bicolored: green (labeled “planar nodes”) and red (labeled “3D nodes”). Adjacent nodes may have the same color, so the graph does not need not be “2-colorable”;
ii. Edges are bicolored: dashed blue (folds) and black (beams);
iii. Each fold starts and ends at a 3D node. A node is labelled planar if and only if it has no incident fold;
iv. At least two folds and two beams meet at a 3D node (except on the boundary);

Condition iv is due to the facts that we do not allow a lone cantilevered beam in the mesh, and that at least two fold lines must meet for the node not to be planar. Despite condition i, a Caravel graph need not be 2-colorable: two adjacent nodes can have the same color. Figure 4.12 shows two examples of Caravel graphs. The graph of the structural mesh can be retrieved from a caravel graph by taking the beams and all the nodes. Similarly, the fold mesh is retrieved by taking the folds and the 3D nodes.

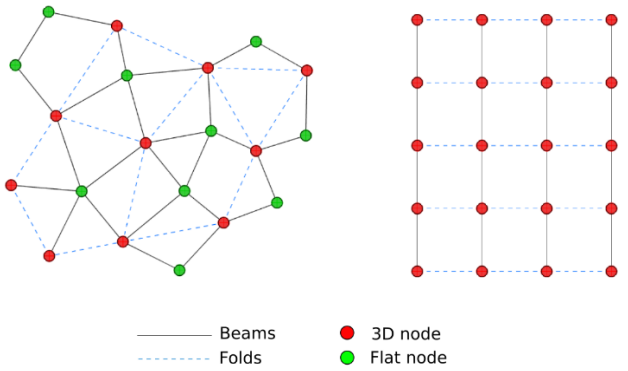

Figure 4.12: Caravel graphs

The structural and the fold mesh are not dual of each other. In particular, one cannot in general swap the colors of the edges and nodes, as the condition of having two folds and two beams meeting at a 3D node gets violated.

4.3.3 Periodic patterns

There is a great variety of mesh topologies satisfying the Caravel properties. In particular, many patterns with periodic combinatorics are possible, such as the quadrangular pattern shown in Figure 4.11. The *semi-regular* tessellations of the plane (also called Archimedean tilings) provide a good basis to generate new combinations of fold and structural meshes. Semi-regular tessellations are planar periodic patterns obtained by assembling regular polygons (e.g. equilateral triangle, square, regular pentagon…) such that at each vertex, the same types and numbers of polygons meet, in the same order. These tessellations are described by a sequence of digits that correspond to the number of edges of each polygon around a node. For example, a Kagome pattern is called (3,6,3,6), because at each vertex, two regular triangles and hexagons meet alternatively. From a semi-regular tessellation, one can build a *dual* tiling by connecting the centers of all the pairs of adjacent polygons.

Figure 4.13 shows twelve combinations of structural and fold meshes, most of them generated from semi-regular tessellations or from their duals. Colors correspond to faces of the structure mesh, and therefore to panels.

- In pattern (a) (the same as in Figure 4.11), both fold mesh and structure mesh are quadrangular. There is one fold in each face of the structure mesh.

- Patterns (b) to (d) show other ways to arrange quadrangular panels with one fold. Each of them gives a very different fold mesh and structure mesh combinatorics. For example, in pattern (c), the structure mesh is the dual of the Archimedean tiling (3,3,3,3,6), and the fold mesh is a Kagome mesh.
- In pattern (e), the structure mesh is hexagonal. This type of mesh can be realized by tri-folded hexagonal panels. This type will be the object of section 4.5. The fold mesh is a triangular mesh.
- Pattern (f) is derived from a (3,4,6,4) fold mesh. The structure mesh is composed of quadrangles with one fold and hexagons with three folds.
- In patterns (g) and (h), some faces of the structure mesh are not folded. These can be used to insert panels made of materials that cannot be folded, such as glass. Pattern (g) is based on a structure mesh composed of hexagons and quadrangles, while pattern (h) is derived from an octo-quad fold mesh.
- Patterns (i) and (j) shows patterns with quadrangular panels that have respectively two and four folds. In pattern (j), the 3D nodes have only two incoming beams, which correspond to a kink in a beam.
- Pattern (k) is based on a Penrose pattern, a non-periodic pattern with a rotation symmetry of order five.
- Pattern (l) uses a dodecahedron as a fold mesh. Its flat nodes are 5-valent, while its 3D nodes are only 3-valent.

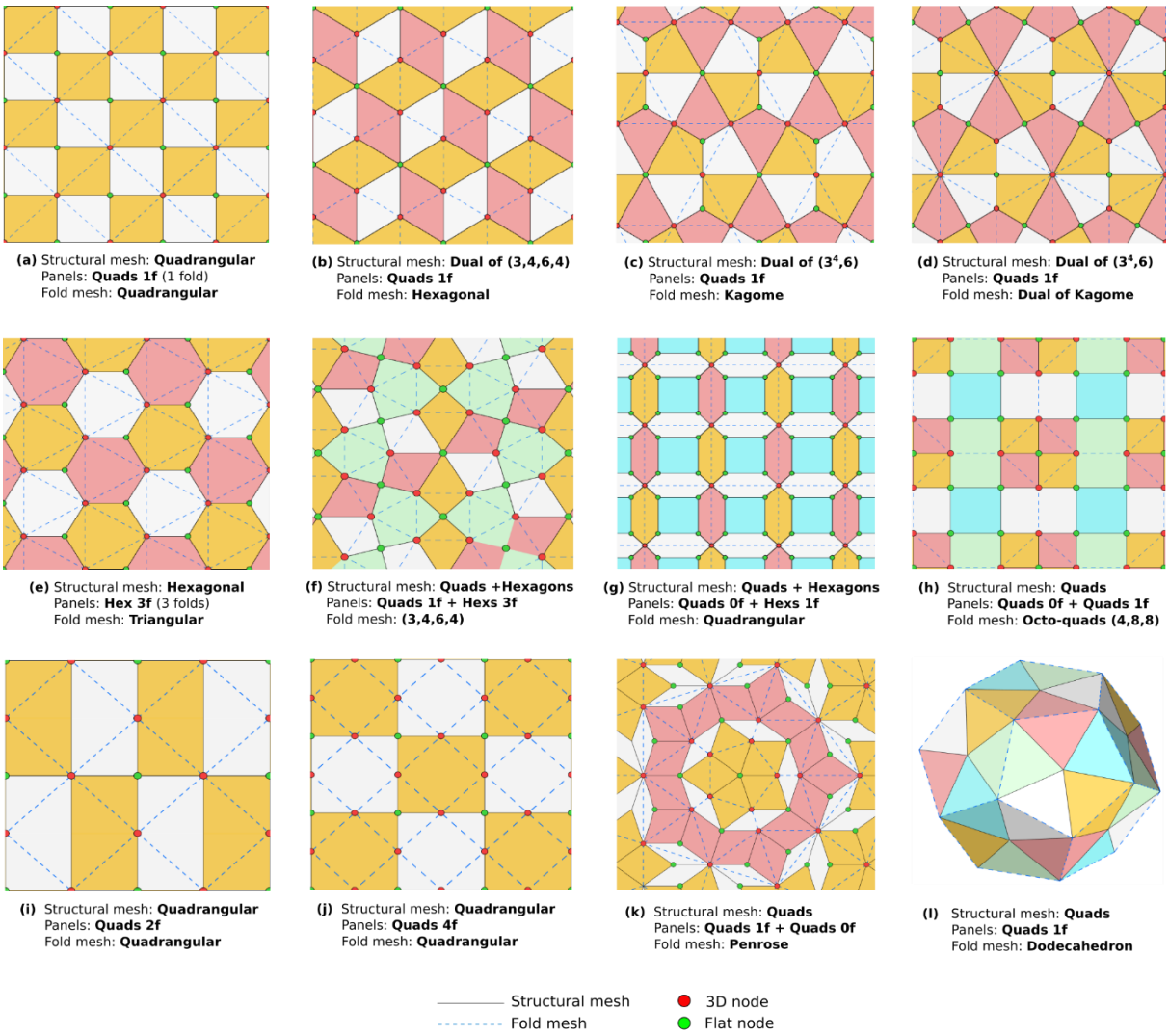

Figure 4.13: Various combinations of structural and fold meshes

4.3.4 Generation

The simplest way to generate a fold mesh and a structure mesh is to first generate a fold mesh, and then draw the structure mesh on it. The fold mesh only needs to have planar faces. There are many available methods in the literature to achieve this. One general method to obtain polyhedral patterns was proposed in (Jiang *et al.* 2015). Many methods exist to generate planar quad meshes for patterns (a), (g), (i), and (j) ((Glymph *et al.* 2004) , (Mesnil *et al.* 2017)), planar hexagonal meshes for pattern (b) (Wang and Liu 2009), (Vaxman and Ben-chen 2015) and Kagome meshes for pattern (c) (Mesnil *et al.* 2017). Figure 4.14 shows a realization of pattern (c) where a Kagome mesh has been generated by the method described in (Mesnil *et al.* 2017). Mechanically, the structure mesh can be efficiently decomposed into a principal load carrying system made of a triangular network of near planar arches, and a secondary system to support the panels, forming a hexagonal pattern. The resulting structure combines elegantly four different types of meshes: Kagome, triangular, hexagonal, and dual (3^4,6).

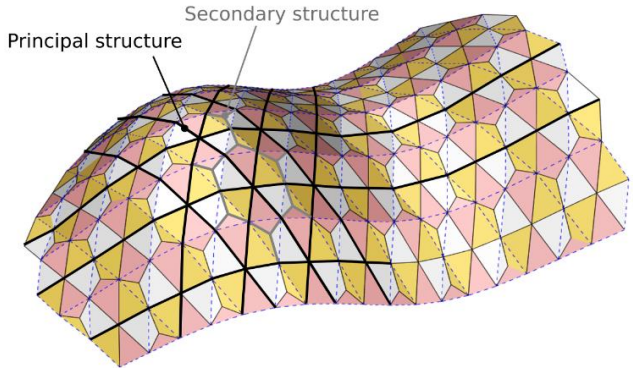

Figure 4.14: A geometric realization of the graph (c) of Figure 4.13: the fold mesh is a Kagome mesh with planar faces,

4.3.5 Caravel meshes

The strategy of diagonal folds can be combined with a structure mesh with torsion-free nodes. In order to describe geometrically a torsion-free structure, we need to introduce axes at the nodes. The absence of kink angle implies that the midplane of any beam is orthogonal to the face of the fold mesh in which it lies. Therefore, the axis of a planar node is orthogonal to its plane. Figure 4.5 shows these constraints on a portion of quadrangular pattern (pattern *a* in Figure 4.13). This geometric structure, that we name *Caravel mesh*, can be defined formally as follows:

Definition: A Caravel mesh is a mesh with Caravel graph combinatorics and axes at each vertex such that:

(a) The axes of two adjacent nodes are coplanar - their common plane corresponds to the median plane of the beam;
(b) At “planar nodes”, the incoming edges are coplanar;
(c) Axes at “planar nodes” are perpendicular to the plane defined by the adjacent edges.

The name Caravel is chosen as in invitation to explore new structural systems using *meshes with CoplanAR fAce and VErtex normaLs*. This name highlights the interplay of vertex normals and face normals of the fold mesh. Previous literature on torsion-free structures has focused on the geometric torsion between node normals combined with a constraint on face planarity (for example (Pottmann and Wallner 2007), (Liu *et al.* 2006)), the study of these meshes constitutes therefore a new topic and poses new geometric challenges.

Amongst all the combinatorics showed in Figure 4.13, we will study in more details patterns (a) in section 4, as it is simple and efficient mechanically. We will also study pattern (e) in section 5 because of the greater design freedom it offers.

4.4 Quadrangular Caravel meshes

Quadrangular Caravel meshes is probably the most easily useable type of Caravel mesh for construction purposes. An example is shown in Figure 4.5. They can be generated on any synclastic surface, but not on an anticlastic surface. This can be intuitively understood looking at Figure 4.15. The planes passing through the axes of planar nodes and an adjacent edge are drawn in blue. If the node at the center has a negative curvature, we cannot find an axis which is coplanar with the axes of the flat nodes. A consequence is that perfect quadrangular Caravel meshes can only be used for structures like domes or "blobs", in which the Gaussian curvature is everywhere positive.

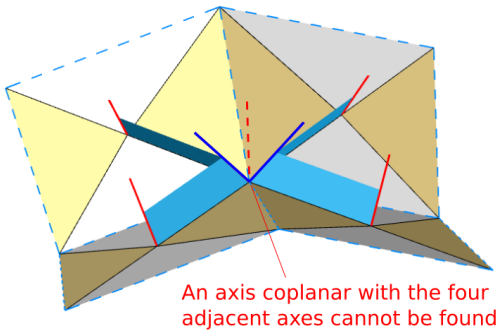

Figure 4.15: A quadrangular Caravel mesh cannot be anticlastic.

4.4.1 Asymptotic construction

In this part, we show how the geometric structure of quadrangular Caravel meshes behave in the asymptotic case, i.e. in the case where a smooth surface is approximated by a series of meshes with smaller and smaller face size. We will show in particular the following results:

Asymptotic behavior:

- A surface approximated by quadrangular Caravel meshes is necessarily synclastic;
- Beams tend to align with principal curvature directions of the surface;
- The aspect ratio of the faces of the mesh is prescribed by the ratio of the principal curvatures.

Proof:

In this asymptotic case, properties can be described in the setting of smooth differential geometry. On a smooth surface S, the only directions in which the surface normal does not undergo torsion are the curvature directions (do Carmo 1976). Because of the torsion-free property of the structure mesh, it necessarily tends towards a curvature line network in this asymptotic case. Let us introduce the associated parametrization by curvature lines $(u, v) \longmapsto x(u, v)$. A line $x(u, v)$ with $u = constant$ or $v = constant$ is then a line of the structure mesh.

Because of the planarity constraint, the fold mesh tends in the limit case towards a conjugate net (Sauer 1970). As a result, the "diagonal directions" of the parametrization x, $x_u + x_v$ and $x_u - x_v$, must be conjugate to each other (Figure 4.16). Let us note dn the second fundamental form of the surface (i.e. $dn(w)$ is the vector giving the rate of change of the surface normal when we move on the surface with a velocity vector w, (see (do Carmo 1976) for a thorough treatment). The conjugate condition can be written:

$$dn(x_u + x_v).(x_u - x_v) = 0$$

$$dn(x_u).x_u - dn(x_u).x_v + dn(x_v).x_u - dn(x_v).x_v = 0$$

Since x_u and x_v are principal curvature directions, $dn(x_u).x_v = 0$ and $dn(x_v).x_u = 0$. As a result:

$$dn(x_u).x_u = dn(x_v).x_v$$

The matrix of the second fundamental form in the (u, v) plane can then be written:

$$\mathrm{II} = \begin{bmatrix} dn(x_u).x_u & dn(x_u).x_v \\ dn(x_v).x_u & dn(x_v).x_v \end{bmatrix} = \lambda_P \begin{bmatrix} 1 & 0 \\ 0 & 1 \end{bmatrix}$$

with λ_P a real number, function of the position on the surface. Noting k_1 and k_2 the principal curvatures in the directions x_u and x_v (i.e. $k_1 = dn(x_u).x_u/\|x_u\|^2$), the matrix of the first fundamental form is (if $k_1 \neq 0 \neq k_2$):

$$\mathrm{I} = \begin{bmatrix} x_u.x_u & x_v.x_u \\ x_u.x_v & x_v.x_v \end{bmatrix} = \lambda_P \begin{bmatrix} 1 & 0 \\ 0 & 1 \end{bmatrix} \begin{bmatrix} k_1 & 0 \\ 0 & k_2 \end{bmatrix}^{-1} = \lambda_P \begin{bmatrix} k_1^{-1} & 0 \\ 0 & k_2^{-1} \end{bmatrix}$$

The diagonal coefficients of the first fundamental form are positive. Therefore, k_1 and k_2 must have the same sign: the Gaussian curvature $K = k_1 k_2$ is necessarily positive. This confirms the intuition showed in Figure 4.15. Furthermore, the ratio of the metrics $\|x_u\|$ and $\|x_v\|$ of the parametrization is imposed by the curvature of the surface:

$$\frac{\|x_u\|}{\|x_v\|} = \sqrt{\frac{k_2}{k_1}} \tag{4.2}$$

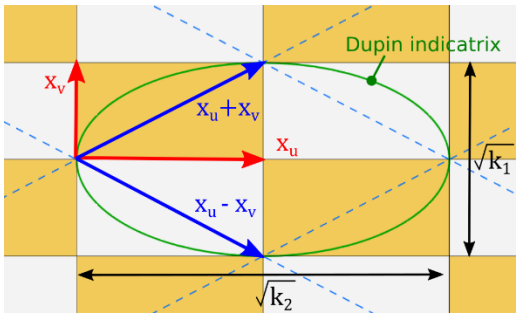

Figure 4.16: Quadrangular Caravel mesh: In the asymptotic case, a face of the fold mesh is a diamond inscribed in a homothetic image of the Dupin indicatrix

Finally, we remark that one cannot find *a priori* a parametrization fulfilling the equations $x_u.x_v = 0$ and $\mathrm{II} = \lambda_P \begin{bmatrix} 1 & 0 \\ 0 & 1 \end{bmatrix}$ on an arbitrary synclastic surface. The description of the possible shapes is an open problem.

Note:
The fact that the aspect ratio of the faces of the fold mesh is constrained by the principal curvatures ratio can be more intuitively understood using the concept of Dupin indicatrix (which will be recalled in section 4.5). In the asymptotic case:

- A face is congruent to the neighboring faces. As a consequence, faces must have central symmetry;
- The fold mesh is a conjugate net, its faces are therefore inscribed in a Dupin indicatrix;
- The diagonals of the fold mesh are aligned with curvature directions, i.e. with the main axes of the indicatrix.

The only solution to this set of constraints is for the faces of the fold mesh to be diamonds inscribed in the Dupin indicatrix in Figure 4.16. As such, their shape is entirely prescribed by the ratio of the major and minor axes of the indicatrix, which are proportional to the square roots of the principal curvatures.

4.4.2 Node repetition

For the planar nodes of Caravel meshes, the vertical angle is zero (angles of nodes were presented in section 2.2.3). This property can simplify significantly their fabrication. The geometry can be further rationalized to introduce repetitivity in the 3D nodes. Since the structure mesh approximates a curvature line network, its lines crosses at angle near 90°. We can optimize the geometry to make this angle exactly 90° at the 3D nodes. The geodesic curvature (k_g) of a mesh polyline is then concentrated in the planar nodes, while the normal curvature (k_n) is concentrated at 3D nodes – an example is shown in Figure 4.17. Table 4.1 summarizes the repetition properties, and study the comparison with circular and conical meshes, the most popular torsion-free quad structures.

	Planar Quad meshes	**Circular/conical mesh**	**Quad Caravel mesh**	
Nodes			2D nodes	3D nodes
Horizontal angle	Variable	Variable	Variable	90°
Vertical angle	Variable	Variable	0°	Variable
Torsion angle	Variable	0°	0°	0°
Faces			Fold mesh	Structure mesh
Planarity	Planar	Planar	Planar	Non-planar
Beam-panel assembly				
Beam-panel angle	Variable	Variable	0°	

Table 4.1: Comparison of repetitivity between quad Caravel mesh other torsion-free quad mesh structures

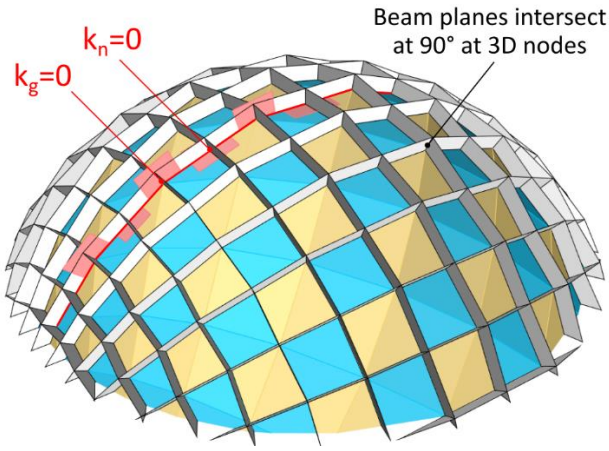

Figure 4.17: Mesh of revolution with torsion-free nodes and repetitive 3D nodes

4.4.3 Singularities

Quadrangular Caravel meshes have nodes of valence four and faces with four edges. However, singularities can be introduced, in which one node is not four-valent, or one face is not quadrangular. Singularities are topologically necessary for a pattern to cover a closed surface. They also allow to introduce significant curvature with limited distortion of the pattern. Singularities can be concisely described by the notion of *index*. Intuitively (see Figure 4.18, right), the index can be calculated as follows: looping around a singularity in the positive direction, a vector field aligned with one family of edges does not align with its starting orientation after a loop. The number of turns it did is called the index. A positive index most often occurs in synclastic surfaces, while negative indexes occur generally in anticlastic surfaces (see (Takens 1974) for a thorough treatment).

For quadrangular patterns, the index is always a multiple of ¼. Singularities of index k/4 with k>0 are shown in Figure 4.18. Because of the two-colorability constraints on the nodes, only indexes + ½ and +1 are possible for Caravel meshes. This constraint is also imposed by the fact that the mesh needs to be aligned with curvature lines: Singularities of curvature line networks (umbilics) always have an index which is a multiple of ½ (Gutierrez and Sotomayor 1998). For example, the mesh of revolution in Figure 4.19 would require a singularity +1 to close the middle hole.

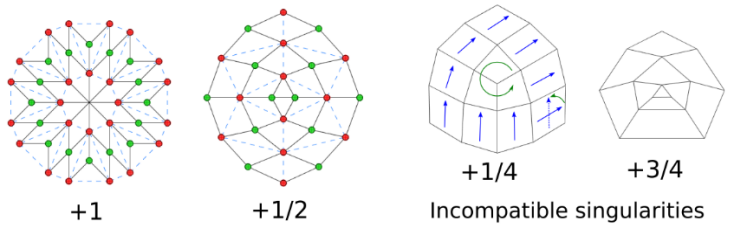

Figure 4.18: Singularities of a quadrangular Caravel meshes may only have an index +1 or +1/2

4.4.4 Generation

4.4.4.1 Mesh of revolution

The easiest quadrangular Caravel mesh to generate are meshes of revolution. For such meshes, one needs only to generate a proper strip of quads along a meridian. The degrees of freedom are shown in Figure 4.19, and can be chosen in this order: the angular width of the strip θ, the slope of the meridian at the base α, the lengths $l_1, l_2 \dots l_n$ of the exterior edges of the strip. The choice of these lengths will automatically define the curvature of the meridian. This method can be tedious for a designer because the degrees of freedom are not intuitive to control. However, it is a simple way to obtain the Caravel properties exactly. The 90° angle at 3D node can be obtained by this method by choosing proper values of $l_2, l_4 \dots l_{2k}$. For sake of concision, we will omit further details.

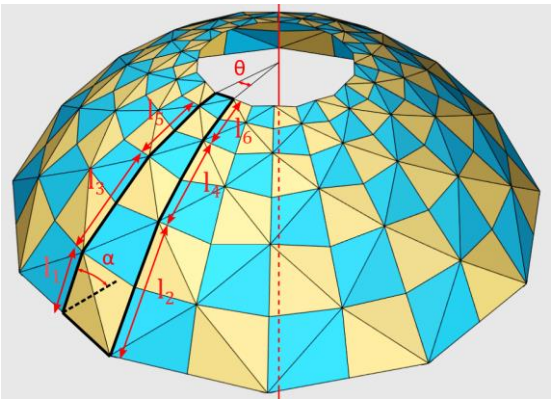

Figure 4.19: Degrees of freedom to generate a quad Caravel mesh of revolution

4.4.4.2 *From a synclastic surface*

Quadrangular Caravel meshes can also be generated from an arbitrary synclastic surface. The following steps may be performed:

i. Generate vector field of symmetrical conjugate directions;
ii. Integrate it to form a network of curves in two directions;
iii. Compute intersection points of this curve network: the intersection points are the 3D nodes, they define a fold mesh, in which faces are approximately planar;
iv. Construct planar nodes at the center of each face of the fold mesh;
v. Optimize the geometry so that it satisfies all the properties of a Caravel mesh, using for example the projection-based optimization framework described in (Deng *et al.* 2015).

This method is being implemented in a student project at Ecole des Ponts by Maureen Tricard and Raul Andrei Brebenaru. Figure 4.20 shows a quad Caravel mesh with 3D nodes intersecting at 90° generated from a curvature line network on a synclastic Monge surface. Geometrical properties are fulfilled with a remarkable precision. Preliminary explorations highlight the importance of respecting the metric constraint (4.1) in the initialization of the mesh to obtain a fair result.

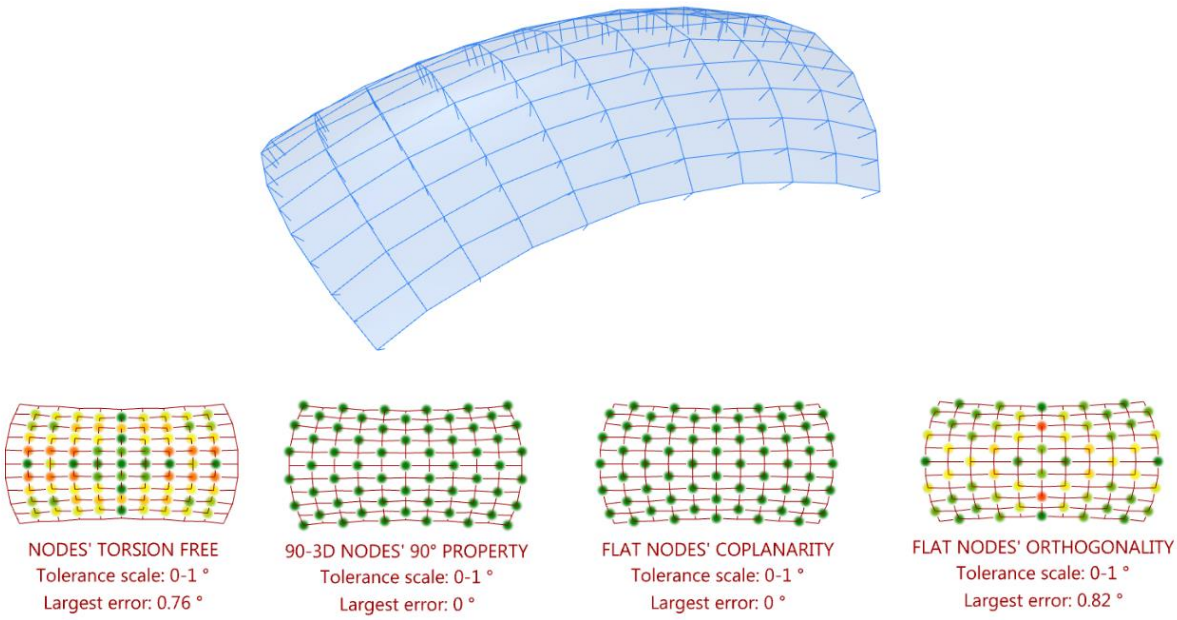

Figure 4.20: Caravel quad mesh generated from a synclastic surface (picture courtesy of Maureen Tricard and Raul Andrei Brebenaru)

4.5 Hexagonal Caravel meshes

One major drawback of Caravel quad meshes is that they do not allow negative curvature, and the spacing between beams is imposed by the ratio of the principal curvatures. Thanks to the lower valence of the nodes, hexagonal Caravel meshes (pattern (e) in Figure 4.13) do not suffer from this limitation, and their geometry is much less constrained. Their geometry and generation is therefore studied more in detail in this section. The geometrical structure of Caravel hexagonal meshes is summarized in Figure 4.21.

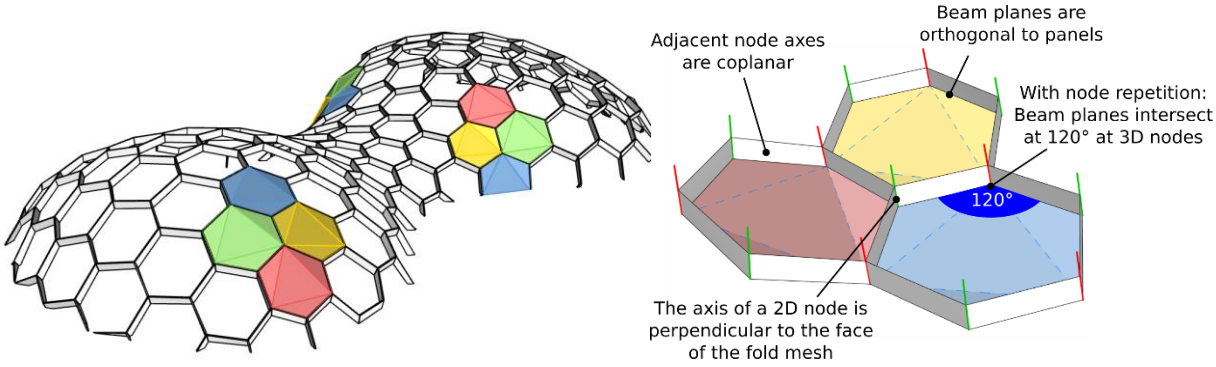

Figure 4.21: Left: A hexagonal Carvel mesh. Right: Geometrical properties

Hexagonal paneling

There exists a few examples of hexagonal panelling of curved envelopes in architecture, like the Eden Project gridshell in Cornwall (Figure 4.22), or the Landesgartenschau Exhibition Hall at the University of Stuttgart. Hexagons yield an aesthetic quite different from the more common quadrangular or triangular meshes. They are well suited to cover trapezoidal or triangular surface patches, like the one shown in Figure 4.4, for which quadrangular paneling would result in many face trimmings at the boundaries or uneven face sizes. The research on hexagonal paneling has focused mainly on face planarity (Troche 2008; Wang *et al.* 2008; Wang and Liu 2009; Li *et al.* 2015; Vaxman and Ben-chen 2015). However, a major drawback of planar hexagon meshes is that faces are necessarily non-convex (shaped like bow-ties) when curvature is anticlastic, as shown in Figure 4.23. This causes poor mechanical performance for a gridshell, and arguably strange aesthetic. Caravel hexagon meshes, because their faces are not planar, do not suffer from this limitation, as can be seen in Figure 4.21.

Figure 4.22: The hexagonal gridshell of the Eden Project in Cornwall, England (picture in public domain)

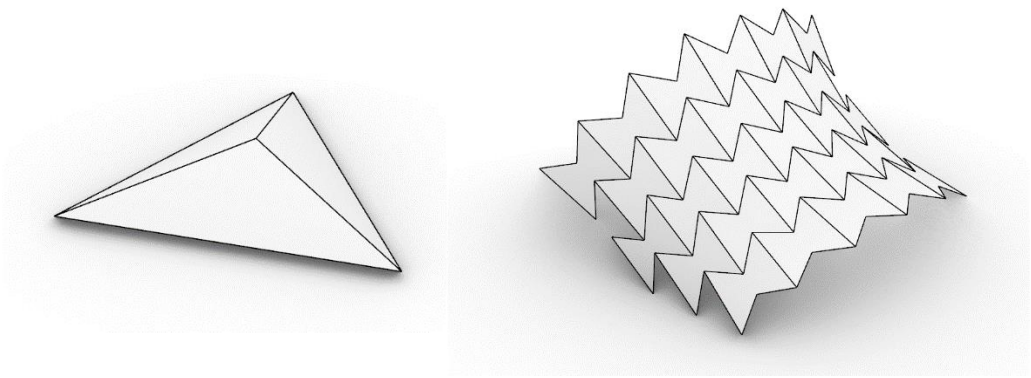

Figure 4.23: A 3-valent node with incident angles below 180° is necessarily convex, and can therefore only be found on a synclastic surface. As a result, nodes of an anticlastic mesh with planar hexagons have one angle above 180°: faces are necessarily non-convex.

4.5.1 Asymptotic construction

As in section 4.4.1 for quad Caravel meshes, we study in this section the behavior of hexagonal Caravel mesh in the asymptotic case. We obtain the following results:

Asymptotic behavior:

- Any smooth surface can be approximated by a hexagonal Caravel mesh (even though the presence of umbilics might result in some pattern discontinuities, singularities will be discussed in section 5.4);
- A hexagonal Caravel mesh can be constructed from a planar hexagonal (PHex) mesh.

The proof will be detailed in the following three subsections, 4.5.1.1 to 4.5.1.3.

4.5.1.1 Preliminary: Designing a gridshell on a surface which is torsion-free at the first order

Contrary to quad meshes, hex meshes do not tend towards a surface parametrization at the limit, so we start by introducing a geometrical method to design grids on a surface which are torsion-free at the first order.

The Gauss map

Let us start by recalling some elementary concepts of surface geometry. Let us consider a point P on a smooth surface, as shown in Figure 4.24. The unit normal at P, called the Gauss map of P, $n(P)$, can be described by a point on the unit sphere. Considering a small displacement u on the surface, P + u is at the first order included in the tangent plane at P, T_P. The variation of the normal from P to P + u is at the first order a vector of the tangent plane of the sphere at n(P). We identify this tangent plane to T_P. The variation of the normal at P is given by the second fundamental form of the surface. This form can be expressed as a linear map on T_P:

$$dn(u) = -\begin{bmatrix} k_1 & 0 \\ 0 & k_2 \end{bmatrix} \begin{pmatrix} u_1 \\ u_2 \end{pmatrix}$$

where u $= u_1 e_1 + u_2 e_2$ is the decomposition of u in the basis of principal curvature directions (e_1, e_2) of T_P. The second fundamental form can be interpreted as a combination of two 1D-scalings, respectively in the directions e_1 and e_2, with factors $-k_1$ and $-k_2$.

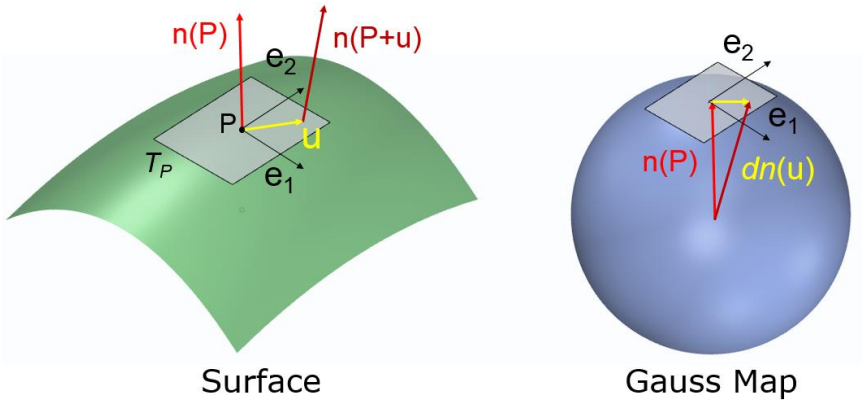

Figure 4.24: Gauss map of a smooth surface

First-order periodicity

All the planar patterns shown in Figure 4.13 are *periodic*: there exist non-colinear vectors t_1 and t_2 such that the pattern is invariant under a translation by t_1 or t_2.

When covering an arbitrary surface with one of these patterns, they cannot be geometrically periodic anymore because of the variations of metric on the surface (the combinatorics is still periodic though). However, in the limit case where the face size is much smaller than the curvature radii of the surface and pattern, the pattern is locally periodic at the first order in the tangent plane of the surface. The Gauss map of the pattern is then also locally periodic, with period $dn(t_1)$ and $dn(t_2)$.

Torsion-free grids at first order

Let us now consider a grid of beams based on a periodic pattern in this first-order limit case. If the node axes coincide with the surface normals, the geometrical torsion can be assessed by looking at whether beams are parallel with their Gauss map. More precisely, the torsion of the surface normal along the beam is the tangent of the angle between an edge and its Gauss map. This is illustrated in Figure 4.25. The mesh on the top-left is aligned with curvature directions, and has therefore no torsion: $dn(t_1) \parallel t_1$. The mesh on the bottom left is not aligned with curvature direction. As a result, $(dn(t_1), t_1) = \alpha \neq 0$, and the torsion along the mesh is $\tau_g = \tan \alpha$ (expressed in rad/m). The only way to obtain a torsion-free structure is then to align all the edges with curvature directions, which is quite restrictive. This is the strategy used for quad Caravel meshes.

However, there is much more design freedom if we allow the node axes to deviate from surface normals. This is illustrated in Figure 4.25 (right) for an octo-quad pattern. If axes coincide with surface normals, beams of the diamonds undergo a torsion proportional to α. Now, axes can also be chosen such that beams are parallel to their Gauss map (thus yielding a torsion-free structure) *and* such that the Gauss map pattern still has periods $dn(t_1)$ and $dn(t_2)$. This is illustrated in Figure 4.25 at the bottom-right. The second property allows to keep the angle between the node axes and the surface normals to the first order. Without is, the axes would deviate more and more from the surface normals as we move away.

In order to differentiate node axes from surface normals, we will use a capital N for the former, and a lowercase n for the latter.

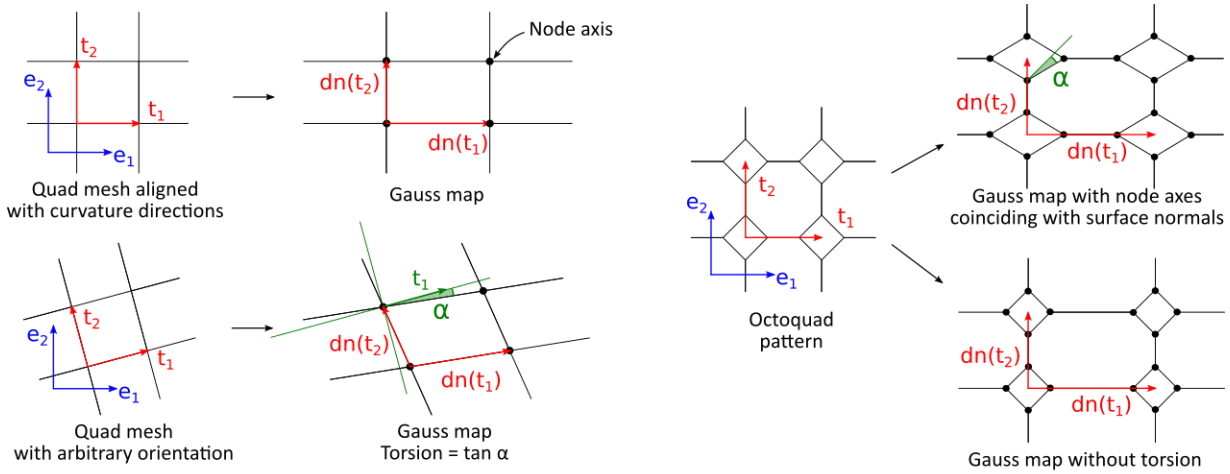

Figure 4.25: Understanding torsion free patterns with the Gauss map. Left: A quad pattern is torsion free only if it is aligned with principal curvature directions. Right: An octo-quad pattern can be made torsion-free even if some edges are not aligned with principal curvature direction by allowing node axes to deviate from surface normals

4.5.1.2 Construction of Caravel hexagonal meshes on a smooth surface

The strategy that we just described to generate torsion-free gridshells can be used to obtain hexagonal meshes with Caravel properties at the first-order from a mesh with planar hexagons.

Step 1: Construction of a PHex mesh

Any smooth surface can be approximated by a PHex mesh. There are locally two degrees of freedom in the orientation of a PHex hexagonal pattern (Wang and Liu 2009), for example directions S_1 and S_2 in Figure 4.26 (edges directions e_i are conjugate to strip directions S_i). As illustrated in Figure 4.27 (left), when face size tends to zero, each hexagon tends to be planar, congruent to its neighbor, to have central symmetry and to be inscribed in a homothetic copy of the Dupin indicatrix (Wang and Liu 2009) – the Dupin indicatrix being the conic resulting from the intersection between the paraboloid and the plane z=1. As shown in Figure 4.27 (right), the surface Gauss map of the Dupin indicatrix is also a conic, with equation $\frac{x^2}{k_1} + \frac{y^2}{k_2} = 1$.

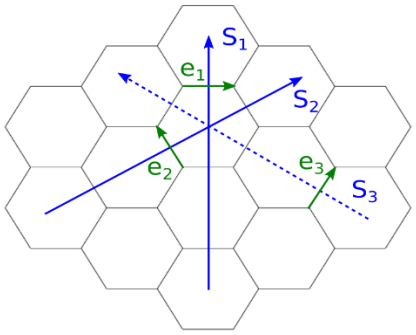

Figure 4.26: Asymptotical structure of a planar hexagon mesh approximating a surface

Step 2 : Construction of staggered hex grid

Once a PHex mesh is drawn on the surface, the 2nd step is to build a staggered grid. Such a grid is shown in red in Figure 4.27. It is built by combining half of the points of the PHex mesh (e.g. A,C and E) and one point inside each hexagon (e.g. P). This point is *on* the plane ACE, not on the surface – this is a second order nuance.

As proven in the following subsection, whatever the orientations of the hexagons, it is possible to find center points (for example P, Q and R in Figure 4.27) such that all the Caravel properties (see definition in section 4.3.5) are fulfilled:

(a) There exist node axes N_P, N_Q... such that the grid is torsion-free (this is insured by parallelism of edges with their Gauss map, for example $PE \parallel N_P N_E$).
(b) P, Q, R are located on the planar hexagons, and are therefore planar nodes (for example $P \in (ACE)$);
(c) The normal at P, N_p is perpendicular to the face ACE;

A, C, E are the 3D nodes (there is no geometrical constraint associated to them).

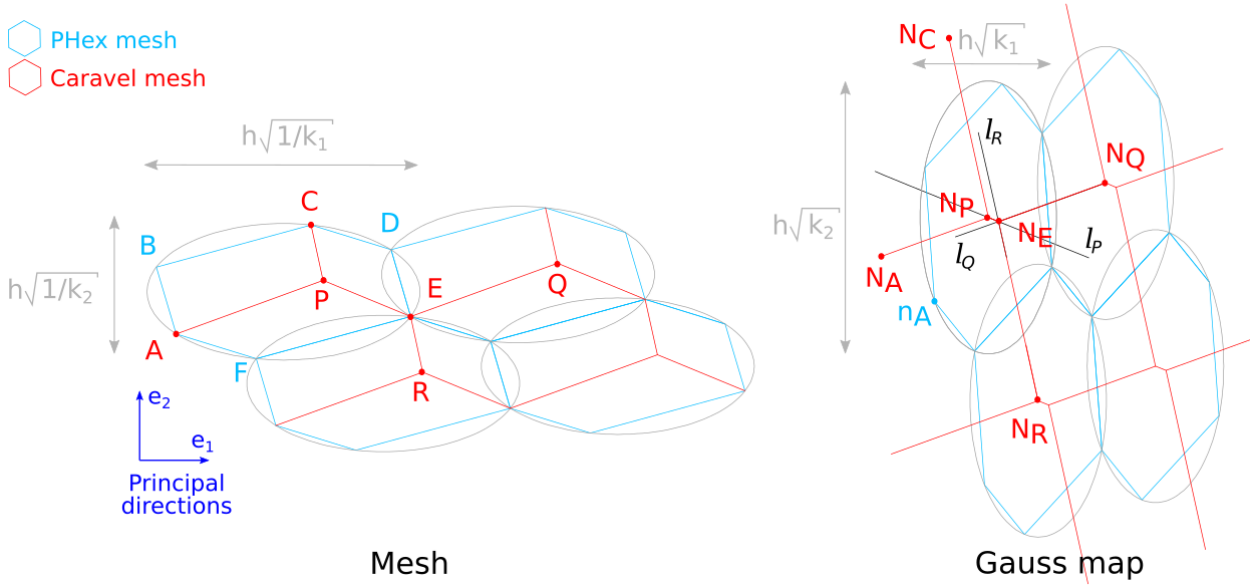

Figure 4.27: Asymptotic construction of a hexagonal Caravel mesh from a mesh of planar hexagons (left). Right: Gauss map

4.5.1.3 Proof of the first order constructability

We will now show how a hexagonal Caravel mesh can be constructed at the first order from a PHex mesh with infinitely small face sizes inscribed in a smooth surface. By "infinitely small", we mean much smaller than both surface curvature radii and curvature radius of pattern. We refer to Figure 4.27. The key is to find the position of vertex P inside a PHex face: this is done in the third part.

Property (b): Planar "Planar nodes"
This property is verified by constructing points P, Q and R on the faces of the PHex mesh.

Property (c): Axes at planar nodes normal to the plane of the node
Because of the central symmetry of hexagon (ABCDEF), the normal to the plane (ACE) coincides with the surface normal at the center of the indicatrix. On the Gauss map, this normal is the center of the conic. Property (c) is obtained by locating the normal N_p precisely at this center.

Property (a): Torsion-free structure

Analysis of the constraints
Let us assume we have a point P fulfilling conditions (a) to (c). We recall that in our asymptotic model, adjacent hexagons are congruent. In particular, $\overrightarrow{AP} = \overrightarrow{EQ}$: the position of Q and R is function of the position of P.

Let us build the lines l_P, l_Q, and l_R where l_P (resp. l_Q, l_R) is the line parallel to (PE) (resp. (QE) and (RE)) passing through N_P (resp. N_Q, N_R). For the structure to be torsion-free, these lines need to be concurrent in a point N_E. The condition $N_E \in l_p$ can be expressed as:

$$N_E = N_P + \lambda \overrightarrow{EP}$$

With λ a real number. Since N_E also belongs to l_Q:

$$\overrightarrow{N_Q N_E} \wedge \overrightarrow{QE} = 0$$

$$(\overrightarrow{N_Q N_P} + \lambda \overrightarrow{EP}) \wedge \overrightarrow{PA} = 0$$

We take the dot product of this quantity with N_P (which is the normal to the plane ACE). We obtain the value of λ as a function of mixed products that depend on the position of P:

$$\lambda = \frac{[\overrightarrow{N_Q N_P}, \overrightarrow{PA}, \overrightarrow{N_P}]}{[\overrightarrow{PE}, \overrightarrow{PA}, \overrightarrow{N_P}]} \tag{4.3}$$

Finally, N_E also belongs to l_R:

$$\overrightarrow{N_R N_E} \wedge \overrightarrow{ER} = 0 \tag{4.4}$$

$$\lambda = \frac{[\overrightarrow{N_R N_P}, \overrightarrow{PC}, \overrightarrow{N_P}]}{[\overrightarrow{PE}, \overrightarrow{PC}, \overrightarrow{N_P}]}$$

Combining equations (1) and (2), we obtain the following condition necessarily fulfilled by P for a point N_E incident to the three lines l_P, l_Q, and l_R to exist:

$$[\overrightarrow{N_Q N_P}, \overrightarrow{PA}, \overrightarrow{N_P}][\overrightarrow{PE}, \overrightarrow{PC}, \overrightarrow{N_P}] = [\overrightarrow{N_R N_P}, \overrightarrow{PC}, \overrightarrow{N_P}][\overrightarrow{PE}, \overrightarrow{PA}, \overrightarrow{N_P}]$$

Synthesis

The above equation is a cubic equation in which the only unknown are the coordinates (x, y) of point P. For any given x_0, we can find at least one solution (x_0, y) in y (a cubic equation of one variable always has at least one root). Doing the reasoning of the "analysis" part upwards, for a solution P of the cubic equation, the lines l_P, l_Q and l_R are concurrent, and the structure is therefore torsion-free.

As a conclusion, the construction showed in Figure 4.27 is always possible. The hexagonal network (in red) along with the attached normals described by the hexagonal mesh on the Gauss map (also in red) verify all the properties of a Caravel mesh. This construction is made possible by allowing the node axes to deviate at the 1st order from the surface normal.

4.5.2 Node repetition

Similarly to quad Caravel meshes, repetition can be introduced in the 3D nodes by setting the horizontal angles between beams at 120° for each 3D node. The asymptotic construction described in the previous section does not yield this property in general. It is however still possible to obtain it from an arbitrary smooth surface:

Asymptotic behavior:

- Any smooth surface can be approximated by a hexagonal Caravel mesh with the "120°" node repetition (umbilics might lead to pattern discontinuities);

- One family of edges and the associated diagonals (for example e_1 and S_1 in Figure 4.26) tend to be aligned with principal curvature directions;

We will prove this by a construction in two steps:

Step 1: Construction of a principal PHex mesh
The first step is to construct a PHex mesh aligned with principal curvature directions. Referring to Figure 4.26, this means that there is a direction i such that e_i and S_i are principal curvature directions. Each hexagon is then symmetric with respect to the principal curvature directions (the axes of the Dupin indicatrix). The Gauss map of the hexagons has the same symmetry.

Step 2: Construction of staggered hex grid from Fermat points
Referring to Figure 4.28, we pick three vertices on a hexagon ABCDEF to form a triangle ACE. We build the Fermat center P of ACE, i.e. the point such that $(\overrightarrow{PA},\overrightarrow{PC}) = (\overrightarrow{PC},\overrightarrow{PE}) = (\overrightarrow{PE},\overrightarrow{PA}) = 120°$. P will be a flat node of the mesh, and A,C and E will be 3D nodes (incident edges at 3D nodes also have 120° angles because of the symmetries). As discussed in the previous section, the node axis at P, N_P, is at the center of the Gauss map of the Dupin indicatrix. It may not coincide with the surface normal at P, n_P. We also build the Fermat points of the adjacent hexagons, Q and R, and their node axes.

We then build on the Gauss map the lines l_p, $l_Q$and l_R, which are respectively the lines parallel to (PE), (QE) and (RE)) passing through N_P, N_Q and N_R. We observe that, thanks to the symmetry of the Gauss map, the lines l_P, l_Q and l_R are concurrent. The point of concurrency gives the node axis at E, N_E.

The hexagonal network (in red) along with the attached normals described by the hexagonal mesh on the Gauss map (also in red) verify all the Caravel properties and also have a 120° angle between the beam planes of the 3D nodes. We remark that this construction is also valid for surfaces with negative curvature, as illustrated in the right part of Figure 4.28 (with $k_2 < 0$, so the Gauss map is "inverted" in direction 2). In particular, the process yields convex hexagons, whereas the PHex mesh used as a basis has "bow-tie" shaped hexagons.

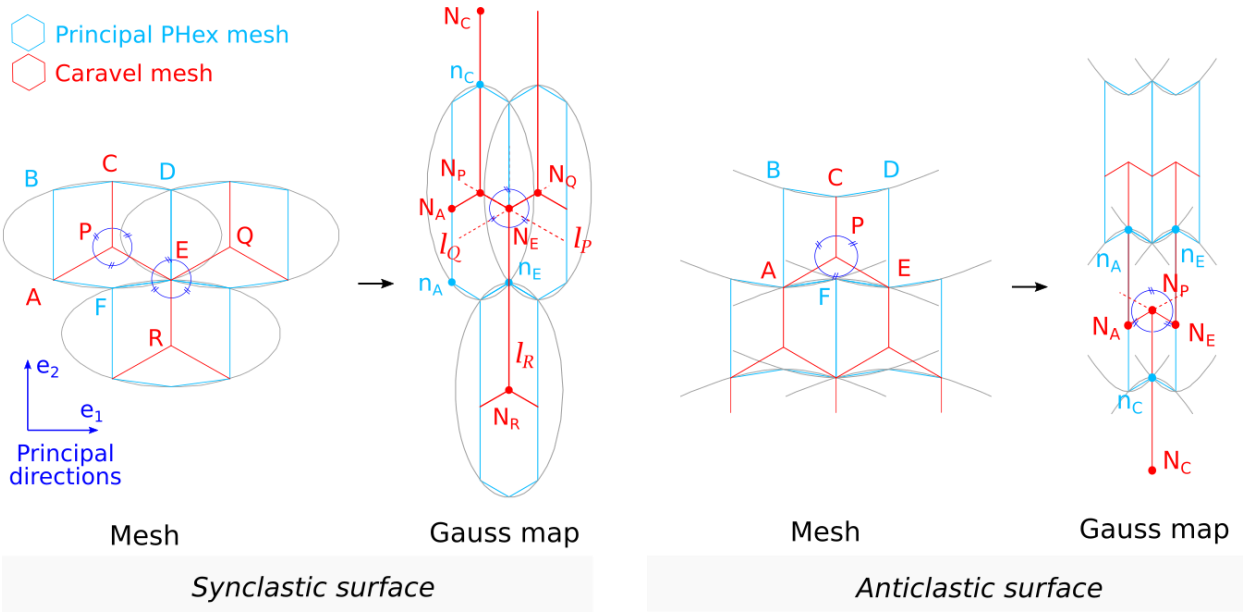

Figure 4.28: Asymptotic construction of a hexagonal Caravel mesh with 3D nodes at 120°

4.5.3 Combining node repetition and edge offset

As discussed in the introduction, having a mesh with an edge offset offers remarkable fabrication possibilities. Figure 4.29 (left) shows a counter-example: the three beams have different vertical angles, such that kinks are observable at the top and bottom of the node.

It is possible to construct hexagonal Caravel meshes with both edge offset and the 120° node repetition strategy. We remark that the 2D nodes are already perfect, as the vertical angle is 0° for each beam. Making a 3D node perfect imposes a strong symmetry on the node: the horizontal angle between beams is constant (120°), and the vertical angle is also constant, up to a -1 factor. Examples of 3D nodes with edge offset and 120° in plane angles are shown in Figure 4.29, both with positive and negative curvature.

These properties strongly constrain the Gauss mesh. Indeed, the Gauss map of a 3D node verifies the following properties:

- Because of the 120° horizontal angle and the torsion-free property, the spherical angles between the Gauss map of the edges is also 120°;
- Since the vertical angles are equal, the distance between the Gauss image of a 3D node and Gauss images of the adjacent 2D nodes is constant.

Combining these two properties together, the Gauss images of three 2D nodes adjacent to a given 3D nodes form an equilateral triangle if curvature is positive (triangle $N_1N_2N_3$ in Figure 4.29, middle bottom). If curvature is negative, they form an isosceles triangle, in which the height at the apex is half of the length of the two equal edges – the 3D node is then outside of this triangle (Figure 4.29, right bottom). We remark that, because faces of Caravel meshes are not planar, the Gauss image is not a Koebe polyhedron, contrary to the previous studies of edge offset meshes in the literature (for example (Pottmann *et al.* 2010)). Gauss map for surfaces with positive and negative curvature are shown in Figure 4.30.

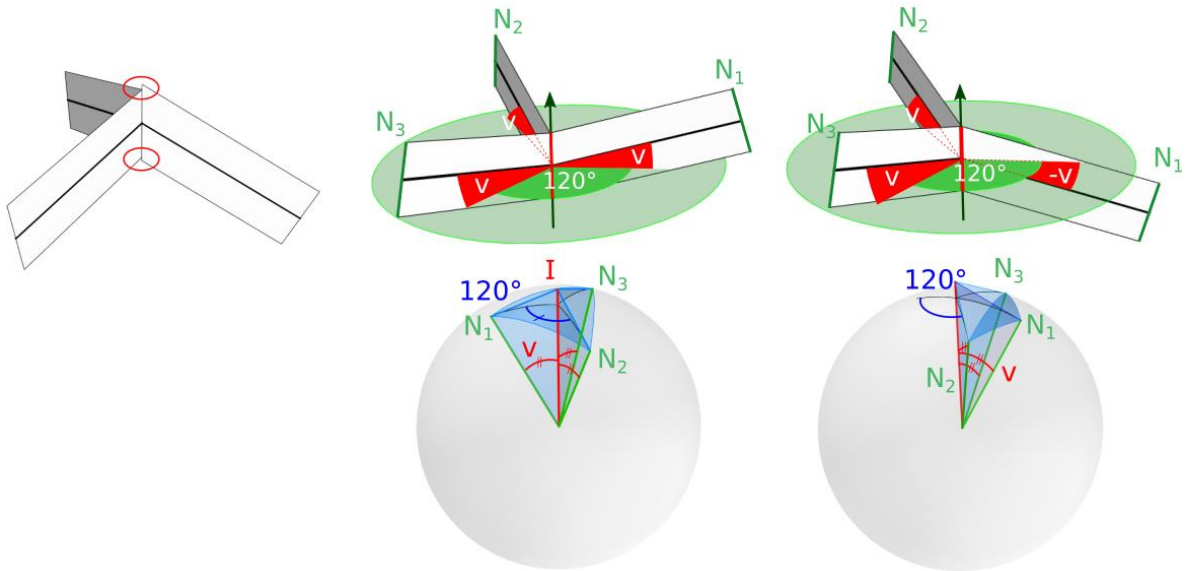

Figure 4.29: Left node: Non perfect node. Middle and right: Perfect nodes with 120° horizontal angle, with positive (middle) and negative (right) curvature. Bottom: corresponding Gauss map.

Because of this structure of the Gauss map, the geometry of hexagonal gridshells with edge offset is highly constrained. This is best understood by, again, looking at the asymptotic case. In that case, as discussed in section 4.5.1.3, the mesh tends to be aligned with principal curvature directions of an underlying surface S. We can then parametrize the surface by curvature lines with a function $(u, v) \mapsto x(u, v)$ such that the

ratio of metrics in principal directions corresponds to the aspect ratio of the hexagons, as shown in Figure 4.30.

Synclastic surfaces

If curvature is positive, the fact that the Gauss mesh is built from equilateral triangles (shown in green) yields:

$$\|n_u\| = \|n_v\| \tag{4.5}$$

Curvature in directions u and v are then given by:

$$k_1 = \frac{\|n_u\|}{\|x_u\|} \; ; \; k_2 = \frac{\|n_v\|}{\|x_v\|}$$

We obtain:

$$\frac{\|x_u\|}{\|x_v\|} = \frac{k_2}{k_1}$$

This equation can be directly compared with equation (4.2). Similarly to quad meshes, the aspect ratio of the hexagons (the ratio $\|x_u\|/\|x_v\|$) is imposed by the curvature of S. However, this aspect ratio is now proportional to k_2/k_1 instead of $\sqrt{k_2/k_1}$. Therefore, a much higher variation of aspect ratio is required to mesh non-spherical surfaces. If one wants to design a grid with an aspect ratio close to 1 ($\|x_u\| \simeq \|x_v\|$), one is restricted to near-spherical surfaces ($k_2 \simeq k_1$).

Furthermore, equation (4.5) implies that we can find a parametrization by curvature lines on S for which the Gauss map is conformal. For this parametrization to exist, the surface has to belong to the family of so-called "L-isothermic surfaces" (Blascke 1929; Pottmann *et al.* 2007), so meshing an arbitrary surface is not possible.

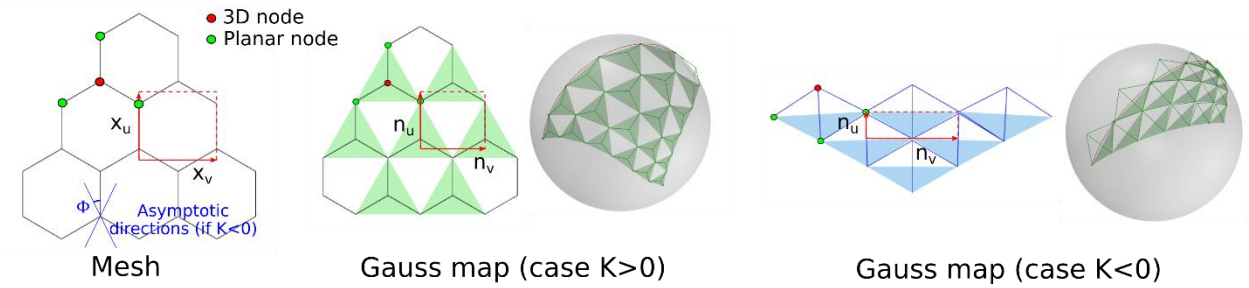

Figure 4.30: Gauss map of hexagonal Caravel mesh with edge offset

Anticlastic surfaces

If Gaussian curvature is negative, we have $k_2 < 0 < k_1$. Basic trigonometry yields (Figure 4.30, right):

$$\|n_u\| = \frac{1}{2\sqrt{3}}\|n_v\|$$

Therefore:

$$\frac{\|x_u\|}{\|x_v\|} = -\frac{1}{2\sqrt{3}}\frac{k_2}{k_1}$$

To design a grid with an aspect ratio close to 1, we now need the surface to verify $k_2 \simeq -2\sqrt{3}k_1 \simeq -3.5k_1$. That is, the surface is both isothermic and close to a Weingarten surface $2\sqrt{3}k_1 + k_2 = 0$ in which the ratio of principal curvature is a constant. This type of surface was recently studied in (Jimenez *et al.* 2019). One

of their particularity is that the angle 2Φ between asymptotic directions is constant, and given by $tan^2\Phi = -\frac{k_1}{k_2} = \frac{1}{2\sqrt{3}}$ which gives $2\Phi \simeq 56°$ (Figure 4.30 left).

4.5.4 Singularities

As for the case of quad Caravel meshes discussed in section 4.4.3, not all types of singularity are possible in a hexagonal mesh. As shown in Figure 4.31, singularities in hexagonal meshes have an index k/6. In order to keep the two-colorability of the nodes in the pattern, the index must be k/3 (otherwise, a rupture of the pattern would be visible along a line). Four configurations of interest are shown in Figure 4.31. Singularities are more constrained for a Caravel mesh with the 120° node repetition strategy, because these must be aligned with principal curvature directions. As a consequence, only indexes that are multiple of 1/2 and 1/3 are possible, i.e. indexes +1 and -1. These two types of singularity require a high variation of the metrics of the pattern.

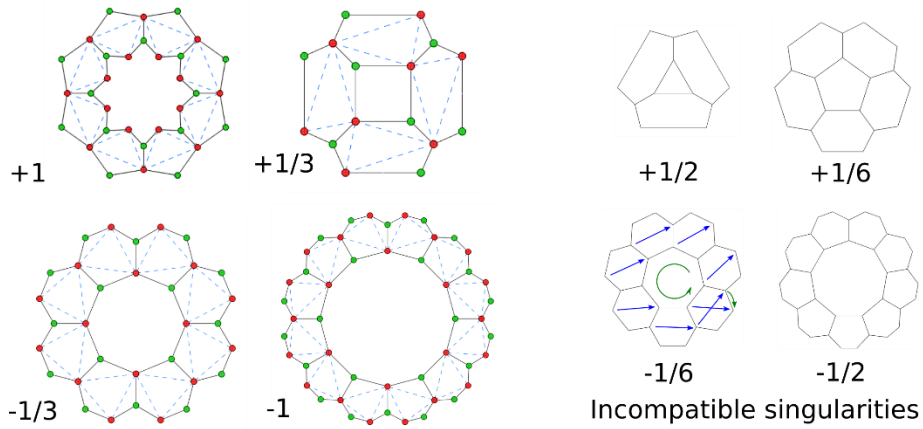

Figure 4.31: Allowable singularities of hexagonal Caravel meshes and their index. Only singularities of index +1 and -1 are compatible with the 120° node repetition strategy

4.5.5 Generation

4.5.5.1 General case

General hexagonal Caravel meshes can be generated from an arbitrary surface:

i. Generate a PHex mesh on the surface, for example following (Wang *et al.* 2008).
ii. Construct a staggered grid as in Figure 4.27:
Construction of 3D nodes: extract every other node of the PHex mesh;
Construction of planar nodes: locate one point inside each hexagon.
iii. Optimize the geometry so that it satisfies all the properties of a Caravel mesh, using for example the projection-based optimization framework described in (Deng *et al.* 2015).

4.5.5.2 Node repetition

In order to obtain the 120° node repetition, the initial mesh must follow the curvature directions of the surface. The construction steps can be decomposed as follows:

i. Generate a hexagonal network aligned with principal curvature directions (for example, in Figure 4.26, align directions e_1 and S_1 with principal curvature directions).

ii. Construct a staggered grid as in Figure 4.28:
Construction of 3D nodes: extract every other node of the hexagonal mesh;
Construction of planar nodes: construct the Fermat center the triangles formed by the 3D nodes.

iii. (as in the general case) Optimize the geometry so that it satisfies all the properties of a Caravel mesh, using for example the projection-based optimization framework described in (Deng *et al.* 2015).

If the target surface has umbilics, the pattern may have discontinuities. This method was implemented numerically by Mathieu Lerouge during his Master's thesis at Ecole des Ponts (Lerouge 2019).

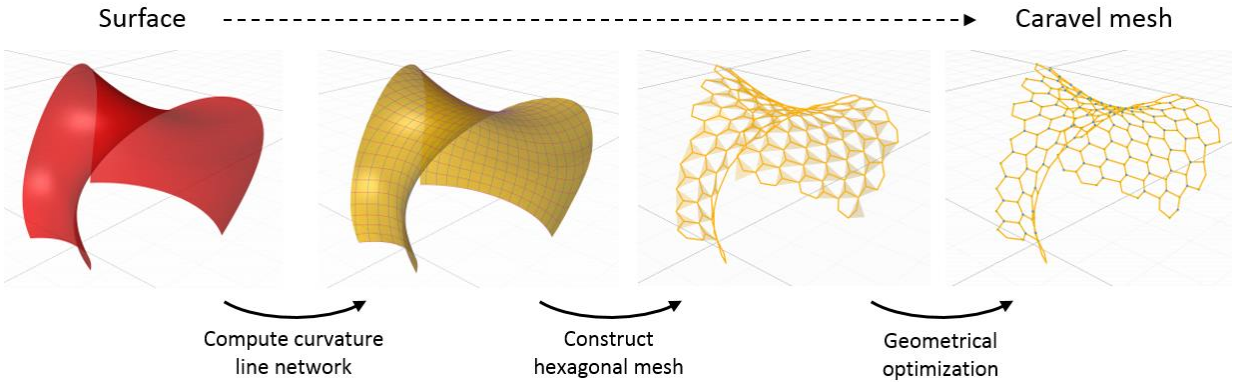

Figure 4.32: Workflow to generate a Caravel mesh with node repetition (numerical images courtesy of Mathieu Lerouge)

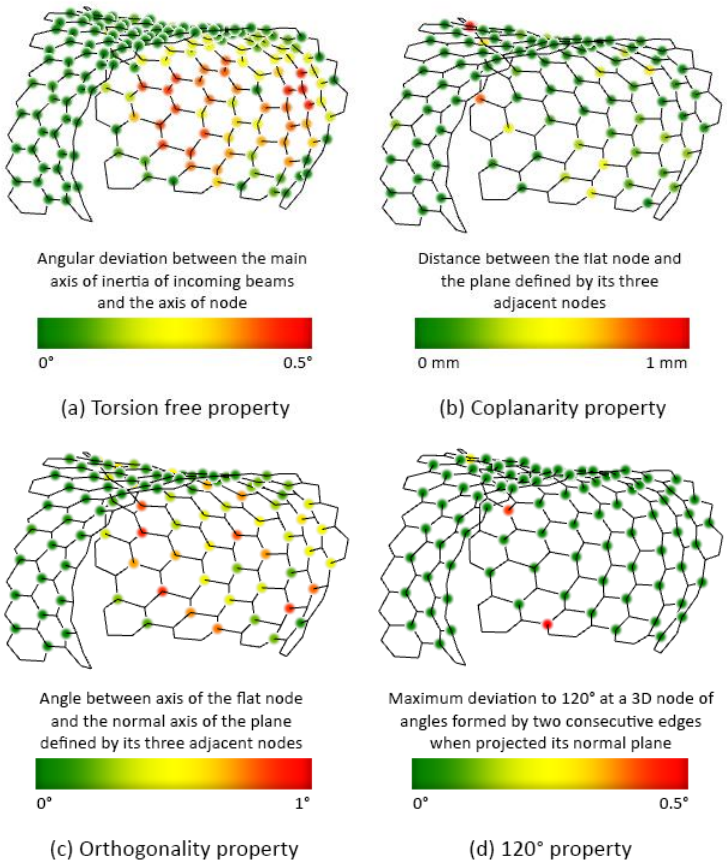

Figure 4.33: Fulfillment of Caravel properties for the heX-mesh Pavilion (image courtesy of Mathieu Lerouge)

4.5.5.3 Node repetition and edge offset

Because of the particular structure of their Gauss map, hexagonal Caravel meshes with edge offset cannot be generated on a random surface. We propose a generation method adapted to their geometry that starts from the construction of a valid Gauss map. This is a similar approach to the construction of planar quad meshes with edge offset from a Koebe polyhedron proposed in (Pottmann *et al.* 2007).

The Gauss map of a synclastic surface is conformal, and would be best constructed using tools from discrete differential geometry on that topic. However, things are much more complicated for a surface combining both synclastic and anticlastic portions. As illustrated in chapter 5, a fold appears on the Gauss map. This fold connects a portion of positive curvature with $\|n_u\| = \|n_v\|$ to a portion of negative curvature with $\|n_u\| = \frac{1}{2\sqrt{3}}\|n_v\|$. There is no existing numerical tool to handle this. We therefore propose a propagation method from a user-defined row of points.

We start by remarking that, in the case K>0, meshes of equilateral triangles can be controlled by the position of vertices along a line, as shown in Figure 4.34: If the position of the red nodes is known, the position of all the other vertices is entirely determined (for example, the position of C is entirely determined by the position of A and B). We can then build the Fermat points and obtain a hex mesh with 120° property. The same result holds if K<0.

Change of curvature sign (fold on the Gauss map) can be easily handled between two rows of hexagons. An example is shown in Figure 4.34, where the first two rows at the bottom have a positive curvature, while the top two rows have a negative curvature, and are therefore built downwards.

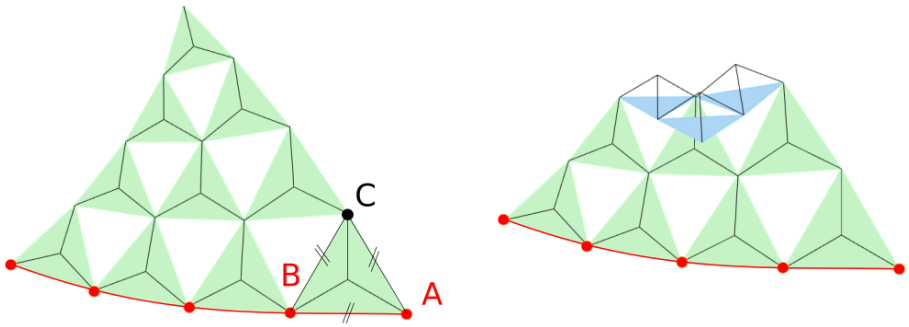

Figure 4.34: Construction of a valid Gauss map from a row of points (in red). Left: K>0 everywhere. Right: K>0 for the bottom two rows, K<0 for the top two rows (in blue).

The hexagons can then be deformed by a *Combescure transform*. A Combescure transform, also called parallel transform, modifies edge lengths while keeping fixed the orientation of edges and faces. These can be controlled by the lengths of some boundary edges, as done in (Mesnil *et al.* 2015). The proposed degrees of freedom are shown in Figure 4.35.

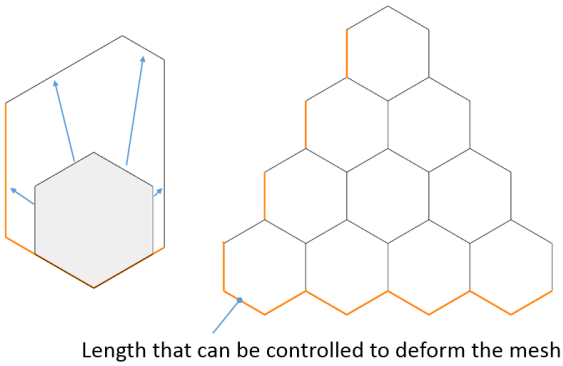

Figure 4.35: Deformation of the Gauss mesh by Combescure transform

We can then generate edge offset meshes with the following method:

i. Explore meshes of equilateral triangles by drawing rows of points on the sphere, and trying out changes of curvature at different rows;
ii. Build the tangent planes to the unit sphere at the planar nodes. For each equilateral triangles, the tangent planes at the vertices intersect at a point which is aligned with the sphere center and the Fermat point of the triangle, and thus has the 120° angle between beam planes. This intersection point is therefore a planar node. We postpone the proof to the end of the section.
iii. Deform the mesh by Combescure transform by varying the edge lengths along the boundary.

Examples of structures designed with this method are shown in Figure 4.4 and Figure 4.36.

Limitations

Some trials and errors are often needed to construct an interesting Gauss map without self-intersecting faces.

Proof of the construction in step ii

Let us consider a spherical equilateral triangle $N_1N_2N_3$ (Figure 4.29), the tangent planes at the vertices, and the intersection point I of these three tangent planes. I is equidistant to the vertices : $IN_1 = IN_2 = IN_3$. It is therefore aligned with the sphere center and the circumcenter of the triangle. Since the triangle is equilateral, the circumcenter coincides with the Fermat center.

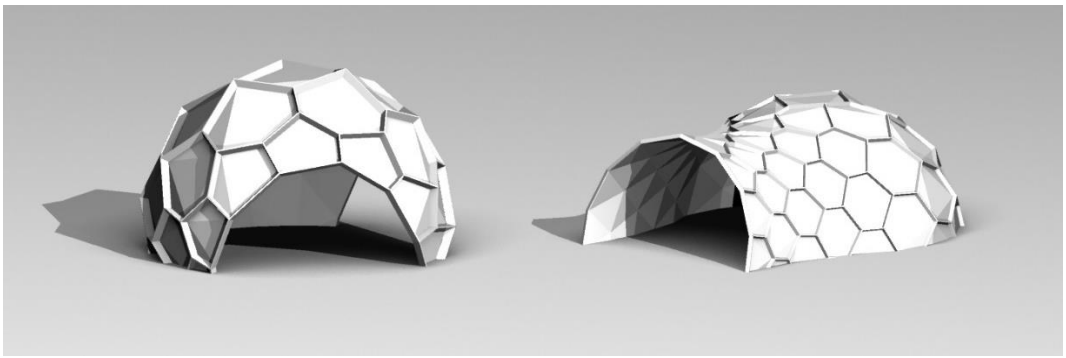

Figure 4.36: Structures based on Caravel meshes with exact edge offset and node repetition

4.6 Applications

Caravel meshes were introduced to simplify all the connections of a gridshell. There are many ways to take advantage of their geometrical properties. We will suggest here a few applications.

4.6.1 Structural beam-panel connection

Since panels lay flat on the top beam surface, the connection between beams and panels can be structural – for example bolted or nailed. This connection can be used to design various structural systems.

Gridshell braced by panels
Panels can be used as bracing elements for the beams. In that case, diagonal cables or moment connection are not needed anymore, thus lowering the cost of the structure.

Gridshell with beams reinforced by panels
Panels can also be used to strengthen the beams. For example, in the heX-Mesh pavilion showed in Figure 4.39, the panels on top and bottom restrain the beams from buckling in their weak direction.

Double-layer shell
If panels are the load carrying elements, our geometry allows to connect two layers. Beams can then transfer the shear forces between the top and bottom layer, and give a significant bending strength to the shell. The hexagonal Caravel mesh with edge offset (section 4.5.3) is particularly adapted for this application, as the two layers of panels can be connected with beams of constant height (the same beam section can be used throughout the structure). This is illustrated in Figure 4.37. Without edge offset, panels cannot be fitted on both sides because of kinks at the 3D nodes (as shown in Figure 4.29).

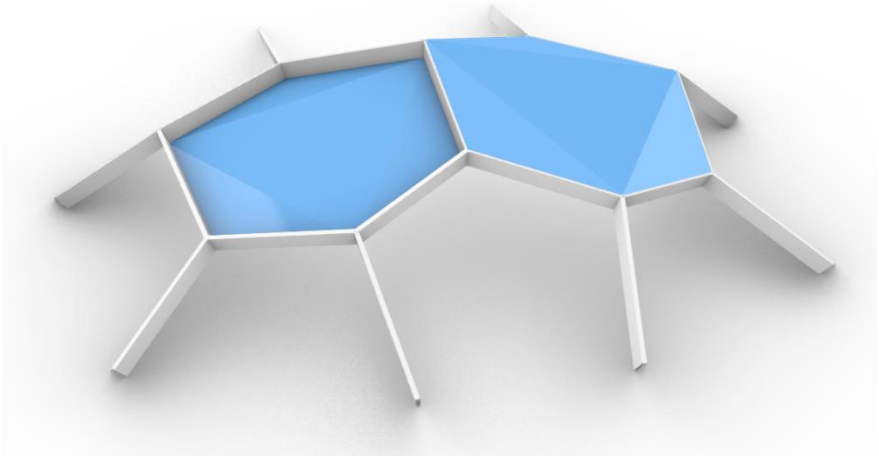

Figure 4.37: With edge offset, panels can be located on top and bottom of beams of constant section

4.6.2 Use fold mesh for paneling

The application of Caravel meshes described in sections 2 and 4 deals with folded panels for which the boundaries coincide with the beams. However, since the fold mesh has planar faces, it can be constructed from planar panels. In that case, the torsion-free beam structure does not coincide with the panel edges anymore. An example is shown in Figure 4.38. This system still offers many geometric properties useful for rationalization:

- Beams are orthogonal to panels,
- 2D nodes are planar,
- 3D nodes intersect at 90°,
- No torsion at nodes.

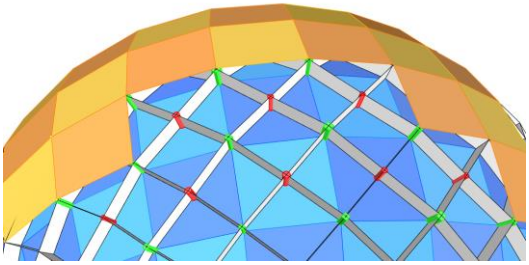

Figure 4.38: Laying flat panels on the fold mesh, another way to use Caravel meshes for rationalization

4.6.3 Rationalization of nodes

The geometrical properties of Caravel meshes can be used in many different ways to rationalize the fabrication of the nodes of a gridshell. The potential has been demonstrated by the fabrication of two pavilions.

4.6.3.1 Caravel heX-Mesh pavilion

The Caravel heX-Mesh pavilion, showed in Figure 4.2, demonstrates one way to use the many geometrical properties of Caravel meshes to produce an expressive double-curvature shape with limited fabrication complexity. The optimization setup implemented by Mathieu Lerouge (section 4.5.5.2) was used by architecture students to design a structure for the 2019 IASS lightweight pavilion contest (Lerouge 2019; Tellier *et al.* 2019). The project gathered researchers at the Navier laboratory, students and professor at the school of architecture ENSA Paris-Malaquais, steel contractor Viry, and the LAMA laboratory.

The geometry of the pavilion is a hexagonal Caravel mesh with 120° node repetition. The structure is composed of laser-cut aluminum sheets, bolts and standard stamped 120° connectors. One family of plates acts as beams, and is located between node axes. Connection details are showed in Figure 4.39. As plates are weak in bending, they are reinforced on their top and bottom faces by orthogonal plates, also laser-cut. The 90° angle between panels and beams allows a connection by inserts and slits that can be carved by laser (the laser cuts only at a right angle). The 120° is used to design a standard 3D node, realized from a thick aluminum plate which is cut and stamped. The variations of the vertical angle at the node are accommodated by proper cuts at the beam ends. Only one bolt and one screw is needed at each axis.

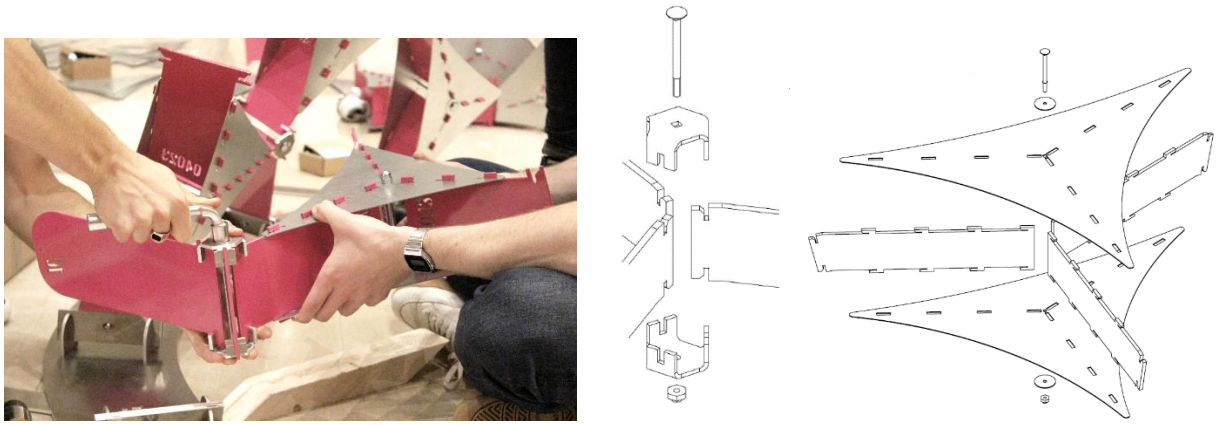

Figure 4.39: Details of the Caravel heX-mesh pavilion. The pavilions is made of planar laser-cut sheets, bolts, and standard stamped 120° connectors.

4.6.3.2 Pavilion Construire Le Courbe 2019

The structure showed in Figure 4.1 also materializes a hexagonal Caravel mesh, but with a timber structure. It was built during the workshop course Construire Le Courbe at Ecole des Ponts (Figure 4.40), with the support of Simonin, Würth and HAL. It is composed of straight 6x14cm timber beams. Only two types of connectors are used (Figure 4.41). Planar nodes are realized by plywood planks, screwed on top and bottom of beams. The 3D nodes are built from a timber profile with hexagonal cross-section, chopped up in segments of 18 cm. Beams are connected to the 3D nodes with 24cm-long 8mm screws. The vertical angle at 3D nodes is accommodated by sawing the beams ends with an inclined angle. The cut plane is perpendicular to the beam, this allows for a high precision even if sawing is done by hand without numerical tools. Column heads are clamped with a detail taking advantage of the 120° angle (Figure 4.1). The structure is designed to Eurocode 5 for dead load and a point load of 100kg. Cladding could not be included within the time frame and budget of the class, but could have been realized with folded aluminium panels.

Figure 4.40: Erection of the pavilion Construire le Courbe 2019

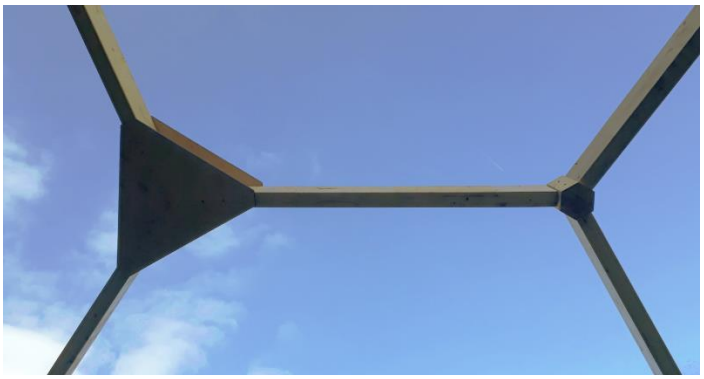

Figure 4.41: Planar and 3D nodes

4.6.4 Staggered offset

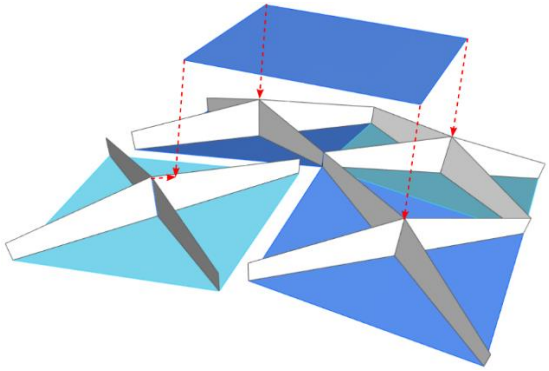

Figure 4.42: Caravel mesh realized from modules with staggered offset.

Caravel meshes are well suited for multi-layer systems thanks to the absence of torsion. Figure 4.38 shows a structure in which two layers are arranged such that one face corresponds to one face of the offset. However, it is also possible to lay the second layer in a staggered fashion, such that one face corresponds to a node of the offset. An example is shown in Figure 4.42. In this configuration, the grid separating the two layers of plates has tapered beams. Each node has one planar face, and one 3D face. This configuration can allow different rationalization strategies.

4.7 Summary of contributions

This chapter introduced a new family of meshes, baptized Caravel meshes. It allows to design gridshells without kink angle between beams and cladding panels, with torsion-free nodes, and with node repetition. Many mesh patterns can be obtained. We studied the geometrical structure and the formal potential of quad and hexagonal ones. In particular, we showed that it is asymptotically possible to approximate smooth surfaces by hexagonal Caravel meshes. We proposed generation methods, and showed how to obtain the additional constructive property of edge offset in hexagonal meshes. We showed some of the ways in which Caravel meshes can be used to rationalize the connections of a gridshell or a hybrid shell-gridshell structure. Two full scale pavilions were built and demonstrate the structural potential of the proposed geometry.

References

Baldassini, N. (2005) 'Glass and geometry', in *Glass Processing Days*.

Berrubé, A., Leduc, N., Hidalgo, J., Aubry, S. (2019) 'Forming process of façade panels by curved folding with combined geometric and mechanical optimisation', in *Proceedings of the International International Fib Symposium on Conceptual Design of Structures*, 271–276.

Blascke, W. (1929) *Vorlesungen Über Differentialgeometrie, Vol. 3*, Springer. ed.

Blassel, J., Pfadler, A. (2008) 'La gare de Strasbourg', *Construction métallique*, 45(1), 15–36.

do Carmo, M.P. (1976) *Differential Geometry of Curves and Surfaces*, Prentice-Hall, Inc.

Deng, B., Bouaziz, S., Deuss, M., Kaspar, A., Schwartzburg, Y., Pauly, M. (2015) 'Interactive design exploration for constrained meshes', *CAD Computer Aided Design*, 61, 13–23, available: http://dx.doi.org/10.1016/j.cad.2014.01.004.

Douthe, C., Mesnil, R., Baverel, O., Gobin, T., Tellier, X. (2018) 'Design and construction of a shell-nexorade hybrid timber structure', *Proceedings of the IASS Symposium 2018: Creativity in Structural Design, Boston, USA*, (July), 1–8.

Eversmann, P., Schling, E., Ihde, A., Louter, C. (2016) 'Low-Cost Double Curvature : Geometrical and Structural Potentials of Rectangular , Cold-Bent Glass Construction', in *Proceedings of the IASS Annual Symposium*.

Fildhuth, T., Schieber, R., Oppe, M. (2018) 'Design and Construction with Curved Glass', in *Engineered Transparency 2018. Glass in Architecture and Structural Engineering,* 369–381.

Glymph, J., Shelden, D., Ceccato, C., Mussel, J., Schober, H. (2004) 'A Parametric Strategy for Freeform Glass Structures Using Quadrilateral Planar Facets', *Automation in Construction*, 13(2), 187–202.

Gutierrez, C., Sotomayor, J. (1998) 'Lines of curvature , umbilic points and Carathéodory conjecture Introduction', *Resenhas IME-USP*, 3(3), 291–322.

Jiang, C., Tang, C., Vaxman, A., Wonka, P., Pottmann, H. (2015) 'Polyhedral Patterns', *ACM Transactions on Graphics (TOG)*, 34(6).

Jimenez, M.R., Müller, C., Pottmann, H. (2019) 'Discretizations of surfaces with constant ratio of principal curvatures', *Discrete & Computational Geometry*.

Lebée, A. (2015) 'From Folds to Structures , a Review', *International Journal of Space Structures*, 30(2), 55–74.

Lerouge, M. (2019) 'Rationalization and optimization of meshes for generating gridshells with nodes congruence', *Master's Thesis, Ecole des Ponts ParisTech*.

Li, Y., Liu, Y., Wang, W. (2015) 'Planar hexagonal meshing for architecture', *IEEE Transactions on Visualization and Computer Graphics*, 21(1), 95–106.

Liu, Y., Pottmann, H., Wallner, J., Yang, Y.-L., Wang, W. (2006) 'Geometric modeling with conical meshes and developable surfaces', *ACM Transactions on Graphics*, 25(3), 681.

Mesnil, R., Douthe, C., Baverel, O., Leger, B. (2017) 'Marionette Meshes : Modelling free-form architecture with planar facets', *International Journal of Space Structures*, 32(3–4), 184–198.

Mesnil, R., Douthe, C., Baverel, O., Léger, B., Caron, J.F. (2015) 'Isogonal moulding surfaces: A family of shapes for high node congruence in free-form structures', *Automation in Construction*, 59, 38–47.

Pottmann, H., Grohs, P., Blaschitz, B. (2010) 'Edge offset meshes in Laguerre geometry', *Advances in Computational Mathematics*, 33(1), 45–73.

Pottmann, H., Liu, Y., Wallner, J., Bobenko, A.I., Wang, W. (2007) 'Geometry of multi-layer freeform structures for architecture', *ACM Transactions on Graphics*, 26(3), 65.

Pottmann, H., Wallner, J. (2007) 'The focal geometry of circular and conical meshes', *Advances in Computational Mathematics*, 29(3), 249–268.

Sauer, R. (1970) *Differenzengeometrie*, Springer, Berlin.

Schober, H. (2015) *Transparent Shells: Form, Topology, Structure*, Ernst & Sohn.

Takens, F. (1974) 'Singularities of vector fields', *Publications mathématiques de l'I.H.É.S.*, 43, 47–100, available: http://www.numdam.org/item?id=PMIHES_1974__43__47_0.

Tellier, X., Zerhouni, S., Jami, G., Le Pavec, A., Lenart, T., Lerouge, M., Leduc, N., Douthe, C., Hauswirth, L., Baverel, O. (2019) 'Hybridizing vertex and face normals to design torsion free structures : application to the X-mesh pavilion', in *Proceedings of the IASS Annual Symposium: Form & Forces, Barcelona*, 505–512.

Trautz, M., Herkrath, R. (2009) 'The application of folded plate principles on spatial structures with regular, irregular and free-form geometries', *Proc. IASS*, (October), 1019–1031.

Troche, C. (2008) 'Planar hexagonal meshes by tangent plane intersection.', in *Advances in Architectural Geometry*, 57–60.

Vaxman, A., Ben-chen, M. (2015) *Dupin Meshing : A Parameterization Approach to Planar Hex-Dominant Meshing*, Tech. Rep. CS-2015-01, Department of Computer Science, technion-IIT.

Wang, W., Liu, Y. (2009) 'A Note on Planar Hexagonal Meshes', in *Nonlinear Computational Geometry*, 221–233.

Wang, W., Liu, Y., Yan, D., Chan, B., Ling, R., Sun, F. (2008) *Hexagonal Meshes with Planar Faces*, HKU CS Tech Report TR-2008-13.

Chapter 5 Discrete CMC surfaces

The previous two chapters addressed surfaces with fabrication properties. In this chapter, we aim at combining fabrication and mechanics using surfaces with constant mean curvature (CMCs), which are funicular for a uniform pressure load. The discretization of these surfaces has been a focus of research amongst the discrete differential geometry community. Many of the proposed discretizations have remarkable properties for envelope rationalization purposes. However, little attention has been paid to generation methods intended for designers.

This chapter proposes a method to generate the so-called S-CMC meshes, introduced in (Hoffmann 2010). The method is an extension to CMCs of the one developed by Bobenko, Hoffmann and Springborn (2006) to generate S-minimal nets. The method takes as input a CMC (smooth or finely triangulated), remeshes its Gauss map with a new type of circle packing, and rebuilds an S-CMC mesh via a parallel transformation. The method allows to generate a wide variety of S-CMC meshes, which have remarkable fabrication and mechanical properties for gridshells. An example is shown in Figure 5.1.

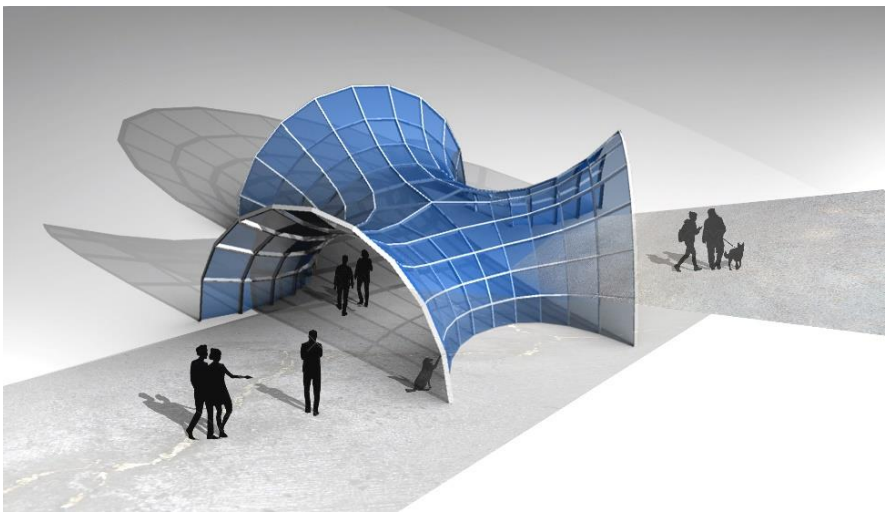

Figure 5.1: A steel-glass gridshell with geometry based on an S-CMC trinoid

5.1 Introduction

The mean curvature H of a surface at a given point is the arithmetic mean of the maximum and the minimum principal curvatures. A surface whose mean curvature is the same at each point is called a constant mean curvature surface (CMC). CMCs occur naturally around us: any soap bubble at equilibrium, like the one shown in Figure 5.2, takes the shape of a CMC. However, the family of CMCs also contains surfaces that could theoretically take the form of a bubble, but that are unstable, and therefore not observable. CMCs have other unique properties, including the fact that they solve the Plateau problem: CMCs are the surfaces with minimal area fitting a given boundary and englobing a given volume.

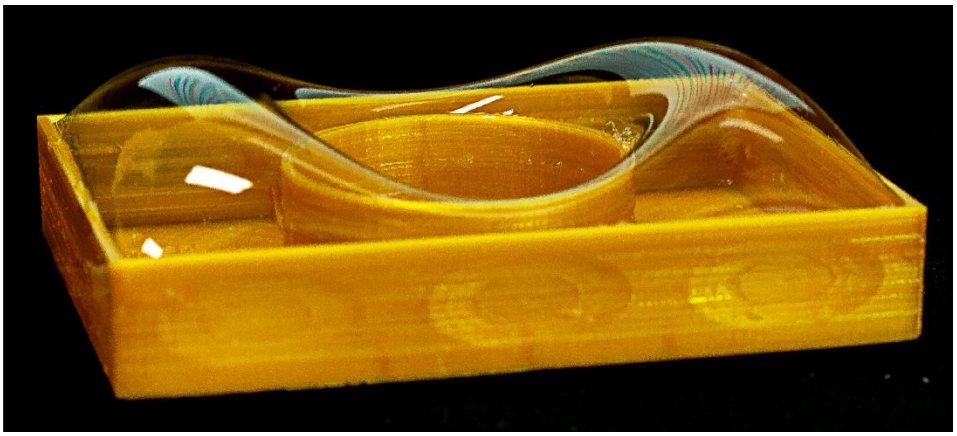

Figure 5.2 : A soap bubble (CMC surface) on a boundary similar to the one of the atrium of the British Museum (picture: Xavier Tellier and Siavash Ghabezloo)

5.1.1 Application to architecture

CMCs are particularly interesting for the design of building envelopes for the following reasons:

- They can be fitted on any boundary. This property is interesting for applications such as covering courtyards;
- Under normal pressure, they are funicular, with isotropic uniform membrane stresses. This means that the material is used in an optimal fashion for that load case;
- They are aesthetically pleasing, as they take the harmonious shape of an inflated soap bubble;
- They are a rich family of surfaces, offering many possibilities for design.

Minimal surfaces are the most well-known CMCs. They are a special subclass of CMC surfaces for which the mean curvature is null. Because of their null mean curvature and due to the estimate of curvature for a stable minimal disk (Schoen 1983), they tend to be flat at their center. They thus require a boundary with a high variation of height in order to be interesting aesthetically, mechanically and functionally. Allowing the mean curvature to be different from zero significantly broadens the spectrum of possible shapes: minimal surfaces can be ‘‘inflated” – as can be seen in Figure 5.3.

(Bach *et al.* 1988) performed a vast exploration program of the shape potential of soap films at the IL in Stuttgart. They tested several types of film support: frames, ropes, friction-free surfaces, and even other soap films. Each type of support has a different flow of forces and yield different forms. They also explored the effect of a difference of pressure between the two sides of a film. Their work revealed the ability of CMCs to fit boundaries with holes and thus assume complex topologies. Trying to fit the same boundaries with common numerical methods such as NURBS surfaces would be tedious. Figure 5.2 is inspired by their work, the boundary support is a model of the British Museum atrium.

In architecture, CMCs have been used frequently in the work of Frei Otto. The most famous example is the Munich Olympic stadium, whose cable net describe a minimal surface. Other examples include membrane envelopes and inflatable structures, such as the Unite Pneu or the Airhall of Expo64. Despite the interest for smooth CMCs, the potential of discrete CMCs for building envelopes has not yet been exploited.

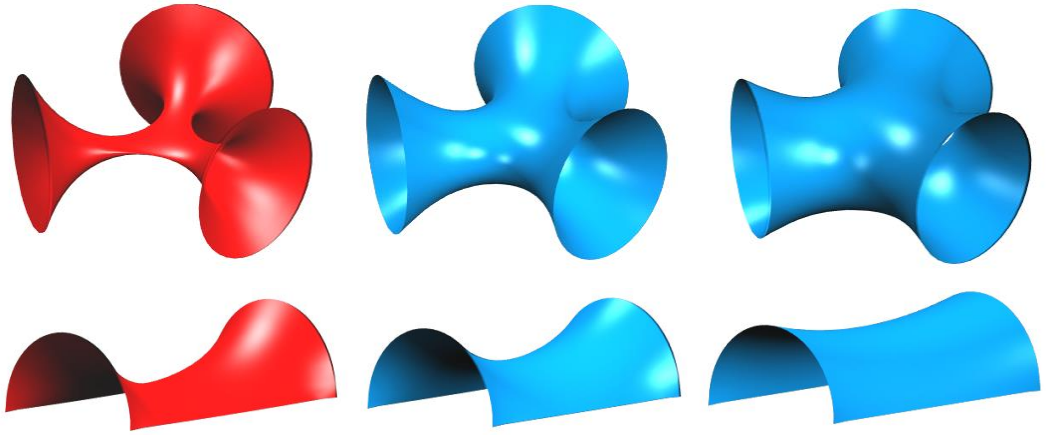

Figure 5.3: Comparison of minimal surfaces (left) and non-minimal CMCs (middle and right) with the same boundary.

Figure 5.4: The geometry of the cable net of the Olympic stadium at Münich is based on a minimal surface (picture in public domain)

5.1.2 Geometry of CMC surfaces

The property of having a constant mean curvature ($H = c$) is a partial differential equation on the surface coordinates. More precisely, it is an elliptical quasi-linear equation (Kenmotsu 2003). Solutions of this type of equations verify the maximum principle, which can be expressed geometrically as follows: If two CMCs with same mean curvature are tangent at a given point, and if one surface is locally on one side of the other (i.e. surfaces do not intersect), then the two surfaces are necessarily identical! This principle has strong geometrical implications. For example, the only CMCs with the topology of a sphere are round spheres – there exists no oval-shaped CMC balls. Also, a CMC without self-intersection verifying $H = c$ cannot enclose a sphere of radius $1/c$. More surprising, a CMC is entirely defined by its local geometry around a point: it can be uniquely extended by propagation, this is known as the analytical continuation theorem.

5.1.3 Morphogenesis methods

Most available methods to construct CMC surfaces can be classified within two categories: methods to construct smooth surfaces, which are mostly analytical, and methods to build discrete CMC, in which CMC are usually discretized by meshes.

5.1.3.1 Smooth CMCs

Back in the XIXth century, (Delaunay 1841) classified CMC surfaces of revolutions, and derived their equations. An example is the unduloid of Figure 5.11, and the nodoid showed in Figure 5.5 (left).

A first way to generate a broader family of CMCs is to copy nature. Every physical system tends to get to a configuration in which its energy is minimal. For a soap film, this energy is proportional to its area. If the film encloses a gas, its volume is imposed. The resulting shape minimizes its area under a volume constraint. CMCs can be generated by solving this variational problem, known as the Plateau problem.

A second method is to construct minimal surfaces in the three-dimensional unit sphere (noted S^3) by minimization of the area on a fixed boundary. Such a minimal surface is defined in a four-dimensional space, but can be isometrically transformed into a CMC surface of R^3 using the Lawson correspondence (Lawson 1970). (Karcher 1989; Grosse-Brauckmann 1993) solve the Plateau problem in S^3 for boundaries constituted of straight lines. These boundaries map to lines of symmetry by the Lawson correspondence. They use this property to construct periodic and symmetrical CMCs.

There exists a geometrical construction, called the Weierstrass representation, that allows to construct any minimal surfaces from two arbitrary analytic complex functions (these can be understood as conform deformations of the plane). This is for example detailed in (Gray 1998). This construction was extended to CMCs by Kenmotsu (Kenmotsu 1979), who proposes to construct harmonic Gauss maps on the unit sphere, and to reconstruct CMC surfaces by integration. A smooth surface can be constructed by integrating a metric and a curvature fields provided that these fulfill the Gauss-Codazzi equations. For CMCs, these equations are encoded by the harmonicity of the Gauss map: One can always reconstruct a CMC from a given harmonic map of the unit sphere. The generation method proposed in the current chapter is a discrete version of this approach.

Later, (Abresch 1987) describes CMC surfaces with planar curvature lines in one direction. This geometrical condition results in the separation of variables of the Gauss-Codazzi equations, which can then be integrated explicitly. These new solution will allow to construct a surprising immersed CMC torus, whose existence had been discovered by Wente (Wente 1986). This torus is showed in Figure 5.6. Inspired by this work, (Dorfmeister *et al.* 1998) propose methods from the theory of integrable systems to construct harmonic Gauss maps. They are implemented in the free software CMCLab (Schmitt 2001).

(Kapouleas 1991) and later (Mazzeo and Pacard 2001) developed technics based on partial differential equations (PDE) to glue elementary CMC blocs together. By perturbation theory in nonlinear PDEs, they merge these blocs to obtain new smooth CMC surfaces. For example, the CMC shown in Figure 5.6 (right) is constructed by removing seven disks to a central sphere and attaching half unduloids – with necks of catenoids at the junctions. The geometry of the CMCs showed in Figure 5.7 is based on the same principle (Schmitt 2007).

CMC surfaces can also be deformed isometrically into other CMCs. The set of surfaces obtained in the process is called the associate family. The *twizzler* showed in Figure 5.5 (middle) is in the associate family of an unduloid.

Many other methods have been proposed to construct CMCs in other spaces than the ambient space ($\mathbb{R}^3$) – in particular hyperbolic and spherical spaces of arbitrary dimensions.

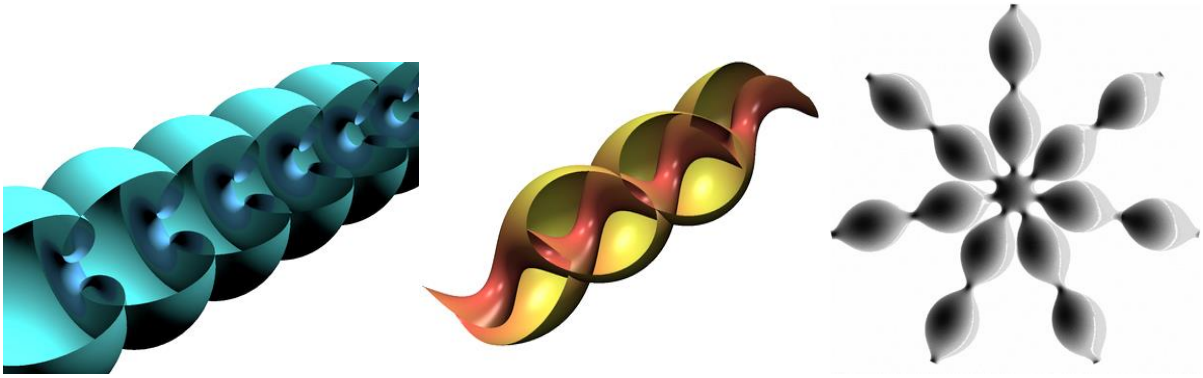

Figure 5.5 : Analytical CMC surfaces (©GANG, Nicholas Schmitt)

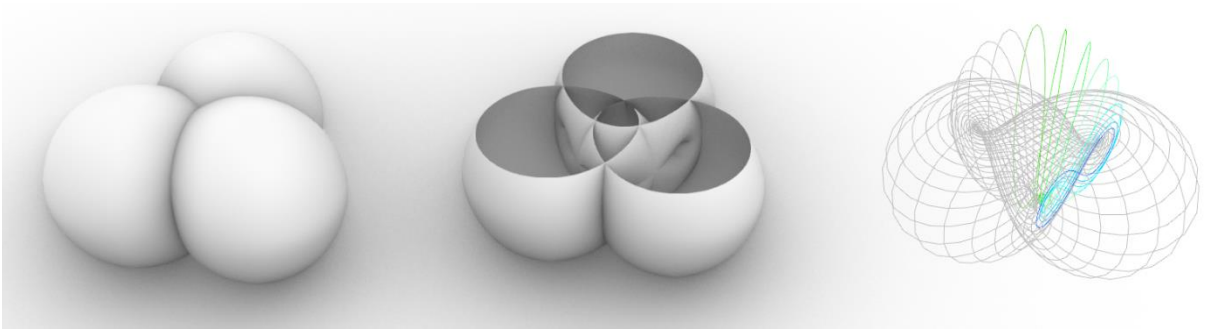

Figure 5.6 : The Wente torus. Left: Outside view. Middle: A section that highlights the complex geometrical structure. Right: The curvature lines in one direction form planar 8-loops

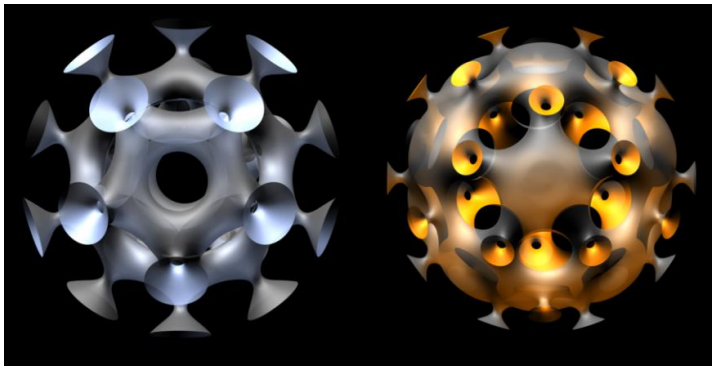

Figure 5.7 : CMC surfaces based on platonic solids
(image courtesy of GeometryWerkstatt, University of Hannover, ©Nicholas Schmitt)

5.1.3.2 Discrete CMCs

Many methods have been developed to generate triangulated solutions of the Plateau problem with optimization algorithms. The idea is to iteratively move the vertices of the mesh in order to minimize the area under a volume constraint, which is equivalent to minimizing a linear combination of the area and volume. One well-known software is the Surface Evolver, developed by (Brakke 1992). It minimizes the energy of a triangular mesh by a conjugate gradient descent. In order to improve the robustness and speed, (Pan *et al.* 2012) propose to minimize an energy based on a Centroidal Voronoi Tessellation instead of the area. A remeshing method allows to deal with topology changes as a bubble is inflated or deflated.

For designers, one of the most accessible tools to generate CMCs is the plugin Kangaroo2 for Grasshopper, which is based on the algorithm developed by (Bouaziz *et al.* 2012) to handle various geometric constraints. This tool was used to generate the surfaces shown in Figure 5.3.

Instead of controlling the position of the boundary, these methods also allow to constrain the boundary of a CMC to a base surface. If a soap film is free to slide on a base surface, its tangent planes will be everywhere orthogonal to the base surface. For example, a soap bubble on a table takes the shape of a half sphere. It is then possible to control the orientation of the surface at the boundary.

These methods are intuitive for designers, as they are equivalent to blowing a bubble. In particular, the boundary can be controlled. However, they are not well suited to the construction of unstable CMCs or CMCs with complex topologies. They are also not adapted to the generation of periodic surfaces: It is not possible to prescribe both position and slope at the boundary, so it is not possible to construct C^2 surfaces by repeating or mirroring a patch.

(Oberknappl and Polthier 1997) create triangulated minimal surfaces of the three-dimensional unit sphere, and transform them into CMCs of R^3 using a discrete Lawson correspondence. The method allows to construct periodic CMCs. A discrete version of the Lawson correspondence based on quadrangular meshes was recently proposed in (Bobenko *et al.* 2017).

(Bobenko *et al.* 2006) developed a theory of discrete minimal surfaces based on S-isothermic meshes (which are introduced in the next section). These meshes are based on circles packings, and their radii are solutions of a variational problem. (Bücking 2007) solved this problem on piecewise-linear boundaries, and constructed discrete equivalents of well-known smooth periodic minimal surfaces. Contrary to the methods mentioned in the first paragraph, this approach is based on quadrangle meshes: Edge orientations are discrete equivalent to the principal curvature directions of a smooth surface.

5.1.4 S-CMC meshes

This chapter is based on the so-called S-CMC meshes introduced in (Hoffmann 2010). This section introduced their structure and their application to architecture.

5.1.4.1 S-isothermic meshes

As smooth CMCs are isothermic, they can be covered with a conformal curvature line network (where each face roughly forms a square). (Bobenko and Hoffmann 2016) propose a discretization of this property with the S-isothermic meshes, constituted of planar quadrangles. A subclass of this family (referred to as type 1), have the particularity of having an inscribed circle in each face, and sphere associated with each summit, as shown in Figure 5.8. Two spheres are tangent if the corresponding nodes share an edge, thus forming a sphere packing, and the spheres intersect the circles at a right angle.

Christoffel transform
One particularity of smooth isothermic surfaces is that they allow a Christoffel transformation. To introduce this notion, let us consider a conform parametrization by curvature lines of an isothermic surface:

$$f: D \subset \mathbb{R}^2 \to \mathbb{R}^3$$

$$(x, y) \mapsto f(x, y)$$

The fact that f is conform means that for any (x, y):

$$\|f_x\| = \|f_y\| \quad ; \quad f_x . f_y = 0$$

A Christoffel dual $f^*(x, y)$ is constructed by integrating the following derivatives:

$$f_x^* = \lambda \frac{f_x}{\|f_x\|^2} \quad ; \quad f_y^* = \lambda \frac{-f_y}{\|f_y\|^2}$$

where λ is a constant. It is defined up to a translation. This integration is possible only if the surface is isothermic. For a given coordinate (x, y), we remark that:

$$f_x^* \parallel f_x \quad ; \quad f_y^* \parallel f_y$$

This means that f^* is a parallel transformation: it conserves the orientation of the iso-parameter lines. Furthermore:

$$\|f_x^*\| = \frac{\lambda}{\|f_x\|} \quad ; \quad \|f_y^*\| = \frac{\lambda}{\|f_y\|}$$

This means that the metrics of the Christoffel transform is the inverse of the one on f. When applied to a minimal surface, the Christoffel dual coincides with the Gauss map if $\lambda = 1$. Also, the dual of a synclastic surface is anticlastic, and vice versa.

For an S-isothermic mesh, a discrete version of the Christoffel transform can be defined as follows: Invert the radius of each sphere, and re-pack them such that the center-to-center edges keep their direction. It is therefore a parallel transformation, with a similar metric inversion as the smooth Christoffel dual. This construction is illustrated in Figure 5.8. It yields an S-isothermic mesh.

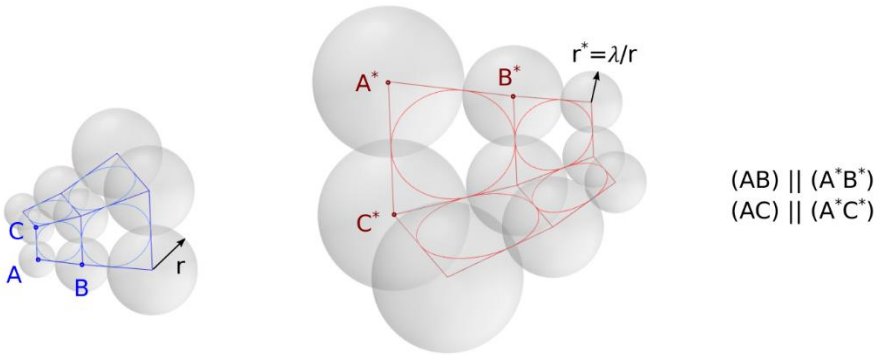

Figure 5.8 : A type 1 S-isothermic mesh (blue) and its Christoffel transform (red)

Darboux transforms

Isothermic surfaces also allow Darboux transforms. Two surfaces are said to be Darboux transforms of each other if they envelope a two-parameter family of spheres such that the spheres tangent to a surface along a curvature line are also tangent to the other surface along a curvature line.

S-CMC meshes

(Hertrich-Jeromin and Pedit 1997) showed that smooth CMCs are characterized by the fact that their Christoffel dual is also a Darboux transform of the surface. S-CMC meshes are S-isothermic meshes that have a discrete equivalent of this property: The (discrete) Christoffel dual can be positioned in space such that, for each quad, there exists a sphere containing its inscribed circle and the inscribed circle of the dual quad (Figure 5.9).

(Hoffmann 2010) showed that the distance between edges and their dual is constant in a given direction: The distance is either t_1 or t_2. These distances are related by the equation:

$$4\lambda = t_2^2 - t_1^2$$

Where λ is the scaling coefficient of the Christoffel dual (the radius of the spheres and of their dual are related by $r^* = \lambda/r$). For two dual edges, the line (in red) linking the points of tangency of the Darboux sphere is orthogonal to both edges. Pythagorean theorem thus yields:

$$CC^* = (r + r^*)^2 + t_2^2 = (r - r^*)^2 + t_1^2$$

The position of the Christoffel dual defines the discrete normals at the vertices, which can be used to construct offsets and torsion-free nodes. For example, the normal at C is the vector:

$$\vec{n} = \frac{\overrightarrow{CC^*}}{\|CC^*\|}$$

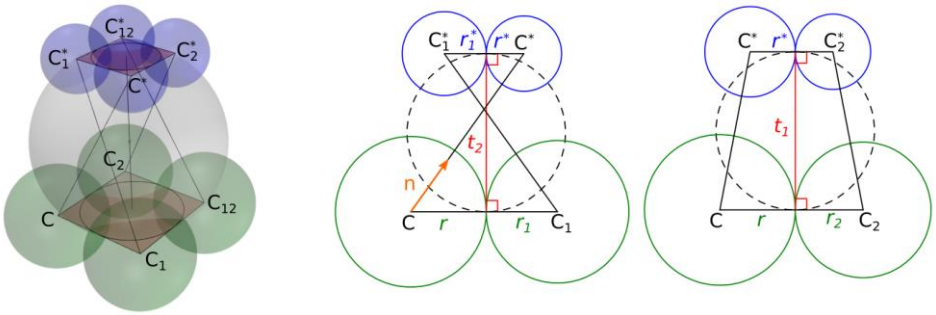

Figure 5.9 : The S-CMC structure

Architectural application

S-CMC surfaces have geometric properties which are of particular interest for the fabrication of a gridshell. Firstly, they are quad meshes with planar faces and torsion-free nodes. Secondly, they admit an offset in which some edges are located at constant distance h_1 from the mesh, and the other edges are located at a distance h_2. This property enables a perfect alignment of the beams at the node while using only two different beam cross sections, as illustrated in Figure 5.10. We will use the term *orthotropic edge offsets* to refer to this property. Thirdly, each face has an inscribed circle. As a result, faces are « roughly square », which provides aesthetic value to the mesh, and also minimizes material loss if panels are cut out of a larger sheet. Also, S-CMC meshes have interesting mechanical properties. They are close to smooth CMCs, which are funicular under a uniform pressure loading with isotropic membrane stresses. As a result, very low in-plane shear is expected under normal pressure. Finally, there exists spheres centered on vertices which form a sphere packing, as shown in Figure 5.28. Each sphere intersects the in-circles of the adjacent faces at 90°. This rare and fascinating property might give creative ideas to designers.

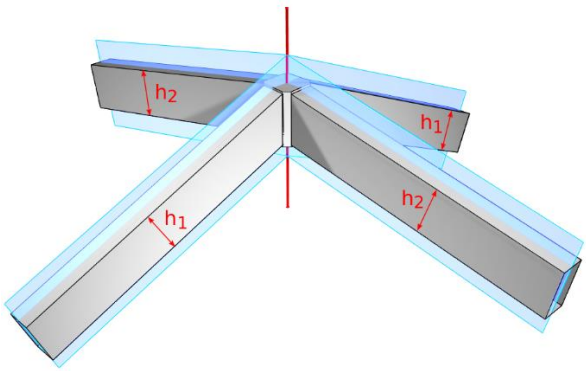

Figure 5.10: A torsion free node in an orthotropic edge offset mesh

5.1.5 Overview of the proposed generation method

The workflow is similar to the one used by Bobenko, Hoffmann and Springborn (2006) to generate minimal meshes. The process consists of four steps, which are shown in Figure 5.11. In the first step, a CMC surface – smooth or triangulated – is generated. A conformal network of curvature lines is then constructed. In the second step, the Gauss map of the surface is calculated. The boundary of the Gauss map and the topology of the curvature lines are used to generate a discrete Gauss map in the third step. Finally, in a fourth step, the Gauss map is transformed into an S-CMC mesh by a parallel transformation.

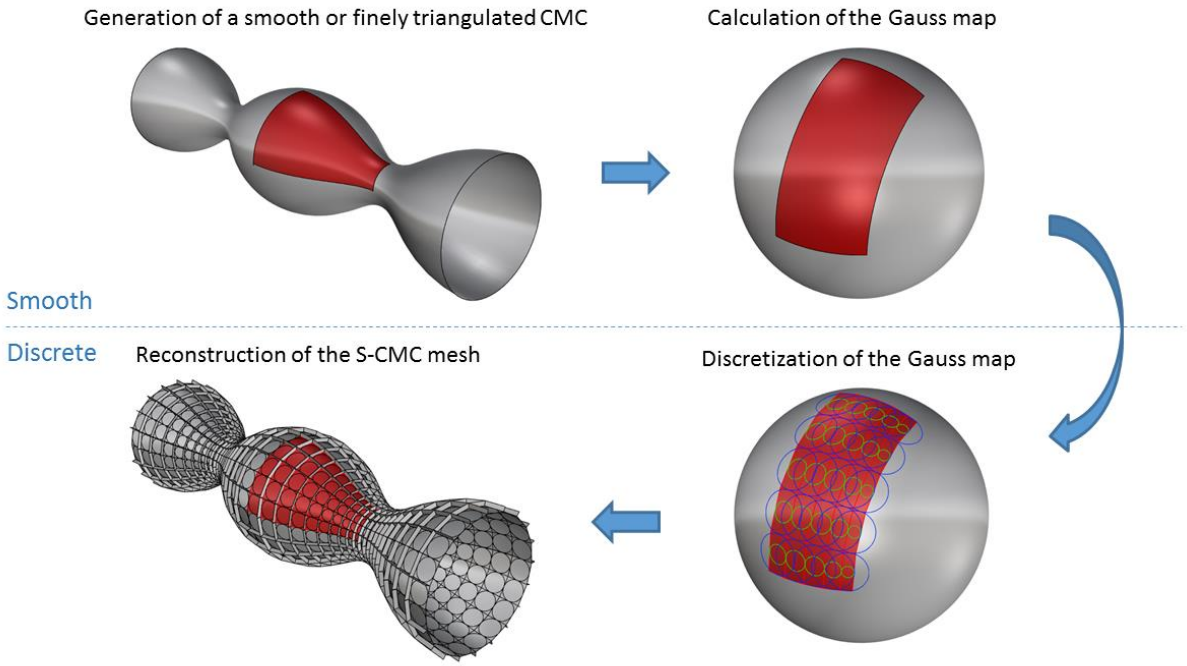

Figure 5.11: Overview of the discretization method

5.2 Generation of input smooth CMCs

This section presents how smooth CMC surfaces can be generated for use as an input in the algorithm.

CMC generation

For the first step, smooth or finely triangulated CMCs are generated. The former option is used when an analytical equation is known for the surface. An example is the unduloid, shown in Figure 5.11. When no analytical equation is available, a CMC triangular mesh is generated by using the functions « SoapFilm » and « Volume » of the software Kangaroo2. CMC surfaces shown in Figure 5.3 are generated by this method.

Isothermic orthogonal net

An isothermic network of curvature lines is then drawn on the surface. The isothermic property means that each face is "square", this is necessary for the net to be approximated by an S-CMC mesh. This part is performed in the CAD software Rhino. For smooth surfaces, a code was developed for this purpose using the geometry functions of RhinoScriptSyntax. For triangulated surfaces obtained by Kangaroo2, a network of curvature lines is drawn using the software EvoluteTools T.MAP. Singularities of the network shall be located on the umbilical points of the surface. The order of these umbilical points is a multiple of

½ (Gutierrez and Sotomayor 1986), so the singularities (except on boundaries) have an even valence: singularities of valence 3, 5 and 7 are not possible.

Gauss map
The Gauss map of the surface is then computed. For analytical surfaces, the exact normal is computed. For triangulated surfaces, the direction of the normal at a given vertex is computed as the gradient of the area of the adjacent faces.

5.3 Discretization of the Gauss map

The discretization of the Gauss map is done by generating an orthogonal double circle packing (ODCP) on the unit sphere for which the boundary approximates the one of the smooth Gauss map. The geometric structure of ODCP is explained in section 5.3.1 and the generation method in Section 5.3.2. The transformation of the ODCP into a discrete Gauss map is described in Section 5.3.3.

5.3.1 Orthogonal double circle packings

An *orthogonal double-circle packing* (ODCP) in the plane consists of pairs of circles, where two circles of a given pair are concentric. Such a structure is shown in Figure 5.12. (Bobenko *et al.* 2019) recently studied this structure in the plane, introduced variational formulations, and showed how such patterns can discretize well known harmonic functions.

Such a packing can be decomposed into two families of circles, represented in red and blue in Figure 5.12. Having in mind the construction of the Gauss map, one family will be called the *node-centered circles* (in red), and the other one the *inscribed circles* (in blue). For each family, the smaller circles are tangent in one direction, and the larger circles in the other one.

When a pair of circles from each family intersect, they fulfill the following rule: the smaller circle of one pair intersects orthogonally the larger circle of the other pair. This property is shown in Figure 5.13. Thanks to this rule, a quad mesh can be drawn between the node-centered circles, and the inscribed circles (in blue) are then tangent to the edges of this mesh.

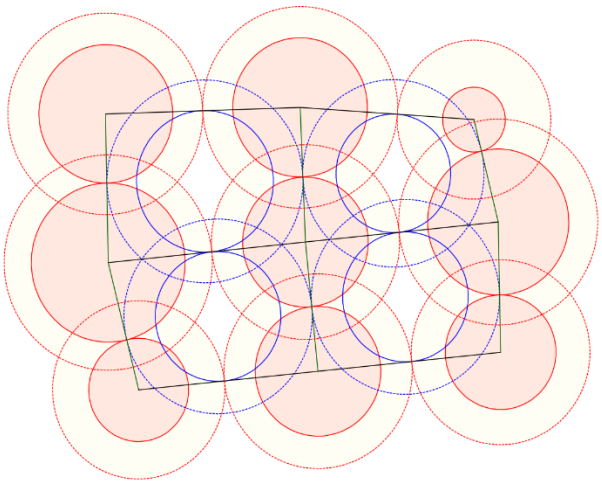

Figure 5.12: Orthogonal double-circle packing (ODCP)

In order to generate the Gauss map, ODCP will be generated on S^2, the unit sphere. The rules described above are applied in the same way as in the plane, except that straight lines are replaced by arcs of great circles.

5.3.2 Generation of an ODCP

In this section, we show how an ODCP can be generated with given combinatorics and boundary angles. In a first step, radii of circles compatible with the ODCP structure and the boundary conditions are found using a Newton algorithm. The compatibility of the circles can be expressed by two sets of constraints. In a second step, the ODCP is constructed using the radii and the orthogonal properties.

First Constraint on radii: orthogonal intersection

The orthogonality condition between two secant pairs of circles yields one constraint per pair of circles. As shown in Figure 5.13, let r_0 and R_0 be the spherical radii of one pair of circles, and r_1 and R_1 the radii of the second one. The geodesic distance d between the centers of the two pairs can be calculated by the spherical cosine rule:

$$\cos(d) = \cos(r_0)\cos(R_1)$$

$$\cos(d) = \cos(R_0)\cos(r_1)$$

Assuming that all circles have a radius lower than $\pi/2$, and thus a non-null cosine, we obtain the following relation:

$$\frac{\cos(r_0)}{\cos(R_0)} = \frac{\cos(r_1)}{\cos(R_1)}$$

Since this relation must hold for all intersecting pairs of circles, the cosine ratio must be identical for all pairs of circles:

$$\frac{\cos(r)}{\cos(R)} = t = cte \geq 1 \qquad (1)$$

The constant t will play an important role in the structure of the offset, as will be shown in section 5.4.

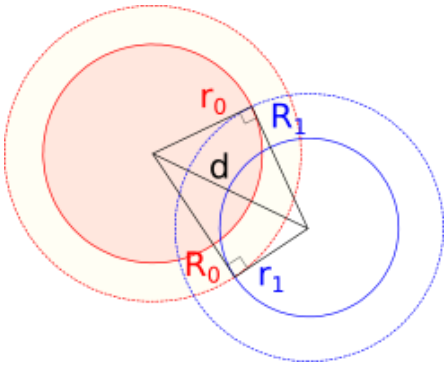

Figure 5.13: Two secant pairs of circle of an ODCP

Second constraint on radii: closure of mesh faces

The second set of constraints concerns how all the neighboring circles of a given circle close around it.

Bobenko *et al* (2006) showed that the Napier formula for a right spherical triangle can be expressed as follows:

$$\varphi = \arctan(e^{\gamma_2-\gamma_1}) + \arctan(e^{\gamma_2+\gamma_1})$$

in which $\gamma_i = \ln(\tan\frac{r_i}{2})$ and r_1, r_2 and φ are shown in Figure 5.14 :

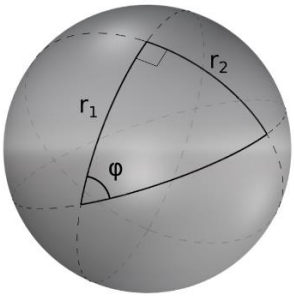

Figure 5.14: Napier rule for a right spherical triangle

Since circles intersect orthogonally, the Napier formula can be used to compute all the angles centered at a point M, as shown in Figure 5.15:

$$\varphi_k = \arctan(e^{\Gamma_k - \gamma_i}) + \arctan(e^{\Gamma_k + \gamma_i})$$

$$\psi_k = \arctan(e^{\gamma_k - \Gamma_i}) + \arctan(e^{\gamma_k + \Gamma_i})$$

Where $\gamma_i = \ln\left(tan\frac{r_i}{2}\right)$; $\Gamma_i = \ln\left(tan\frac{R_i}{2}\right)$; $\varphi_k = \widehat{A_k M P_k}$ and $\psi_k = \widehat{P_k M B_k}$

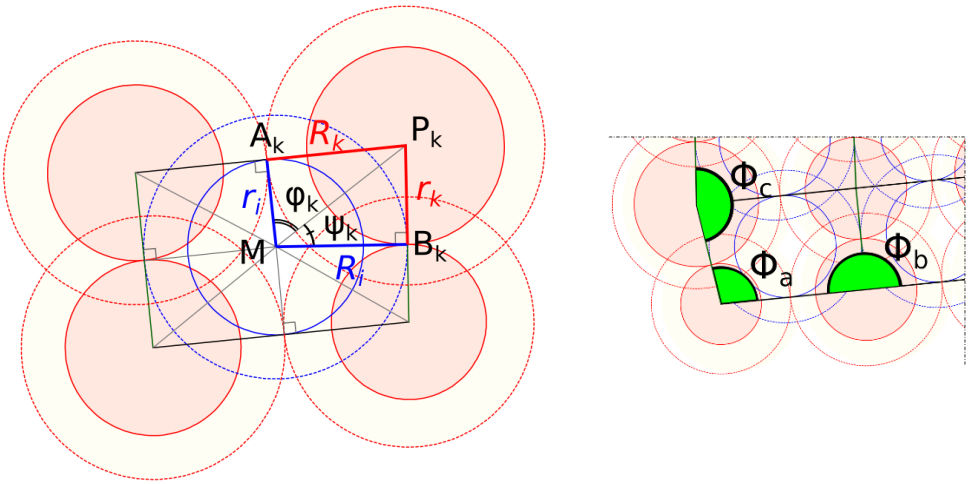

Figure 5.15: Angles around the center of a circle (left) and boundary angles Φ (right)

For a pair of circles not located on the boundary, the angles must add up to 2π:

$$\sum_{k=1}^{n}(\varphi_k + \psi_k) = 2\pi \qquad (5.2a)$$

For pairs located on the boundary, the sum of the angles around a point is a boundary angle Φ (Figure 5.15, right):

$$\sum_{k=1}^{n}(\varphi_k + \psi_k) = \Phi \qquad (5.2b)$$

The angles Φ needs to be calculated from the smooth Gauss map, they are the input parameters that allow to control the geometry of the ODCP for a given combinatorics.

Calculation of the radii

The system of nonlinear equations determined in the two previous sub-sections is square: the number of equations is the same as the number of unknowns. Since the equations are analytical, the Jacobian matrix of the system can be calculated exactly. Radii fulfilling all the constraints are searched using the Newton-Raphson method. Note that the values of the radii need to be higher than 0 and lower than π. This constraint is automatically fulfilled using the logarithmic radii as variables. The following initial spherical radii were used for the pictures shown in this chapter: *0.24 rad* for the larger circles of each pair, and *0.15 rad* for the smaller. This algorithm converges fairly quickly. Eight iterations are sufficient to generate the trinoid shown in Figure 5.1.

Construction of the ODCP

These two sets of constraints are sufficient for radii to be compatible with a simply connected ODCP structure. The ODCP is built from the circles as follow:

- Firstly, pairs of circles are placed on two edges of the boundaries of the packing. Only the circle radii and the boundary angles are needed for this purpose.
- The remaining circles are added by propagation from the edges using the orthogonality property and the radii.

5.3.3 Construction of the discrete Gauss map

The construction of the Gauss map starts with the construction of the circular cones which are tangent to S^2 along the larger node-centered circles of the ODCP. Such cones are shown on the right side of Figure 5.16.

Proposition 5.1

The apexes of these cones are the vertices of a polyhedral mesh with planar faces and orthotropic edge offset property, i.e. each edge is tangent to either S^2 or tS^2 (a sphere or radius t concentric with S^2).

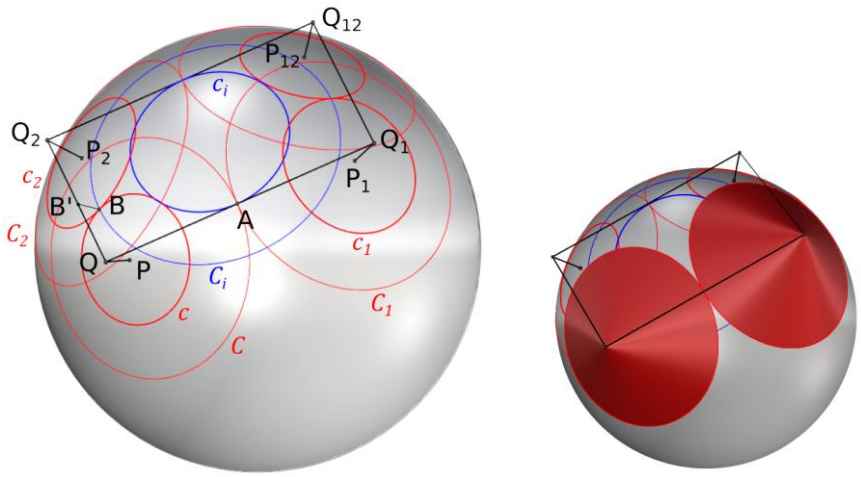

Figure 5.16: Construction of the Gauss map from the ODCP. Cones used to build the mesh are shown on the right.

Proof:

Starting from an object X of the ODCP, we will call X_1 (resp. X_2) the next object in the direction of higher (resp. lower) curvature – i.e. the direction in which the larger (resp. smaller) circles are tangent.

Let us call (see Figure 5.16):

- P the center of a node-centered circle of the ODCP ($P \in S^2$) ;

- Q the cone apex corresponding to P ;
- O the center of S^2 ;
- C and c the node-centered circles centered at P, whose spherical radii are respectively R and r (spherical radii are angles in S^2, see Figure 5.17);
- C_i and c_i the inscribed circles of the spherical face $PP_1P_{12}P_2$.

Q, Q_1 and A are aligned, because the cones centered on P and P_1 are tangent to S^2 at A, and A belongs to the plane OPP_1. Since (QQ_1) and c_i are incident (at A) and since (QQ_1) is tangent to S^2 at A, (QQ_1) and c_i are necessarily coplanar. The same argument can be used to show that (Q_2Q_{12}) and c_i are coplanar. Therefore the quad $QQ_1Q_{12}Q_2$ is planar.

Let us now build the circle c', which is the projection of c onto tS^2, and then build the cones tangent to tS^2 along c'. Q', the apex of this cone belongs to (OP), and its distance to O is (see Figure 5.17), using equation (5.1):

$$OQ' = OB' / \cos r = t / \cos r = 1 / \cos R = OQ$$

Therefore Q' = Q, and we conclude that (QQ_2) and (Q_1Q_{12}) are tangent to tS^2.

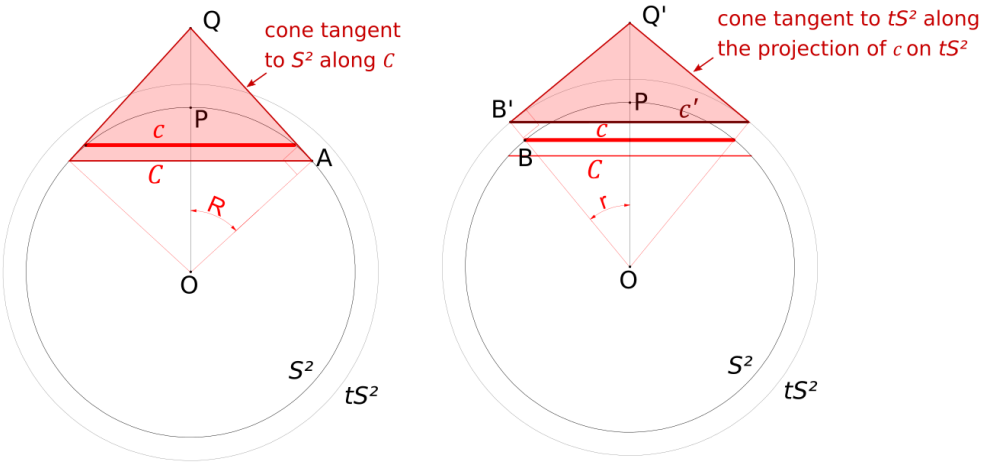

Figure 5.17 : Tangency of edges with tS²

5.4 Reconstruction of the surface from the Gauss map

In this section, we will show how to construct an S-CMC surface from the Gauss map built in the previous section. We start by constructing a double-sphere packing thanks to the underlying ODCP. To each node-centered pair of circles, we associate a pair of spheres centered on the node of the Gauss mesh. Figure 5.18 shows on the left (resp. right) a section of the double-sphere-packing along the edge of the mesh where the larger (resp. smaller) spheres touch each other:

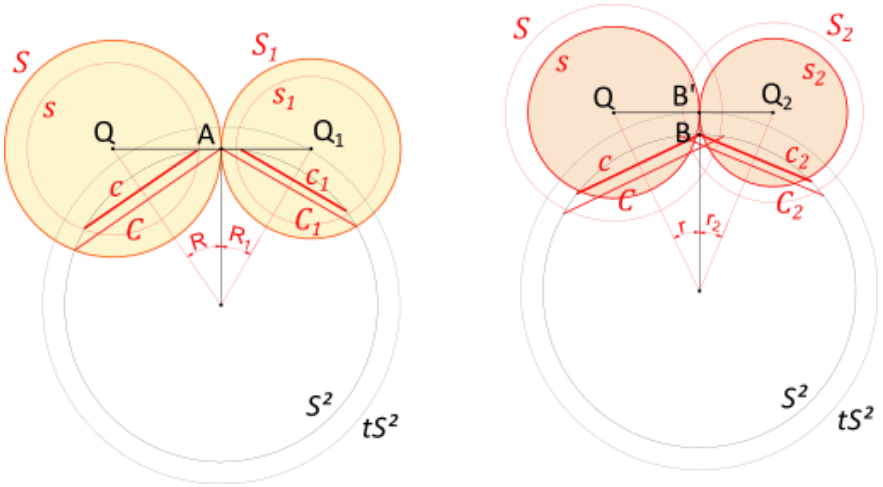

Figure 5.18 : Double-sphere packing associated with the Gauss map

The radii of the larger and the small spheres are given respectively by:

$$R_S = AQ = \tan(R)$$

$$r_s = B'Q = t * \tan(r)$$

Proposition 5.2

Let G be a Gauss map constructed in section 5.3. Let R and r be the radii of the associated double sphere packing. There exist two S-isothermic meshes, M^+ and M^-, which are edgewise parallel to G (Figure 5.19). The radii of the associated spheres are $(R + r)/2$ for M^+, and $(R - r)/2$ for M^-.

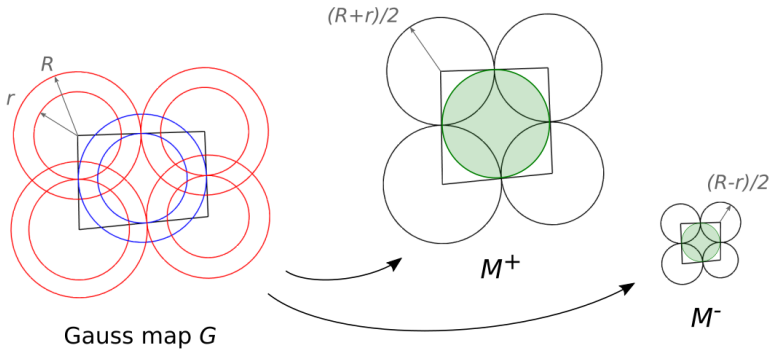

Figure 5.19 : Reconstruction of S-isothermic meshes from the ODCP of the Gauss map

Proof:

Figure 5.20 shows a top view of a face of the Gauss map, with the associated double-spheres. Since the face is closed, we have:

$$(R + R_1)u + (r_1 + r_{12})v_1 - (R_{12} + R_2)u_2 - (r_2 + r)v = 0$$

In which $u = \frac{\overrightarrow{QQ_1}}{QQ_1}$ and $v = \frac{\overrightarrow{QQ_2}}{QQ_2}$

As shown in Figure 5.20, we can obtain a second sphere packing by switching the direction of tangency of the smaller spheres with that of the larger spheres. This switch can be executed by applying a reflection to each colored quad.

Thanks to the fact that each colored quad has two right angles, the flipped Gauss mesh is parallel to the original one. Therefore, we obtain the following equations, which corresponds to the closure of the quad $\widetilde{Q}\widetilde{Q_1}\widetilde{Q_{12}}\widetilde{Q_2}$:

$$(r + r_1)u + (R_1 + R_{12})v_1 - (r_{12} + r_2)u_2 - (R_2 + R)v = 0$$

As a result, spheres of radius $(R + r)/2$ can be packed in directions parallel to the Gauss mesh:

$$\left(\frac{R + r}{2} + \frac{R_1 + r_1}{2}\right)u + \left(\frac{R_1 + r_1}{2} + \frac{R_{12} + r_{12}}{2}\right)v_1 - \left(\frac{R_{12} + r_{12}}{2} + \frac{R_2 + r_2}{2}\right)u_2 - \left(\frac{R_2 + r_2}{2} + \frac{R + r}{2}\right)v = 0$$

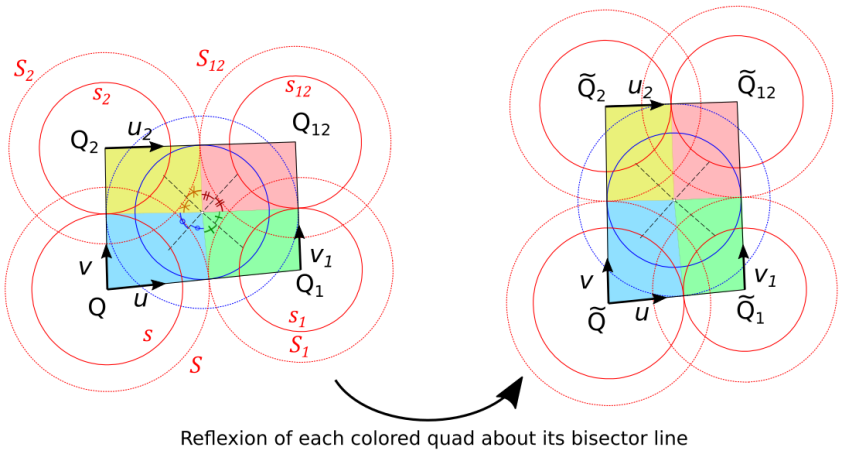

Figure 5.20 : Change of the direction of the packing of double spheres

This compatibility equation insures that the whole Gauss map can be deformed into an S-isothermic mesh by a Combescure transformation. The edge length modification ratios of this transformation are simply obtained from the sphere radii.

The same result holds for a packing of spheres of radii *(R-r)/2*.

Proposition 5.3

The S-isothermic meshes M^+ and M^- mentioned in proposition 5.2 are also S-CMC.

Proof:

We start by constructing the mesh $M^* = M^+ + n$ where n is the Gauss map and "+" is the sum on vertices. We call C_i the vertices of M^+, C_i^* those of M^*, and A_i the points of tangency of the spheres of M^+.

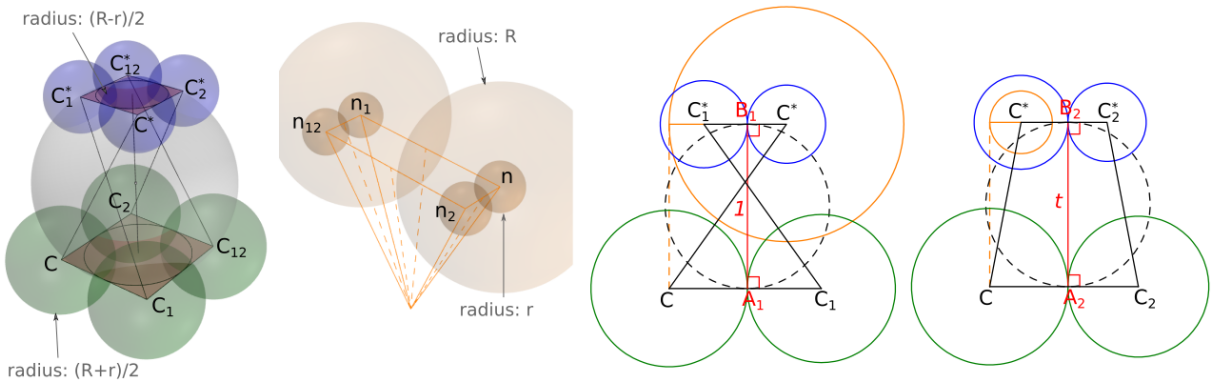

Figure 5.21 : Construction of the Christoffel dual. From left to right: 3D view of meshes, 3D view of Gauss map (larger spheres centered on n_2 and n_{12} are hidden for clarity), section in higher curvature direction, section in lower curvature direction.

Figure 5.21 shows the construction in the planes (CC_1C^*) and (CC_2C^*). In each of these planes, we draw a line perpendicular to (CC_i) going through A_i. We call B_i the intersection of this line with $(C^*C_i^*)$. Since edges of the Gauss map n are tangent to S^2 and tS^2, $A_1B_1 = 1$ and $A_2B_2 = t$. We note that:

$$C^*B_1 = R - \frac{R+r}{2} = \frac{R-r}{2}$$

$$C^*B_2 = \frac{R+r}{2} - r = \frac{R-r}{2} = C^*B_1$$

Therefore, we can construct a packing of tangent spheres of radii $\frac{R-r}{2}$ centered on vertices of M^*. Since M^* is parallel to M^+, it is also parallel to M^-. As a result, M^* corresponds to the mesh M^-.

The product of the radii of corresponding spheres of M^+ and M^* is:

$$\frac{R+r}{2}\frac{R-r}{2} = \frac{R^2-r^2}{4} = \frac{t^2-1^2}{4} = cte \tag{5.3}$$

where we use the fact that:

$$CC^{*2} = R^2 + 1 = r^2 + t^2$$

Therefore M^* is the Christoffel dual of M^+.

The circles inscribed in the quads $CC_1C_{12}C_2$ et $C^*C_1^*C_{12}^*C_2^*$ are coaxial. The sphere containing these two circles is orthogonal with the eight spheres centered on each vertex. Therefore, M^* is a Darboux transform of M^+. We can then conclude that M^+ is S-CMC.

5.5 Change of curvature sign

The junctions between zones of positive and negative curvature require a specific treatment. At such a location, the Gauss map of the surface is "folded". This section describes how the discrete Gauss map can be folded while keeping the geometric properties described in the previous sections.

5.5.1 Structure of the Gauss map on a fold

In the model presented in this chapter, the curvature is defined on the nodes of the mesh: if a node has a positive (resp. negative) curvature, the associated sphere in the S-CMC mesh has a radius of *(R+r)/2* (resp. *(R-r)/2*). In the cases treated in the previous sections, each face had four nodes with the same curvature sign. As a result, all the circles of the ODCP (and consequently all the spheres of the sphere packing) were tangent on the outside. When a change of curvature occurs, two adjacent smaller circles touch each other on the inside, as shown in Figure 5.22 :

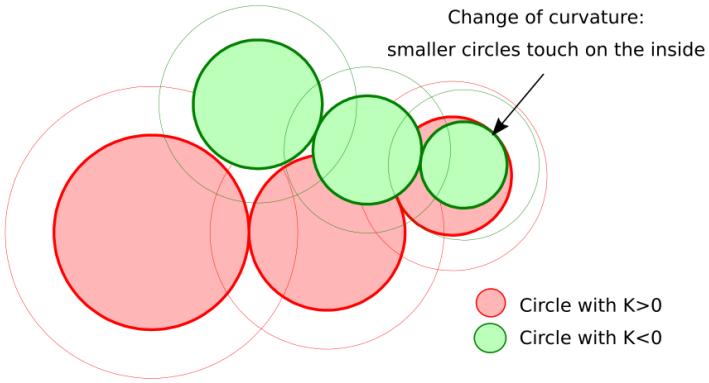

Figure 5.22 : Change of curvature sign in a line of double-circles of an ODCP of a Gauss mesh

Quads of the Gauss map with nodes of different curvature signs can be classified in the following types, as represented in Figure 5.23:

- Faces of type A: two nodes have positive curvature, and the two others have negative curvature. The change of curvature occurs when traveling in the direction of low curvature (the direction in which smaller circles are tangent).
- Faces of type B: same as type A, except that the change of curvature occurs when traveling in the direction of higher curvature (the direction in which larger circles are tangent). In that particular case, the inside tangency shown in Figure 5.22 does not apply.
- Faces of type C: this type is only encountered in highly coarse meshes and will not be treated here.
- Faces of type D: one node has a curvature sign different from the other three.

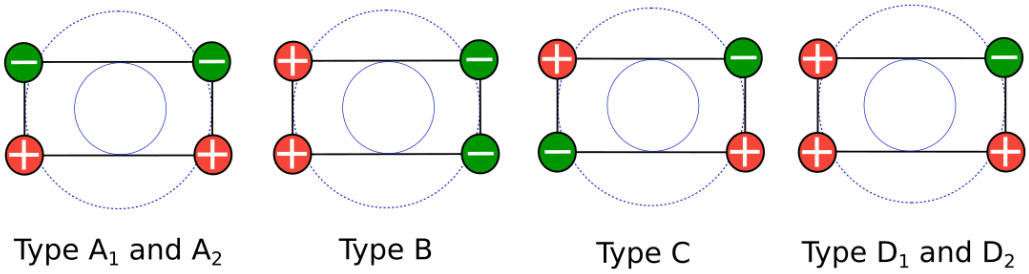

Figure 5.23: Types of quads with non-uniform node curvature signs

The full tangency pattern for each type of face is shown in Figure 5.24. For faces of type A and D, it can be noted that, depending on relative size of the adjacent circles, the quad can auto-intersect. Faces of type B always auto-intersect, in the way of a candy wrapping paper. For faces A and D, the tangency of quad edges with tS^2 happens outside of the quad. The types of fold of a quad are analogous to how a rectangle of fabric can be folded, as shown in Figure 5.25.

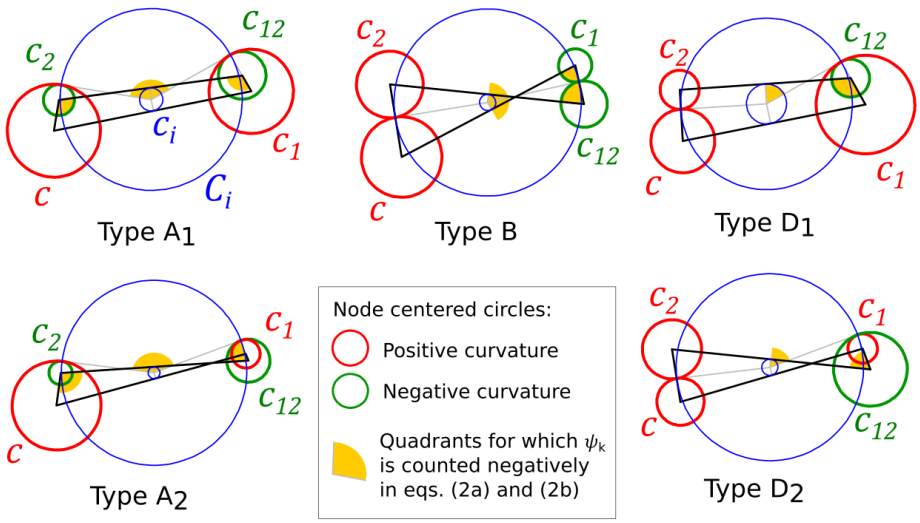

Figure 5.24: Tangency of circles for the five types of face with a change of curvature sign (larger node centered circles not shown for clarity)

Figure 5.25: An illustration of the five types of fold with a piece of fabric

5.5.2 Reconstruction of the surface

Proposition 5.4

Each of the five proposed Gauss map folds can yield a transition part between synclastic and anticlastic portions of a mesh that conserves the S-CMC property.

Proof:

We will only prove the result for faces of type A_1: The proof follows the exact same pattern for other face types. Looking at one face $QQ_1Q_{12}Q_2$ on Figure 5.26, we notice that we can pack spheres of radius $(R_i+r_i)/2$ at Q and Q_1 and $(R_i-r_i)/2$ at Q_2 and Q_{12} to form a quad with an inscribed circle:

$$(R + R_1)u + (r_1 - r_{12})v_1 - (R_{12} + R_2)u_2 - (r - r_2)v = 0$$

$$(r + r_1)u + (R_1 + R_{12})v_1 + (r_{12} + r_2)u_2 - (R + R_2)v = 0$$

$$\Rightarrow \quad \left(\frac{R + r}{2} + \frac{R_1 + r_1}{2}\right)u + \left(\frac{R_1 + r_1}{2} + \frac{R_{12} - r_{12}}{2}\right)v_1 - \left(\frac{R_{12} - r_{12}}{2} + \frac{R_2 - r_2}{2}\right)u_2 - \left(\frac{R_2 - r_2}{2} + \frac{R + r}{2}\right)v = 0$$

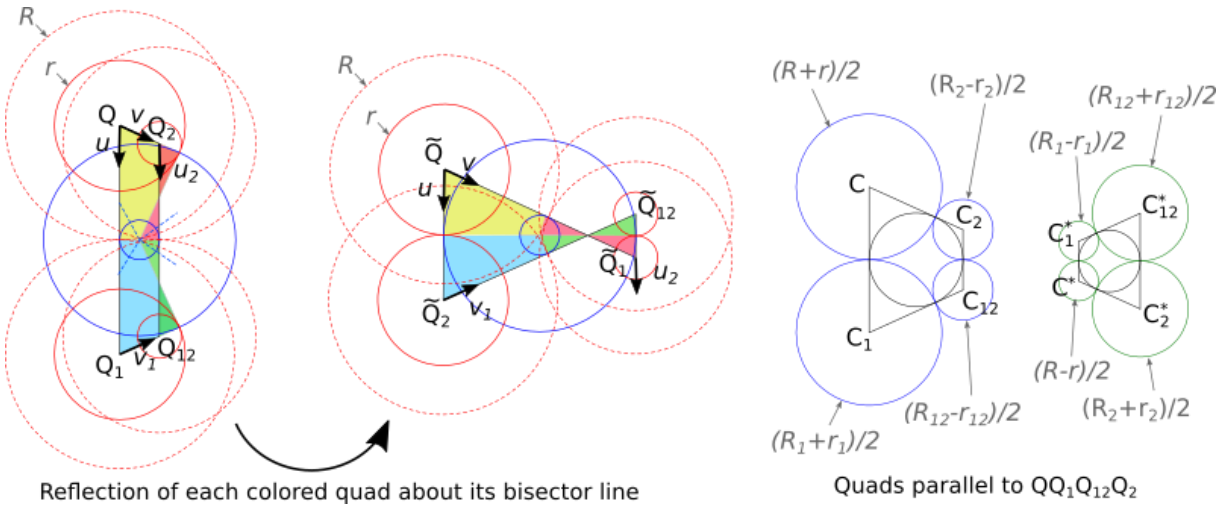

Figure 5.26 : Construction of faces with inscribed circle from a Gauss face of type A_1 (circle radii are indicated in grey with an arrow)

Note that the same result can be achieved with spheres of radii $(R_i\text{-}r_i)/2$ at Q and Q_1 and $(R_i\text{+}r_i)/2$ at Q_2 and Q_{12}:

$$-\left(\frac{R-r}{2}+\frac{R_1-r_1}{2}\right)u+\left(\frac{R_1-r_1}{2}+\frac{R_{12}+r_{12}}{2}\right)v_1+\left(\frac{R_{12}+r_{12}}{2}+\frac{R_2+r_2}{2}\right)u_2-\left(\frac{R_2+r_2}{2}+\frac{R-r}{2}\right)v=0$$

If we look at a strip of quads (*i.e.* a mesh with only one row) of type A_1, we can now obtain a strip of S-isothermic mesh Str^+. Vertices can be assigned a sphere or radius $(R_i\text{+}r_i)/2$ on side of the strip and $(R_i\text{-}r_i)/2$ on the other side.

If we now look at $Str^* = Str^+ + n$, the same reasoning as in the proof of proposition 5.3 shows that Str^* is the dual and a Darboux transform of $Str+$. Therefore, $Str+$ is S-CMC. It can thus connect an S-CMC mesh with spheres of radii $(R+r)/2$ (synclastic) to an S-CMC mesh with radii $(R-r)/2$ (anticlastic). Figure 5.27 shows the connection of the face A_1 with adjacent faces.

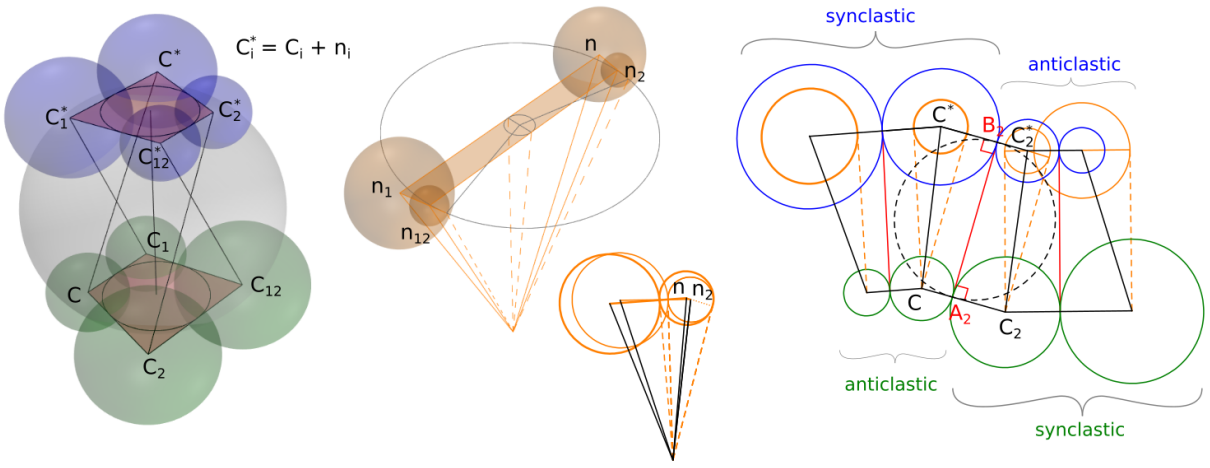

Figure 5.27 : Arrangement of spheres at a face of type A_1. Left: The face and its dual form a Darboux pair ; Middle: Corresponding Gauss map in 3D and in side view including adjacent faces ; Right: Side view of M and M*.

It can be noted that equations (5.2a) and (5.2b) need to be modified on the fold of the Gauss map: the angles ψ_k shall be counted negatively at locations shown on Figure 5.24. The type of quad is thus a necessary input of the algorithm. The convergence is much less robust when there is a change of curvature.

5.6 Applications and discussion

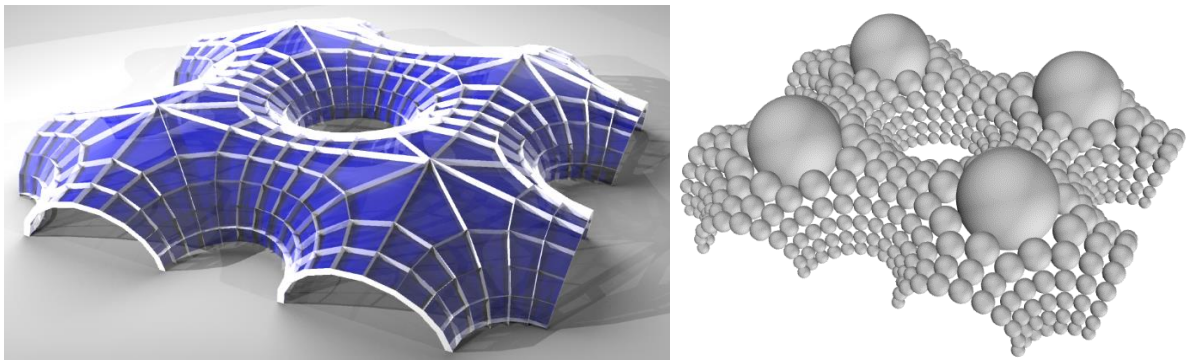

Figure 5.28 : An S-CMC mesh with changing curvature sign

Examples

The unduloid is a periodic cylindrical CMC. Although a discrete S-CMC unduloid can be generated analytically by a so-called elliptic billiard, as explained in Hoffmann (2010), the unduloid shown in Figure 5.11 was generated with the proposed framework, using as input the smooth unduloid.

Figure 5.1 shows an S-CMC version of the trinoid, another well-known CMC surface. Singularities, such as the valence-6 node at the center, can be efficiently handled by the method. The constant t for this mesh is 1.004. Therefore, the edge offset in the higher curvature direction is only 0.4% lower than in the lower curvature direction. This fact is particularly interesting considering one major limitation of the edge offset meshes: at locations of a surface where there is a significant difference between the higher and the lower principal curvature, faces are highly elongated. This effect can be observed in (Pottmann *et al.* 2007). In the case of this trinoid, we observe that by allowing a slight change between the edge offsets in the two curvature directions, we can obtain faces with an aspect ratio close to one. Furthermore, the difference between the two offsets is low enough to be considered as a regular edge offset for fabrication purposes. Finally, it is important to note that this S-CMC mesh can fulfill the properties (planarity, offset, etc.) with arbitrary precision.

Figure 5.28 shows an S-CMC mesh with changing curvature sign. The associated sphere packing is shown on the right. The mesh is generated from a portion of 4-noid, and successive reflections yield the full mesh. The eight-valent nodes could be replaced by planar octagons for improved uniformity of panel sizes.

Figure 5.29 shows multiple morphologies that can be obtained with a given trinoid combinatorics. The boundaries of the meshes are planar, this simplifies the fabrication of the edge beams. The various shapes are obtained by varying the position and orientation of the boundary planes.

Figure 5.30 shows a mesh in which multiple singularities are positioned along the boundary. This allows to obtain a curved CMC with relatively uniform face sizes.

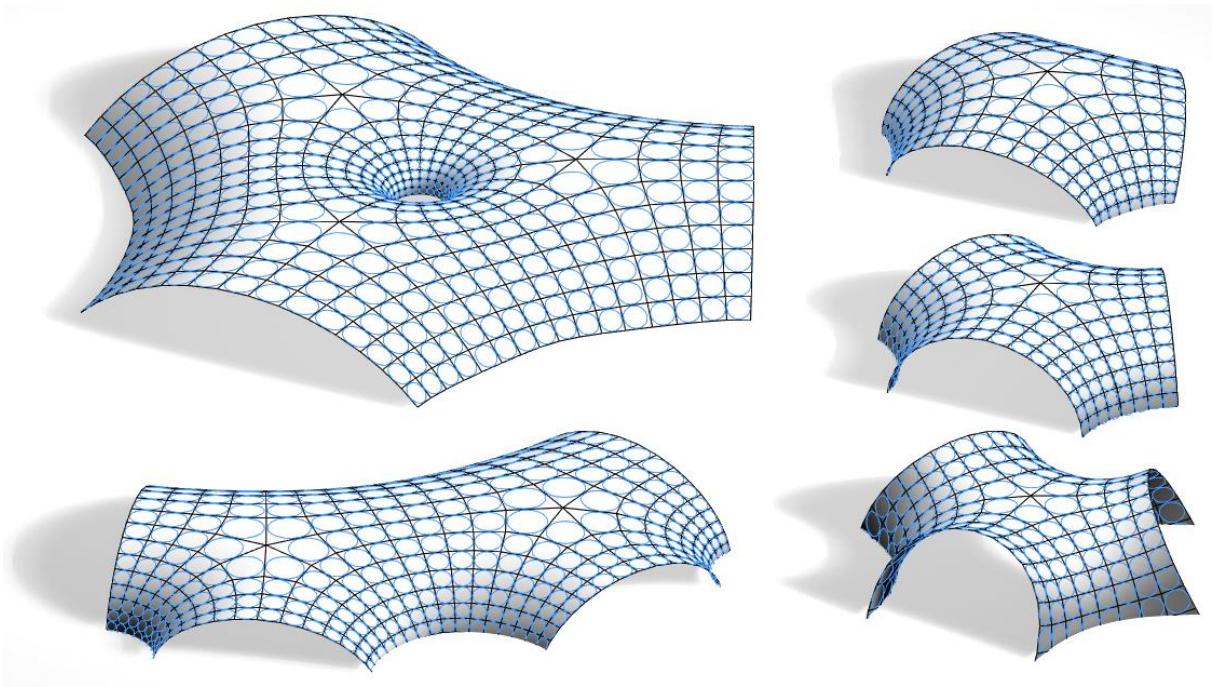

Figure 5.29 : Several S-CMC trinoids. Left: combining three and two trinoids ; Right: different ways to "inflate" a trinoid

Periodic surfaces

Triply periodic surfaces (i.e. periodic in x, y and z), like the ones showed in Figure 5.31, can be discovered by controlling the Gauss map instead of trying to fit a target surface. These two surfaces were generated from the same base patch, highlighted in red, which is then iteratively mirrored – with an additional vertical translation for the bottom one. To generate the Gauss map of this patch, the boundary angles are set to 90° at corners and 180° everywhere else, as the patch is bordered by planar curvature lines. Three additional constraints are added to force the sum of the radii along borders B_1 and B_2 to be 90°, and the sum along B_4 to be 0°. These constraints are added to the system of equations. As the system of equation is overconstrained (there are more equations than variables), a quadratic trust-region algorithm was used instead of Newton-Raphson. Resulting surfaces have a C1 junction along the straight lines (boundary B_4), the mean curvature changes sign across the line.

Limitations

The following limitations apply:

- As with other types of meshes with torsion-free nodes, S-CMC meshes can be interpreted as a curvature line network. As such, one cannot choose the orientation of the mesh.
- The final geometry is highly dependent on the combinatorics of the curvature line network. The isothermic condition and the positioning of singularities on umbilics can be difficult to obtain with commercially available software. Furthermore, the network (and therefore the S-CMC mesh) might need significant refinement when some umbilics are located close to each other.
- In the meshes shown in this chapter, boundaries are planar curvature lines. Other types of boundaries can be difficult to fit with this method. They would require an additional preprocessing. For example, if a target boundary is not a curvature line, one could cut the surface near the boundary in a zigzag following curvature lines in one of the two directions. Because of this preprocessing, the method is less likely to approximate well the target surface, and would require an additional optimization loop on the boundary angles. The overall process then becomes labor intensive.

- CMC surfaces that are not simply connected (e.g. surfaces with holes) need periodicity constraints on the top of the ones given in Section 5.4.2 to ensure proper closing.
- When a surface has both synclastic and anticlastic portions, the user needs to input the curvature sign of each vertex to let the algorithm know which faces are of type A, B, C and D. Trials and errors are often required. A wrong choice leads to non-convergence: Equations 5.2 are then not fulfilled exactly. However, vertices with improper sign choice can usually be spotted by the fact that the face radius tends to 0. Signs can therefore be iteratively adjusted until convergence is met.

Comparison with other generation methods

S-CMCs could also be generated by optimizing directly a mesh built from a curvature line network on a smooth CMC. Both vertex positions and vertex normals would need to be optimized simultaneously, as in the proposed method for generating Caravel meshes from a reference surface. This would make the optimization quite more complex than for circular and conical meshes, for which vertex positions are the only variables. An advantage of such a method would be a stronger control of the boundary, allowed by the ability to "relax" the S-CMC property and the fact that positions are variables, rather than circle radii. Comparatively, the proposed method uses less degrees of freedom, fulfills the S-CMC property exactly and fit boundaries in an approximate manner. Although less suited for a boundary problem, the control of the Gauss map allows to construct symmetrical and periodical surfaces. A surface like the one showed in Figure 5.31 would be hard to generate by controlling boundaries of the surface, in particular because it is not possible to control both the position and the slope of a CMC along a closed boundary.

Generation of non-CMC meshes with orthotropic edge offset

The proposed algorithm generates ODCPs on the unit sphere, which give a Gauss mesh with planar faces, torsion-free nodes and orthotropic edge offset. In this chapter, this Gauss mesh was only used to construct S-CMCs. However, these properties are conserved by arbitrary parallel transformations. By combining the Gauss map generator with these transformations, it is possible to generate a wider range of meshes (much wider than CMCs) with orthotropic edge-offset. This could be explored in future work.

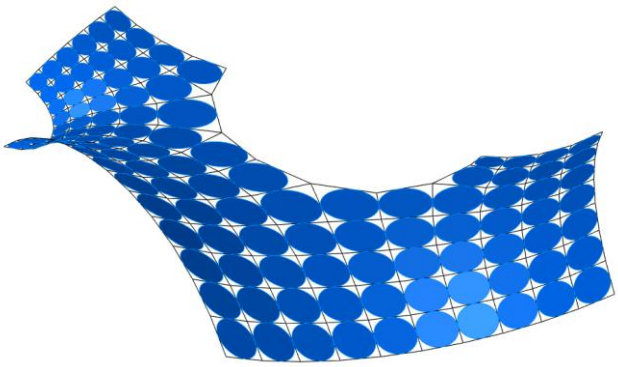

Figure 5.30 : S-CMC mesh with singularities at the boundary

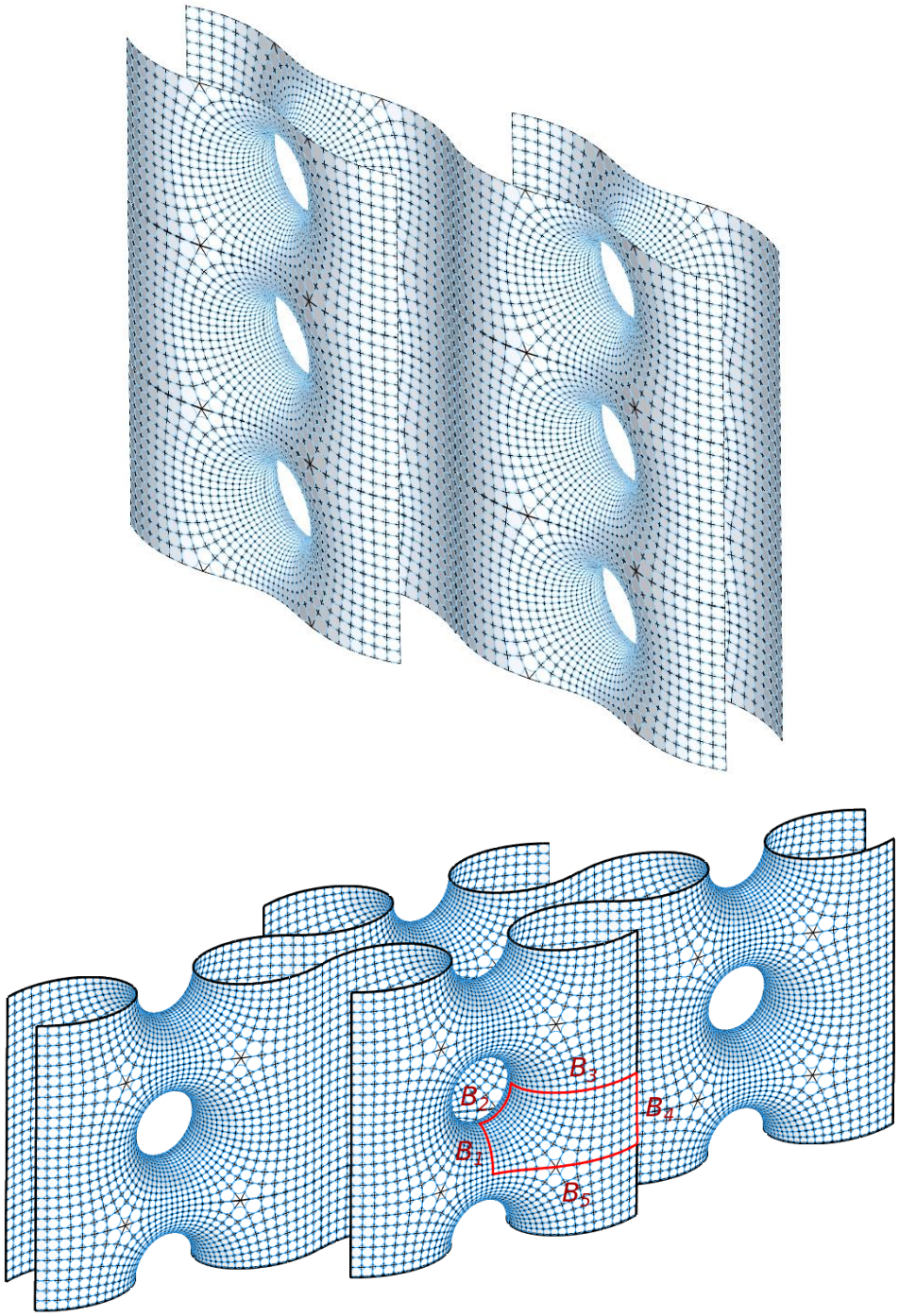

Figure 5.31 : Two triply periodic surfaces created by joining S-CMC patches

5.7 Summary of contributions

This chapter identified the potential of S-CMC meshes for construction-aware design of free-form architectural envelopes. It proposed a method to generate them by discretizing smooth CMCs. A discrete geometrical structure of the Gauss map was developed, based on circle packings. It was showed how this Gauss map structure yields meshes with orthotropic edge offsets. It can also deal with a change in curvature sign of the surface – this being a usual limitation when trying to control a surface from its Gauss map. The morphological potential of S-CMCs was demonstrated on several examples.

References

Abresch, U. (1987) 'Constant mean curvature tori in terms of elliptic functions', *Journal fur die Reine und Angewandte Mathematik*, (374), 169–192.

Bach, K., Burkhard, B., Otto, F. (1988) *IL18 Forming Bubbles*, Institute for Lightweight structures, University of Stuttgart.

Bobenko, A.I., Hoffmann, T. (2016) 'S-Conical CMC Surfaces. Towards a Unified Theory of Discrete Surfaces with Constant Mean Curvature', in *Advances in Discrete Differential Geometry*, 287–308.

Bobenko, A.I., Hoffmann, T., Rörig, T. (2019) *Orthogonal Ring Patterns*, available: http://arxiv.org/abs/1911.07095 (November 2019).

Bobenko, A.I., Hoffmann, T., Springborn, B.A. (2006) 'Minimal surfaces from circle patterns : Geometry from combinatorics', *Annals of Mathematics*, 164, 231–264.

Bobenko, A.I., Romon, P., May, D.G. (2017) 'Discrete CMC surfaces in R3 and discrete minimal surfaces in S3 . A discrete Lawson correspondence', 1–13.

Bouaziz, S., Deuss, M., Schwartzburg, Y., Weise, T., Pauly, M. (2012) 'Shape-Up : Shaping Discrete Geometry with Projections', *Eurographics Symposium on Geometry Processing*, 31.

Brakke, K.A. (1992) 'The surface evolver', *Experimental Mathematics*, 1(2), 141–165.

Bücking, U. (2007) 'Approximation of conformal mappings by circle patterns and discrete minimal surfaces', *PhD diss., Technischen Universität Berlin*.

Delaunay, C. (1841) 'Sur la surface de revolution dont la courbure moyenne est constante', *J. Math. Pures et Appliquées*, 6, 309–320.

Dorfmeister, J., Pedit, F., Wu, H. (1998) 'Weierstrass type representation of harmonic maps into symmetric spaces', *Communications in Analysis and Geometry*, 6(4), 633–668.

Gray, A. (1998) *Modern Differential Geometry - Curves and Surfaces with Mathematica*.

Grosse-Brauckmann, K. (1993) 'New surfaces of constant mean curvature', *Mathematische Zeitschrift*, 214, 527–565.

Gutierrez, C., Sotomayor, J. (1986) 'Principal lines on surfaces immersed with constant mean curvature', *Transactions of the american mathematical society*, 293(February).

Hertrich-Jeromin, U., Pedit, F. (1997) 'Remarks on the Darboux Transform of Isothermic Surfaces', *Documenta Mathematica*, 2, 313–334.

Hoffmann, T. (2010) 'A Darboux transformation for discrete s-isothermic surfaces', *Journal of Math-for-Industry*, 2((2010B-6)), 157–169.

Kapouleas, N. (1991) 'Compact constant mean curvature surfaces in Euclidean three-space.', *Journal of Differential Geometry*, 33(3), 683–715.

Karcher, H. (1989) 'The triply periodic minimal surfaces of Alan Schoen and their constant mean curvature companions.', *Manuscripta mathematica*, 64(3), 291–357.

Kenmotsu, K. (1979) 'Weierstrass formula for surfaces of prescribed mean curvature', *Mathematische Annalen*, 245(2), 89–99.

Kenmotsu, K. (2003) *Surfaces with Constant Mean Curvature*.

Lawson, H.B. (1970) 'Complete minimal surfaces in S3', *Annals of Mathematics*, 92(3), 335–374.

Mazzeo, R., Pacard, F. (2001) 'Constant mean curvature surfaces with Delaunay ends.', *Communications in Analysis and Geometry*, 9(1), 169–237.

Oberknappl, B., Polthier, K. (1997) 'An Algorithm for Discrete Constant Mean Curvature Surfaces', *Visualization and Mathematics*, 141–161.

Pan, H., Choi, Y.-K., Liu, Y., Hu, W., Du, Q., Polthier, K., Zhang, C., Wang, W. (2012) 'Robust modeling of constant mean curvature surfaces', *ACM Transactions on Graphics (TOG)*, 31(4), 11–85.

Pottmann, H., Liu, Y., Wallner, J., Bobenko, A.I., Wang, W. (2007) 'Geometry of multi-layer freeform structures for architecture', *ACM Transactions on Graphics*, 26(3), 65.

Schmitt, N. (2001) 'CMCLab', available: http://www.gang.umass.edu/software/cmclab/.

Schoen, R. (1983) 'Estimates for stable minimal surfaces in three dimensional manifolds', in *Seminar on Minimal Submanifolds*, Princeton Univ. Press., 111–126.

Wente, H.C. (1986) 'Counter example to a conjecture of H. Hopf', *Pacific Journal of Mathematics*, 121(1), 193–244.

Chapter 6 Linear Weingarten surfaces

CMC surfaces studied in the previous chapter offer one degree of freedom to a designer to construct a surfaces on a given boundary. CMC surfaces actually belong to a wider family: elliptical Linear Weingarten (LW) surfaces. Similarly to CMCs, LW surfaces – like the ones showed in Figure 6.1 – can be generated from closed boundary curves and have remarkable mechanical properties under a uniform pressure load. However, compared to CMCs, they offer an additional degree of freedom, thus enlarging the design space.

The formal potential of LW surfaces has not been explored, mainly because of the lack of generation method. Part A of this chapter fills this gap by introducing a generative algorithm. It is based on the optimization of the vertex coordinates of triangular meshes. A key to the robustness of the algorithm is the identification of two sub-families of elliptical LW surfaces, namely type I and II. The use of triangular meshes is a major difference with the previous chapter: mesh edges will not correspond to beams anymore, a quad remeshing is necessary to obtain the beam layout of a gridshell. However, this formulation is much better suited for controlling a surface from its boundaries.

Part B shows how the properties of CMC and LW surface under a pressure load can be transposed to a vertical load with the isotropic CMC and Linear Weingarten surfaces (i-CMC, i-LW). Based on discrete models of isotropic geometry, a generation method similar to LW surfaces is proposed.

LW and i-LW surfaces appear to be interesting tools for membrane, shell and gridshell design, by allowing a designer to design surfaces with both fabrication and mechanical properties.

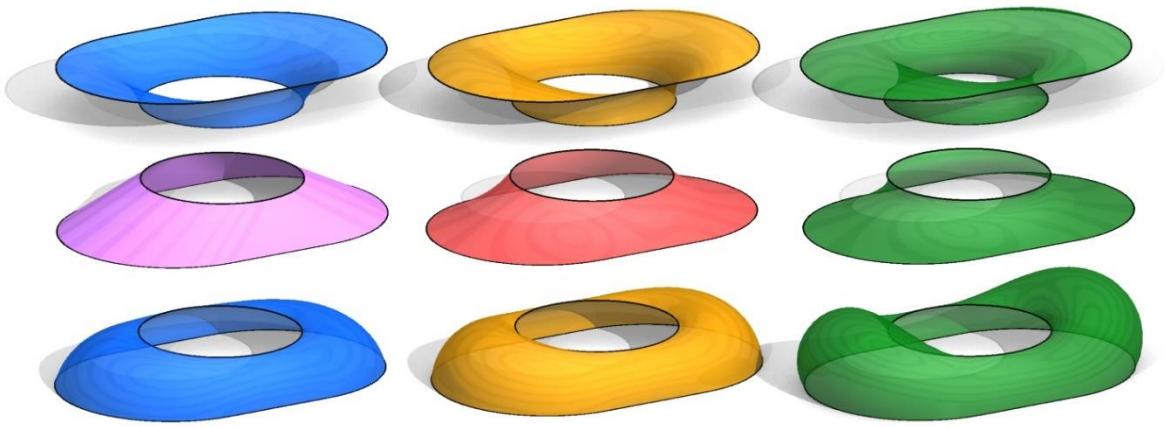

Figure 6.1: These nine triangulated surfaces are Linear Weingarten: they verify at each point a relation aH+bK=c with constant parameters (a,b,c). They are generated on the same two boundary curves (top row is mirrored about the horizontal plane), but with different values of parameters (a, b,c). Red: Minimal surface (H=0). Orange: CMC surfaces (H=c). Purple: developable surface (K=0). Green and blue: Linear Weingarten surfaces with respectively b>0 and b<0. Top, middle, bottom rows: c>0 (funicular surfaces), c=0 (self-stressed surfaces), c<0 (funicular). Left, middle, right columns: b<0, b=0, b>0.

Part A - Euclidian LW surfaces

Linear Weingarten (LW) surfaces are a wide family of surfaces that contains in particular minimal, constant mean curvature (CMC) and developable surfaces. LW surfaces remarkably combine geometrical and mechanical properties, exposed in section 6.1. Section 6.2 to 6.4 expose a new generation method of these surfaces. First, a discrete model by triangular meshes is exposed (section 6.2). Then, section 6.3 presents some preliminary analytical studies on which the generation method (section 6.4) is based. This method can be used to explore the geometry of LW surfaces (section 6.5). Two applications to architectural design are identified: the first one is the design of tensile membranes, the second one is the design of gridshells that combine structural efficiency and fabricability (section 6.6). Finally, section 6.7 shows how LW surfaces can model membranes with boundary cables and funicular vaults with openings, and shows how the generation method can be adapted for that purpose.

6.1 Review of properties

Linear Weingarten (LW) surfaces are characterized by the fact that a linear combination of their Gaussian and mean curvature is constant:

$$aH + bK = c \quad / \quad a, b, c \in \mathbb{R} \tag{6.1}$$

where a and b are not both null. These surfaces are a subset of the Weingarten surfaces, i.e. the surfaces for which there exist a real smooth function U such that at any point $U(H, K) = 0$. Those were introduced by Weingarten to study the surfaces isometric to surfaces of revolution (Weingarten 1861).

LW surfaces, such as the ones shown in Figure 6.1, have many interesting properties for computer-aided design and for the design of curved structures. They have been well studied by mathematicians. However, to the best of our knowledge, their application to design, and in particular to architectural design, has been hardly explored. For example, a search in Scopus (as of August 2019) for "Linear Weingarten" in the title or key-words yields 91 articles, all of them being published in mathematical journals. These 91 articles are also only cited in mathematical journals - apart from (Van-Brunt and Grant 1996) that looked at properties of nonlinear Weingarten surfaces for CAD. One major issue for their use in design is probably the absence of a general generation method. The few articles that address generation of LW surfaces focused on particular sub-families of LW surfaces, such as hyperbolic LW surfaces of revolution (López 2008), channel LW surfaces (Hertrich-Jeromin *et al.* 2015) and LW surfaces invariant by Ribeaucour transforms (Corro *et al.* 2003).

A vast list of properties has been discovered about LW through the past centuries. In the next two sub-sections, we will review properties that are relevant to their generation, the understanding of their morphology, and their applications to CAD and architecture.

6.1.1 Geometrical properties

For a given parametrized surface S, equation (6.1) is a second order partial differential equation on the parametrization. (Hopf 1983) showed that if $a^2 + 4bc > 0$, the equation is elliptic – the surface being then called *LW elliptic*. In that case, one can solve the following Dirichlet problem: building a surface with a prescribed closed boundary curve. This condition is automatically fulfilled for minimal and CMC surfaces, as they verify $b = 0$. (Reilly 1973) showed that LW surfaces are the critical points of the following functional E:

$$E(S) = \frac{a}{2} Area(S) + bH_{tot}(S) + cVol(S) \quad (6.2)$$

In which *Area(S)* is the area of the surface *S*, *Vol(S)* is the volume under the surface, and $H_{tot}(S)$ is the total mean curvature, defined as the integral of the mean curvature over the whole surface.

LW surfaces also correspond to the offset of a minimal surface if $c = 0$, and to the offset of a constant Gaussian curvature or CMC surface if $c \neq 0$ (Eisenhart 1909). More precisely, the offset at distance t of a minimal (resp. an H-CMC) surface is a LW surface with parameters $(a, b, c) = (1, t, 0)$ (resp. $(a, b, c) = (\frac{1}{H} - 2t, \frac{t}{H} - t^2, 1)$). The offset of any LW surface is actually also a LW surface: this family of surface is invariant by offsetting.

One interesting consequence of this offset property is that LW surfaces inherit the fairness and regularity of the curvature line networks of CMCs. Curvature lines have many applications for rationalization of curved architectural envelopes (Pottmann *et al.* 2007). A strong limitation is that, on an arbitrary surface, they usually form a network with bad structural properties and unaesthetic: This is not the case for LW surfaces.

Hartman and Wintner (Hartman and Wintner 1954) studied *special* Weingarten surfaces, for which the function U such that $U(H, K) = 0$ verifies $\frac{1}{2} U_H + H\, U_K \neq 0$ when $K = H^2$. They proved that any umbilic point of a non-planar, non-spherical portion of a special Weingarten surface is necessarily isolated, and its index is negative. If $a^2 + 4bc \neq 0$, a LW surface falls into that category. Therefore, for a non-spherical LW surface, umbilics are isolated, and their index is negative. As a consequence, their cannot be an umbilic of index +1/2 like the one showed in section 4.4.3.

(Van-Brunt and Grant 1996) pointed out some other applications of Weingarten surfaces (linear or not). For example, surface investigation is made easier, and curvature lines can be obtained by quadrature: If we have two secant curvature lines on a LW triangular mesh, we can construct a grid of curvature lines without having to diagonalize shape operators. However, they do not propose a method to generate these surfaces.

For architectural purposes, one interesting property of Weingarten surfaces is mentioned in (Jimenez *et al.* 2019). The covering of an envelope with double-curvature panels necessitates the fabrication of many costly molds. Since there is only a one-parameter family of osculating paraboloids on Weingarten surfaces (as illustrated in Figure 6.7), they are likely to be covered using a small number of molds.

From a designer point of view, elliptical LW surfaces allow to control globally complex shapes from their boundary and two sliders (i.e. two parameters). This is illustrated in Figure 6.2. This will be detailed in section 6.5.2.

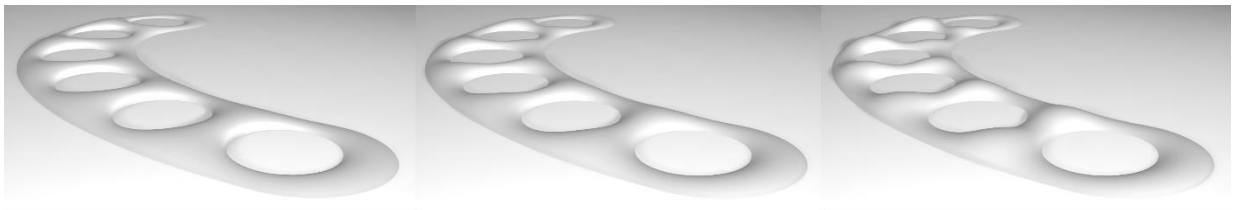

Figure 6.2: Linear Weingarten surfaces allow a global shape control. Starting from a CMC (middle), the user can control the height difference between saddle points and "hill tops" with just one slider

6.1.2 Mechanical properties

(Rogers and Schief 2003) showed an interesting link between LW surfaces and shell mechanics. LW surfaces correspond to equilibrium shapes of membranes under uniform pressure. Membranes are highly efficient mechanical structures: they are shell structures that can resist a given load with pure in-plane stresses, without bending stresses. Furthermore, for a LW membrane subject to uniform pressure of amplitude c, membrane stresses are known explicitly, and principal stresses are aligned with principal curvature directions:

$$N_{11} = a + \frac{b}{2}k_2 \tag{6.3}$$

$$N_{22} = a + \frac{b}{2}k_1 \tag{6.4}$$

$$N_{12} = 0 \tag{6.5}$$

Where directions 1 and 2 are the principal curvature directions, k_1 and k_2 are the associated principal normal curvatures, and N_{ij} are the components of the membrane stress tensor $\mathbf{N}$. These equations can be written in intrinsic form:

$$\mathbf{N} = a\mathbf{I} + \frac{b}{2}\hat{\mathbf{S}} \tag{6.6}$$

Where $\mathbf{I}$ is the identity of the tangent plane of the surface and $\hat{\mathbf{S}}$ is the curvature tensor (known as shape operator in surface theory), rotated by 90° in the tangent plane. It can be expressed as $\hat{\mathbf{S}} = \mathbf{J}\,\mathbf{S}\,\mathbf{J}^{-1}$, where $\mathbf{J} = \begin{bmatrix} 0 & 1 \\ -1 & 0 \end{bmatrix}$.

A particular case is obtained when $c = 0$: the LW surfaces then correspond to self-stressed membranes, like the ones showed in Figure 6.3. The fact that stresses are known analytically allows to give quick structural feedback to the designer, without having to transfer the geometry to an FE software. Such an application will be further detailed in section 6.6.

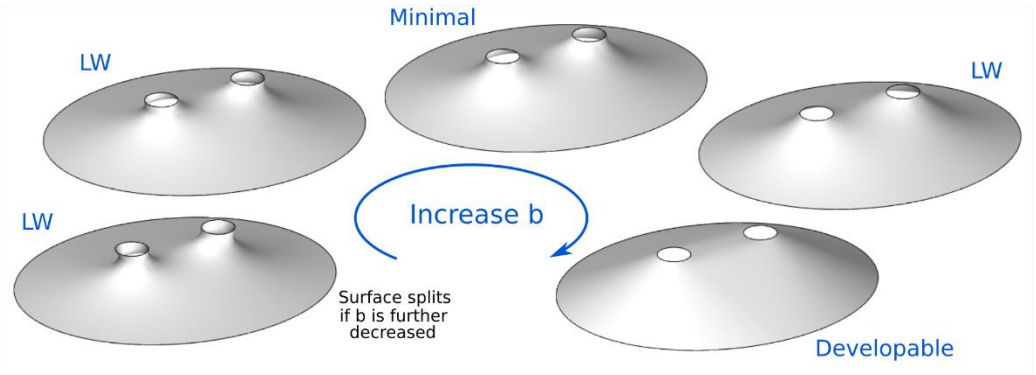

Figure 6.3 Linear Weingarten surfaces with c=0 generated on the boundaries of a circus big top tent. Each shape is the equilibrium position of a self-stressed membrane. These shapes can be transformed one into another by controlling the weight of the total mean curvature in the minimization process exposed in section 6.4. Modifying this weight changes the prestressing ratio between principal curvature directions.

6.2 Discrete model

In this section, we introduce a new discrete model of LW surfaces. The definition is variational and will allow generation by a minimization process in section 6.4.

6.2.1 Variational definition

By similarity with equation (6.2) in the smooth case, we define discrete LW surfaces as the critical points of a functional:

Definition: A triangular mesh T with a prescribed boundary is called Linear Weingarten if it is a critical point of the following functional:

$$E_1(T) = \frac{a}{2} Area(T) + bH_{tot}(T) - cVol(T) \tag{6.7}$$

Which means that at each vertex p of T, the following relationship holds:

$$\nabla_p E_1(T) = \frac{a}{2} \nabla_p Area(T) + b \nabla_p H_{tot}(T) - c \nabla_p Vol(T) = 0 \tag{6.8}$$

Where $Area(T)$, $Vol(T)$ and $H_{tot}(T)$ are respectively the mesh area (the sum of the area of the faces), the volume under the mesh and the total mean curvature. There exists several discrete models for the mean curvature of a mesh. We choose the one proposed by (Cohen-steiner and Morvan 2006), in which the mean curvature is defined on the edges. We define the total mean curvature of a triangular mesh as the sum of the mean curvature of each edge:

$$H_{tot}(T) = \sum_{e \in T} \mathrm{H}(e) = \sum_{e \in T} \frac{1}{2} \|\vec{e}\| \theta_e \tag{6.9}$$

in which θ_e is the dihedral angle of edge e, defined as the signed angle between the normals of the adjacent faces. Boundary edges require a specific treatment: We compute the dihedral angle of an edge as the angle between the adjacent face and a virtual arbitrary fixed face. The resulting total mean curvature is then defined up to an arbitrary constant.

Sign convention

The signs and normal orientations are critical in the formulas introduced above, and deserve a short clarification. In this chapter, we only work with orientable surfaces. A half-edge data structure (see for example (Botsch *et al.* 2010)) is used in the algorithms, and helps clarifying the mean curvature sign: Once the orientation of the normals is chosen, the sign of the diedral angle and mean curvature of an edge is induced as follows:

$$H(e) > 0 \Leftrightarrow \theta_e > 0 \Leftrightarrow \det(n_1, n_2, he_2) > 0$$
$$H(e) < 0 \Leftrightarrow \theta_e < 0 \Leftrightarrow \det(n_1, n_2, he_2) < 0$$

Notations are explained in Figure 6.4 (left) (note: half-edges always loop around the face following a "cork-screw" direction given by the face normal).

We refer as "volume of a surface" the volume on the side of the normal. This value is defined up to an arbitrary constant. Therefore, the gradient of the volume is in a direction opposite to the normal.

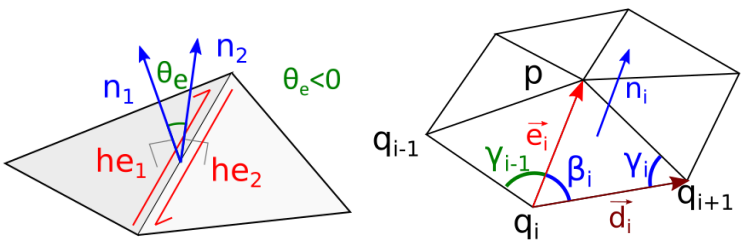

Figure 6.4: (Left) Sign convention for the dihedral angles. (Right) Derivation of gradient of total mean curvature.

6.2.2 Gradient

The gradient of E_1 will be needed for minimization purposes. The gradient of the area and of the volume of a triangular mesh with respect to the position of a vertex p are well known (see for example (Romon 2013)):

$$\nabla_p \text{Area(T)} = \frac{1}{2} \sum_{opposite\ e} J\vec{e}$$

where J is an operator that applies a +90° rotation in the plane of the face (the orientation is given by the face normal) and where the sum is taken over the edges at the boundary of the 1-star of p.

$$\nabla_p \text{Vol(T)} = -\frac{1}{6} \sum_{opposite\ e} q_i \wedge q_{i+1} = -\frac{1}{3}\vec{A}_p$$

where $\wedge$ denotes the vector cross product, and $\vec{A}_p$ is the *vector area* of the star of p. The vector area of a surface is defined as the integral of the normal vector $\vec{A}_S = \iint_S \vec{n}\, dA$. This quantity depends only on the geometry of the boundary, such that we can by extension refer to the vector area of a 3D curve. The discretization to a segmented closed line (which is used above) is given for example in (Crane 2013).

The gradient of the total mean curvature has apparently not been published in the literature. It turns out that the choice of discrete mean curvature model yields a remarkably compact expression:

Proposition 6.1: The gradient of the total mean curvature of mesh given by equation 6.9 with respect to the position of an interior vertex p is:

$$\nabla_p H_{tot}(T) = \sum_{adjacent\ e} \frac{1}{2}\theta_e \frac{\vec{e}}{L_e} \tag{6.10}$$

where $L_e = \|\vec{e}\|$ is the length of edge $\vec{e}$, and where the sum is taken over the edges adjacent to p ($\vec{e}$ are incoming edge vectors).

Proof:
A displacement of a point p modifies the mean curvature of the edges adjacent to p, but also the curvature of the edges on the boundary of its 1-star (referred to as *opposite edges*), as illustrated in Figure 6.4 (right):

$$\nabla_p H_{tot}(T) = \sum_{\substack{all\ mesh \\ edges\ e}} \nabla_p H(e) = \sum_{\substack{incident \\ edges\ e}} \nabla_p H(e) + \sum_{\substack{opposite \\ edges\ d}} \nabla_p H(d) \tag{6.11}$$

Using the gradient of diedral angles given in (Wardetzky *et al.* 2007):

$$\sum_{\substack{incident \\ edges\ e}} \nabla_p \text{H}(e) = \sum_{incident\ e} \nabla_p \left(\frac{1}{2} L_e \theta_e\right)$$

$$= \sum_{incident\ e} \frac{1}{2} L_e\, \nabla_p \theta_e + \sum_{incident\ e} \frac{1}{2}\theta_e\, \nabla_p L_e$$

$$= \sum_{i\sim p} \frac{1}{2} L_{e_i} \frac{1}{L_{e_i}} [cot\, \gamma_i n_i + cot\, \beta_{i+1}\, n_{i+1}] + \sum_{i\sim p} \frac{1}{2}\theta_{e_i} \frac{p - q_i}{\|p - q_i\|} \tag{6.12}$$

Where the sums in the last line are taken over the indexes of the vertices q_i adjacent to p (indexes are numbered 1,2 ... v_p where v_p is the valence of p, with the convention $q_{v_p+1} = q_1$).

$$\sum_{\substack{opposite \\ edges\ d}} \nabla_p \mathrm{H}(d) = \sum_d \frac{1}{2} L_d \nabla_p \theta_d$$
$$= \sum_{i \sim p} \frac{1}{2} L_{d_i} \frac{-1}{L_{d_i}} [\cot \gamma_i n_i + \cot \beta_i\, n_i]$$
$$= \sum_{i \sim p} \frac{-1}{2} [cot\, \gamma_i n_i + cot\, \beta_{i+1}\, n_{i+1}] \tag{6.13}$$

Introducing equations (6.12) and (6.13) in equation (6.11), the cotangent terms cancel each other such that equality (6.10) is retrieved.

Note: The fact that the gradient depends only on the 1-ring is due to the linearity of expression (6.10) with respect to the dihedral angle: the position of the 2nd neighbors of a vertex p does not affect the rate of change of H_{tot} with respect to a displacement of p.

6.2.3 Discrete Gaussian curvature

For a smooth surface, the first order variation of H_{tot} is given by the Gaussian curvature (Giaquinta and Hildebrandt 1996; Overgaard and Solem 2007). More precisely, if a surface S is subjected to a small normal perturbation field ξ with an amplitude proportional to a parameter t such that the deformed surface is defined as $S_t = \{P + t\, \xi(P)\, n(P) \mid P \in S\}$, then the variation of the total mean curvature is given by:

$$\frac{d}{dt}\left(H_{tot}(S_t)\right)_{t=0} = \int_S -K\, \xi\, dA$$

To our knowledge, there is no discrete equivalent of this property. By similarity with the smooth case, we propose the following discrete model of the Gaussian curvature:

Definition: The discrete Gaussian curvature at a vertex p is:

$$\overrightarrow{K_p}(T) = -\sum_{edges\ e} \frac{1}{2} \theta_e \frac{\vec{e}}{\|\vec{e}\|} \tag{6.14}$$

Where the sum is taken over the incoming edge vectors at vertex p.

Comparison with angular defect

Quite a few discrete model for the discrete Gaussian curvature has been proposed in the literature (Xu and Xu 2009), but this one does not appear to have been proposed yet. The most popular ones use the angular defect at a vertex p divided by a measure of its tributary area, where the angular defect is defined as:

$$\alpha_p = 2\pi - \sum_{faces\ i} \alpha_i$$

where α_i is the angle at p of triangle i.

Contrary to the angular defect, the proposed model of K comes with an associated vector direction, and does not satisfy the Gauss-Bonnet theorem. However, both models behave asymptotically in a very similar

way. By "asymptotically", we refer to the case where a target surface is approximated by meshes with decreasing face sizes, such that edge lengths converge to zero. In that case, in the absence of crease on the target surface, the dihedral angles tend towards zero. Additionally, we restrict to meshes such that at each vertex, the set of normal vectors at each face adjacent to the vertex define a non-intersecting polygonal line in the unit sphere (like the one showed in Figure 6.5). We say that such a vertex is *simple*. Non-simple vertices do not tend to occur when a mesh approximates a smooth surface with vertices on the surface. The asymptotic behavior can be then quantified as follows:

Proposition 6.2: With θ_M being the maximum dihedral angle amongst the incident edges to a vertex p, for $\theta_M \to 0$:

$$\left\|\overrightarrow{K_p}(T)\right\| = \alpha_p\left(1 + O(\theta_M)\right) \quad where\ \alpha_p = O(\theta_M^2)$$

Proof:

We consider a point p of valence v in a mesh T which is a simple vertex. We start by remarking that $\overrightarrow{K_p}$ is the vector area of a portion of cone D_c with apex at point p, faces in the planes $(p, p+n_i, p+n_{i+1})$, and bounded by the unit sphere centered at p (Figure 6.5):

$$\overrightarrow{K_p}(T) = -\sum_{edges\ e} \frac{1}{2}\theta_e \frac{\vec{e}}{\|\vec{e}\|}$$

$$= -\sum_{edges\ e} A_e \frac{\vec{e}}{\|\vec{e}\|}$$

$$= -\overrightarrow{A_{D_c}}$$

where $A_e = \frac{1}{2}\theta_e$ is the area of a face of the cone D_c, which is a portion of disk of radius 1 and aperture θ_e. We call D_s spherical cap bounded by geodesic arcs $n_i n_{i+1}$. As the vertex is simple, the boundary of the cone is a closed curve of winding numer ± 1 (it does not form an 8 loop). Therefore the surface $D_s \cup D_c$ is closed, Stokes theorem implies that it its vector area is null: $\overrightarrow{A_{D_c}} + \overrightarrow{A_{D_s}} = \vec{0}$. Consequently, the proposed Gaussian curvature is merely the vector area of D_s:

$$\overrightarrow{K_p}(T) = \overrightarrow{A_{D_s}} = \int_{Ds} N dA$$

Each edge of D_s has length θ_e , hence its perimeter verifies:

$$P(D_s) \leq v\theta_M$$

The area of D_s is given by the angular defect (see for example (Romon 2013)): $\alpha_p = Area(D_s)$. As $P(D_s) \to 0$, the isoperimetric inequality yields:

$$\frac{\alpha_p}{P(D_s)^2} \leq c \ , c \in \mathbb{R}$$

Therefore:

$$\alpha_p = O(\theta_M^2)$$

The disc D_s converges uniformly to a point n_0. As two points in D_s are separated by a distance at most $P(D_s)/2$, we have:

$$n = n_0 + O(\theta_M)$$

All together, this implies that:

$$\frac{\|\overrightarrow{K_p}(T)\|}{|\alpha_p|} = \left|\frac{1}{\alpha_p}\int_{D_s} n\, dA\right| = \left|\frac{1}{\alpha_p}\int_{D_s} n_0\, dA + O(\theta_M)\right| = 1 + O(\theta_M)$$

which proves our estimate.

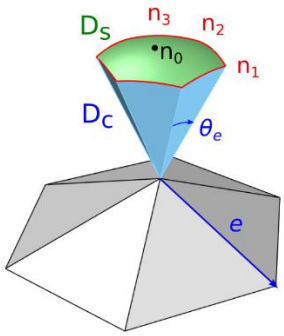

Figure 6.5: Star of a vertex *p*. The face normals n_i describe a spherical polygon D_s

6.2.4 Local definition

Using the usual definition of the discrete mean curvature vector of a point in a mesh as $\overrightarrow{H_p}(T) = -\frac{1}{2}\nabla_p \mathrm{Area(T)}$, we obtain the following result from equation (6.8):

Proposition 6.3: A mesh is LW if and only if at any vertex p:

$$a\,\overrightarrow{H_p} + b\,\overrightarrow{K_p} = c\,\frac{\overrightarrow{A_p}}{3} \tag{6.15}$$

This expression is a discrete equivalent of equation (6.1). We note that $\overrightarrow{H_p}$ and $\overrightarrow{K_p}$ are defined at the vertices, that can be understood as an integration of the mean and Gaussian curvatures over a tributary area of vertex p. In order to compare them with their smooth analogues, one need to normalize them by dividing them by a measure of this tributary area. By choosing this area as $\|\overrightarrow{A_p}\|/3$, we retrieve the same expression as equation (6.1).

Note: One could regret that our model uses two different discrete mean curvatures. Indeed, the mean curvature of a node defined as $\overrightarrow{H_p}(T) = -\frac{1}{2}\nabla_p \mathrm{Area(T)}$ is the sum of the mean curvature of the adjacent edges defined as $H_e(T) = \|\vec{e}\| \sin(\frac{\theta_e}{2})$ (see for example (Romon 2013)). This edge curvature model is different from the one we use to define H_{tot}.

Note 2: Conservation of invariance from the smooth setting has been at the core of many recent discrete models in the discrete differential geometry community (Bobenko and Suris 2008). As stated in section 6.2, smooth LW surfaces are invariant by offset. Because of the fact that $\overrightarrow{H_p}$, $\overrightarrow{K_p}$ and $\overrightarrow{A_p}$ have a different directions, it is highly unlikely that the proposed LW triangulations have exact analytical LW offsets (one cannot even find a good candidate for the offset direction at the nodes).

6.3 Preliminary studies

Before diving into generation in the next section, this section presents some analytical results on LW surfaces that will help understanding their behavior and the variety of solutions to a given boundary problem.

6.3.1 Elliptical LW of type I and II

Elliptical LW surfaces can be split in two families:

Proposition 6.4: For given parameters a,b,c such that $a^2 + 4bc > 0$, the LW surfaces verifying $aH + bK = c$ are divided into two families, namely type I and type II. Given two surfaces of different types and one arbitrary point on each surface, the two points cannot have identical mean or Gaussian curvature.

Proof:
One useful tool to study LW surfaces is the curvature diagram (Figure 6.6). This diagram gives the values of H and K for all points of a surface. At any surface point, the mean and Gaussian curvatures verify:

$$H^2 - K = \left(\frac{k_1 + k_2}{2}\right)^2 - k_1 k_2 = \left(\frac{k_1 - k_2}{2}\right)^2 \geq 0 \tag{6.16}$$

As a result, the red portion of the diagram bounded by a parabola cannot be reached. For a LW surface, the curvature diagram is included in the line given by equation (6.1) $aH + bK = c$. Basic calculations show that this line intersect the parabola $H^2 = K$ if and only if $a^2 + 4bc > 0$ (the line and the parabola are tangent if $a^2 + 4bc = 0$). This condition is precisely the condition for the surface to be elliptical, as discussed in section 6.1.1. In that case, the curvature diagram is included in the union of two rays (semi-infinite lines). In a smooth surface, curvatures vary continuously: the curvature diagram is connected. As a result, the curvature diagram of a LW surface cannot be on both rays. We will call *type I* (resp. *type II*) the elliptical LW surfaces having their curvature diagram entirely in the left (resp. right) ray. We remark that minimal and CMC surfaces can only be of type I, because their curvature diagram is horizontal.

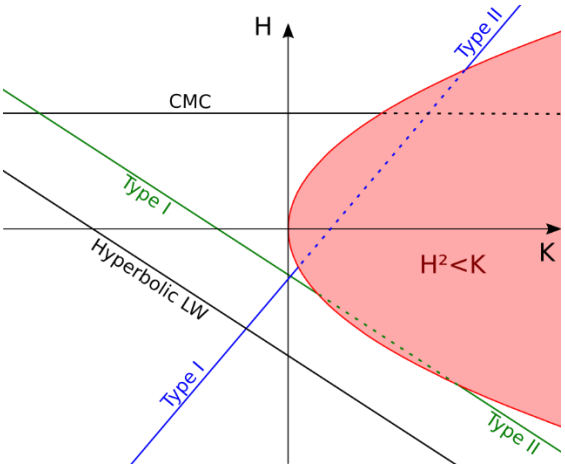

Figure 6.6: Curvature diagram of LW surfaces with various parameters (a,b,c)

6.3.2 Local geometry

In order to help the reader get intuition about the local geometry of LW surfaces, we illustrate in Figure 6.7 the curvature diagram of Figure 6.6 with portions of paraboloids $z = \frac{1}{2}(k_1 x^2 + k_2 y^2)$, where k_1 and k_2 are given by:

$$k_1 = H + \sqrt{H^2 - K}$$

$$k_2 = H - \sqrt{H^2 - K}$$

The local geometry of minimal surfaces and CMC surfaces with H=-1 are shown respectively in red and blue. In comparison we show in green the possible local geometries of a LW surface H+K=0.

The following observations can be made:

- For a type I surface, as K tends towards $-\infty$, one principal curvature gets much larger than the other one. This behaviour is very different from minimal surfaces, for which the ratio of principal curvatures is constant.
- When increasing b/a , this behavior is amplified until the surface becomes developable (column K=0).
- The LW condition $aH + bK = c$ is a strong restriction on the surface geometry: only a limited portion of the possible surface curvatures can be attained.

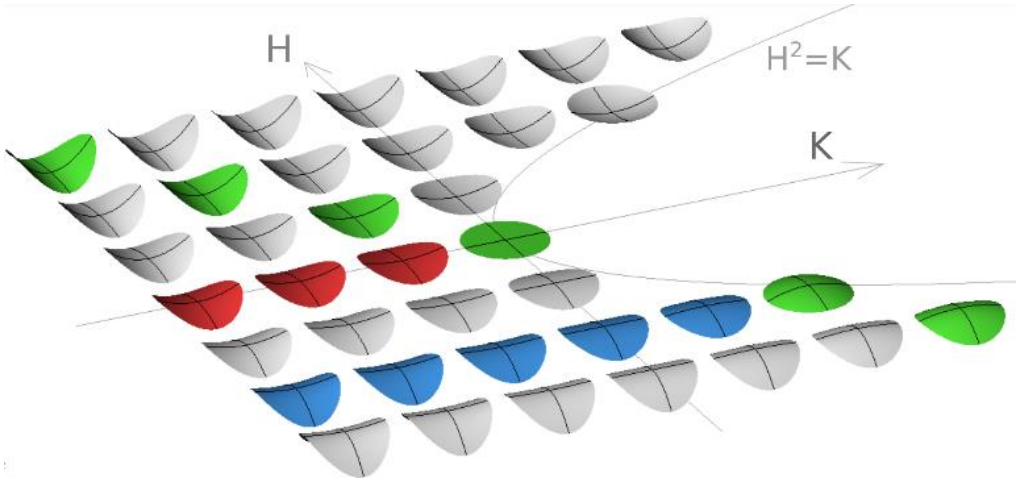

Figure 6.7: Local geometry of LW surfaces. Red: Minimal surfaces. Blue: CMC H=-1. Green: LW surfaces H+K=0

6.3.3 LW surfaces on a circular boundary

In this sub-section, we investigate the spherical LW surfaces fitting a circular boundary of unit radius (Figure 6.8) with upwards normal. This study provides valuable insight on the number of solutions of boundary problems and on whether they correspond to minima or maxima of E_1.

Number of solutions

Let us pick three parameters (a,b,c) verifying $a^2 + 4bc > 0$ and $a > 0$. On a sphere, we have $H^2 = \frac{1}{R^2} = K$. Therefore, a spherical cap satisfying $aH + bK = c$ verifies:

$$bH^2 + aH - c = 0$$

If $\boldsymbol{b = 0, a \neq 0}$, the surface is a CMC, we just get one possible value for H :

$$H = c/a$$

There are two CMC surfaces satisfying $H = c/a$: a small and a large spherical cap.

If $b \neq 0$, there are now two possible values for H. With $\Delta = a^2 + 4bc$, these values are:

$$H = \frac{-a \pm \sqrt{\Delta}}{2b}$$

The solutions with the smallest absolute mean curvature (and therefore the smallest Gaussian curvature) correspond to Type I LW surfaces, while the others are of type II. Similarly to the CMC case, each of these two values of H corresponds to two spherical caps. Therefore, there are now up to four possible LW surfaces satisfying the boundary condition: two caps of type I, and two caps of type II.

Since the boundary circle has a radius of 1, the radius of a spherical cap is necessarily higher than 1. As a result: $|H| < 1$. The existence of the four solutions is subjected to the conditions:

$$\left|\frac{-a \pm \sqrt{\Delta}}{2b}\right| \leq 1$$

Depending on the values of a,b,c, there can be 0,1,2 or 4 different solutions.

Maxima and minima of E_1

We can compute analytically the energies E_1 of spherical caps as a function of the sphere height. A cap of height z and base radius 1 is a portion of sphere of radius $r = \frac{1+z^2}{2z}$. Its area and volume are well-known formula:

$$Area(z) = \pi(1 + z^2)$$

$$Vol(z) = -\frac{\pi}{6}z(3 + z^2)$$

Note: As the normal is upwards, we use the volume *above* the spherical cap. For our purpose, we can define it up to an arbitrary constant. Hence, we define it as the opposite of the volume of inside the cap.

Computation of the total mean curvature is a bit more complex. The fact that a LW surface is a critical point of functional (6.2) is true if the surface does not have a boundary. In our case, the cap does have a boundary. We therefore compute the total mean curvature on an extended surface which is the union of the cap with a plane with a circular hole. This surface has a crease along the circle. This crease has a non-zero total mean curvature H_{circle}, which varies with the cap height. The total mean curvature can be written:

$$H_{tot}(z) = H_{plane}(z) + H_{circle}(z) + H_{cap}(z)$$

The total curvature of the planar portion, H_{plane}, is zero. Since the mean curvature in the cap is constant, its total curvature is:

$$H_{cap}(z) = Area(z)\, H(z) = \pi(1 + z^2)\frac{-2z}{1 + z^2} = -2\pi z$$

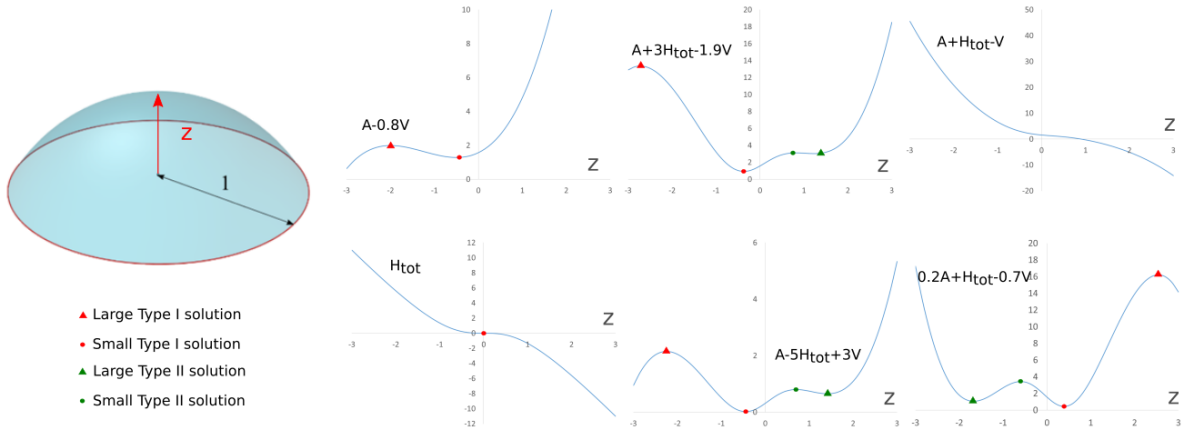

Figure 6.8: Energy E_1 of a spherical cap as a function of the cap height for various sets of parameters (a,b,c). Critical points correspond to LW spherical caps. Depending on the values of (a,b,c), there can be 0 to 4 solutions.

In order to compute the total curvature of the crease between the plane and the cap, we assume it is a portion of torus of inner radius b. We compute the total mean curvature of a portion of torus using the parametrization and formulas given in (Gray 1998) for a torus with circular section of radius β and radius of centers of sections α:

$$x(u,v) = \begin{pmatrix} (\alpha + \beta\cos v\ )\cos u \\ (\alpha + \beta\cos v\ )\sin u \\ \beta \sin v \end{pmatrix}$$

The mean curvature at a point of parameter (u,v) is:

$$H(u,v) = \frac{\alpha + 2\beta\cos v}{2\beta\ (\alpha + \beta\cos v)}$$

The total mean curvature is:

$$H_{torus} = \iint HdA = \iint \frac{\alpha + 2\beta\cos v}{2b\ (\alpha + \beta\cos v)}(\alpha + \beta\cos v)\ du\ dv$$

$$= 2\pi \int_{v=-\frac{\pi}{2}}^{-\pi/2+\theta} (\frac{\alpha}{2} + \beta\cos v)dv$$

Where θ is the angle between the plane and the sphere along the circle, which value is given by $\cos\theta = \frac{1-z^2}{1+z^2}$. With $\alpha = 1+\beta$ we obtain:

$$H_{torus} = \ (1+\beta)\pi\theta + 2\beta\pi(1 - cos\theta)$$

In the limit case $\beta \to 0$:

$$H_{torus} \to\ H_{circle} = \pi\theta$$

We obtain:

$$H_{tot}(z) = -2\pi z + \pi\theta$$

Figure 6.8 shows the value of E_1 as a function of cap height for different sets of parameters (a,b,c). The critical points correspond to LW spherical caps. In each case, we observe that:

- The large cap of type I is a local maximum of E_1,
- The small cap of type I is a local minimum of E_1,
- The small cap of type II is a local maximum of E_1,
- The large cap of type II is a local minimum of E_1,

6.3.4 LW surfaces of revolution on two circular boundaries

We now look at analytical solutions with a boundary composed of two coaxial circles of radius R, spaced at a distance of 1. This study will provide insight on splitting of LW surfaces, show how LW surfaces can be understood as a deformation of a minimal or CMC surface, and provide more insights on how boundary conditions affect the admissible values of (a,b,c) (i.e. the values for which we can find a LW solution).

We look for LW surfaces of revolution fitting the two circles and satisfying $H + bK = 0$ (i.e. $a = 1$ and $c = 0$). As discussed in section 6.1, such surfaces are offsets at distance b of minimal surfaces. Since the only minimal surface of revolution is the catenoid, solutions are offsets of catenoids. The meridian of a catenoid with x-axis of revolution is a catenary, which equation is (Giaquinta and Hildebrandt 1996):

$$\begin{pmatrix} x(t) \\ z(t) \end{pmatrix} = \begin{pmatrix} k\cosh(t) \\ kt \end{pmatrix}$$

Where k is a scaling parameter. The normal vector of this curve is, at parameter t:

$$\begin{pmatrix} x(t) \\ z(t) \end{pmatrix} = \frac{1}{\cosh(t)} \begin{pmatrix} -1 \\ \sinh(t) \end{pmatrix}$$

Therefore, the equation of the meridian of a (1,b,0) LW surface is:

$$\begin{pmatrix} x_{LW}(t) \\ z_{LW}(t) \end{pmatrix} = \begin{pmatrix} k\cosh(t) - \dfrac{b}{\cosh(t)} \\ kt + b\tanh(t) \end{pmatrix}$$

The search for solutions to the boundary problem amounts to finding the parameter k such that the meridian fits the two boundary conditions:

$$\exists t_0 \ , \begin{pmatrix} x_{LW}(t_0) \\ z_{LW}(t_0) \end{pmatrix} = \begin{pmatrix} R \\ 1/2 \end{pmatrix} \quad and \quad \begin{pmatrix} x(-t_0) \\ z(-t_0) \end{pmatrix} = \begin{pmatrix} R \\ -1/2 \end{pmatrix}$$

We will omit the discussion on the numerical resolution of this system, and present in Figure 6.9 the shape of the meridians for different values of b. With $b = 0$, we have two solutions: one stable and one narrower unstable catenoid. Let us first consider the case $b < 0$. As b is decreased from 0, the two solutions get closer to each other. They end up being identical at a certain value of b. Below this value, there is no more solution. In the case $b > 0$, if b is increased from 0, the two solutions get further away from each other. One solution tends towards a cylinder, while the other, unstable, gets a narrower and narrower neck until it auto-intersects. If b is further increased, a solution with positive Gaussian curvature (therefore of Type II) appears. It corresponds to the offset of catenary curve located on the other side of the axis of revolution. Existence of solutions as a function of b is summarized in Figure 6.9 (bottom).

Two important observations can be made out of this study:

- The neck diameter of a catenoid can be narrowed or widened by varying parameter b;
- There is a minimum neck diameter for stable LW surfaces (at least in the case c=0): whatever the value of b, a thinner stable neck cannot be obtained. We will see in section 7 that reaching this minimum numerically leads to splitting.

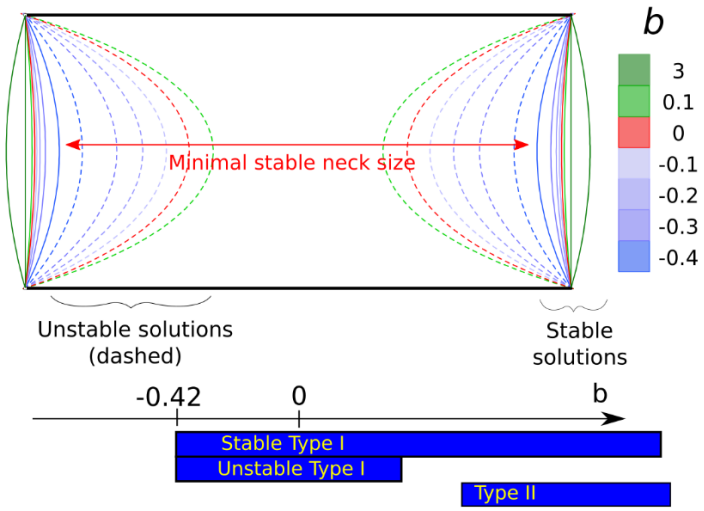

Figure 6.9: LW surfaces of revolution on two circles of equal radius. Top: Meridians of solutions. Bottom: Overview of solutions as a function of *b*

6.3.5 Dimensions and scaling

It is important to remark that parameters a, b and c have dimensions. If c is dimensionless, then a is homogenous to a length, and b to a squared length. Therefore, keeping a,b,c constant, if a homothety of factor k is applied to a boundary curve, the LW surface built on the scaled boundary is not homothetic to the one built on the original boundary. To obtain a scaled surface, one needs to multiply parameter a by k, and parameter b by k^2.

6.4 Generation method

After these preliminary considerations, we present in this section a novel method to generate LW meshes on target closed boundaries. CMC meshes can be generated on a given boundary curve by minimizing a combination of the mesh area and volume. This approach was for example used in (Brakke 1992) and (Pan *et al.* 2012). In the same fashion, we introduce a generation method for discrete LW surfaces based on the search of critical points of a combination of area, volume and total mean curvature of a mesh.

6.4.1 Modified functional

For most values of (a,b,c), both the small and the large type I solutions can be reached by minimizing a modified functional E_2:

$$E_2(T) = \lambda\, Area^2(T) + b\, H_{tot}(T) - c\, Vol(T) \tag{6.17}$$

The use of a squared area is directly inspired by (Pan *et al.* 2012). The critical points of E_2 are the same as the previously defined E_1:

$$\nabla_p E_2(T) = \lambda\, 2\, \mathrm{Area}(T)\, \nabla_p \mathrm{Area} + \mathrm{b}\, \nabla_p \mathrm{H_{tot}}(T) - \mathrm{c}\, \nabla_p \mathrm{Vol}(T) = 0$$

$$\Leftrightarrow \frac{a}{2}\, \nabla_p \mathrm{Area}(T) + \mathrm{b}\, \nabla_p \mathrm{H_{tot}}(T) - \mathrm{c}\, \nabla_p \mathrm{Vol}(T) = 0$$

$$with \quad a = 4\, \lambda\, \mathrm{Area}(T)$$

The reason for using this functional is that it allows a continuous exploration of the small and large solutions. This phenomenon is illustrated in Figure 6.10: let us consider a circular boundary of radius 1, and let us look for the CMC surfaces bounded by the circle and verifying $1.2H = 1$ (we therefore have (a,b,c) = (1.2, 0, 1)). As discussed in section 6.3.3, this problems has two solutions: a small and a large spherical cap. The small cap correspond to a local minimum of E_1, but the large one correspond to a local maximum, and is therefore not reachable by minimization. However, both caps are minima of E_2, with (λ,b,c) parameters being respectively (0.075, 0, 1) and (0.022, 0, 1). Therefore controlling the shape with parameters (λ,b,c) allows to reach both surfaces, contrary to a control with parameters (a,b,c).

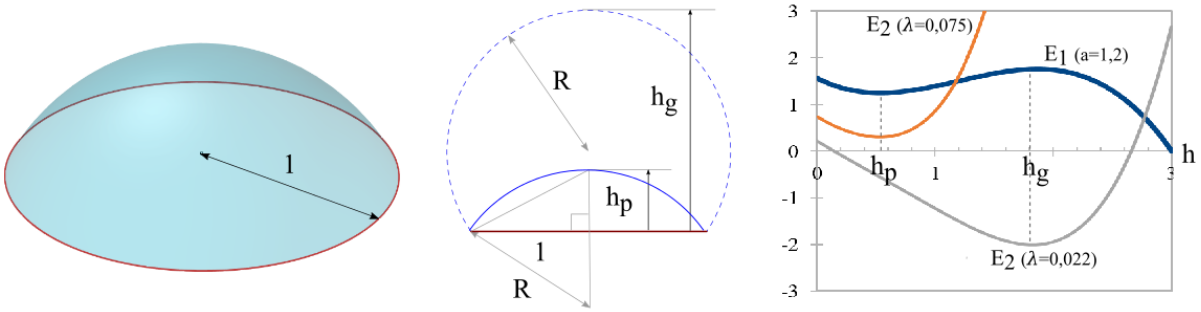

Figure 6.10: CMCs on a circular boundary. Only the small cap can be reached by minimizing E1, whereas minimizing E2 allows to also reach the large cap

Note: The large spherical cap of Figure 6.10 can also be reached by minimizing the area under a volume constraint. This approach can be used to generate discrete triangular CMCs in software Surface Evolver and Kangaroo2 for Grasshopper™. Similarly, LW triangular meshes could be generated by minimizing the area under two equality constraints, one on the volume and one on the total mean curvature:

$$\min_T Area(T)$$

$$subject\ to \begin{matrix} H_{tot}(T) = H_0 \\ Vol(T) = V_0 \end{matrix}$$

In which the variables are the x, y, z coordinates of the interior vertices of a triangular mesh T. Except in degenerate cases (e.g. a planar mesh), $\nabla Vol(T)$ and $\nabla H_{tot}(T)$ form a free family: the constraints are qualified. The Karush, Kuhn and Tücker theorem involves that, for a solution T^* of this constrained problem, there exist coefficients b and c such that:

$$\nabla_p \mathrm{Area}(T^*) + \mathrm{b}\ \nabla_p \mathrm{H_{tot}}(T^*) - \mathrm{c}\ \nabla_p \mathrm{Vol}(T^*) = 0$$

Therefore T^* is indeed linear Weingarten.

6.4.2 Issues with gradient descent

Instability

The term bH_{tot} in E_2 is not present in CMC models, it constitutes the major difference of this chapter with previous work on CMCs. As discussed in section 6.2.2, the first order variation of the total mean curvature is given by the Gaussian curvature. Deformation of a surface by a normal Gauss curvature flow (K-flow) was first studied in (Firey 1974) as a model of the smoothing process of beach pebbles. (Tso 1985; Andrews 2000) proved that this flow makes a convex surface converge to a point. However, K-flow is highly unstable on non-convex surfaces, as shown by (Zhao and Xu 2006), who studied the use of K-flow for smoothing purposes. They state that the flow is unstable in areas of negative mean curvature, and propose a smoothing flow with an amplitude related to K, but with an orientation based on the sign of K and H.

The fact that K-flow is stable in portions of surface of positive mean curvature, and instable in negative curvature areas, can be understood by looking at the stability of a small bump on a surface in Figure 6.11. The bump is smoothed or amplified depending on the sign of H. This fact leads to the degeneracy behavior showed in Figure 6.12: when applied to a torus, K-flow smoothes areas where H>0, and results in spikes of diverging amplitude in areas where H<0. We note that the opposite behavior is observed if the orientation of the flow is reversed (that is, doing a flow by –K).

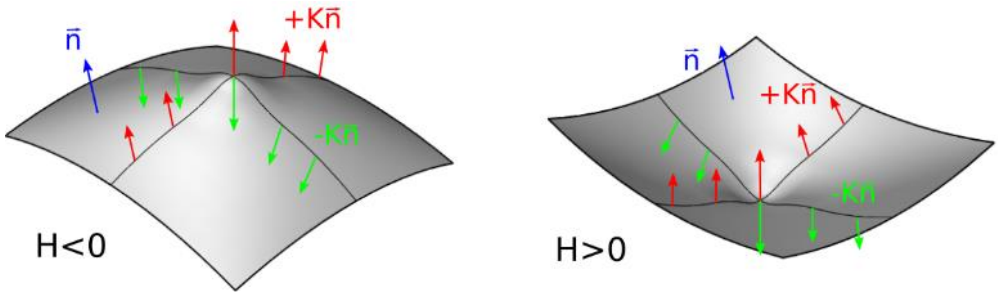

Figure 6.11: Gaussian curvature flow amplifies or smoothes of a bump depending on the sign of the mean curvature and whether the flow is by +K or –K

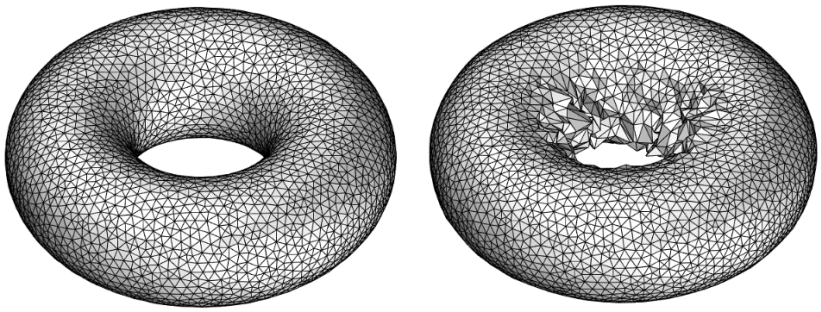

Figure 6.12: Gaussian curvature flow applied to a torus. Left: Initial geometry. Right: After 10 iterations

In LW surfaces, the K-flow is combined with a mean-curvature flow. The presence of this flow stabilizes locally the flow. On an energy point of view, the presence of the area convexifies locally E_1 and E_2 around most LW triangulations (this was noted in the case of a smooth spherical cap in section 6.3.3), thus allowing a minimization process to succeed. However, the convexity can be extremely local. This can be observed on the following example.

Figure 6.13 shows spherical LW meshes of unit radius, with parameters (λ,b,c) = (0.019,0.2,-0.8) (that is (a,b,c) = (1,0.2,-0.8)), with different face size. The variation of E_2 with the height of a bump on the surface, due to the displacement of only one vertex, is shown on the graph. We can observe that the desired surface (a sphere), is local minimum of E_2. However, if the bump height increases beyond a certain value z_{max}, the bump wants to increases even more to lower its energy, and tends towards an infinite size. The stable domain of bumps depend on their size and on the size of the mesh faces: the highest frequencies become unstable at a much lower deflection.

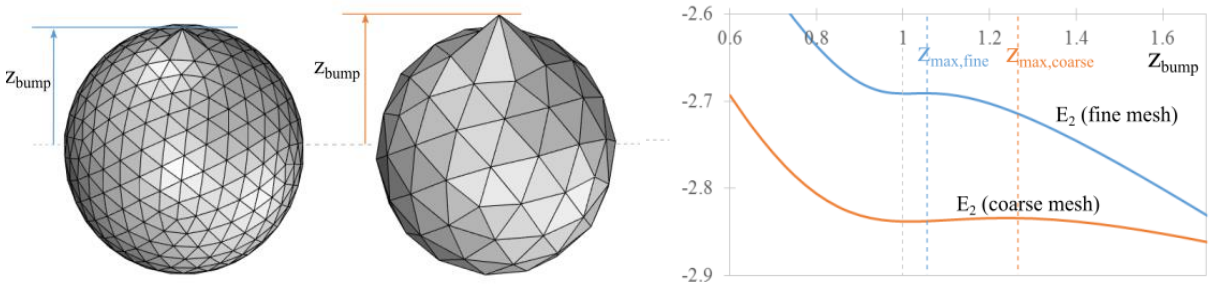

Figure 6.13: Domain of stability for a bump on a fine (left) and a coarse (middle) spherical mesh of unit radius. (right) Total energy as a function of the bump height

Numerically, a gradient descent needs to have very small steps in order to avoid that any vertex falls out of the convex portion. This method can be extremely slow, and experience show that it is not robust.

Stabilization by gradient smoothing

One way to stabilize the minimization consist in smoothing the Gaussian curvature vector field before including it in the descent direction. Smoothing can for example be obtained by applying successive Laplacian smoothing to the norm of the discrete Gauss curvature field:

$$K_s(\mathrm{m}) = (1 - \eta \mathrm{L})^{\mathrm{m}}\, K$$

Where K is a vector containing the Gaussian curvature at each vertex, $K_s(\mathrm{m})$ is the smoothed Gauss curvature vector field, η is a fixed parameter (for example 0.5), L is the Laplacian matrix with constant weights (to avoid recomputing at each step) and m is a smoothing radius (for example $m=10$ for a smoothing on the 10 nearest neighbors). With $m > 0$, one does not obtain exactly a LW surface as defined in section 3.1. However, the result of the minimization with a given m can be used as an initialization of another minimization with a lower value of m. The proximity of the mesh to the solution makes it much less likely to fall out of the stability zone. This smoothing stabilizes significantly the minimization. However, low frequency instabilities are still possible if parameters (a,b,c) are varied too quickly (Figure 6.14). Special care needs to be taken with the calculation of L near the boundaries, as K cannot be computed on the boundary vertices.

Issues with nodes not 6-valent

We showed in section 6.3 that our discrete Gaussian curvature model behaves asymptotically like the classical discrete Gaussian curvature based on the angular defect. (Borrelli *et al.* 2003) proved that for a mesh inscribed in a surface, this discrete Gaussian curvature depends on the node valence: the value usually does not converge to the Gaussian curvature of the smooth surface if the valence of the node is not six. In a gradient descent, this leads to the following problem: the nodes of valence 4, 5 and 7 tend to stick out and to lead to local instabilities (they fall out of the "convex zone"). Smoothing scheme describes in the previous section helps limiting this problem, but we still encounter numerical issues when the term bK has an equal or higher amplitude than aH. This phenomenon is showed in Figure 6.14 (the small visible bumps make the flow diverge in the following steps). One solution is to use meshes where each node is 6-valence, but this is often impossible topologically.

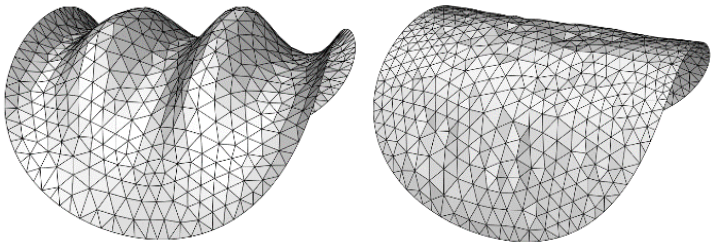

Figure 6.14: Issues with gradient descent. (Left) Smoothing described in section 5.3.2 stabilizes the flow such that the high freqency instability showed in Figure 6.12 cannot happen anymore. However, low frequency instabilities can still happen. (Right) Valence based instability: bumps appear on nodes of valence four and five, and lead to instabilities.

6.4.3 A robust descent direction

We showed in the previous section that using the gradient as a descent direction leads to many stability issues. In this section, we introduce a robust descent direction. The idea is simple: at each vertex, we search for the position it should have to be LW considering that its neighbors are fixed. This approach is similar to the projection based approach proposed in (Bouaziz *et al.* 2012). A key observation is that there are two solutions for given parameters (a,b,c): One corresponds to a type I LW mesh, and the other to a type II. As proved in section 6.3.1, a surface is either entirely of type I or entirely of type II. We can therefore choose consistently the right solution throughout the whole mesh.

LW position for a vertex in its star

In this section, we study how H, K and a linear combination $aH + bK - c = 0$ vary when moving the central vertex of a star. The behavior of these quantities is illustrated in Figure 6.15 for an arbitrary vertex star. We simplify this study by looking at the case where the central vertex M is on an axis:

- Passing through the center of gravity G of the star boundary edges,
- Parallel with the vector area.

We parametrize this axis by a coordinate z, where $z = 0$ at G, and $z > 0$ corresponds to $\overrightarrow{GM}.\overrightarrow{A_p} < 0$. Numerical experiments show that, for a given set of parameters *(a,b,c)* with $a > 0$ and for an arbitrary vertex star, there are two solutions to $aH(z) + bK(z) - c = 0$ provided that these two conditions are fulfilled:

- $a^2 + 4bc$ is "not too low". This condition is analogous to $a^2 + 4bc > 0$ from the smooth setting, but the right hand member is not exactly zero in the discrete case (the value depends on the neighbors' location). For example, in the bottom graph of Figure 6.15, we see that the equation $H + 2K - A_p = 0$ does not have a solution;
- $|b/a|$ is high enough. If $|b/a| \ll 1$, there is just one solution.

Figure 6.15 shows the evolution of the quantity $aH(z) + bK(z) - c$ as a function of z for different values of a, b and c. It allows to observe how the solution $aH(z) + bK(z) - c = 0$ evolves when varying parameters b and c. One could be surprised to find only two solutions to the discrete star problem, while the smooth spherical cap discussed in section 4.2 has up to four solutions. The reason is that a vertex star describes the local geometry of a surface. In the smooth cap problem, there are usually only two possible local geometries (i.e. two possible values for H). However, one local geometry can be used to construct two global solutions (a small or a large cap).

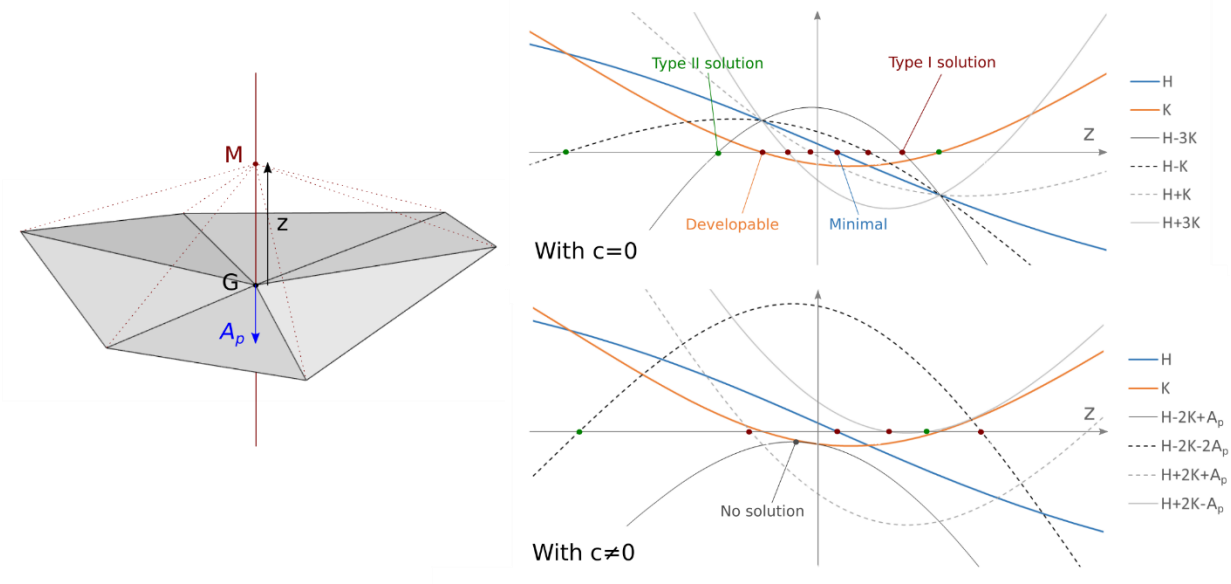

Figure 6.15: Search of the position at which a point is LW, considering that its neighbours are fixed. For a set of parameters (a,b,c), the LW positions are given by the z at which (aH+bK-cAp)(z)= 0. There are up to two solutions, the solution of type I is the one with negative slope

Furthermore, we observe that, when there are two solutions, one solution is a minimum of E_1 (i.e. $\frac{d}{dz}(aH + bK - cA_p) < 0$, these solutions are shown with red dots in Figure 6.15, and the other is a minimum (i.e. $\frac{d}{dz}(aH + bK - cA_p) > 0$, green dots). By analogy with the smooth case of LW surfaces fitting a boundary circle discussed in section 6.3.3 (and more precisely, to the "small cap" solution), we will call:

- *Type I solution* the local minimum of E_1;
- *Type II solution* the local maximum of E_1. This solution is actually also a minimum of E_1 if we replace (a,b,c) by (-a,-b,-c) (we then have $-a < 0$).

Search

We propose a modified Newton algorithm to look for the type I solution of each vertex (we are still considering that neighbor vertices are fixed). This solution will be used as a descent direction in our minimization algorithm. In order to reduce the search to a 1-degree of freedom problem, we look for a minimum along the axis described in the previous section. This helps make the mesh uniform, as vertices are attracted to the center of gravity of their star. We modify the standard Newton algorithm as follows to insure that we reach the solution of $aH(z) + bK(z) - c = 0$ with a negative slope:

Initialization: We project the current position of a vertex on the axis to obtain the initial value z_0. However, if the slope at z_0 is positive (i.e. $\frac{d}{dz}(aH(z) + bK(z)) > 0$), or if $|z_0| > d$ (where d is the average edge length of the boundary of the star), then we set:

$$z_0 = -sign(b)\, d$$

This starting point is always on the side of the type I solution, which has a negative slope (the solution with positive slope is further away). The reason for using the distance d is that a vertex should never form too sharp of an angle. A sharp vertex with $|z| > d$ can only happen in an extremely coarse mesh.

Iterations: At any Newton iteration $z_{i+1} = z_i + t_i$, we divide the increment t_i by two as many times as necessary so that the slope at z_{i+1} is negative and so that $|z_{i+1}| < d$.

Since the resolution yields a descent direction, the resolution needs not be extremely precise. A loose convergence tolerance ε can be set on $|aH(z) + bK(z) - c| < \varepsilon$. In practice, no more than two Newton iterations are performed per vertex. The number of iterations is bounded to deal with the cases where there is no solution with negative slope. This situation typically occurs if $a^2 + 4bc < 0$ (like for $H + 2K - A_p$ in Figure 6.15): our algorithm then converges to the minimum of $|aH(z) + bK(z) - c|$. Our algorithm returns a type I solution if the user has chosen a positive value of a, and a type II solution if $a < 0$.

Note 1: This algorithm is based on the observations made in section 6.3.3, which are not backed by theoretical demonstrations. However, it proved to be robust in practice.

Note 2: One way to understand why this method is stable, while the gradient descent is not, is that the gradient descent can lead some vertex towards a type I solution, and others towards a type II solution. As discussed in section 6.3.1, types I and II are incompatible, this approach cannot succeed.

6.4.4 Minimization

We apply the descent direction from section 6.4.3 directly, without performing a line search and without using previous descent directions to accelerate convergence. Future work could address implementing this descent in an L-BFGS solver, which is well suited to the high number of degrees of freedom of a typical mesh (Pan *et al.* 2012). One benefit of the proposed implementation is that it can be directly included in a projection based framework such as Shape-Op or Kangaroo2 (Deuss *et al.* 2015).

We remark that the global minimization is performed on E_2 (with parameters (λ, b, c)), while the local solving to compute the descent direction of a given vertex is performed by minimizing E_1, with parameters $(a, b, c) = (4\lambda Area, b, c)$. We neglect the variation of a due to the change of area in the local solving. Edge flipping can be triggered by designer if the aspect ratio of some triangles is unaesthetic.

6.4.5 Constraints

The proposed approach naturally handles fixed point constraints. Those are assigned a null displacement.

6.4.6 Validation

In this section, we compare the geometry of discrete LW surfaces generated with our method to analytical LW surfaces.

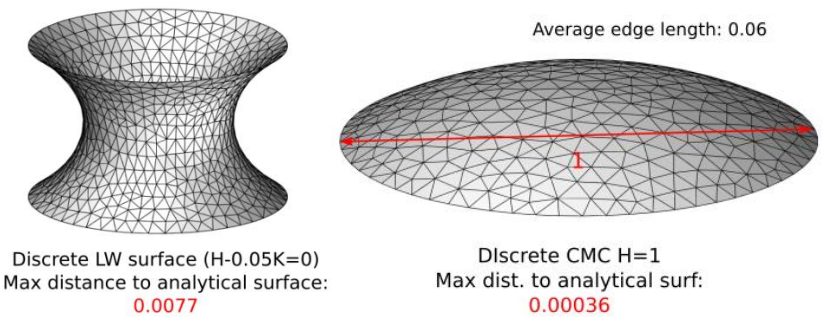

Figure 6.16: Discrete LW surfaces of revolution and maximum distance to analytical solutions

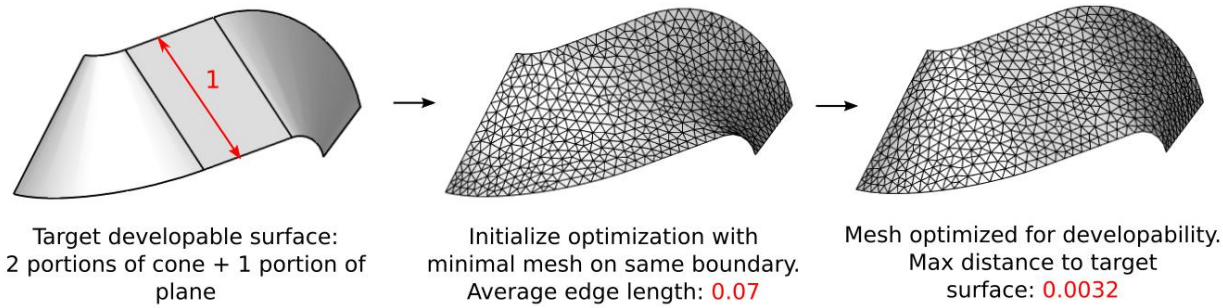

Figure 6.17: Developable surface generated with our method

The first one (Figure 6.16) is the offsets of a catenoid. The construction of such a surface was discussed in section 6.3. We compute a portion of a LW of revolution $H - 0.05K = 0$. We then build a discrete LW mesh with our method (with 1000 iterations) by using two circles of the smooth surface as boundaries, located at a unit distance from each other. The diameter of the base circle is 1, while the maximum distance between a vertex and the analytical surface is very low: 0.0077.

The second analytical surface is a spherical cap of unit radius, resting on a circle of diameter 1. It can be approximated with our method as a CMC (H=1) with extremely good precision (maximum error at a vertex: 0.00036).

The third theoretical surface is a developable strip (thus verifying $K = 0$) of unit width composed of two portions of right circular cones and a portion of plane. Initializing our method with a minimal surface fitting the boundary, we obtain the surface shown in (Figure 6.17). The maximum distance between our surface and the target one is 0.0032 for an average face size of 0.07.

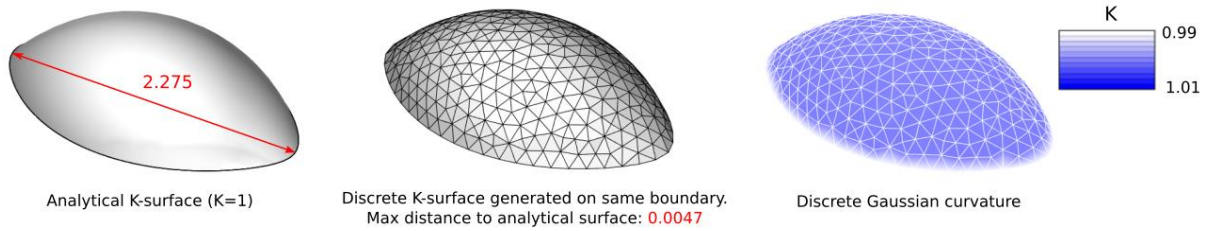

Figure 6.18: Discrete K-surface

The fourth surface (Figure 6.18) is a portion of an analytical K-surface of revolution, for which the meridian equation is:

$$\begin{pmatrix} x(t) \\ y(t) \end{pmatrix} = \left(\int_0^t \frac{\cos t}{\sqrt{1 - 0.75^2 \sin^2 \theta}} \, d\theta \right)$$

This surface has a Gaussian curvature of 1. Generating a surface with our method on the same boundary with (a,b,c) = (0,1,1) yields the mesh shown in the middle. The maximum distance between vertices and the analytical surface is still very low: 0.0047. Furthermore, the Gaussian curvature $K_p/3A_p$ is constant (maximum deviation 0.00023, obtained after 1000 iterations). The generation of K-surfaces with our method is further discussed in section 6.5.3.

6.5 Exploration of the LW surfaces on a given boundary

6.5.1 Case aH+bK = 0

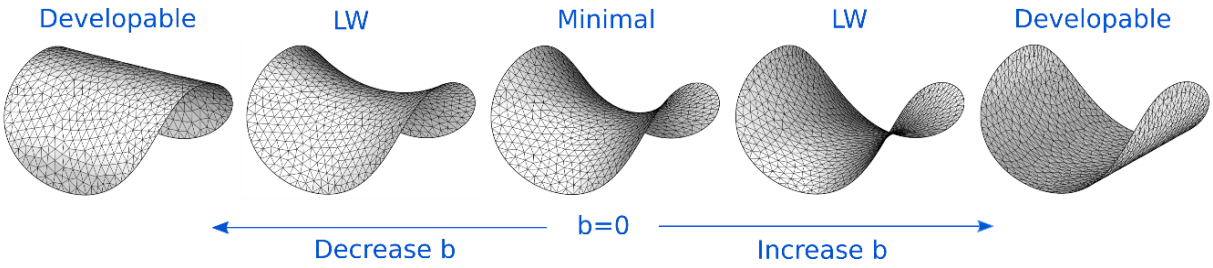

Figure 6.19: Minimal and developable surfaces generated on the same boundary curve

We start our exploration by considering the case $c = 0, a \neq 0$. In that case, the elliptic condition $a^2 + 4bc > 0$ is automatically verified. Furthermore, in the curvature diagram H-K, the line $aH + bK = 0$ passes through the origin, where it meets the parabola $H^2 = K$ (see section 6.3.1). A consequence is that a type I surface is entirely anticlastic, while a type II surface is (as usual) entirely synclastic.

Type I solutions: Deforming minimal surfaces

Figure 6.19 shows how a minimal surface fitting a boundary curve can be transformed by controlling the parameter b. Varying b from $b = 0$, the surface is deformed into a LW surface, we observe that the average height increases or decreases. When $|b/a| \gg 1$, the surface becomes developable ($K = 0$). We can therefore understand the parameter b as a mean to explore surfaces intermediate between minimal and developable surfaces on a same boundary curve.

Figure 6.3 shows a boundary condition similar to the one of a circus “big-top”. It is composed of three closed curves. Similarly to the surface in Figure 6.19, with $b \geq 0$, we can deform a minimal surface ($b = 0$) into a developable surface with $b/a \gg 1$. Increasing b makes the surface flatter and flatter. When decreasing b ($b < 0$), the surface in Figure 6.19 tends towards another developable surface. However, for the surface in Figure 6.3, curvature increases, in particular near the two boundary circles. At some point, we reach a value of b at which there is no more connected LW solution. This is the same phenomenon as observed in the case of LW of revolution in section 6.3. Numerically, when we reach this value, the neck size suddenly starts converging towards 0. If a mesh splitting method were implemented, as in (Pan *et al.* 2012), the mesh would split into three parts.

As recalled in section 2, LW surfaces with $c = 0$ correspond to shapes of self-stressed membranes without external loads. In minimal surfaces, self-stresses are isotropic and uniform. This property tends to make minimal surfaces flat in large sections, as shown in Figure 6.20 (left). Varying parameter b modifies the ratio of self-stress between the two principal curvature directions, as shown in equation 3 and 4. This effect can be observed on the LW surface of Figure 6.20 (right), in which the longitudinal tension was increased. Therefore, the parameter b gives access to a family of surfaces that are equilibrium position of surfaces, and that has a much wider potential for a designer than minimal surfaces.

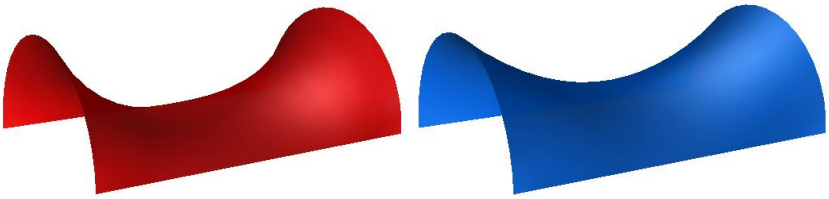

Figure 6.20: Minimal (left) and LW (right) surfaces on the same boundary. In a tensile membrane, the parameter *b* modifies the prestressing ratio between the two principal curvature directions.

Type II solutions

Getting back to the curvature diagram H-K (Figure 6.6), we observe that a type II solution verifies $K \geq K_0$ for some real number $K_0 > 0$. As a result, type II solutions tend to look quite spherical, and are less interesting aesthetically than type I. Furthermore, as they are necessarily convex, their existence is subject to strong conditions on the boundary cures. For example, a Type II surface cannot be generated on a planar non-convex boundary. Examples are shown in Figure 6.21.

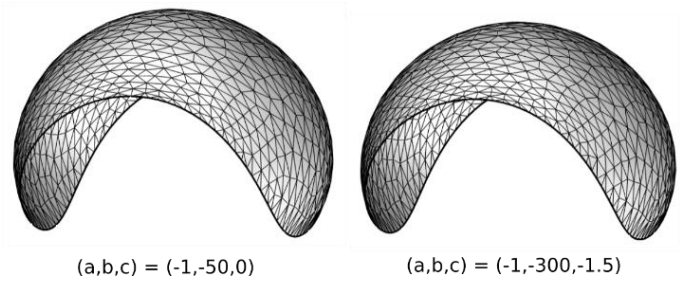

Figure 6.21: Type II LW surfaces tend to be quite spherical. There is a large difference in parameters (a,b,c) for these two surfaces, but they look quite similar to each other.

6.5.2 Case aH+bK = c

In the case $c \neq 0, a \neq 0$, LW surfaces are offsets of CMCs. It is therefore intuitive to think of them as a deformation of CMC surfaces. Figure 6.22 shows a CMC generated on a boundary similar to the one of the Great Roof of the British museum. This CMC can be deformed into a LW surface by controlling parameter *b*. One notable effect is that, if c>0:

- With $b<0$, saddle points are lowered, hill tops are pushed up. This makes the surface more expressive;
- With $b>0$, the height difference between saddle points and hill tops is decreased – the Gaussian curvature is more uniform.

We remark that this boundary is planar and non-convex. Therefore, it does not admit a synclastic K-surface. A consequence is that, if is b/a and c/a are increased up to a certain value, there is no more LW solution, and the algorithm slowly diverges. For the mesh shown at the bottom of Figure 6.22, parameters (a,b,c) are close to the hyperbolic limit. If bc is decreased further, there is no more solution, and our algorithm stops thanks to the condition described in section 6..3.2. The same deformations on saddles and hill tops can be observed in Figure 6.1, Figure 6.3. Figure 6.2 highlights the convenience of a global shape control. There are a dozen of saddles and as many hill tops on these surfaces. In a traditional surface design method, one would need to control all of them individually. However, they can all be controlled at the same time with the global parameters *a,b,c*.

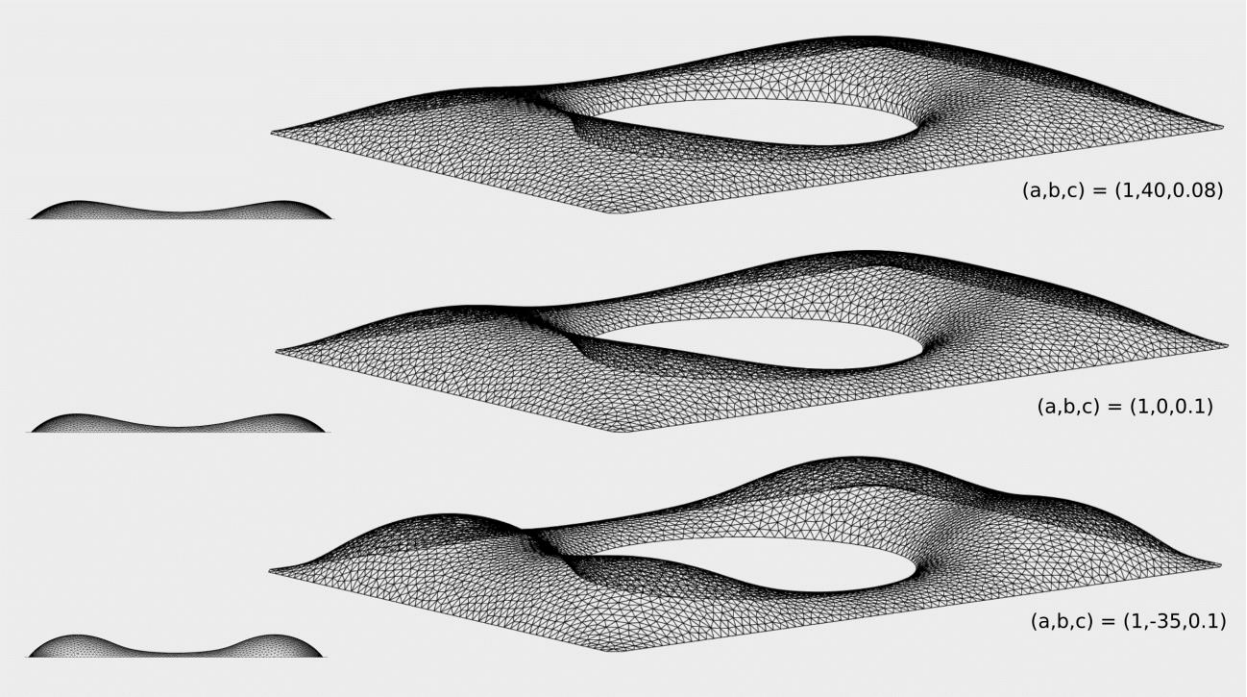

Figure 6.22: Effect of parameter b on a boundary similar to the one of the British Museum. Middle: CMC surface. Top: LW surface with b<0. Bottom: LW surface with b>0.

6.5.3 K-surfaces

Surfaces with constant Gaussian curvature, called *K-surfaces*, are elliptical (i.e. $a^2 + 4bc > 0$) if the Gaussian curvature is positive. The notion of Type I / Type II is not relevant for K-surfaces, since the two portions of the curvature diagram are symmetrical with respect to the line $H = 0$. We rather talk about a solution with $H > 0$ or $H < 0$.

K=0 : Developable surfaces

Developable surfaces have null Gaussian curvature, they are therefore a sub-family of LW surfaces, with parameters (a,b,c) = (0,1,0). The method described in section 6.4 allows to generate such surfaces.

Developable surfaces have been widely studied in the literature, as they offer the possibility to build curved objects from flat, unstretchable yet bendable sheets like paper, fabric, or thin metal plates - see for example (Leduc *et al.* 2018).

Generation methods proposed in the literature can be split into three main categories: shape approximation (Chen *et al.* 1999; Wang 2008), interactive deformation (English 2008; Rabinovich *et al.* 2018), and contour interpolation (Rose *et al.* 2007). Our method falls in the last category. It is however close to the shape approximation method by triangular meshes proposed in (Wang 2008), that minimizes the absolute Gaussian curvature of a mesh to make it developable. One notable difference is that, in our method, the initial mesh need not be close to a developable surface. A sample mesh generated by our method is shown in Figure 6.23.

However, since we minimize bH_{tot}, we can only build developable surfaces in which the sign of the mean curvature is constant. For example, a curved fold cannot be generated, because the sign of the mean curvature is different on both sides of the fold. Future work could address generation of general developable surfaces by prescribing which portion of the mesh should be convex (i.e. H>0), and which should be concave (H<0).

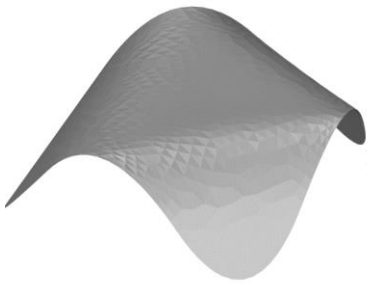

Figure 6.23: Developable surfaces generated with our method

K>0

To our knowledge, there is no general method in the literature to generate K-surfaces (with K>0) on a boundary. Figure 6.18 and Figure 6.24 show a few examples. Similarly to type II surfaces, K-surfaces cannot be constructed on any boundary curve. For example, we cannot build one on a planar non-convex boundary.

Applications of synclastic K-surfaces have not been considered in the literature. We remark that, as they are smooth isometric deformations of a portion of sphere, they can be fabricated by bending and connecting spherical plates.

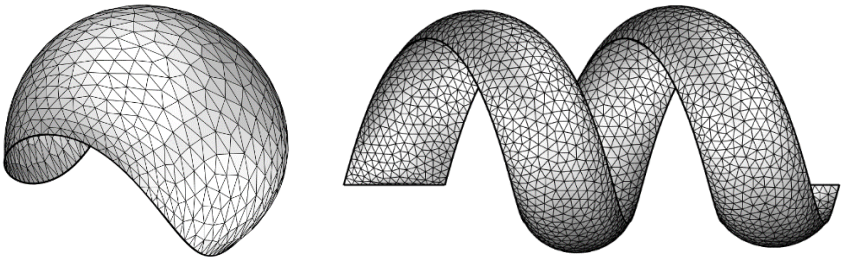

Figure 6.24: Meshes with constant Gaussian curvature

6.6 Design applications

In this section, we look at applications of LW surfaces for the design of tensile membranes and gridshells.

6.6.1 Tensile membranes

As discussed in section 6.1, LW surfaces with $c = 0$ correspond to equilibrium shapes of self-stressed membranes. Therefore, our generation method can be used as a form-finding tool for membranes. Compared to minimal surfaces, which have been a widely used form-finding tool before the 90's, LW surfaces offer one degree of freedom to design a membrane fitting a fixed boundary. The parameter a can be chosen as $a = 1$, so the shape can be directly controlled by the parameter b – we are then exploring the surfaces $H + bK = 0$ fitting the target boundary. This degree of freedom can be used for aesthetic and functional purposes, but also to avoid structural issues:

Height of canvas

By adjusting the value of b, one can change the average height of the surface. This effect is shown in Figure 6.25, where a minimal surface and a LW surface are built on the same two contours.

Water ponding

Tensile membranes must have a minimum slope in order to prevent the formation of water ponds. There is one sign of *b* for which this minimum slope is increased.

Expressivity

Minimal surfaces tend to be relatively flat over large portions, this effect can be seen in Figure 6.20. By modifying parameter *b*, one can control the prestressing ratios, and introduce curvature in these flat areas.

Stability

If the Gaussian curvature of a portion of membrane is too low, it is becomes flat and prone to oscillations and beating under wind load. Parameter *b* allows to modify the distribution of the Gaussian curvature to avoid this problem, as shown in Figure 6.25.

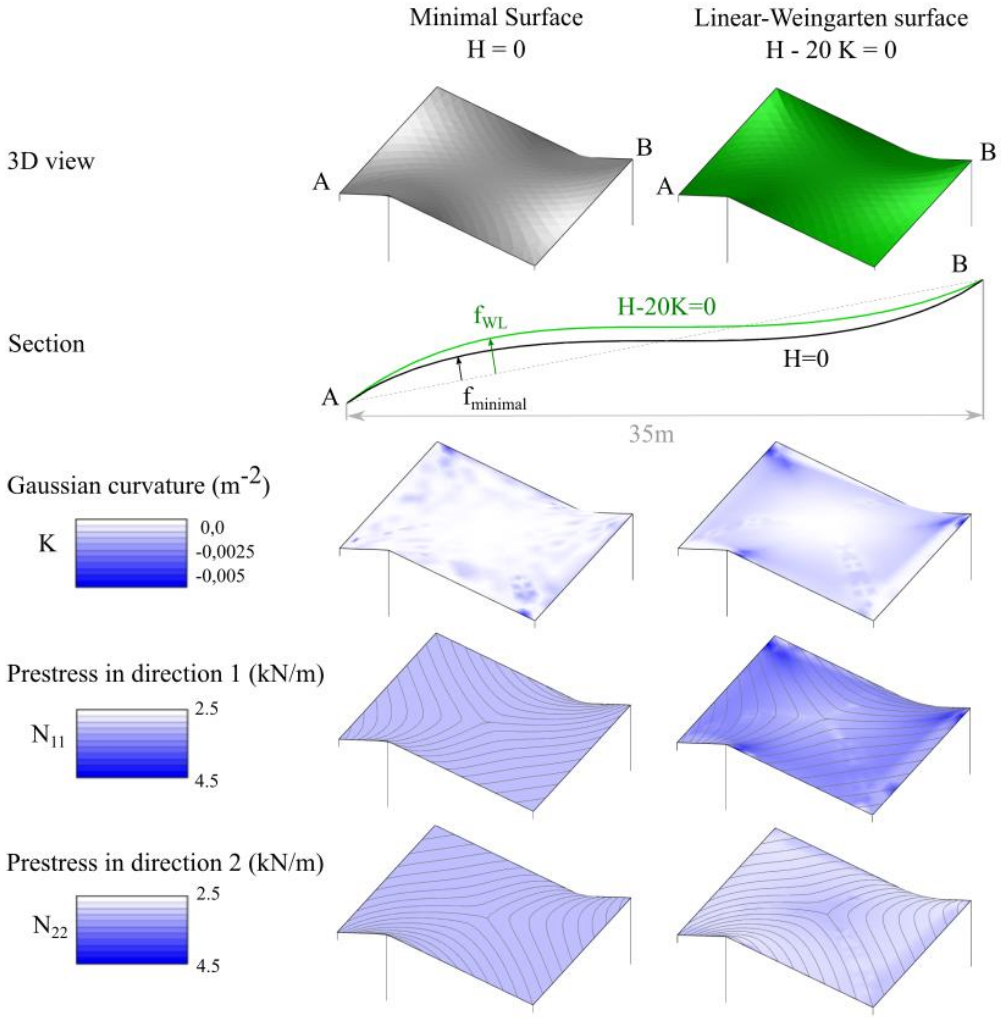

Figure 6.25: Comparison of the geometry and prestressing of a minimal and a LW membrane

One strength of our method is that prestressing stresses can be obtained directly from surface curvature, no additional mechanical calculations are required (Figure 6.25, bottom).

Comparison with other form-finding methods

Compared to modern form-finding methods like finite elements or the updated-reference strategy (Bletzinger and Ramm 1999), LW surfaces do not allow to explore the entire design space of membranes. However, advanced methods often require significant preprocessing work from a designer in order to assign prestress orientations and ratios. This task can be long, especially if the membrane has a complex topology. Our method does not require preprocessing work, a designer can readily draw a boundary and

explore an entire family of shapes by just controlling one “slider”. Therefore, LW surfaces constitute an interesting tool for conceptual design stages.

6.6.2 Gridshells

Gridshells are shells composed of a network of beams. As discussed in chapter 2, aligning beams with principal curvature directions of the underlying surface offers many fabrication properties: the surface can then be cladded by planar glass panels, only four beams meet at the nodes (unlike triangular meshes with complex 6-valent nodes), and the nodes are torsion-free, i.e. the median planes of the beams meet on a common axis. This last property simplifies significantly the fabrication of the nodes, which are the costliest elements of this type of structure.

As discussed in section 6.2, curvature lines on LW surfaces have two properties: they form a regular pattern, and they are aligned with principal stresses under uniform pressure loading (assuming membrane-compatible supports are provided). When beams are not aligned with principal stresses, the grid is subjected to shear forces. Contrary to triangular lattices, quadrangular ones have a shear mechanism. Strength and rigidity in shear is usually obtained by one of the following means: adding diagonals (e.g. cables) or having clamped beam-beam connections. The second option is usually cheaper and preferred by architects, because cables tend to obstruct the view. However, it is impractical if shear forces are too high. In LW gridshells, the shear is null for one major load case: uniform wind pressure. LW gridshells are therefore good candidates to design cable-free gridshells. Future case studies will be performed to assess the variation of the orientation of the principal stresses under asymmetrical loads.

Figure 6.26 shows how a LW gridshell can be used to design an alternative structure for the glass roof of the British Museum in London, whose geometry is based on a triangular mesh. A surface surprisingly close to the real one can be obtained with a LW surface. The beam orientation is obtained by remeshing the LW triangular mesh following principal curvature directions and then optimizing for circularity of quads.

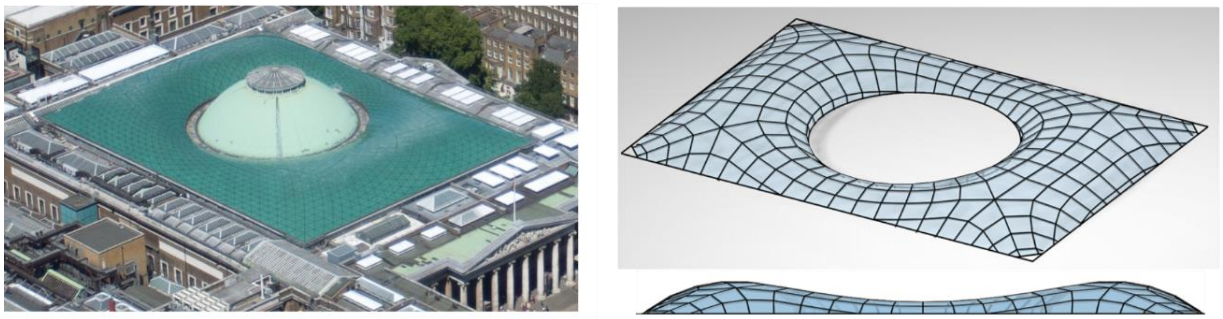

Canopy of the great court of the British Museum. The steel gridshell follows a triangular mesh.

Linear-Weingarten surface on the same boundary, with beams aligned with principal curvature directions.

Figure 6.26: Proposition of an alternative geometry for the glass roof of the British Museum. The proposed geometry lies on a LW surface, and has flat panels, torsion-free nodes, and perfect mechanical beam orientation under uniform wind load. (left: picture in public domain)

6.7 Cable boundaries

Tensile membranes are usually held at their boundaries by cables. In this section, we investigate how this can be modeled with LW surfaces, and how to generate the shape of LW surfaces bordered by cables. This question is also of interest for the design of funicular shells with openings, for which openings are realized with funicular arches.

This problem can be understood as a generalization of the *Euler-Plateau* problem introduced in (Giomi and Mahadevan 2012). This problem considers minimal surfaces for which the boundary is an elastica, i.e. a curve of imposed length minimizing the integral of its squared curvature. (Pérez *et al.* 2017) generalized this problem to Kirchoff rods, which are minimizers of a sum of a curvature and a torsional energy. Our problem is a generalization of the one of Giomi in a sense that we do not consider minimal, but LW surfaces. We are however interested only in boundaries curves without bending energy, as we aim at obtaining funicular shapes.

6.7.1 Equilibrium and geometry

One convenient method to generate LW surfaces bordered by cables would be to minimize an energy composed of the sum of an energy associated with the LW surface and the elastic energy of the cable: $E = E_{LW} + E_{cable}$. However, the variational formulations of LW surfaces in the literature address only surfaces without boundaries. We therefore use an equilibrium approach to treat the boundary.

Equilibrium of cable boundary

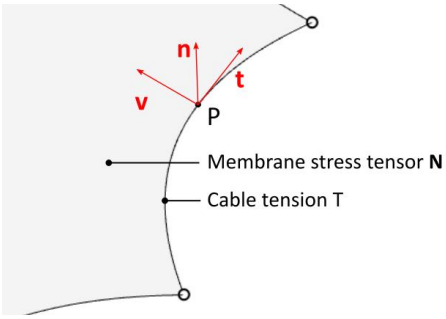

Figure 6.27: Equilibirum of a boundary cable

Let us consider a cable parametrized by arc length s with an associated Darboux frame $(\mathbf{t}, \mathbf{v}, \mathbf{n})$, where $\mathbf{t}$ is the tangent vector to the cable, $\mathbf{n}$ is the surface normal, and $\mathbf{v}$ is a unit vector in the tangent plane orthogonal to the boundary (Figure 6.27). The cable has a tension T and is subjected only to membrane stresses (with stress tensor $\mathbf{N}$), other forces are supposed to be negligible. The equilibrium of the cable can then be written:

$$\frac{d}{ds}(T\mathbf{t}) + \mathbf{N}.\mathbf{v} = 0$$

This can be developed into:

$$\frac{dT}{ds}\mathbf{t} + T\frac{d\mathbf{t}}{ds} + N_{vv}\mathbf{v} + N_{tv}\mathbf{t} = 0$$

We can express the derivative of the tangent vector **t** using the derivatives of the vectors of the Darboux frame:

$$\frac{d\mathbf{t}}{ds} = k_g \mathbf{v} + k_n \mathbf{n}$$

Projecting the equilibrium equation along **v**, **t** and **n**, we obtain successively:

$$T\, k_g + N_{vv} = 0 \tag{6.18}$$

$$\frac{dT}{ds} = -N_{tv} \tag{6.19}$$

$$k_n = 0 \tag{6.20}$$

We note that, in the case of a sliding cable, $N_{tv} = 0$, so $\frac{dT}{ds} = 0$: the tension in the cable is constant.

LW membrane stresses at boundary

Let us now express the LW membrane stresses at the boundary. We recall that the corresponding membrane stress tensor is:

$$\mathbf{N} = a\, \mathbf{I} + \frac{b}{2}\, \hat{\mathbf{S}}$$

For a unit vector **v** of the tangent plane perpendicular to the boundary:

$$\mathbf{N}.\mathbf{v} = a\, \mathbf{v} + \frac{b}{2} \hat{\mathbf{S}}.\mathbf{v}$$

In order to obtain the component N_{vv} of the membrane stress tensor, we express **v** in the basis of principal curvature directions: $\mathbf{v} = \cos\theta\, \boldsymbol{e_1} + \sin\theta\, \boldsymbol{e_2}$ where $\boldsymbol{e_1}$ and $\boldsymbol{e_2}$ are unit vectors aligned with principal directions. The vector **t** can be expressed in that same basis: $\mathbf{t} = \cos\left(\theta - \frac{\pi}{2}\right) \boldsymbol{e_1} + \sin\left(\theta - \frac{\pi}{2}\right) \boldsymbol{e_2}$. We obtain:

$$\mathbf{v}.\mathbf{N}.\mathbf{v} = a + \frac{b}{2} \begin{pmatrix} \cos\theta & \sin\theta \end{pmatrix} \begin{bmatrix} k_2 & 0 \\ 0 & k_1 \end{bmatrix} \begin{pmatrix} \cos\theta \\ \sin\theta \end{pmatrix} = a + \frac{b}{2} (k_2 \cos^2\theta + k_1 \sin^2\theta)$$

$$= a + \frac{b}{2} \left(k_2 \sin^2\left(\theta - \frac{\pi}{2}\right) + k_1 \cos^2\left(\theta - \frac{\pi}{2}\right) \right)$$

$$N_{vv} = a + \frac{b}{2} k_n \tag{6.21}$$

where k_n is the normal curvature of the boundary. We observe that the normal membrane stress component due to the term bK in $aH + bK = c$ is proportional to the normal curvature of the boundary, which vanishes at equilibrium (equation 6.20).

The shear component is:

$$\mathbf{t}.\mathbf{N}.\mathbf{v} = a + \frac{b}{2} \begin{pmatrix} \sin\theta & -\cos\theta \end{pmatrix} \begin{bmatrix} k_2 & 0 \\ 0 & k_1 \end{bmatrix} \begin{pmatrix} \cos\theta \\ \sin\theta \end{pmatrix} = \frac{b}{2} (k_2 - k_1) \cos\theta \sin\theta$$

$$N_{tv} = \frac{b}{2} \tau_g \tag{6.22}$$

where τ_g is the geodesic torsion of the boundary (see (do Carmo 1976) for the derivation of $\tau_g = (k_2 - k_1) \cos\theta \sin\theta$).

Geometry of a boundary cable

By combining the equilibrium equations of the cables with the LW stresses, we find that the geometry of the boundary must fulfill two geometrical differential equations.

The first one was already derived from the equilibrium of the cable (equation 6.20):

$$k_n = 0$$

It implies that the cable follows an asymptotic line on the surface. For the second one, we first observe that the normal stress at the boundary is $N_{vv} = a$. Equation 6.18 implies:

$$k_g = \frac{a}{T}$$

This equation can be combined with the equation 6.19 to remove variable T. It has different geometrical implications depending on whether b is null or not.

- **If $b = 0$** (i.e. the surface is CMC), we obtain from equation (6.22) that the shear is null:

$$N_{tv} = 0$$

Consequently, equation (6.19) yields:

$$\frac{dT}{ds} = 0$$

As a result:

$$\frac{dk_g}{ds} = 0 \tag{6.23}$$

Not all CMC surfaces admit an asymptotic line with constant geodesic curvature. For example, one can find such lines on a helicoid, but not on a catenoid. The presence of a boundary cable has therefore a strong impact on the surface geometry.

- **If $b \neq 0$**, we have to consider separately the case of a sliding cable or a cable attached to the membrane:
  - Sliding cable: $N_{tv} = 0$ implies that :

$$\tau_g = 0 \tag{6.24}$$

$\tau_g = 0$ means that the cable follows a curvature line. Since both the normal curvature and the torsion of the boundary are null, it is necessarily planar.

  - Fixed cable:

$$\frac{b}{2}\tau_g = N_{tv} = \frac{dT}{ds} = a\frac{d}{ds}\left(\frac{1}{k_g}\right)$$

$$\frac{b}{2}\tau_g = \frac{a}{k_g^2}\frac{dk_g}{ds} \tag{6.25}$$

Similarly to the case $b = 0$, the quantity $\frac{k_g'}{\tau_g k_g^2}$ is not constant for an arbitrary asymptotic line of an arbitrary LW surface: the presence of a boundary cable has significant impact on surface geometry.

6.7.2 Generation

In this section, we will show how boundary cables can be modeled numerically and combined with the algorithm described in section 6.4 in order to generate LW surfaces bordered by cables which are at equilibrium with the stress field of equation 6.6. Computation of the cable position is done by a dynamic relaxation approach.

6.7.2.1 Discrete model

Boundary cables are discretized as series of particles connected by springs. This section describes the discrete model of forces acting on each particle for a non-sliding cable. Each particle is subject to a tension from the cable and to membrane stresses (Figure 6.28). Cable forces are computed from the elongation and stiffness of the cable:

$$\boldsymbol{f_{cable}} = k\left(l_1 - l_{1,i}\right)\mathbf{u_1} + k\left(l_2 - l_{2,i}\right)\mathbf{u_2}$$

Where:

- $\mathbf{u_i}$ is the unit vector from P to P_i: $\mathbf{u_1} = \frac{\overrightarrow{PP_1}}{\|\overrightarrow{PP_1}\|}$; $\mathbf{u_2} = \frac{\overrightarrow{PP_2}}{\|\overrightarrow{PP_2}\|}$
- l_1 and $l_{1,i}$ are respectively the current and the initial length of line PP_1.

Membrane forces are computed by integrating the stresses calculated in the previous section over a portion of cable of length $\frac{\|\overrightarrow{PP_1}\|+\|\overrightarrow{PP_2}\|}{2}$ centered at P:

$$\boldsymbol{f_{membrane}} = -a\,\nabla_{\mathrm{p}}\mathrm{A} - \frac{b}{2}T_g\,\mathbf{t}$$

Where:

- $\nabla_{\mathrm{p}}\mathrm{A}$ is the gradient of the summed areas of the mesh triangles adjacent to P. This term corresponds to the normal component of membrane stresses $N_{vv} = a$ (equation 6.21) integrated over the length of the portion of cable. We ignore the term $\frac{b}{2}k_n(\boldsymbol{t})$ of equation 6.21, because it vanishes at convergence anyway.
- **t** is the tangent vector of the boundary curve, computed as :
$$\mathbf{t} = \frac{\mathrm{P}_2 - \mathrm{P}_1}{\|\mathrm{P}_2\mathrm{P}_1\|}$$
- T_g is the halved torsion angle from the normal at P2 to the normal at P1, computed as:
$$T_g = \frac{1}{2}\arcsin\left(\det(\mathbf{n_1^p}, \mathbf{n_2^p}, \mathbf{t})\right)$$
Where $\mathbf{n_i^p}$ is the projection of the normal vector $\mathbf{n_i}$ at $\mathrm{P_i}$ onto the plane (P,**t**,**n**). The normal vector **n** is simply computed as the normal of the plane $(\mathrm{P}\mathrm{P}_1\mathrm{P}_2)$.
Note 1: This way of computing the normal requires a special treatment if boundary points are aligned (or nearly aligned). A more robust scheme would be to approximate locally the surface by a paraboloid.
Note 2: The calculation of the torsion requires a consistent orientation of the boundary curve. This orientation is determined by the orientation of the tangent vector **t**.

To model a sliding cable, one just needs to write the membrane force as $\boldsymbol{f_{membrane}} = -a\,\nabla_{\mathrm{p}}\mathrm{A}$.

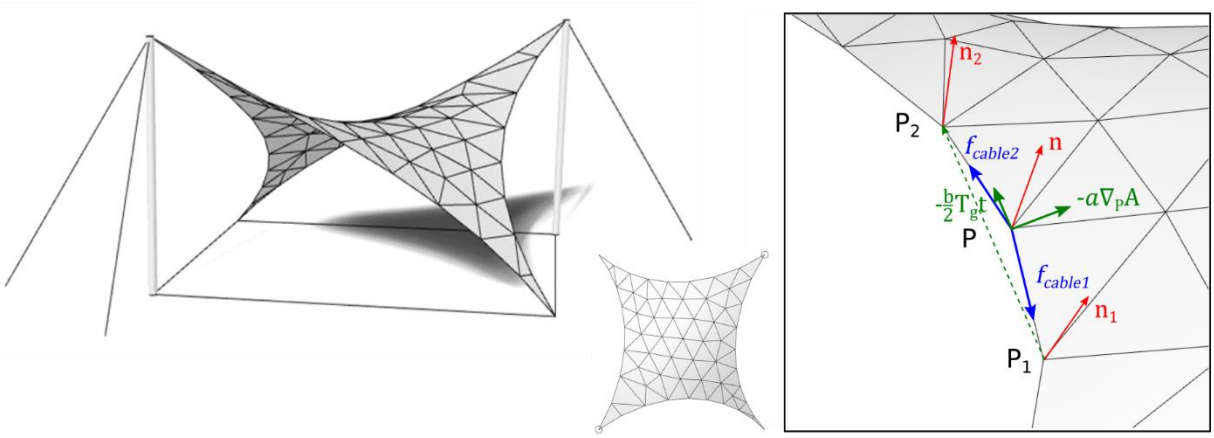

Figure 6.28: Equilibrium of vertex of a boundary cable

6.7.2.2 Numerical resolution

We look for the equilibrium position of the boundary with a dynamic relaxation approach. The motion of a particle P of a cable is given by:

$$m\ddot{P} = \boldsymbol{f_{cable}} + \boldsymbol{f_{membrane}}$$

This equation can for example be discretized as (Douthe 2007):

$$P_{i,t} = P_{i,t-1} + \dot{P}_{i,t-1}\Delta t + \frac{\Delta t^2}{m_i}(\boldsymbol{f_{cable}} + \boldsymbol{f_{membrane}})$$

The interior points are computed by projections at each iteration (as explained in section 6.4), so they do not conserve their momentum. In order to have a consistent model for both boundary and interior points, we ignore particle momentum at the boundaries by setting $\dot{P}_{i,t-1} = 0$. This is equivalent to applying a so-called kinematic damping at each step. Our numerical scheme therefore reads:

$$P_{i,t} = P_{i,t-1} + \frac{\Delta t^2}{m_i}(\boldsymbol{f_{cable}} + \boldsymbol{f_{membrane}})$$

We use $\Delta t = 1$ and a mass proportional to the length of cable, with constant lineic mass:

$$m_i = \rho \frac{\|\overrightarrow{PP_1}\| + \|\overrightarrow{PP_2}\|}{2}$$

Where ρ is adjusted manually to obtain proper speed while avoiding oscillations (which appear near equilibrium if a value too low is chosen).

We iterate until a position is found where $\|\boldsymbol{f_{cable}} + \boldsymbol{f_{membrane}}\| < \boldsymbol{\varepsilon}$. This algorithm converged in all the tested cases. Once convergence is reached, equilibrium is guaranteed.

6.7.2.3 Global resolution

The projection algorithm for interior points and the dynamic relaxation are used simultaneously in an interactive manner to deform a mesh towards a LW shape with valid cable boundaries. A user has four parameters at hand: the LW parameters a, b and c, and the cable stiffness k. The global resolution is summarized in Figure 6.29. Iterations are stopped if vertex displacements are below a certain value.

Mode advanced numerical schemes could be developed to deal with boundary and interior points in a more uniform approach. This could be achieved by deriving a variational formulation of the cable-boundary problem.

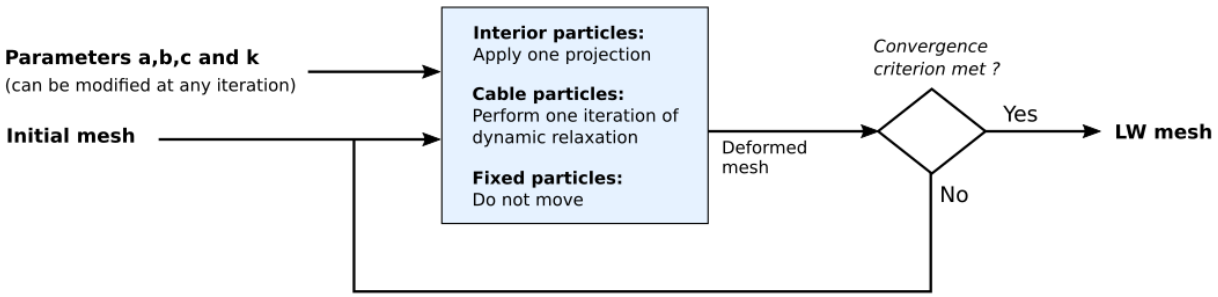

Figure 6.29: Combined resolution of interior points, cables and fixed points

6.7.2.4 Validation

Once the algorithm has converged, the geometry of boundaries can be validated by checking that the two differential equations 6.20 and 6.25 are verified.

$k_n = 0$ is automatically verified at equilibrium: since $\boldsymbol{t}$,$\boldsymbol{u_1}$ and $\boldsymbol{u_2}$ are always coplanar, the membrane force $\nabla_p A$ belongs to that plane at equilibrium. The tangent plane of the membrane, oriented by $\boldsymbol{t}$ and $\nabla_p A$, contains then the circle fitting PP_1P_2: the curvature of the cable is purely geodesic, so the normal curvature is null.

Equation 6.25 can be validated by calculating the geodesic curvature at each point. We evaluate it by taking the inverse of the radius of the circle fitting PP_1P_2. We then use a finite difference scheme to evaluate the derivative :

$$\frac{dk_g}{ds} = \frac{k_g(P_2) - k_g(P_1)}{l_1 + l_2}$$

Figure 6.30 shows how equation 6.25 is verified for a LW surface bordered by cables anchored at four points. The ratio $\frac{b}{2}\tau_g / -a\frac{k_g'}{k_g^2}$ is theoretically 1. Its value is not exactly 1, but remains between 0.9 and 1.1, except at cable extremities (blue spheres) and at one point near the middle of the cables (red spheres) for which the numerator and denominator are near zero. The fact that the value is not exactly 1 can be mostly explained by the the fact that torsion and geodesic curvature are calculated by different discrete models. Therefore, the generation method yields a cable position at equilibrium with the membrane tension, with a precision that is sufficient for our purpose.

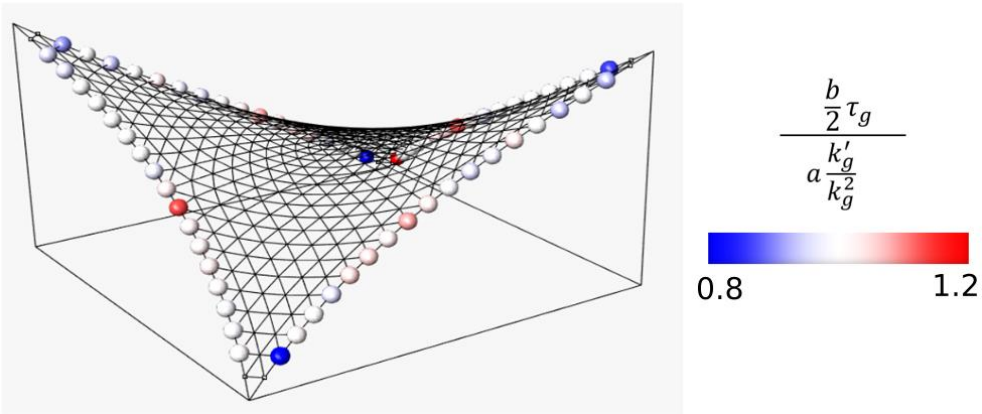

Figure 6.30: Verification of the geometry of boundary cables relatively to equation 6.25

6.7.3 Applications

Membranes attached by cables

Figure 6.32 shows examples of LW membranes ($c = 0$) bordered by (non-sliding) cables, shown in red. Anchor points of cables are shown with black dots. The left image shows a membrane bordered by a cable anchored at eight points – lighting of mesh faces is voluntarily not smoothed to highlight the mesh geometry. The right image shows a LW surface with a hole bordered by a cable anchored at only one point.

Coming back to the LW surface of Figure 6.28, we observe in the top view that boundary cables are not circular. Geodesic curvature is higher near the low points. This is expected as the tension is higher in the direction of the diagonal between the high points.

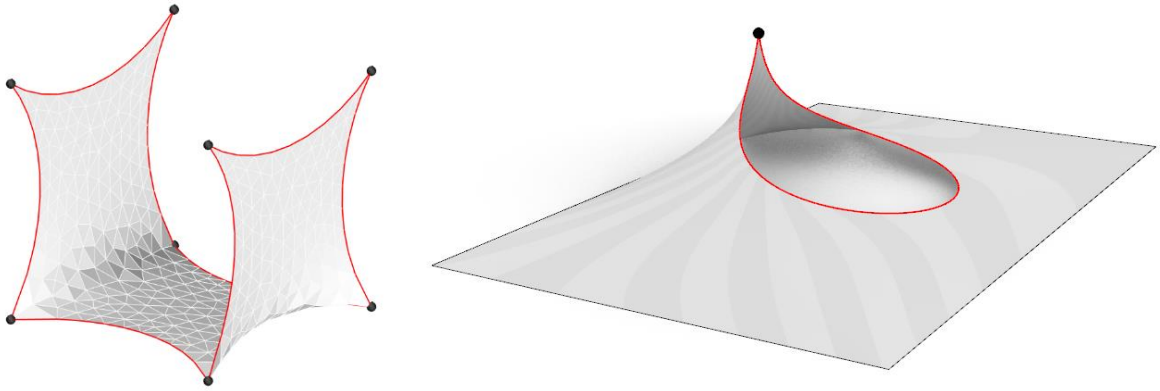

Figure 6.31: Examples of LW membranes bordered by cables

Funicular vaults with funicular edges

Figure 6.32 shows two LW vaults which are funicular in tension under a uniform upwards pressure load. The top image shows a CMC surface constructed on a circular boundary. Only a portion of the boundary is modeled as a cable. The resulting surface is not spherical, and is somehow shaped like a water droplet. When subjected to a downwards pressure load, the cable becomes a compression funicular polygon, which can be materialized by an arch with very low bending and tension resistance – such as a masonry arch.

The surface at the bottom is bordered by cables which are anchored at six points. Forces are transmitted only to the corners – this is often a constraint for covering of existing atriums. Interestingly, a small dome emerges at the angle of the L.

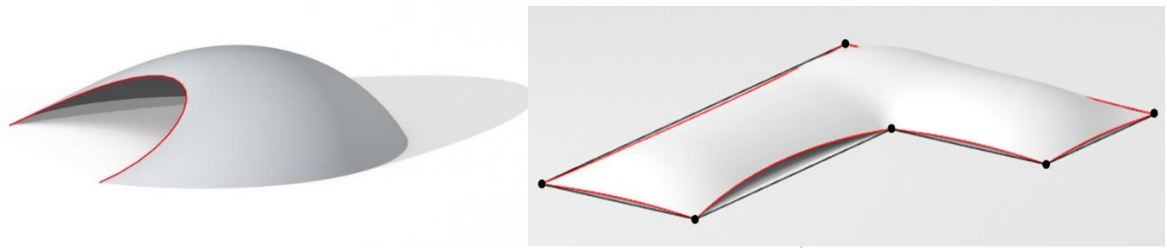

Figure 6.32: Examples of LW surfaces bordered by funicular arches

Part B - Isotropic LW surfaces

Linear Weingarten surfaces are funicular for a uniform pressure load, that is, a load that always act in the direction normal to the surface. In this part, we will show that it is possible to transpose this result to the case of a uniform load with constant direction (for example vertical) with the so-called *isotropic Linear Weingarten surfaces* (abbreviated as *i-LW*). A family of surfaces well-known to builders fall into this category: paraboloids. We will then use existing discrete curvature models to propose a generation method from boundaries (section 6.9), very similar to the one presented for Euclidian LW surfaces. An exploration of i-LW surfaces and a comparison of their geometry with Euclidian surfaces is presented (section 6.10).

6.8 Linear Weingarten surfaces in isotropic geometry

6.8.1 Introduction to isotropic geometry

Isotropic Linear Weingarten surfaces are objects of *isotropic geometry*. Isotropic geometry is a way to describe the geometry of shapes with a specific set of tools, in which the vertical direction plays a particular role. A thorough treatment can be found in (Sachs 1990). (Pottmann and Liu 2007) gives a concise introduction, on which this subsection is based: it will present the specificities of isotropic geometry needed for the next sections.

In isotropic geometry, the notions of distance, angles and curvature differ from the traditional Euclidian geometry. They are all computed relatively to a vertical projection on the horizontal plane. For example, the usual notion of distance between two points P1 and P2 is replaced by the *isotropic distance*, which measures the distance between the projections of the points in the xy plane:

$$dist_i(P_1, P_2) = \sqrt{(x_1 - x_2)^2 + (y_1 - y_2)^2}$$

Similarly, the i-angle between two lines is the angle between the projections of the lines in the horizontal plane.

Surface curvature is also described differently. This difference is best understood by looking at a planar curve $z = f(x)$ (Figure 6.33). There are two ways to describe the inclination of the tangent of such a curve:

- The angle it makes with a reference axis (e.g. a horizontal axis) ;
- The slope dz/dx.

With the first one (the angle), the curvature is naturally understood as the variation of the angle of the tangent as we move along the curve ($d\alpha/ds$, with $ds = \sqrt{dx^2 + dz^2}$), which is the inverse of the radius of the tangent circle: this is the Euclidian curvature. With the second one (the slope), the curvature is best defined as the variation of slope with respect to x (d^2z/dx^2): this is the isotropic curvature.

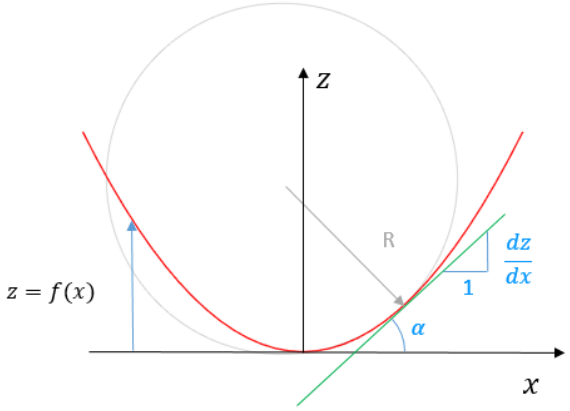

	Euclidian geometry	Isotropic geometry
Inclination	α	$\frac{dz}{dx}$
Curvature	$k = \frac{d\alpha}{ds} = \frac{1}{R}$	$k^i = \frac{d^2z}{dx^2}$

Figure 6.33: Description of curvature in Euclidian and isotropic geometry

We remark that the slope of a vertical line is infinite: isotropic geometry is not the right tool to describe curves with vertical tangents or surfaces with vertical tangent planes. It is then natural to describe surfaces as field heights $(x, y) \mapsto (x, y, f(x, y))$. The role of the curvature tensor is then played by the hessian of f:

$$\nabla^2 f = \begin{bmatrix} \partial_{xx} f & \partial_{xy} f \\ \partial_{xy} f & \partial_{yy} f \end{bmatrix}$$

$\nabla^2 f$ is symmetric, so it admits two orthogonal eigenvectors in the xy plane, which are called the *i-principal directions*. The maximum and minimum eigenvalues, $f_1$and f_2, are called *i-principal curvatures*. By integrating the principal directions, one obtains the i-principal curvature lines. They differ from the Euclidian principal curvature lines. However, they still form a conjugate net, and their vertical projection on the xy plane is an orthogonal net. They are therefore interesting to obtain PQ meshes.
Similarly to Euclidian geometry, the Gauss and mean curvature can be defined as the determinant and half-trace of the curvature tensor (an i superscript is used to differentiate them from the traditional Euclidian curvatures):

$$K^i = \partial_{xx} f \partial_{yy} f - \partial_{xy} f^2 = f_1 f_2$$
$$H^i = \frac{1}{2}(\partial_{xx} f + \partial_{yy} f) = \frac{1}{2}\Delta f = \frac{1}{2}(f_1 + f_2)$$

(We use the notation $\partial_{xx} f$ rather than f_{xx} to avoid confusion with tensor components). i-LW can then be defined as the surfaces verifying at each point:

$$aH^i + bK^i = c \qquad (6.26)$$

for given constant real coefficients a, b and c.

In isotropic geometry, the best way to define the Gauss map is to have it map surface points to the Maxwell paraboloid – instead of the sphere. The Maxwell paraboloid is defined as:

$$\Sigma : (x, y) \mapsto (x, y, \frac{1}{2}(x^2 + y^2))$$

The Gauss map associates to any point of a surface the point of the paraboloid for which the tangent plane is parallel to the surface tangent plane. Using that definition of the Gauss map, the i-Gaussian curvature at a point P has for example the same asymptotic property as its Euclidian counterpart:

$$K^i = \lim_{A \to 0} \frac{A'}{A}$$

Where A is the area of a neighborhood of P, and A' the area of the Gauss map of this neighborhood.

A common tool in isotropic geometry is the *metric duality*. It assigns to any point P with coordinates (p_1, p_2, p_3) a plane of equation $z = p_1 x + p_2 y - p_3$. Reciprocally, a point can be assigned to any plane.

Isotropic geometry and structures

Special types of i-LW surfaces have been used by structural engineers, but with a different denomination. The sub-case of *isotropic minimal surfaces* is for example known as *Pelikan surfaces*, introduced in (Pelikan 1958)[8]. These surfaces correspond to membranes for which the membrane stress tensor, when projected in the horizontal plane, is isotropic and uniform. These surfaces have been generated by dynamic relaxation (Hincz and Gaspar 1999), and have been used for example to design of membranes and concrete shells, such as the Keramion ceramics museum in Frechen (Figure 6.34), for which a tensile membrane was used as a formwork for a concrete shell (www.keramion.de 2019).

The link between isotropic geometry and shell mechanics appears when considering vertical loads. Although not labeled as such, isotropic geometry is at the basis of the Thrust Network Analysis (Block 2009). Links often appears via the Airy stress function, as observed in (Strubecker 1962). The Airy stress function is a common tool to find divergence-free stress tensors in plates. A notable application to funicular shells discretized by meshes with planar faces was made by (Vouga *et al.* 2012). (Kilian *et al.* 2017) showed how to design optimal gridshells by minimizing the total isotropic curvature of the Airy stress function.

Figure 6.34: The concrete shell of the Keramion museum in Frechen, Germany, is a Pelikan surface – a special type of i-LW surface also referred to as i-minimal. ©Klaas Vermaas

6.8.2 Mechanical properties

This section shows that i-LW surfaces enjoy a mechanical property very similar to their Euclidian counterparts. This property is best expressed using the tensor $\mathbf{N^i}$ of projected membrane stresses in the xy plane.

6.8.2.1 Funicularitty of i-LW surfaces

Proposition 6.5 (a)

Let us consider a shell with membrane-compatible support conditions and with an i-LW reference surface $aH^i + bK^i = c$, where $a, b, c \in \mathbb{R}$ are constants.

If $c \neq 0$, the shell is funicular for uniform vertical loads we_z. The projected membrane stresses are given by:

$$\mathbf{N^i} = \frac{w}{2c}\left(a\,\mathbf{I} + b\,\widehat{\nabla^2 f}\right)$$

[8] *I would like to warmly thank Pr. István Sajtos for bringing this work to my attention, as it initiated this project on isotropic LW surfaces.*

Where **I** the identity tensor of the xy plane, and $\widehat{\nabla^2 f}$ is the tensor obtained by rotating the hessian $\nabla^2 f$ by +90° around the z axis:

$$\widehat{\nabla^2 f} = \begin{bmatrix} \partial_{yy} f & -\partial_{xy} f \\ -\partial_{xy} f & \partial_{xx} f \end{bmatrix}$$

If $c = 0$, the shell admits a one parameter family of self-stress fields given by:

$$\mathbf{N^i} = \lambda\left(a\,\mathbf{I} + b\widehat{\nabla^2 f}\right)\ , \lambda \in \mathbb{R}$$

Corollary
Under a uniform vertical load, principal membrane stresses on an i-LW shell form a conjugate net. Discretization by stress lines hence give quadrangles which are near-planar.

Proof:
Membrane equations can be written in Cartesian coordinates, as detailed for example in (Ventsel and Krauthammer 2001). The projected membrane stress field $\mathbf{N^i}$ is at equilibrium under a vertical load Ge_z if it verifies:

$$div\ \mathbf{N^i} = \mathbf{0}$$

$$div(\mathbf{N^i}.\nabla f) = G$$

These equations correspond respectively to the horizontal and vertical equilibrium. The fact that $div\ \mathbf{N^i} = 0$ can be used to simplify the vertical equilibrium equation in the form:

$$tr(\mathbf{N^i}.\nabla^2 f) = G$$

The divergence of the stress fields from the proposition are:

$$div\ \mathbf{N^i} = \frac{w}{2c}\left(a\ div\ \mathbf{I} + b\ div(\widehat{\nabla^2 f}\right)$$

Obviously, $div\ \mathbf{I} = 0$. Furthermore, by expressing $\widehat{\nabla^2 f}$ in x, y coordinates:

$$div\left(\widehat{\nabla^2 f}\right) = div\begin{bmatrix} \partial_{yy} f & -\partial_{xy} f \\ -\partial_{xy} f & \partial_{xx} f \end{bmatrix} = 0$$

The proposed stress fields are therefore at horizontal equilibrium.

The vertical equilibrium is obtained by expressing $\nabla^2 f$ and $\widehat{\nabla^2 f}$ in the i-principal curvature directions:
If $c \neq 0$:

$$\begin{aligned} tr(\mathbf{N^i}.\nabla^2 f) &= \frac{w}{2c} tr\left(\left(a\begin{bmatrix}1 & 0\\ 0 & 1\end{bmatrix} + b\begin{bmatrix}f_2 & 0\\ 0 & f_1\end{bmatrix}\right)\begin{bmatrix}f_1 & 0\\ 0 & f_2\end{bmatrix}\right) \\ &= \frac{w}{2c}(a(f_1 + f_2) + 2bf_1 f_2) \\ &= \frac{w}{2c}(2aH^i + 2bK^i) \\ &= w \end{aligned}$$

The same reasoning applies to the case $c = 0$.

6.8.2.2 Generalization

Pelikan surfaces actually form a wider family than i-minimal surfaces. They are membrane shapes which admit a constant projected stress tensor, not necessarily isotropic (i.e. not necessarily proportional the identity tensor). Designers use this property for example to create membranes with more tension in x

direction than in y. To include this, we can generalize the former proposition by weighting differenttly the curvature in x and y in the calculation of the mean curvature:

Proposition 6.5 (b)
Let us consider a shell with membrane-compatible support conditions and with a reference surface verifying:

$$a_x \partial_{xx} f + a_y \partial_{yy} f + bK^i = c$$

where $a_x, a_y, b, c \in \mathbb{R}$ are constants.
If $c \neq 0$, the shell is funicular for a uniform vertical loads we_z. The projected membrane stresses are given by:

$$\mathbf{N^i} = \frac{w}{2c}\left(2 \begin{bmatrix} a_x & 0 \\ 0 & a_y \end{bmatrix} + b\, \widehat{\nabla^2 f}\right)$$

Where the first matrix is expressed in the basis (e_x, e_y).

If $c = 0$, the shell admits a one parameter family of self-stress fields given by:

$$\mathbf{N^i} = \lambda\left(2 \begin{bmatrix} a_x & 0 \\ 0 & a_y \end{bmatrix} + b\widehat{\nabla^2 f}\right) \ , \lambda \in \mathbb{R}$$

Proof:
We obviously have horizontal equilibrim:

$$div\, \mathbf{N^i} = \mathbf{0}$$

Regarding vertical equilibrium:

$$\frac{2c}{w} tr(\mathbf{N^i}.\nabla^2 f) = \mathrm{tr}\left(2 \begin{bmatrix} a_x & 0 \\ 0 & a_y \end{bmatrix} . \begin{bmatrix} \partial_{xx} f & \partial_{xy} f \\ \partial_{xy} f & \partial_{yy} f \end{bmatrix}\right) + b\, tr\left(\begin{bmatrix} f_2 & 0 \\ 0 & f_1 \end{bmatrix} . \begin{bmatrix} f_1 & 0 \\ 0 & f_2 \end{bmatrix}\right)$$

$$= 2\, a_x \partial_{xx} f + 2 a_y \partial_{yy} f + 2bK^i = 2c$$

Hence:

$$tr(\mathbf{N^i}.\nabla^2 f) = w$$

The stress field therefore verifies also vertical equilibrium.

We shall not consider further the surfaces $a_x \partial_{xx} f + a_y \partial_{yy} f + bK^i = c$ in this chapter, they could be addressed in future work. We will just remark a link with relative differential differential geometry: Surfaces $a_x \partial_{xx} f + a_y \partial_{yy} f = c$ are CMC relatively to a Gauss map on a paraboloid, not necessarily of revolution.

6.8.2.3 Self-weight load

We have considered so far uniform pressure loads and uniform vertical loads. Each load can be resisted in a funicular manner by a surface with constant mean curvature, but using a different definition of the mean curvature. Similarly, the self-weight of a shell of constant thickness can be addressed by introducing a third type of curvature:

Proposition 6.5 (c)
A shell of constant thickness with reference surface $z = f(x, y)$ such that:

$$\frac{tr(\nabla^2 f)}{\sqrt{1 + \|\nabla f\|^2}} = c \ , c \in \mathbb{R}$$

is self-supported: It can resist its own weight with pure membrane stresses, such that the projected membrane stress tensor in the horizontal plane is isotropic and constant.

Proof:
Self-weight is a vertical load of amplitude:

$$G(x,y) = \mu \sqrt{1 + \|\nabla \mathrm{f}\|^2} \ , \mu \in \mathbb{R}$$

Where G is for expressed for example in kN per m² of projected area in the xy plane. Let us consider the projected stress tensor $\mathbf{N^i} = \frac{\mu}{c}\,\mathbf{I}$. It verifies $div\ \mathbf{N^i} = \mathbf{0}$. Furthermore:

$$tr(\mathbf{N^i}.\nabla^2 f) = tr\left(\frac{\mu}{c}\,\nabla^2 f\right) = \mu \sqrt{1 + \|\nabla \mathrm{f}\|^2} = G$$

$\mathbf{N^i}$ is therefore at equilibirum under the load G.

This equation opens the way to the search of analytical self-supporting surfaces. One could for example search for a family of funicular surfaces of revolution: Their meridians could be found by solving an ordinary differential equation, with one variable. One could also look for funicular surfaces of translations. These surfaces will not be addressed further in this chapter.

6.8.2.4 Recovering membrane stresses

The membrane stress tensor $\mathbf{N}$ can be recovered from the projected tensor $\mathbf{N^i}$ following equations given for example in (Frey and Studer 2003). Let us call:

- e_x and e_y the base vectors of the plane xy;
- e_x^S and e_y^S the projections of the base vectors e_x and e_y in the tangent plane of the surface. These vectors are in general not orthogonal;
- N_{xx}, N_{xy}, N_{yy}, the components of the membrane tensor $\mathbf{N}$ in the basis (e_x^S, e_y^S). $N_{xx}\, e_x^S + N_{xy}\, e_y^S$ (respectively $N_{xy}\, e_x^S + N_{yy}\, e_y^S$) is then the membrane stress vectors acting on a facet with normal e_x^S (resp. e_y^S);
- α and β are the slope angles in the x and y directions:

$$\tan\alpha = \partial_x f \ ; \ \tan\beta = \partial_y f$$

The coefficients of the membrane stress tensor are then:

$$N_{xx} = N_{xx}^i \frac{\cos\beta}{\cos\alpha} \ ; \ N_{xy} = N_{xy}^i \ ; \ N_{yy} = N_{yy}^i \frac{\cos\alpha}{\cos\beta}$$

Note: Despite the fact that $N_{xy} = N_{xy}^i$, principal directions of $\mathbf{N^i}$ (for which shear is null) are not the projections of the principal directions of $\mathbf{N}$. This is due to the fact that the x and y axes do not project in general to orthogonal axes on the membrane tangent plane.

6.8.3 Analytical examples of i-LW surfaces

Although the definition of i-LW surfaces given in equation (6.26) might seem quite abstract, there are actually many well-known families of analytical surfaces which verify it. Analytical surfaces are convenient for a designer, as they define precisely the surface geometry. It is relatively easier to derive analytical equations for i-LW surfaces than for the Euclidian ones, in particular because the i-mean curvature is a linear operator with respect to a height function.

6.8.3.1 Paraboloids

Paraboloids as isotropic Linear Weingarten surfaces

Paraboloids are a very common family of shapes for shells (see Figure 6.35). They can be locally described as height field surfaces. With a proper choice of axes and origin, their equation reads:

$$z = \alpha x^2 + \beta y^2$$

If $\alpha\beta < 0$, the surface is called a hyperbolic paraboloid (or « hypar »), and contains two families of straight lines. If $\alpha\beta > 0$, the surface is called an elliptic paraboloid. The Hessian of the height field reads:

$$\nabla^2 f = \begin{bmatrix} 2\alpha & 0 \\ 0 & 2\beta \end{bmatrix}$$

Paraboloids are isotropic LW surfaces, as their mean and Gaussian curvature are both constant:

$$H^i = \alpha + \beta$$

$$K^i = 4\alpha\beta$$

There is actually one degree of freedom to define the (a, b, c) coefficients of the LW relationship (more precisely, one more degree of freedom than the trivial scaling of a, b and c):

$$aH^i + bK^i = c \iff a(\alpha + \beta) + b\,4\alpha\beta = c$$

We fix the trivial scaling of (a, b, c) by setting either $c = 0$ or $c = 1$. In both cases, this equation is verified for any value of a if:

$$b = \frac{c - a(\alpha + \beta)}{4\alpha\beta} \tag{27}$$

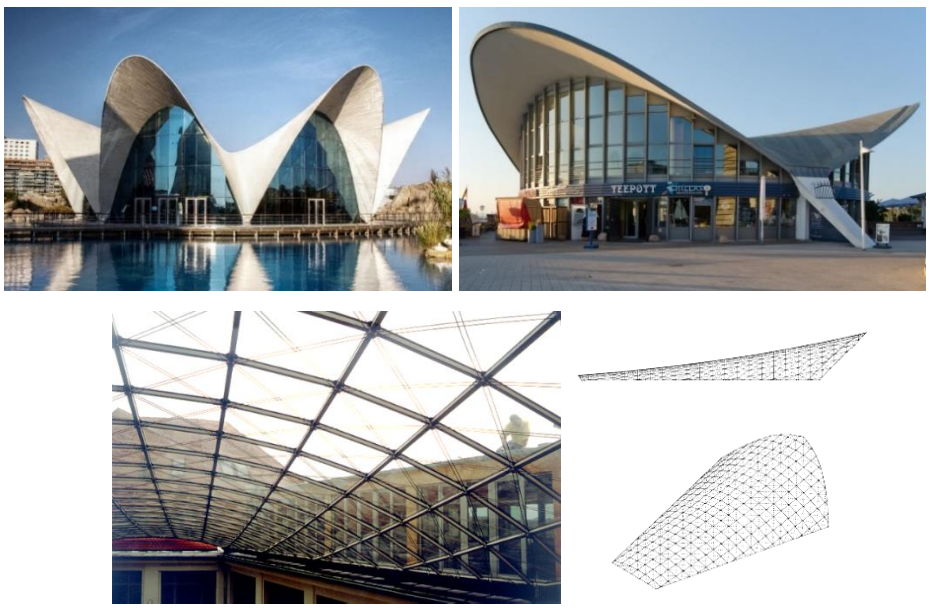

Figure 6.35: These three structure are composed of paraboloids, which are a special types of isotropic LW surfaces.
Top left: El Oceanográfico (F. Candela), Valencia, Spain (©Felipe Gabaldón);
Top right: Teepott restaurant, Warnemünde, Germany (©An-D) ;
Bottom: Courtyard roof Industriepalast, Leipzig (reproduced with permission from (Glymph et al. 2004))

It is well known that the projection of a regular xy grid on a paraboloid of main axis x and y gives a planar quad mesh. This is easily understood when interpreting paraboloids as surfaces resulting from the translation of a parabola along another parabola. An example is the roof of the Industriepalast in Leipzig, shown in Figure 6.35. This property is a consequence of the fact the isotropic principal curvature directions are conjugate.

Mechanics of paraboloids

Mechanical models for hyperbolic paraboloids have been developed by Felix Candela to design and check many of the concrete shells he has built in his career (Candela 1955). He showed that hypars can resist uniform snow loads with pure membrane stresses. He also found clever solutions to obtain free boundaries. For example, if a hypar is bordered by four straight edge beams located along rulings, then these edge beams work in pure compression if the structure is subjected to uniform vertical load. Analytical stress equations for general paraboloids (hyperbolic or elliptic) can be found for example in (Billington 1965).

These mechanical equations can be easily retrieved from our model of i-LW surfaces. Given a paraboloid $z = \alpha x^2 + \beta y^2$, we have two possible choices for parameter c, $c = 0$ or $c = 1$:

- With $c = 1$, we can interpret the shape as funicular under uniform vertical. Using equation (27), there is a one-parameter family of admissible stress fields :

$$\mathbf{N^i} = \frac{w}{2}\left(a\, I + b\, \widehat{\nabla^2 f}\right) = \frac{w}{2}\left(a \begin{bmatrix} 1 & 0 \\ 0 & 1 \end{bmatrix} + \left(\frac{1 - a(\alpha + \beta)}{4\alpha\beta}\right) \begin{bmatrix} 2\beta & 0 \\ 0 & 2\alpha \end{bmatrix}\right), a \in \mathbb{R}$$

  We bring attention to the reader that, in order to be funicular under dead load, a paraboloid needs to be properly oriented: its shape must be described by an equation $z = \alpha x^2 + \beta y^2$, with xy being a *horizontal* plane.
- With $c = 0$, we find another family of admissible stress fields, which corresponds to self-stressed states:

$$\boldsymbol{N^i} = a\, \boldsymbol{I} + b\widehat{\nabla^2 f} = a\left(\begin{bmatrix} 1 & 0 \\ 0 & 1 \end{bmatrix} - \frac{(\alpha + \beta)}{2\alpha\beta} \begin{bmatrix} \beta & 0 \\ 0 & \alpha \end{bmatrix}\right), a \in \mathbb{R}$$

The fact that paraboloids are at the same time self-stress shapes and funicular shaped under uniform load is remarkable. For example, if a hypar membrane is used as a formwork for casting a concrete shell, the membrane deflection under the dead load of the fresh concrete is expected to be very low compared to other arbitrary membrane shapes: deflections will be mostly due to membrane stretching rather than to a deflection to get into a funicular shape. We remark that if $\alpha + \beta = H^i \neq 0$, warp and weft of the membranes need to be aligned with the horizontal x and y axes – otherwise the stress field is not admissible.

Note: To admit both a self-stress state and a funicular stress field under vertical load, a Euclidian LW surface needs to verify the relationship $aH + bK = c$ for different sets of coefficients. This implies that its curvature diagram is the intersection of two straight lines, and is therefore reduced to a point. This implies that its principal curvatures are constant. In isotropic geometry, the paraboloids are the only i-LW surface verifying this property ($f_{xx} = 2\alpha$, $f_{yy} = 2\beta$). One might wonder if it is possible to use this particularity to find Euclidian LW surfaces that enjoy the same mechanical property, with a uniform pressure load instead of a vertical load. Unfortunately, the only surfaces having constant principal curvatures in Euclidian geometry are spheres, cylinders and planes (this is a consequence of the Mainardi-Codazzi equations, see (do Carmo 1976) – chapter 4, equations (7) and (7a)).

Patching paraboloids

Rows of paraboloids can be assembled to form a C^1 surface that is still i-LW. Indeed, let us consider the paraboloids of Figure 6.36 which form a row on the x axis. Blue and white patches can be described respectively by equations $z = \alpha_{blue} x^2 + \beta y^2$ and $z = \alpha_{white} x^2 + \beta y^2$, β being identical to insure continuity. If we set:

$$a = 1\,;\, b = \frac{-1}{4\beta}\,;\, c = \beta$$

Then, for both blue patches:

$$aH^i + bK^i = (\alpha_{blue} + \beta) + \frac{-1}{4\beta}\, 4\alpha_{blue}\beta = \beta = c$$

The same results holds for the white patches. The surface is therefore i-LW. The fact that it is not C^2 does not alter the mechanical properties: we can find a continuous membrane stress field across the whole surface under uniform vertical load. It does not either alter the paneling by planar quads, because the i-principal curvatures are aligned with the x and y axes for all patches.

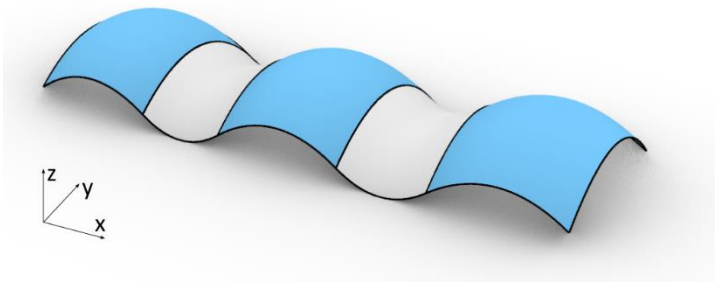

Figure 6.36: C^1 i-LW surface composed of paraboloids

Note:
This reasoning can be actually extended to an arbitrary number of patches $z = \alpha_i x^2 + \beta y^2, i = 1,2 \dots, n$, or even to a translation surface generating by translating a parabola of the yz plane along a curve of the xz plane, i.e. a surface with equation:

$$z = g(x) + \beta y^2$$

where g is an arbitrary real continuous function and β a real number.

6.8.3.2 *Harmonic functions*

Scalar harmonic functions verify $\Delta f = 0$. They are therefore field heights of i-minimal surfaces, and correspond to shapes of self-stressed membranes. There is a rich mathematical theory behind these surfaces. One method to generate a rich variety of analytical harmonic functions is via complex holomorphic functions (Cartan 1963). A holomorphic function of a region $D \subset \mathbb{C}$ is a function $f: D \to \mathbb{C}$ which is conform, i.e. it transforms an infinitesimal square of D into another infinitesimal square of $\mathbb{C}$. Most of the complex functions that one could think about that do not contain the complex conjugate $\bar{z}$ are holomorphic. This is the case in particular of the following functions:

- Polynomials. Ex : $f(z) = z^7 - 42iz \;, z \in \mathbb{C}$
- Rational functions (fractions of polynomials). Ex : $f(z) = \frac{z+1}{z-1}$
- Exponential functions. Ex : $f(z) = \frac{e^{iz}+e^{-iz}}{2} = \cos z$
- Linear combination of harmonic functions. Ex : $f(z) = e^z + 1/z$

The link with i-minimal surfaces appears with an important theorem about holomorphic functions: The real part and imaginary part of a holomorphic function are both harmonic. Figure 6.37 shows several i-minimal surfaces generated using this property (with $z = x + iy$):

- Top left: $f(z) = Re(\log z)$ (where log is a complex logarithm)
- Top middle: Monkey saddle of order 3: $f(z) = Re(z^3) = x^3 - 3xy^2$
- Top right: $f(z) = Re(1/\|z\|^2)$
- Bottom left: $f(x, y) = \cos x \exp(y - 1) + \cos(x + \pi) \exp(-y - 1)$

- Bottom right: $f(z) = \text{atan}(z)$

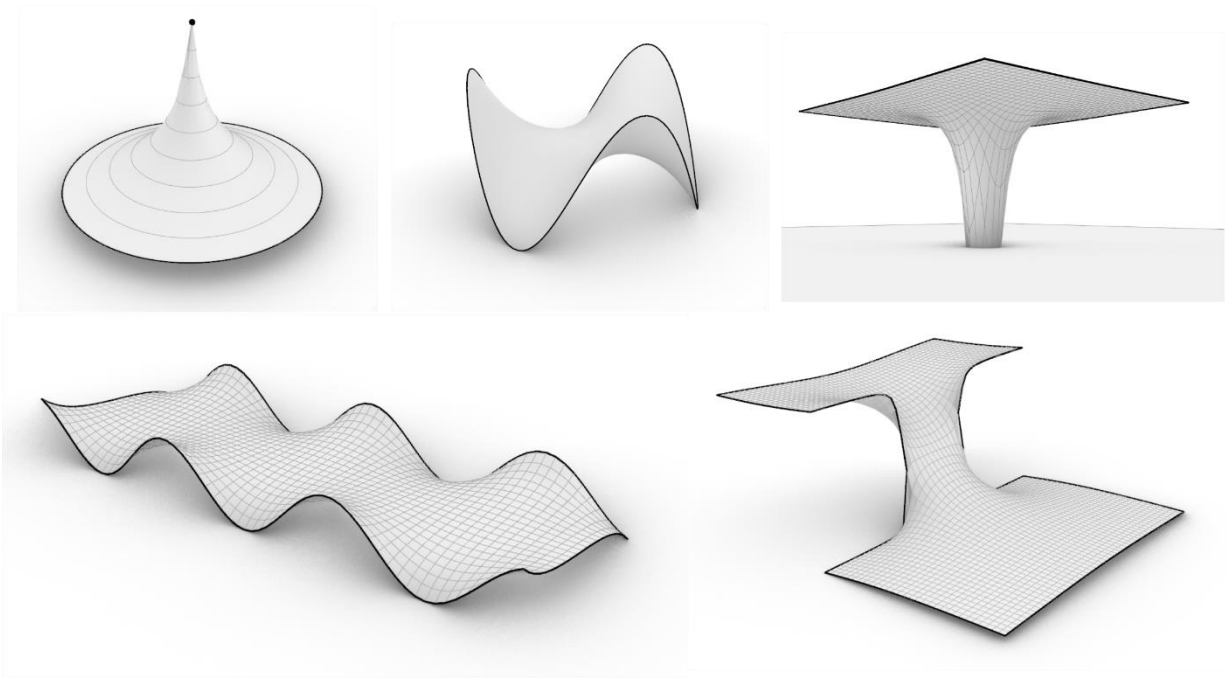

Figure 6.37: Analytical i-minimal surfaces – each surface can be realized as a tension membrane

6.8.3.3 *i-developable surfaces*

i –developable surfaces are characterized by $K^i = 0$. K^i can be written as a function of the euclidian surface curvature. For a height field surface defined as $f: D \subset \mathbb{R}^2 \to \mathbb{R}$ (do Carmo 1976):

$$K = \frac{\partial_{xx} f \partial_{yy} f - \partial_{xy} f^2}{\left(1 + \partial_x f^2 + \partial_y f^2\right)^2} = \frac{K^i}{(1 + \|\nabla f\|^2)^2}$$

Therefore, any developable surface ($K = 0$) that can be described as a height field is i-developable. Reciprocally, any i-developable surface is developable.

Note:
The mean curvature can also be expressed as a function of the isotropic mean curvature:

$$H = \frac{H^i + \frac{1}{2}\,\nabla f . \widehat{\nabla^2 f} . \nabla f}{(1 + \|\nabla f\|^2)^{3/2}}$$

From that expression, it appears clearly that there is no equivalence between minimal and i-minimal.

6.8.3.4 *Surfaces of revolution and helices*

(Ogrenmis 2016) solved the ordinary differential equation fulfilled by the meridian of an i-LW surface of revolution, and gives the analytical solution. There are two degrees of freedom to design the meridian for a given set of coefficients (a, b, c) – except for some degenerate coefficients for which there is only one. (Yoon and Lee 2016) performed the same work for i-LW surfaces with helicoidal symmetry.

6.9 Generation of i-LW surfaces from boundary curves

Despite the great variety of analytical i-LW surfaces, they do not allow for an intuitive exploration of the entire design space. In this section, a generation method for elliptical i-LW surfaces (verifying $a^2 + 4bc > 0$) from boundary curves is presented. It is very similar to the one developed for Euclidian LW surfaces in part A.

6.9.1 Discretization

The proposed generation method requires a vertex-wise discrete model for H^i and K^i for unstructured triangular meshes. Such a model was proposed in (Pottmann and Liu 2007). The calculation steps to compute the curvature of a vertex v in a mesh M are the following:

i. Compute the metric dual of the planes of the faces adjacent to vertex v. The dual of the plane of a face i is a point, which, once projected vertically onto the xy plane, yields a point m_i. The points m_i form a closed polygon L_m. The area of this polygon, $A(L_m)$ can be calculated as:

$$A(L_m) = \frac{1}{2}\sum \det(m_i, m_{i+1})$$

ii. Project the 1-star of v vertically on the Maxwell paraboloid Σ. Compute the metric dual of the projected faces: they form a closed polygon. Project it onto the xy plane, thus forming the polygon $s_1 s_2$ ... called L_s, with oriented area A(L_s).

iii. Compute the mixed area of polygons L_M and L_S, defined as:

$$A(L_M, L_S) = \frac{1}{4}\sum (\det(m_i, s_{i+1}) + \det(s_i, m_{i+1}))$$

iv. The discrete Gaussian and mean curvature are then computed as :

$$K^i(v) = \frac{A(L_m)}{A(L_s)}, \quad H^i(v) = \frac{A(L_m, L_s)}{A(L_s)}$$

Assessment of discrete model

Values are plotted on Figure 6.38 for two triangular meshes inscribed in paraboloids. The discrete curvatures are very close to the ones of the smooth paraboloids for the synclastic paraboloid. However, high discrepancies are observed for K^i for the hypar, especially for nodes of valence different from 6, and in areas of high slope. This problem of approximation of Gaussian curvature for inscribed surfaces was identified in (Borrelli *et al.* 2003) in Euclidian geometry, and already discussed in part A of this chapter. We observe the same issue in isotropic geometry. However, we shall see later that these discrepancies are not an issue.

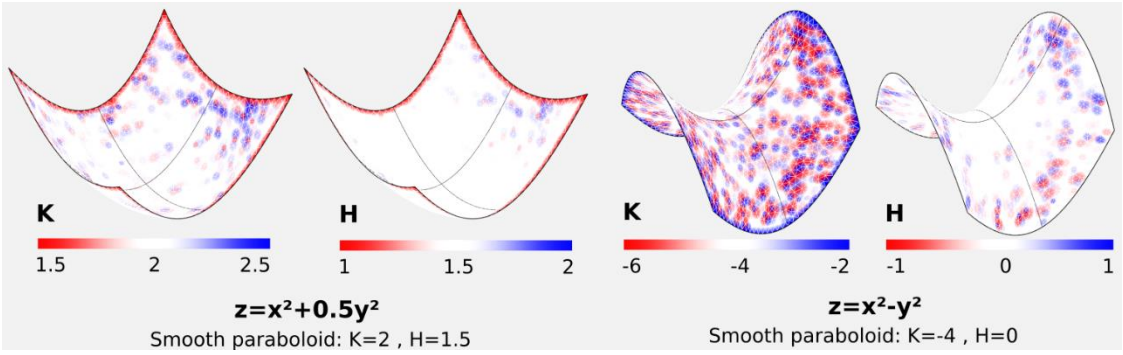

Figure 6.38: Evaluation of discrete models for isotropic Gaussian and mean curvatures

Discrete isotropic Linear-Weingarten surfaces

From these discrete models of isotropic mean and Gaussian curvatures, *i-LW triangular meshes* can naturally be defined as meshes for which a linear combination of these two curvatures is constant for each vertex:

$$\forall\ vertex\ v, \qquad aH^i(v) + bK^i(v) = c, \qquad a, b, c \in \mathbb{R}$$

Notes:

- With this model, vertices should not have too high x or y coordinates: The projection to the i-sphere gets points to an altitude x^2+y^2, working tolerance can be reached easily.
- Contrary to the Euclidian LW surfaces, we are working here with H^i and K^i which are local quantities, and not "integrated quantitities". Therefore, the coefficient c is not factored by the area.
- $H^i(v)$ could be calculated in a more simple way by taking a discrete Laplacian of the z coordinates of the vertices. The chosen discretization is more complex, but more consistent with the discrete model of K^i.

6.9.2 Generation method

Lack of variational approach

i-CMC surfaces (i.e. surfaces $aH^i = c$) are critical points of a combination of the Dirichlet energy and the volume:

$$E = \frac{a}{2}\iint \|\nabla f\|^2 dxdy - c\iint f\ dxdy$$

However, there is no known variational formulation associated with the term bK^i. In particular, we cannot use the total isotropic mean curvature as a functional, because *any* surface is a critical point of this quantity. This is due to the fact that H^i_{tot} depends solely on the value of the function at the boundary. This stems from the 2nd Green identity:

$$H^i_{tot} = \iint H\ dxdy = \frac{1}{2}\iint \Delta f\ dxdy = \frac{1}{2}\int_{boundary} \frac{\partial f}{\partial n}\ ds$$

Monge-Ampere equation

The partial differential equation (PDE) $aH^i + bK^i = c$ is a special case of the Monge-Ampère equation (Courant and Hilbert 1962), as it can be written in the form:

$$E\left(\partial_{xx}f\,\partial_{yy}f - \partial_{xy}f^2\right) + A\,\partial_{xx}f + 2B\,\partial_{xy}f + C\,\partial_{yy}f + D = 0$$

With $E = b\ ;\ A = C = \frac{a}{2}\ ;\ B = 0\ ;\ D = -c$

This is a fully nonlinear PDE, so there is much less knowledge about it compared to simpler PDEs like linear ones. We highlight the following results:

- The theorem of Rellich (Rellich 1933) states that if $4(AC - B^2 - DE) = a^2 + 4bc > 0$, then there exists at most two solutions of $aH^i + bK^i = c$ for a Dirichlet boundary problem (i.e. a problem where f is imposed on closed boundaries). The quantity $a^2 + 4bc$ appears again in relation with Dirichlet problem, as in Euclidian LW surface;
- (Caffarelli *et al.* 1984) proved the unicity of a convex solution if $A = B = C = D = 0$ in the case where the boundaries delimit a convex domain in the xy plane;.

- Many numerical methods have been proposed to solve the Dirichlet problem over a convex domain for the equation $\partial_{xx}f\partial_{yy}f - \partial_{xy}f^2 = g$ where g is a real function (Dean and Glowinski 2003, 2004; Oberman 2008; Benamou *et al.* 2010).

Projection approach

The projection method described in part A can be applied to generate i-LW surfaces. Despite the lack of theoretical results on the existence of solutions, it was found to work satisfyingly well. The only limitation is for non-convex boundaries, for which only a limited range is accessible for parameter b – beyond that range, the algorithm diverges, this will be discussed in the next section.

The basis of the algorithm to generate Euclidian LW surfaces is a division of elliptical LW surface into type I and type II. In isotropic geometry, the Gauss and mean curvature verify the same inequality as their Euclidian counterparts:

$$H^{i\,2} - K^i = \left(\frac{f_1 - f_2}{2}\right)^2 \geq 0$$

As a result, smooth i-LW surfaces can also be separated into type I and type II surfaces provided that $a^2 + 4bc \geq 0$.

Similarly to the method for Euclidian LW, we propose an iterative algorithm in which, at each step, each vertex is projected to a position at which it verifies the i-LW relation $aH^i + bK^i = c$, without taking into account the displacements of its neighbours. Projections are iterated until the entire mesh is i-LW for a given tolerance. i-LW projections are searched along an axis passing through the center of gravity of the boundary edges.

The differences with the Euclidian case algorithm are the following:

- The search axis is vertical (instead of being oriented along the vector area);
- The search process does not require a Newton algorithm, because $aH^i + bK^i = c$ varies quadratically along a vertical axis.

Exact line search

As the center vertex of a 1-star is moved along a vertical axis, we remark that:

- $A(L_s)$ does not change;
- $A(L_m)$ varies quadratically;
- $A(L_m, L_s)$ varies linearly.

Therefore, $aH^i + BK^i - c$ is quadratic in z:

$$aH + bK - c = P(z) = \alpha z^2 + \beta z + \gamma$$

The coefficients α, β and γ can be calculated by evaluating $aH^i + BK^i - c$ at three different altitudes. The resolution in z is then straightforward.

Case $b = 0$

If $b = 0$, the equation is linear. This case corresponds to i-CMC surfaces. α, β and γ are given by:

$$\alpha = 0 \;;\; \gamma = P(0) \;;\; \beta = \frac{P(h) - \gamma}{h}$$

Where h is an arbitrary length, taken for example as the average edge length of the 1-star boundary. Then:

$$z = -\gamma/\beta$$

Case $b \neq 0$

In that case, the equation is quadratic. We calculate coefficients α, β and γ as follows:

$$\gamma = P(0) \ ; \ \beta = \frac{P(h) - P(-h)}{2h} \ ; \ \alpha = \frac{P(h) - \beta h - \gamma}{h^2}$$

We then compute the discriminant $\Delta = \beta^2 - 4\alpha\gamma$. We choose the height z as follows:

- If $\Delta > 0$: For a type I solution, we choose the root solution $z = \frac{-\beta - \sqrt{\Delta}}{2a}$; for a type II solution, we choose $z = \frac{-\beta + \sqrt{\Delta}}{2a}$
- If $\Delta = 0$, we obviously return the only solution;
- If $\Delta < 0$, we output the critical point, which minimizes $|aH + bK - c|$:

$$z = -\frac{\beta}{2\alpha}$$

6.9.3 Instabilities for non-convex domains

The algorithm was found to become unstable if the following two circumstances were combined:

- A high value of -b is used;
- The projection of the boundary in the xy plane defines a non-convex domain (i.e. we can find two points in this domain such that the line segment between the two points is not entirely inside the domain).

This instability can be understood by looking at the i-LW position of the red vertex shown in Figure 6.39 with the coefficients $(a, b, c) = (1,10,0)$. Since $c = 0$, one would expect the solution to lie in the convex hull of the boundary (a tensile membrane always lie within the convex hull of its boundaries). However, it is not the case. The algorithm pushes the point out of the convex hull, this effect can lead to divergence after several iterations.

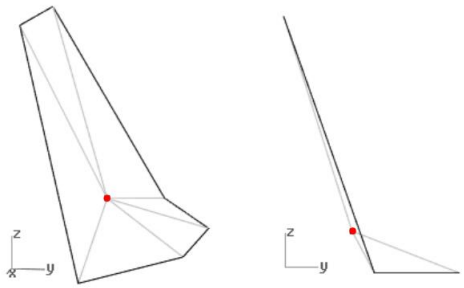

Figure 6.39: The i-LW position of the center vertex is outside of the convex hull of the boundary whereas $c = 0$.

Figure 6.40 and Figure 6.41 highlight the importance of the convexity of the boundary. In Figure 6.40, the boundary projects to a rectangle. Any value of b can be chosen, the algorithm remains stable. In Figure 6.41, the boundary is slightly deformed, such that its plane view does not define a convex domain anymore. Instability then occurs for high (negative) values of b. We remark that all the references given in section 6.9.2 on the numerical resolution of the Monge-Ampere equation address only cases in which the boundary is convex.

This problem is related to the "necking" of Euclidian LW surfaces, which also occurred for low values of b. Intuitively, such an instability is expected. Without it, in Figure 6.41, by decreasing b to $-\infty$, one could reach a convex developable surface that wraps the boundary curve from below and which is also a field height. Such a surface does not exist (it would require a curved fold, which has a convex (H>0) and a

concave (H<0) portion. This is impossible with $|b| \gg a, a \neq 0, c = 0$ because of the separation of i-LW surfaces into type I and type II).

We also remark another issue in Figure 6.40 (left) – which is yet convex. For $-b \gg a$, the surface given by the algorithm, although i-developable with a very good precision, is not quite what a designer would expect: the surface is locally crumply (this is not visible on the picture), we do not obtain a smooth developable surface contrary to the Euclidian case or to the case $b>0$. This is correlated to the way the in-plane smoothing is handled, which results in much sparser vertices in areas of high slopes. This problem has been observed numerically only for "tough" boundaries (combination of sharp angles, sudden height changes, no strict convexity of the projection of boundary) with $-b/a \gg 1$.

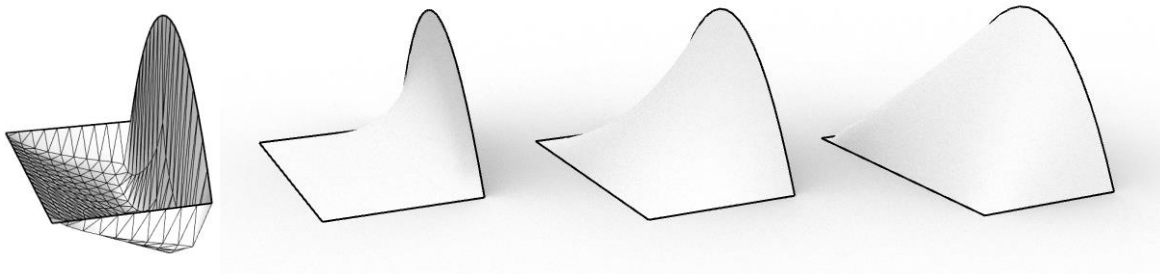

Figure 6.40: Four i-LW surfaces generated on the same boundary curve that projects to a rectangle in the xy plane. Left: (a,b,c)=(0,-1,0). Mid-Left: (a,b,c)=(1,-3,0). Mid-right: i-minimal surface. Right (a,b,c)=(0,+1,0).

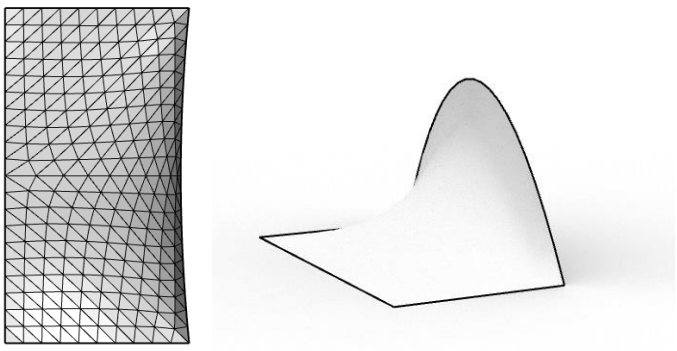

Figure 6.41: The boundary curve of this i-LW surface is slightly deformed compared to Figure 6.40 to make its projection in the xy plane non-convex (as seen in the top view). The algorithms is then unstable for a=1, c=0, b<-2.4. Right: surface near the critical value of b

Note: Referring to Figure 6.39, it is often possible to find an i-LW position within the convex hull of adjacent vertices if we do not restrain the search to a vertical axis passing through the centroid. A modified algorithm was implemented, in which the i-LW found on the vertical axis is projected onto the convex hull if it is out of it. However, this algorithm does not converge to a smooth i-LW surfaces.

6.9.4 Validation

6.9.4.1 Geometrical validation

The generation method is validated using again paraboloids. By generating a surface with the analytical boundaries of a paraboloid, one can obtain an i-LW mesh very close to the paraboloid. Examples are given in Figure 6.42. Curvatures, Gaussian and mean, both converge well to their expected value. Results are given for 1000 iterations

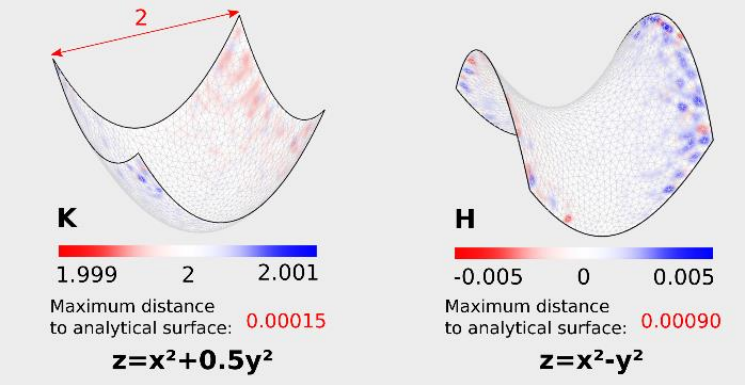

Figure 6.42: Model validation - Construction of paraboloids from their boundaries

Note 1:

To finish our discussion about vertex-wise approximation of curvatures, related to (Borrelli *et al.* 2003), we remark that that the discrete scheme of K^i and H^i, which were giving poor results for a mesh inscribed in an i-LW surface, can actually converge very well to the smooth curvatures of the underlying surface (whatever the vertex valence) if the mesh approximates the surface without being *inscribed* in it, i.e. if its vertices are not constrained to be on the surface.

Note 2:

The proposed algorithm is merely a resolution method for the Monge-Ampere equation. We do not give a general proof of convergence, unlike other methods in the literature that address the case $\partial_{xx}f\,\partial_{yy}f - \partial_{xy}f^2 = g$ where g is a real function of the plane. Future work could address proof of convergence and comparison of performance with other methods. However the algorithm was found to be satisfyingly robust and fast for design applications.

6.10 Designing with i-LW surfaces

6.10.1 Membranes

With $c = 0$, the surfaces $aH^i + bK^i = 0$ correspond to the equilibrium shapes of self-stressed membranes. The shape difference with their Euclidian counterparts is best understood by looking at minimal surfaces. Compared with minimal surfaces, i-minimal surfaces:

- Do no not have uniform stresses. Their projected stresses are uniform, which implies that the membrane stresses are higher in areas of high slope;
- Are restricted to shapes that are field heights;
- Can join boundaries with significant height difference, which cannot be interpolated by a single minimal surface.

The shape differences are illustrated in Figure 6.43. i-minimal and minimal surfaces are created on the same three boundaries, with increasing height differences between the large oval on the ground and the two loops at the center. In the top row, the height difference is quite low, such that the difference between the two surfaces is hardly noticeable. In the middle row, the height difference is increased: the difference between the two surfaces is clear. Necking is observed in the minimal surface around the center loops, but not for the i-minimal surface, which is actually just a scaled copy (in the z-direction) of the one above. In the bottom row, the height difference is further increased. There does not exist anymore a stable minimal surface fitting the boundary curves.

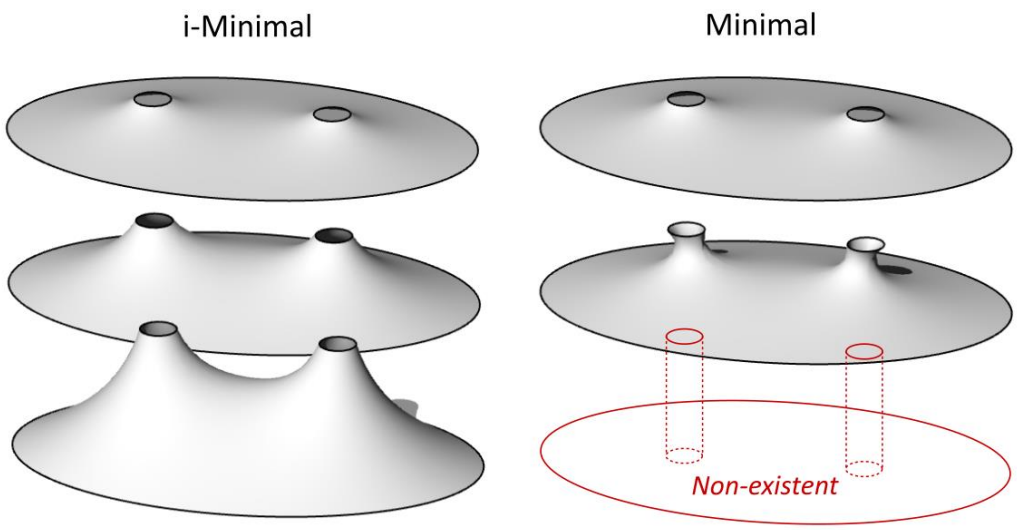

Figure 6.43: Comparison of the shape of i-minimal and minimal membranes on three sets of boundary curves, with increasing height difference.

i-LW membranes do not require that the isotropic direction is vertical: whatever the direction, they correspond to a self-stressed membrane geometry. Therefore, on a given boundary, the isotropic direction can be tilted to explore shape variations. An example is shown in Figure 6.44, where three i-minimal surfaces are generated on the same boundaries (two coaxial circles), but with different isotropic directions (indicated by red arrows). In each case, the stresses projected in the plane perpendicular to the red arrows are constant.

Figure 6.44: i-minimal membranes constructed on the same boundary, but with different isotropic directions

6.10.2 Gridshells

As discussed in section 6.8, for a gridshell, i-principal curvature directions of i-LW surfaces have both fabrication and mechanical properties. An application is illustrated in Figure 6.45. An i-CMC surface is generated on a boundary composed of four closed curves. An i-principal curvature net is computed, and is used to define the position and orientation of the beams of a gridshell. Since the i-principal net forms a conjugate curve network, mesh faces are almost planar (an optimization could make them exactly planar with small vertex displacements). Furthermore, beams are aligned with principal stress directions under uniform vertical pressure (snow load), so they have a relevant orientation. Finally, we can notice that pattern drawn by i-curvature lines is smooth, and gives faces with approximately uniform size.

If one were to search by optimization of vertex positions the geometry of a gridshell combining planar quads and beams aligned with principal stresses, a main question would be: what is the right mesh combinatorics to start with? In i-LW, this combinatorics appears naturally from the curvature field.

Also, if one were to draw i-principal curvature lines on an arbitrary surface (not i-LW), one would also get a planar quad mesh, but that net would most likely have an inefficient beam orientation and a high variation of edge lengths.

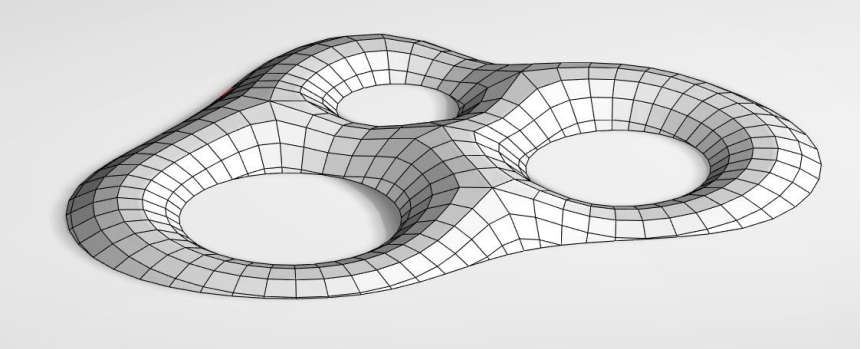

Figure 6.45: Funicular gridshell with planar quads, constructed by discretizing an i-CMC surface along i-principal curvature directions

6.10.3 Funicular shells

i-LW surfaces can also be used to design funicular shells. The method allows a quick exploration of a 2-parameter family of funicular surfaces fitting a target boundary. For a concrete shell, the fact that i-principal curvature lines form a conjugate net could be used to simplify the fabrication of formwork. For example, the surface can be covered with developable strips so that thin flexible panels can be used as formwork.

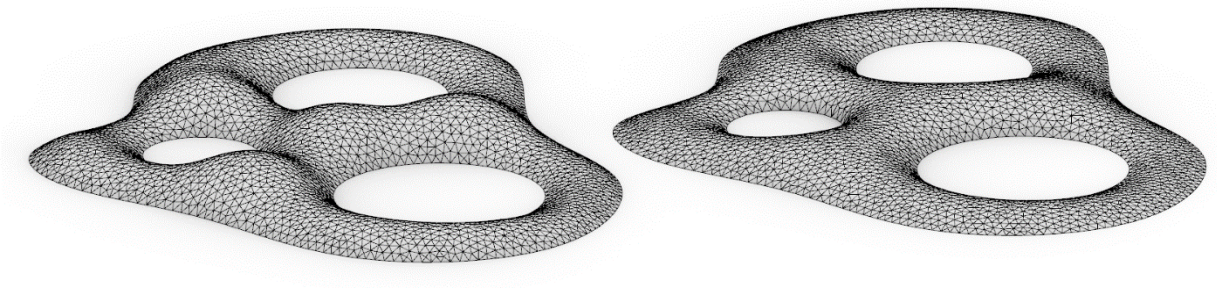

Figure 6.46: i-LW surfaces generated on the same boundaries as the gridshell of Figure 6.45. Left: b>0. Right: b<0, close to the limit $a^2+4bc=0$

The effect of parameters b and c on the surface geometry is similar to the Euclidian case. Parameter c allows to more or less inflate the surface (with a pressure acting vertically), while parameter b allows the control of the height difference between saddles and hill tops. This is illustrated in Figure 6.46, in which the reference surface of Figure 6.45 (which is i-CMC) is deformed. The left picture shows the case $b<0$: the surface looks like domes connected by low corridors. The right picture shows the case $b>0$: the surface now looks level, a more unified space is defined underneath.

Part C - Discussions

6.11 Towards a unification of isotropic and Euclidian LW surfaces

Looking at Figure 6.43, one could legitimately wonder if there exist surfaces "between" isotropic and Euclidian surfaces LW surfaces. It would be interesting for design purposes to have controllable parameters that allows a smooth exploration of the intermediate surfaces. In particular, for a self-stressed membrane, the isotropic direction need not be vertical (as we are interested by the unloaded state). We would then obtain a way to deform a minimal surface in any given direction while keeping its boundary fixed.

One obvious family of surfaces that accomplishes that are the surfaces verifying $a^e H + b^e K + a^i H^i + b^i K^i = c$, with $a^e, b^e, a^i, b^i, c \in \mathbb{R}$. However, there is no guarantee that these surfaces enjoy similar mechanical properties as LW and i-LW. Furthermore, this point of view can only deal with surfaces that are height fields.

Intuition for an interesting mechanical unification can be found in lower dimension, by studying funicular arches and cables. It is well known that circular arches are funicular under uniform normal pressure, and parabolic arches are funicular under uniform vertical forces. They are respectively CMC and i-CMC curves of the plane. Both of these curves are special ellipses: a circle is an ellipse where the two focal points are superposed, while a parabola can be seen as an ellipse with the second focal point at infinity. It turns out that ellipses are also funicular for one particular load:

Proposition 6.6 – Funicularity of ellipses
An elliptical cable is funicular under a distributed load:

- With direction aligned with a focal point;
- With constant angular pressure q (in kN/rad) from the focal point.

The tension force in the cable is given by $T = q\sqrt{e^2 + 2e\cos\theta + 1}$ for an ellipse of eccentricity e (Figure 6.49).

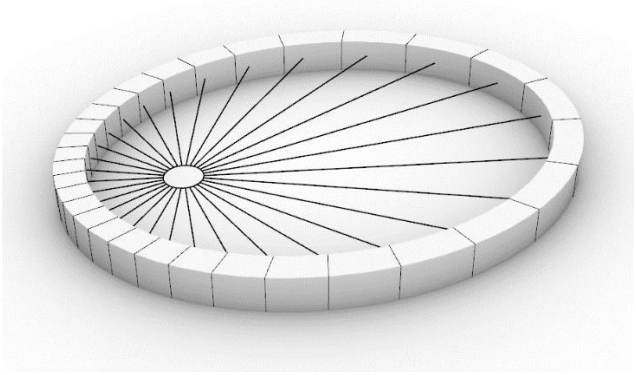

Figure 6.47: A funicular elliptical arch tensioned by radial cables emanating from a focal point with constant cable tension

We postpone the proof to the end of the section. In the special case of the circle and the parabola, we recover the traditional results under uniform pressure or vertical force. This proposition suggest to look for the unified family by considering an ellipsoid of revolution of vertical axis as a Gauss image, and to define the generalized LW surfaces using the relative curvatures with respect to this ellipsoid. This could be explored in future work.

Apart for its application to LW surfaces, this proposition is also interesting for the design of funicular structures. For example, an elliptical arch tensioned by cables emanating from a focal point with constant angle between the cables and constant cable tension is funicular. This is illustrated in the structure shown in Figure 6.47. The radial cables are connected to a circular cable at the focal point: A simple way to insure that the radial tension is uniform is to make sure that the center cable is circular. Compression in the arch can be analytically estimated. Its distribution for various eccentricities is shown in Figure 6.49.

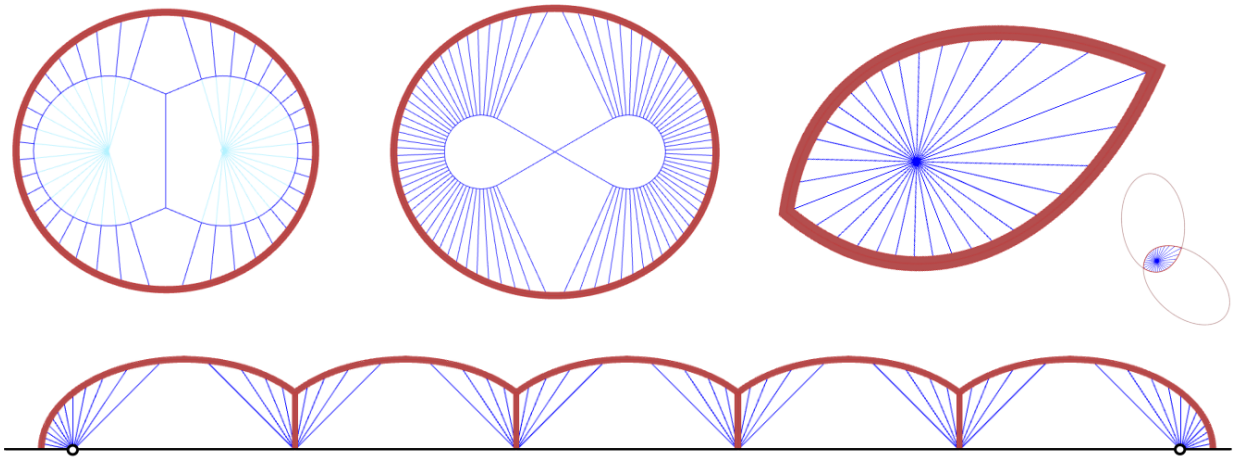

Figure 6.48: Self-stressed funicular structures composed of elliptical arches.
Red: Compression elements. Dark blue: Tension elements. Black: Supports

This proposition is true for the two focal points. Hence ellipses are funicular under two different load cases, which is remarkable. This property is used in Figure 6.48 (top left) to design a funicular arch pretensionned from the two focal points. We use the fact that the two loads cases (one for each focus) give the same axial force at the apex: this allows to pretension the left half from the left focus, and the right half from the right focus. An intermediate vertical cable is necessary to close the circular cables. For the sole purpose of structural delight, this geometry can be tweaked such that this vertical cable is not necessary – closing of cables being realized as an 8-loop (top middle image). Arches from ellipses sharing a common focus but with axes at different angles can be joined as shown in the top right image. The two arches press against each other with the same force because of the symmetry. At the junction of the two arches, because of the lateral push of the arches, the cable takes more tension than its neighbours. Remarkably, this lateral push has the same value at both ends, despite their different slope. This is due to the fact that the projected tension on a radial axis (T_r) as a π-periodic amplitude, as will be shown in the proof. This allows the structure to be indeed self-stressed. The bottom picture shows how ellipses can be joined in series. Bottom of piles are located at focal points. Only the extreme two focii need to withstand lateral loads. An interesting aspect of the proposition is that these structures were designed with simple geometrical rules, without calculation of advanced form-finding software.

The proposition also implies that parabolas are funicular for two load cases: the well-known vertical force, but also for a load emanating from their focal point. This property can be used for example to pretension a parabolic arch. The proposition can also most likely be extended to hyperbolas, this will be addressed in future work.

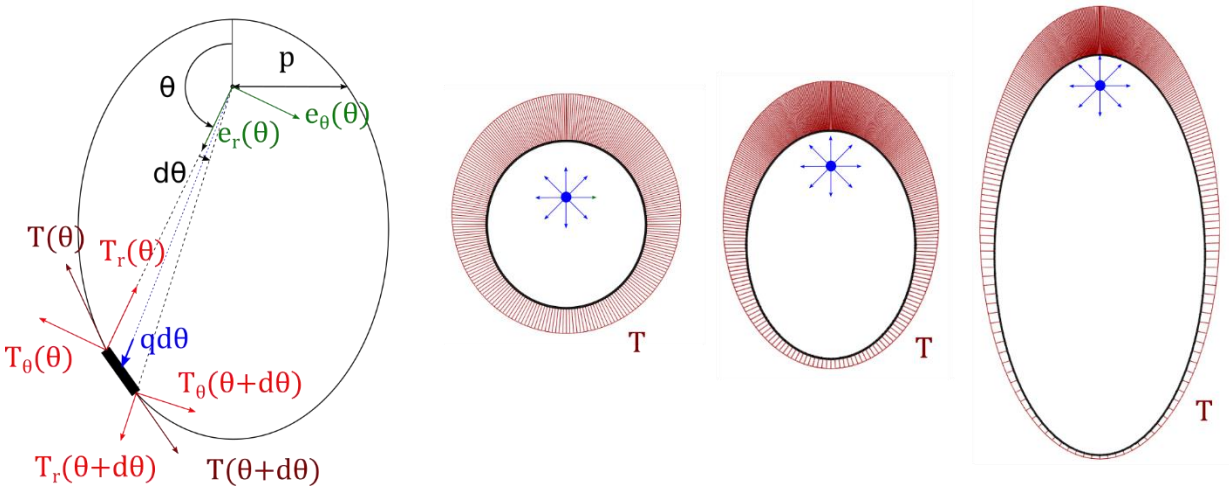

Figure 6.49: Equilibrium of a segment of ellipse under a focal load. Right: distribution of the tension for various eccentricities

Proof of proposition 6.6:

Let us consider an elliptical cable with polar parametrization from a focal point as shown in Figure 6.49:

$$r(\theta) = \frac{p}{1 + e\cos\theta}$$

Where $0 < e < 1$ is the eccentricity and p is shown in Figure 6.49. We use the local orthogonal frame polar frame $(\boldsymbol{e_r}, \boldsymbol{e_\theta})$.

Let us consider radial load emanating from a focal point with constant angular intensity. This means that a segment of aperture $d\theta$ is subjected to a load $qd\theta\boldsymbol{e_r}$ where q is constant. We look for an admissible tension field $\boldsymbol{T}$ in the cable, of amplitude T. We decompose the tension into its radial part T_r and its orthoradial part T_θ, such that $\boldsymbol{T} = T_r\boldsymbol{e_r} + T_\theta\boldsymbol{e_\theta}$.

Analysis

Let us look at the equilibrium of an infinitesimal portion of arch of aperture $d\theta$. Such a tension field must verify equilibrium of moments about the focal point. Keeping only the first order terms, this equilibrium reads:

$$r(\theta)T_\theta(\theta) = r(\theta + d\theta)T_\theta(\theta + d\theta)$$
$$0 = r\, dT_\theta + dr\, T_\theta$$
$$\frac{dT_\theta}{T_\theta} = -\frac{dr}{r}$$

After integration:

$$T_\theta = C/r$$

Where C is a constant, homogenous to a torque.

The tension field must also verify the radial equilibrium, which reads at first order:

$$q\, d\theta + T_r(\theta + d\theta) - T_r(\theta) - T_\theta(\theta + d\theta)d\theta = 0$$
$$dT_r = (T_\theta(\theta) - q)\, d\theta = \left(\frac{C}{p}(1 + e\cos\theta) - q\right) d\theta$$

Integrations yields:

$$T_r = T_0 + \left(\frac{C}{p} - q\right)\theta + \frac{Ce}{p}\sin\theta$$

Where T_0 is a constant. To obtain a periodic tension field, we must have $C = qp$. As a result:

$$T_r = T_0 + qe\sin\theta$$

And T_θ must be of the form $T_\theta = q(1 + e\cos\theta)$

Finally, the tension must fulfill the orthoradial equilibrium (i.e. the equilibrium projected on $\boldsymbol{e_\theta}$. Again, we discard all second order terms:

$$-T_\theta(\theta) + T_\theta(\theta + d\theta) + T_r(\theta + d\theta)d\theta = dT_\theta + T_r d\theta$$
$$= (-qe\sin\theta + T_0 + qe\sin\theta)d\theta$$

We have equilibrium if $T_0 = 0$.

Synthesis

We have found a tension field $\boldsymbol{T} = T_r\boldsymbol{e_r} + T_\theta\boldsymbol{e_\theta}$ with $T_r = qe\sin\theta$ and $T_\theta = q(1 + e\cos\theta)$ at equilibrium with the load. Let us now check that it is aligned with the cable. The cable orientation is given by the tangent vector, which is given in polar coordinates by:

$$\boldsymbol{t} = \frac{dr}{d\theta}\boldsymbol{e_r} + r\boldsymbol{e_\theta} = \frac{e\sin\theta}{1 + e\cos\theta}\, r\, \boldsymbol{e_r} + r\, \boldsymbol{e_\theta}$$

We check colinearity by calculating the cross product:

$$\|\boldsymbol{T} \wedge \boldsymbol{t}\| = \left\| qe\sin\theta\, r - \big(q(1 + e\cos\theta)\big)\frac{e\sin\theta}{1 + e\cos\theta}\, r \right\| = 0$$

The tension field is indeed aligned with the cable.

The value of the tension is given by $T^2 = T_r^2 + T_\theta^2$:

$$T = q\sqrt{e^2 + 2e\cos\theta + 1}$$

We remark that this formula yields the classical results for tension in circles, for which $e = 0$. Indeed, we then get $T = q$. We can convert the angular load into a normal lineic load in kN per meter by looking at a portion of arc of length ds:

$$\mu\, ds = q\, d\theta \;\Rightarrow\; \mu = qk$$

Where k is the curvature. We obtain: $T = \frac{\mu}{k}$, a well-known formula.

Finally, we note that $T_\theta = qp/r$ can be seen as a generalisation of the fact that circles are funicular with a uniform tension and parabolas with a uniform projected tension on the x axis.

6.11.1 Behavior under non-uniform loads

LW surfaces have a remarkable mechanical behavior under uniform pressure (or uniform vertical load for i-LW surfaces). However, real structures are subjected to a large variety of loads. This section presents a brief case study to analyze the mechanical behavior of the LW shell showed in Figure 6.50 under asymmetrical load. We study in particular:

- Whether the shape is still funicular. We check this by looking at the ratio of membrane energy over bending energy.
- Whether the principal stresses are still aligned with principal curvature directions.

Numerical model

The shell is 30m wide, 7m high and 5cm thick. It is made of C30 concrete, and simply supported at the boundaries (translations are blocked for each boundary node, but not rotations). A normal pressure p=4kPa is applied. A linear elastic analysis is performed with the software Karamba3D™ for Rhino/Grasshopper. Shell elements are a modified version of the flat triangular TRIC finite elements, in which shear deformations are neglected (Preisinger 2016).

Results of finite element analysis

Under uniform pressure (Figure 6.50, bottom left), the bending energy is less than 50 times lower than the membrane energy: The shell is indeed funicular. We observe a very good alignment of principal membrane stresses with principal curvature directions. Only a small deviation can be observed in the saddle portion.

If a small pressure 0.1p is added on half of the structure (Figure 6.50, bottom middle), the behavior does not change. However, for an asymmetric pressure of 0.25p, we observe a sudden deviation of principal stresses. Nevertheless, the ratio of energy membrane/bending is still very high, above 40.

If the pressure is entirely asymmetric (Figure 6.50, bottom right), principal curvature and principal stresses are not aligned at all anymore. Furthermore, bending is not negligible anymore, as the bending energy is 1/7.3 of the membrane energy.

Comments

The fact that principal stresses are not exactly aligned with principal curvature directions in the case of a uniform pressure may have the following causes, all due to the finite element model:

- The surface is discretized by flat triangles with very simple deformation modes (the simplified TRIC elements). The kinks probably influence the stress orientations;
- Supports are not perfectly compatible with a membrane behavior: out-of-plane shear can be transmitted, this results in the small amount of flexion observed.

In the case of the asymmetric load 0.25p, it might seem surprising to have such a misalignment of principal stresses and principal curvature directions despite the low asymmetry of the loads. However, it must be noted that the stresses in the domes are nearly isotropic under uniform pressure. Therefore, a very small variation of stresses can induce a large variation of the orientation of the principal stresses.

In the case of the fully asymmetrical load, the orientation of principal stresses differs a lot from principal curvature directions. However, one would not design a structure for an asymmetric load acting only on the right side. If one wants to design a gridshell, orienting the bar along the principal curvature lines of this LW surface would apparently offer a good compromise to resist the following three load cases: a uniform load, a load on the left half, and a load on the right half.

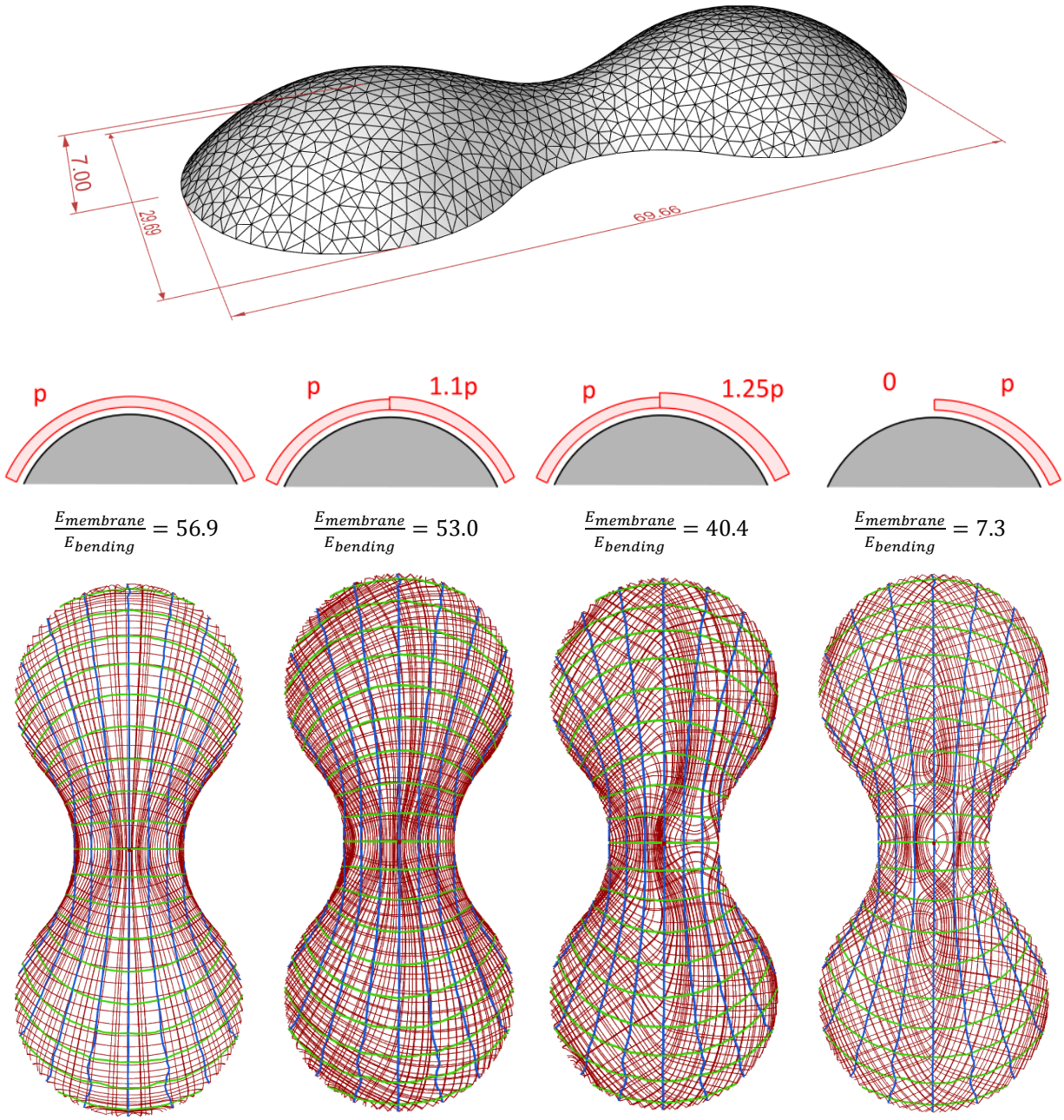

Figure 6.50: Alignment of principal stress directions (in red) and principal curvature lines (blue and green)

6.11.2 Elastic deformations

LW surfaces admit an admissible stress field under uniform pressure. They correspond to equilibrium shapes in a *deformed* configuration. However, there is no guaranty that these surfaces can be obtained exactly by elastic deformation of an initially stress-free material configuration. The study of this problem could be addressed in future work. However, in the considered applications, an exact compatibility of membrane deformations is not required:

- In the case of a funicular shell, displacements are very small. If the initial state is LW, the deformed state will be nearly LW. The LW stress field can then be used for limit analysis, for example for checking that a funicular surface can be found within the middle third of the cross section of a masonry shell (Heyman 1997). In the case of a concrete shell, the surface also does not need to be exactly LW, as it can accommodate some bending.

- In the case of a tensile membrane, our approach is similar to popular methods such as force densities or dynamic relaxation method: Both methods also yield a deformed configuration at equilibrium. Potential incompatibilities are usually not a problem, because patterning and pretensioning is an approximate task anyway: tension is applied in warp and weft directions to membrane patches, so the actual deformed configuration is always a bit different from the target surface. In worst case, this leads to small waves on the surface.

6.12 Implementation details

- The algorithms were implemented by scripting the software Rhino/Grasshopper. All the numerical images of this section were generated from that script.
- In the current setup, a designer can interactively deform a surface by controlling parameters. It takes about 15 seconds to deform a mesh with 500 vertices to a near LW surface on a 3.5GHz CPU with 16Go of RAM. Full convergence (displacements below 1/1000 of surface dimensions) takes about a minute, but could be made much faster by 1/ not displaying intermediate calculation steps and 2/ using a more advanced solver, like L-BFGS.
- A remeshing tool was implemented. It performs an edge flipping when a vertex is found inside the circumscribed of a neighbour triangle (more precisely, if the projection of the vertex is in the circle). This remeshing is particularly necessary for surfaces with cables: The boundary can undergo large deflections the adjacent triangles may have a high anisotropy without remeshing. Remeshing is manually triggered by the user.
- The linear algebra package Math.net numerics is used to diagonalize curvature and stress matrices.
- Principal nets are computed with the software Evolute Tmap. Principal curvatures in the triangular mesh of Figure 6.25 are computed with the plugin Dodo for Grasshopper, which implements the algorithm of (Rusinkiewicz 2004).
- i-Principal net in Figure 6.45 is computed in three steps:
    1. The surface is scaled down in z direction to make it very shallow. In this state, principal and i-principal directions nearly coincide.
    2. A principal net is computed with Evolute Tmap.
    3. The net and the surface are scaled back in the z direction to fit the original geometry. We use the fact that i-principal directions are invariant under z scaling (the eigenvectors of $\nabla^2 f$ are the eigenvectors of $\lambda\nabla^2 f$ (with $\lambda \in \mathbb{R}$)).

6.13 Summary of contributions

This chapter introduced a generation method for LW surfaces from a boundary, thus making their many geometrical and mechanical properties accessible to designers.

Part A presented a variational method to generate elliptical LW surfaces. The method allows to generate classical surfaces such as minimal, CMC, developable and synclastic constant Gaussian curvature surfaces in a common framework. It offers a designer one degree of freedom to deform globally a minimal or CMC surface. The resulting surfaces have direct applications for form-finding of membranes and for the design of gridshells without bracing cables. To allow this, new discrete models of LW surfaces and vertex Gaussian curvature were introduced. Also, a subdivision of LW surfaces into two disjoint families was highlighted.

Part B showed that the mechanical properties of LW surfaces can be extended to the isotropic LW surfaces: these are funicular under a uniform vertical load, and the projected principal stresses are aligned with principal isotropic curvature directions. As a result, they also combine mechanical and fabrication properties for a gridshell, and correspond to self-stressed membrane shapes in the case c=0. A generation method from boundaries was presented.

Part C compared the geometry of LW and i-LW surfaces, and proved that ellipses are funicular under radial loads emanating from a focus. This offers a unified point of view of CMC and i-CMC curves of the planes. Beyond applications to the design of funicular arches and cable systems, this opens the way to the search of a unifying family of LW and i-LW surfaces with similar mechanical properties.

References

Andrews, B. (2000) 'Motion of hypersurfaces by Gauss curvature', *Pacific Journal of Mathematics*, 195(1), 1–34.

Benamou, J.D., Froese, B.D., Oberman, A.M. (2010) 'Two numerical methods for the elliptic Monge-Ampère equation', *ESAIM: Mathematical Modelling and Numerical Analysis*, 44(4), 737–758.

Billington, D. (1965) *Thin Shell Concrete Structures*, McGraw-Hill.

Bletzinger, K., Ramm, E. (1999) 'A General Finite Element Approach to the Form Finding of Tensile Structures by the Updated Reference Strategy', *International Journal of Space Structures*, 14(2), 131–145.

Block, P. (2009) *Thrust Network Analysis. Exploring Three-Dimensional Equilibrium*.

Bobenko, A.I., Suris, Y.B. (2008) 'Discrete differential geometry. Integrable Structure.', *Graduate Studies in Mathematics*, 98.

Borrelli, V., Cazals, F., Morvan, J.M. (2003) 'On the angular defect of triangulations and the pointwise approximation of curvatures', *Computer Aided Geometric Design*, 20(6), 319–341.

Botsch, M., Kobbelt, L., Paully, M., Alliez, P., Lévy, B. (2010) *Polygon Mesh Processing*, AK Peters/CRC Press.

Bouaziz, S., Deuss, M., Schwartzburg, Y., Weise, T., Pauly, M. (2012) 'Shape-Up : Shaping Discrete Geometry with Projections', *Eurographics Symposium on Geometry Processing*, 31.

Brakke, K.A. (1992) 'The surface evolver', *Experimental Mathematics*, 1(2), 141–165.

Caffarelli, L., Nirenberg, L., Spruck, J. (1984) 'The dirichlet problem for nonlinear second-order elliptic equations I. Monge-ampégre equation', *Communications on Pure and Applied Mathematics*, 37(3), 369–402.

Candela, F. (1955) 'Structural applications of hyperbolic paraboloidical shells', *ACI Journal Proceedings*, 51(1), 397–416.

do Carmo, M.P. (1976) *Differential Geometry of Curves and Surfaces*, Prentice-Hall, Inc.

Cartan, H. (1963) *Elementary Theory of Analytic Functions of One or Several Complex Variables*, Editions s. ed, Addison-Wesley Inc.

Chen, H., Lee, I., Leopoldseder, S., Pottmann, H., Randrup, T., Wallner, J. (1999) 'On Surface Approximation using Developable Surfaces', *Graphical Models and Image Processing*, 61(2), 110–124.

Cohen-steiner, D., Morvan, J.-M. (2006) 'Differential geometry on discrete surfaces', in *Effective Computational Geometry for Curves and Surfaces*, 157–179.

Corro, A.V., Ferreira, W., Tenenblat, K. (2003) 'Ribaucour transformations for constant mean curvature

and linear Weingarten surfaces', *Pacific Journal of Mathematics*, 212(2).

Courant, R., Hilbert, D. (1962) *Methods of Mathematical Physics - Volume II - Partial Differential Equations*, Engineering Analysis with Boundary Elements, Wiley-VCH Verlag.

Crane, K. (2013) 'Discrete differential geometry: An applied introduction', in *SIGGRAPH 2013 Course Notes*, available: https://www.cs.cmu.edu/~kmcrane/Projects/DDG/paper.pdf.

Dean, E.J., Glowinski, R. (2003) 'Numerical solution of the two-dimensional elliptic Monge-Ampère equation with Dirichlet boundary conditions: An augmented Lagrangian approach', *Comptes Rendus Mathematique*, 336(9), 779–784.

Dean, E.J., Glowinski, R. (2004) 'Numerical solution of the two-dimensional elliptic Monge-Ampère equation with Dirichlet boundary conditions: A least-squares approach', *Comptes Rendus Mathematique*, 339(12), 887–892.

Deuss, M., Deleuran, A.H., Bouaziz, S., Deng, B., Piker, D., Pauly, M. (2015) 'ShapeOp—A Robust and Extensible Geometric Modelling Paradigm', *Modelling Behaviour*, 505–515, available: http://link.springer.com/10.1007/978-3-319-24208-8_42.

Douthe, C. (2007) *Etude de Structures Élancées Précontraintes En Matériaux Composites , Application à La Conception Des Gridshells*.

Eisenhart, L.P. (1909) *A Treatise on the Differential Geometry of Curves and Surfaces*, Ginn and Company Proprietors, Boston USA.

English, E. (2008) 'Animating Developable Surfaces using Nonconforming Elements', *Transactions on Graphics*, 27(3).

Firey, W.J. (1974) 'Shapes of worn stones', *Mathematika*, 21(1), 1–11.

Frey, F., Studer, M.-A. (2003) *Traité de Génie Civil, Volume 5 - Analyse Des Structures et Milieux Continus - Coques*, Presses polytechniques et universitaires romandes.

Giaquinta, M., Hildebrandt, S. (1996) *Calculus of Variations I - Grundlehren Der Mathematischen Wissenschaften 310*, Springe-Ve. ed.

Giomi, L., Mahadevan, L. (2012) 'Minimal surfaces bounded by elastic lines', *Proceedings of the Royal Society A: Mathematical, Physical and Engineering Sciences*, 468(2143), 1851–1864.

Glymph, J., Shelden, D., Ceccato, C., Mussel, J., Schober, H. (2004) 'A Parametric Strategy for Freeform Glass Structures Using Quadrilateral Planar Facets', *Automation in Construction*, 13(2), 187–202.

Gray, A. (1998) *Modern Differential Geometry - Curves and Surfaces with Mathematica*.

Hartman, P., Wintner, A. (1954) 'Umbilical Points and W-Surfaces', *American Journal of Mathematics*, 76(3), 502–508, available: https://www.jstor.org/stable/2372698.

Hertrich-Jeromin, U., Mundilova, K., Tjaden, E.H. (2015) 'Channel Linear Weingarten Surfaces', *Journal of Geometry and Symmetry in Physics*, 40(July), 25–33.

Heyman, J. (1997) *The Stone Skeleton: Structural Engineering of Masonry Architecture*, Cambridge University Press.

Hincz, K., Gaspar, Z. (1999) 'The effect of the apporximations used during generation of membrane cutting pattern.pdf', *Archives of Civil Engineering*, 45(2), 221–230.

Hopf, H. (1983) *Differential Geometry in the Large, Lecture Notes in Math.*

Jimenez, M.R., Müller, C., Pottmann, H. (2019) 'Discretizations of surfaces with constant ratio of principal curvatures', *Discrete & Computational Geometry*.

Kilian, M., Pellis, D., Wallner, J., Pottmann, H. (2017) 'Material-minimizing forms and structures', *ACM Transactions on Graphics*, 36(6).

Leduc, N., Caron, J.F., Douthe, C., Vaudeville, B., Aubry, S. (2018) 'An Innovative Fabrication Process from Rolled Helicoidal Steel Strips', in *40th IABSE Symposium, Tomorrow's Megastructures*, S14,15-S14,32.

Lopez, R. (2013) *Constant Mean Curvature Surfaces with Boundary*, Springer-V. ed, Springer-Verlag.

López, R. (2008) 'Rotational linear Weingarten surfaces of hyperbolic type', *Israel Journal of Mathematics*, 167(1), 283–301.

Oberman, A.M. (2008) 'Wide stencil finite difference schemes for the elliptic Monge-Ampère equation and functions of the eigenvalues of the Hessian', *Discrete Contin. Dyn. Syst. Ser. B,* 10(1), 221–238.

Ogrenmis, A.O. (2016) 'Rotational Surfaces in Isotropic Spaces Satisfiying Weingarten Conditions', *Open Physics*, 14(1), 221–225, available: http://arxiv.org/abs/1604.00773.

Overgaard, N.C., Solem, J.E. (2007) 'The Variational Origin of Motion by Gaussian Curvature', *International Conference on Scale Space and Variational Methods in Computer Vision*, 430–441.

Pan, H., Choi, Y.-K., Liu, Y., Hu, W., Du, Q., Polthier, K., Zhang, C., Wang, W. (2012) 'Robust modeling of constant mean curvature surfaces', *ACM Transactions on Graphics (TOG)*, 31(4), 11–85.

Pelikan, J. (1958) 'Membrane structures', in A., A.-J. and Al., E., eds., *Proc of the Second Symp. on Concrete Shell Roof Construction, Teknisk Ukeblan, Oslo*.

Pérez, J., Otaduy, M.A., Thomaszewski, B. (2017) 'Computational design and automated fabrication of Kirchhof-Plateau surfaces', *ACM Transactions on Graphics*, 36(4).

Pottmann, H., Asperl, A., Hofer, M., Kilian, A. (2007) *Architectural Geometry*, Bentley Institute Press.

Pottmann, H., Liu, Y. (2007) 'Discrete Surfaces in Isotropic Geometry', *Methods*, (i), 341–363.

Preisinger, C. (2016) *Karamba User Manual, Version 1.2. 2*, http://twl.uni-ak.ac.at/karamba/.

Rabinovich, M., Hoffmann, T., Sorkine-hornung, O. (2018) 'Discrete Geodesic Nets for Modeling Developable Surfaces', *Transactions on Graphics*, 37(2).

Reilly, R. (1973) 'Variational properties of functions of the mean curvatures for hypersurfaces in space forms', *J. Differential Geom*, 8, 465–477, available: http://intlpress.com/JDG/archive/pdf/1973/8-3-465.pdf.

Rellich, F. (1933) 'Zur erssten Randwertaufgabe bei Monge-Ampkreuchen bill-erentialgleichungen vom elliptischen Typus; differentialgeometrische Anwendungen', *Math. Ann.*, 107, 505–513.

Rogers, C., Schief, W.K. (2003) 'On the equilibrium of shell membranes under normal loading. Hidden integrability', *Proceedings of the Royal Society A: Mathematical, Physical and Engineering Sciences*, 459, 2449–2462.

Romon, P. (2013) *Introduction à La Géométrie Différentielle Discrète (Introduction to Discrete Differential Geometry)*, Ellipses.

Rose, K., Sheffer, A., Wither, J., Cani, M., Thibert, B. (2007) 'Developable Surfaces from Arbitrary Sketched Boundaries', *Eurographics Symposium on Geometry Processing*, 163–172.

Rusinkiewicz, S. (2004) 'Estimating Curvatures and Their Derivatives on Triangle Meshes', *Symposium on 3D Data Processing, Visualization, and Transmission*, sep.

Sachs, H. (1990) *Isotrope Geometrie Des Raumes*, Vieweg. ed.

Strubecker, K. (1962) 'Airysche Spannungsfunktion und isotrope Differentialgeometrie', *Mathematische Zeitschrift*, 78(1), 189–198.

Tso, K. (1985) 'Deformation of a surface by its Gauss Kronecker curvature', *Communications on Pure and Applied Mathematics*, XXXVIII, 867–882.

Van-Brunt, B., Grant, K. (1996) 'Potential applications of Weingarten surfaces in CAGD, Part I: Weingarten surfaces and surface shape investigation', *Computer Aided Geometric Design*, 13, 569–582.

Ventsel, E., Krauthammer, T. (2001) *Thin Plates and Shells. Theory, Analysis and Applications*, Marcel Dekker.

Vouga, E., Mathias, H., Wallner, J., Pottmann, H. (2012) 'Design of Self-supporting Surfaces', *ACM Trans.*

Graph., 31(4).

Wang, C.C.L. (2008) 'Towards flattenable mesh surfaces', *CAD Computer Aided Design*, 40(1), 109–122.

Wardetzky, M., Bergou, M., Harmon, D., Zorin, D., Grinspun, E. (2007) 'Discrete quadratic curvature energies', *Computer Aided Geometric Design*, 24(8–9), 499–518.

Weingarten, J. (1861) 'Über eine Klasse auf einander abwickelbarer Flächen (On a class of mutually developable surfaces).', *Journal für die reine und angewandte Mathematik*, 59, 382–393.

www.keramion.de (2019) Foundation KERAMION, Centre of Modern and Historical Ceramics in Frechen [online], available: http://www.keramion.de/ [accessed 10 Dec 2019].

Xu, Z., Xu, G. (2009) 'Discrete Schemes for Gaussian curvature and their convergence', *Computers & Mathematics with Applications*, 57(7), 1187–1195.

Yoon, D.W., Lee, J.W. (2016) 'Linear Weingarten helicoidal surfaces in isotropic space', *Symmetry*, 8(11), 1–7.

Zhao, H., Xu, G. (2006) 'Triangular surface mesh fairing via Gaussian curvature flow', *Journal of Computational and Applied Mathematics*, 195(1–2), 300–311.

Chapter 7 Conclusion and perspectives

7.1 Summary of results

Four new morphogenesis methods
This thesis has introduced four new generation methods to design curved surfaces. If a designer uses one of these methods, sets of geometrical properties are automatically obtained and allow a simplified fabrication of gridshells, plated shells, membranes or vaults.

Four sets of fabrication properties
Each method yields a specific set of properties. Caravel meshes and surfaces with planar curvature lines simplify the fabrication of all the components of a gridshell, with either discrete or continuous beams: cladding panels, beams and connections. S-CMC and linear Weingarten surfaces also include mechanical efficiency. They correspond to shapes of self-stressed membranes or funicular shells, and can therefore be used to design tensile membrane shapes or masonry vaults.

Three new geometrical structures
New mesh structure were introduced: Circular meshes with planar lines, Caravel meshes and triangular LW meshes. For each one, and also for S-CMC meshes, new geometrical properties were demonstrated. They were at core of the proposed generation methods and of the architectural properties.

Opening doors to new structural systems
Many structural applications were proposed, in particular for Caravel meshes and surfaces with planar curvature lines. They include simplified details, new ways to arrange standard construction elements into structurally efficient systems.

Two demonstration pavilions
Two full scale structures were constructed, and demonstrate the potential of hexagonal Caravel meshes to combine expressive forms with innovative structural details which allow to manage fabrication complexity.

Three ways to control the form
Three different generation methods are used: from section curves, from closed boundary curves, and from a surface. In each case, the method is adapted to the geometry of the problems.
Planar curvature lines and elliptical LW surfaces are highly constrained, such that they are entirely determined if constrained to a couple of curves, up to a few parameters. The former correspond to a hyperbolic partial differential equation, and is adapted to Cauchy problem (generation from an open boundary curve, equivalent to defining the initial configuration of a physical system); while the latter corresponds to an elliptical partial differential equation and is adapted to a Dirichlet problem (generation

from closed boundaries). Hexagonal Carvel meshes with edge offset are also well adapted to generation from a curve.
Hexagonal Caravel meshes, on the other hand, have low level of constraint. They can be generated from target surface, which leaves a lot of freedom to a designer.

Interactive design
The proposed method for surfaces with planar curvature lines allows generation in real time, by controlling two characteristic curves. A designer can therefore interactively manipulate the surface and come up with many possibilities. This is opposite to many post-rationalization algorithms that have been proposed in the literature, for which it will take a few minutes to get a single optimized solution.

Although not as fast, the method for Linear-Weingarten surfaces converges fairly quickly, and iterated shapes are visible, such that a designer can interactively shape the surface by modifying parameters and boundaries.

The algorithm for Caravel meshes is not real-time at the moment. There is a workflow to follow, which can take a few minutes once a user is familiar with it. However, as the pattern follows the curvature line network, a user can obtain a very good idea of the final pattern by drawing curvature lines, something that can be automatized and generated very quickly in a parametric software.

Although the algorithm for S-CMC is very fast in itself, some time might be necessary to find proper boundary conditions. The control by the boundary of the Gauss map is not intuitive, and requires some time to get familiar with.

A new conceptual design tool for membranes and vaults
The methods described in chapter 6 allow to quickly explore the vast shape domain of LW and i-LW surfaces. For a given project, they will most likely not give the optimal solution in terms of functionality, mechanics or fabrication. However, in a conceptual design phase, they allow a designer to quickly put some efficient shell and membrane solutions on the table, and to compare them with other concepts.

7.2 Future work

7.2.1 Caravel meshes

Despite the many ways that the two pavilions took advantage of the geometrical properties of the Caravel meshes, there are probably many more innovative structural applications to explore. One particular aspect is the potential they offer for structural use of cladding panels. Also, the questions related to waterproofness and insulation will need more research, and could result in a very cost effective solution for opaque façade.

The asymptotic method used to prove that Caravel meshes fulfil their properties at first order could also be used to design other torsion-free patterns for gridshells, in which beams are not necessarily aligned with curvature lines. Literature on torsion free nodes has most often combined it with a constraint on face planarity. However, this constraint is not relevant for example for ETFE cladding.

7.2.2 LW and CMC surfaces

Chapter 5 and 6 are the longest of the manuscript because CMCs and LW are rich topics. There are still many aspects to explore.

Firstly, the generation and properties of related surfaces could be studied. An example is hyperbolic LW surfaces: These surfaces have the same properties as elliptical ones, but give access to very different formal vocabulary. They could be generated from section curves directly by quadrangular meshes with fabrication properties, without the need for remeshing. Also, as discussed in section 6.11, there might be a family of surfaces that unifies LW and i-LW surfaces with similar mechanical properties. They could enrich significantly the membrane conceptual design tools presented in this thesis.

Secondly, generation methods could be improved. In particular, there is at the moment no variational formulation for LW surfaces with boundaries. This would allow a faster computation of LW membranes with boundary cables by means of more effective algorithms.

Thirdly, on a structural design perspective, the present method does not allow to account for lateral stability of vaults. A simple method to verify stability under lateral wind or seismic load is to tilt the entire vault and then check its funicularity (Gass and Otto 1990; Dejong 2009). Tilting is easily done with i-LW surfaces: One just needs to change the orientation of the isotropic axis. By tilting a vault in different directions, one could get an envelope of funicular meshes that, if included within the shell depth, would insure stability.

Also, CMC, LW and i-LW surfaces are highly efficient mechanically for ideal uniform load cases assuming linear behavior. Their relevance for actual loads, in particular in term of buckling strength, could be addressed in case studies. One could compare how far they are from a numerically optimized structure fitting the same boundaries.

7.2.3 Numerical tools

Even though little attention has been paid to algorithmic and coding details in the manuscript, implementation was a significant part of the work. In particular, many exceptions had to be addressed in the development of the scripts used to illustrate the various chapters. The proper treatment of these exceptions is necessary for a tool to be user-friendly. For example, in the algorithm to generate surfaces with planar curvature lines, if guide curves are straight lines, the code must return a rectangular patch. This cannot be done by the general method based on the Gauss map, and requires a specific piece of code. Although simple, dozens of other special cases needed to be also addressed. Their treatment has sometimes taken more time than the implementation of the core algorithm itself.

The main scripts developed for this thesis will be made available for use as plugins of the commercially available software Rhino/Grasshopper. In a second time, the intent is to make them available on a free computational framework under development at Ecole des Ponts.

7.2.4 Modularity

Most architectural projects are the fruit of composition of geometric primitives. This manuscript presented how new surfaces can enrich the family of available primitives. Composition of surfaces with planar curvature lines was briefly discussed in chapter 3, but a lot more could be done. By classifying surface patches and developing rules to connect them with various levels of smoothness, a shape grammar could be developed. The potential of grammar has been demonstrated for structural exploration in (Mueller 2014) and for patterning in (Oval 2019), and it is a common tool in surface reconstruction (Nishida *et al.* 2016). Such an approach, applied to design of curved envelope, would offer much more flexibility to a designer, and would unleash the full potential of the proposed methods.

7.2.5 New materials for physical models

Even the world's most amazing algorithm, if manipulated via a mouse and a screen, will not be as intuitive and provide an as rich experience as manipulating a physical model. Mockups are a ubiquitous design tool in architecture. Physical tools informing designer on the shapes and patterns that fulfill the desired fabrication properties are of great values. Some examples were given in chapter 2: hanging models, developable surfaces, and cloth nets for modeling Tchebychev meshes.

A further step in that direction was taken with the mockup shown in Figure 7.1. It is constituted of a particular type of drainage pipe that is flexible in bending, has bistable mechanisms to allow length variations, but yet offers a very high torsional stiffness. These pipes are connected at 90° by wooden cubes, to which they are clamped. Hence, they form a network of lines that is forced to behave like a curvature line network.

By manipulating it, one can actually feel with their hands the behavior of curvature lines. In particular, the effect of umbilics can be apprehended intuitively. The umbilic of index -1/2 allows to curve a structure such that three ridge lines meet, while the index +1/2 allows to greatly curve locally the surface, but cannot be placed on an anticlastic surfaces.

The idea behind this mockup could be developed to model other fabrication constraints. One interesting research direction is the use of flexible meta-materials. Meta-materials have a tailored micro-structure that gives them a specific mechanical behavior. Their development has been accelerated by new additive fabrication technics, as can be seen in the review proposed by (Bertoldi *et al.* 2017). There are most-likely many possible micro-structures that could replicate shapes constrained by fabrication.

Figure 7.1: Mockups that replicates the behavior of a curvature line network through mechanical constraints. Left: Without umbilics. Middle: Umbilic of index -1/2. Right: Umbilic of index +1/2

7.2.6 New constraints

New technologies, new fabrication technics and environmental concerns will bring new geometrical constraints, with specific design spaces to explore. Chapter 2 strived to highlight how seemingly different problems can be ruled by common geometrical principles. Some future problems will be solvable by current tools, but other will require new methods and new geometrical structures, and will guide us towards diving further and further in the *terras incognitas* of geometry.

7.3 Final note

This manuscript has proposed ways of making curved structure more accessible. More accessible to designers by introducing intuitive generation methods that help guaranteeing constructability. More accessible to all actors of a project, as the proposed surfaces are well defined primitives. One can describe their geometry precisely with simple words, such as “a surface with planar curvature lines fitting these two elevation curves” – something impossible with a NURBS. Ultimately, more accessible to owners and collectivities by decreasing fabrication and design costs, such that all society can enjoy their benefits.

References

Dejong, M.J. (2009) *Seismic Assessment Strategies for Masonry Structures*.

Gass, S., Otto, F. (1990) ‘Experiments.’, in *Number 25 in Mitteilungen Des Instituts Fr Leichte Flchentragwerke (IL). Stuttgart: Universit¨at Stuttgart*.

Mueller, C.T. (2014) *Computational Exploration of the Structural Design Space*.

Nishida, G., Garcia-Dorado, I., Aliaga, D.G., Benes, B., Bousseau, A. (2016) ‘Interactive sketching of urban procedural models’, *ACM Transactions on Graphics*, 35(4).

Oval, R. (2019) *Topology Finding of Patterns for Structural Design*.

Relevant publications by the author

Journal article (published)

Tellier, X., Baverel, O., Douthe C., Hauswirth, L. 2019, Surfaces with planar curvature lines: discretization, generation and application to the rationalization of curved architectural envelopes. *Automation in Construction, Vol 106*

Tellier, X., Zerhouni, S., Jami, G., Le Pavec, A., Lenart, T., Lerouge, M., Leduc, N., Douthe C., Hauswirth, L., Baverel, O., 2020, The Caravel heX-Mesh pavilion: Demonstration of a new rationalization strategy for curved envelopes. *Springer Nature Applied Sciences 2:781*

Tellier, X., Douthe C., Hauswirth, L., Baverel, O., 2020, Linear Weingarten membranes with funicular boundaries. *Structural Concrete, April 2020*

Journal articles (submitted)

Tellier, X., Douthe C., Hauswirth, L., Baverel, O., Generation of Linear-Weingarten surfaces.

Tellier, X., Douthe C., Hauswirth, L., Baverel, O., Caravel meshes: designing torsion free gridshells with perfect beam-panel contact.

Conference proceedings

Tellier, X., Douthe C., Hauswirth, L., Baverel, O., 2020, Designing membranes and funicular shells with planar facets using isotropic Linear Weingarten surfaces, *Advances in Architectural Geometry 2020 (accepted)*

Tellier, X., Douthe C., Hauswirth, L., Baverel, O., 2018, Discrete CMC surfaces for doubly curved building envelopes, *Advances in Architectural Geometry 2018*

Tellier, X., Hauswirth, L., Baverel, O., Douthe C., 2019, Linear Weingarten surfaces for conceptual design of double-curvature envelopes, *fib Conceptual Design Symposium 2019, Madrid*

Tellier, X., Baverel, O., Douthe C., Hauswirth, L. 2019, Fabrication-aware design of architectural envelopes using surfaces with planar curvature lines, *IASS Symposium 2019*

Tellier, X., Zerhouni, S., Jami, G., Le Pavec, A., Lenart, T., Lerouge, M., Leduc, N., Douthe C., Hauswirth, L., Baverel, O. 2019, Hybridizing vertex and face normals to design torsion free structures: application to the X-mesh pavilion *IASS Symposium 2019*

Tellier, X., Baverel, O., Douthe C., Hauswirth, L. 2019, Concevoir des structures à double courbure avec les surfaces Weingarten-Linéaires, *37e Rencontres Universitaires de Génie Civil de l'AUGC*

Tellier, X., Baverel, O., Douthe C., Hauswirth, L. 2018, Gridshells without kink angle between beams and cladding panels, *IASS Symposium 2018*

Douthe, C., Mesnil, R., Baverel, O., Gobin, T., Tellier, X., Ducoulombiers, N., Montagne, N. 2018, Design and construction of a shell-nexorade hybrid timber structure, *IASS Symposium 2018*